THE ROLE AND REGULATORY MECHANISMS OF NOX1 IN VASCULAR SYSTEMS

A Dissertation
Presented to
The Academic Faculty

by

Weiwei Yin

In Partial Fulfillment
of the Requirements for the Degree
Doctor of Philosophy in the
School of Bioengineering/Biomedical Engineering

Georgia Institute of Technology
August 2012

THE ROLE AND REGULATORY MECHANISMS OF NOX1 IN VASCULAR SYSTEMS

Approved by:

Dr. Eberhard O. Voit, Advisor
Department of Biomedical Engineering
Georgia Institute of Technology

Dr. Hanjoong Jo
School of Medicine
Emory University

Dr. Melissa L. Kemp
Department of Biomedical Engineering
Georgia Institute of Technology

Dr. Kathy K. Griendling
School of Medicine
Emory University

Dr. Manu O. Platt
Department of Biomedical Engineering
Georgia Institute of Technology

Date Approved: June 18, 2012

To Mom, Wei, Changyi and Changxuan

ACKNOWLEDGEMENTS

I would like to acknowledge Dr. Eberhard O. Voit, my advisor and mentor, for his invaluable guidance, constant encouragement, and unconditional support throughout my graduate studies. Without his kindness and willingness to give me a chance, it would have been impossible for me to come this far. He is always willing to share his experience with me, and I have learned innumerable lessons and insights from him not only on research but also on other academic and even life issues. I am especially thankful for his patience when I was stuck in research and when I made slow progress due to personal family reasons.

I would also like to extend my gratitude to all my committee members, Drs. Melissa Kemp, Manu Platt, Kathy Griendling, and Hanjoong Jo, for their support in my research and professional life. Each committee member has been extremely enthusiastic about my research. Their expert input has helped me significantly in completing my research goal.

I would like to thank my previous and current lab members: I-Chun Chou, Gautam Goel, Siren Veflingstad, Yun Lee, Zhen Qi, Jialiang Wu, and many others, for their useful advice in scientific discussions and generous help in sharing their technical skills.

Finally, I cannot thank enough my family members, both here in the US and back home in China, for their constant and unconditional support. I would like to express my deepest gratitude to my husband Jack Wei Chen, who has been always by my side and always being so positive to encourage me to pursue my professional goals.

TABLE OF CONTENTS

LIST OF TABLES

LIST OF FIGURES

LIST OF SYMBOLS

BH_4	Tetrahydrobiopterin
H_2O_2	Hydrogen peroxide
HOCl	Hypochlorous acid
$LO^{\cdot}$	Lipid radicals
$LOO^{\cdot}$	Lipid radicals
$NO^{\cdot}$ (or NO)	Nitric oxide
$O_2^{\cdot -}$	Superoxide
$OH^{\cdot}$	Hydroxyl radicals
$OONO^{-}$	Peroxynitrite

LIST OF ABBREVIATIONS

AngII	Angiotensin II
BST	Biochemical Systems Theory
BMP4	Bone Morphogenic Protein 4
CAT	Catalase
CGD	Chronic Granulomatous Disease
CLC-3	Chloride Channel 3
DPI	Diphenyleneiodonium
ECs	Endothelial Cells
EGFR	Epidermal Growth Factor Receptor
FBA	Flux Balance Analysis
GEFs	Guanine Exchange Factors
GMA	Generalized Mass Action
GPx	Glutathione Peroxidases
GSH	Glutathione
GSSH	Glutathione Disulfide
ICAM1	Intercellular Adhesion Molecule 1
IL-1β	Interleukin-1 Beta
JAK2	Janus Kinase 2
LSS	Laminar Shear Stress
MC1	Model Candidate 1
MC2	Model Candidate 2
MC3	Model Candidate 3
MGP	Matrix Gla Protein

MPO	Myeloperoxidase
NFκB	Nuclear Factor κB
Nox	NADPH oxidase
Nox1	NADPH oxidase 1
Nox2	NADPH oxidase 2
Nox4	NADPH oxidase 4
Nox5	NADPH oxidase 5
NOS	Nitric Oxide Synthase
eNOS	endothelial NOS
iNOS	inducible NOS
nNOS	neuronal NOS
OSS	Oscillatory Shear Stress
ODE	Ordinary Differential Equation
PDGF	Platelet Derived Growth Factor
PI3K	Phosphoinositide 3-Kinase
PIP_2	Phosphatidylinositol (4, 5)-bisphosphate
PIP_3	Phosphatidylinositol (3, 4, 5)-triphosphate
PKA	Protein Kinase A
PKC	Protein Kinase C
PMA	Phorbol-12-myristate-13-acetate
Prx	Peroxiredoxins
PTP	Protein Tyrosine Phosphatase
RASMCs	Rat Aortic Smooth Muscle Cells
RtRS	Ready-to-Respond State
ROS	Reactive Oxygen Species

SOD	Superoxide Dismutase
SMCs	Smooth Muscle Cells
TGF-β	Transforming Growth Factor-β
TNF-α	Tumor Necrosis Factor-α
ULS	Unidirectional Laminar Shear Stress
VCAM1	Vascular Cell Adhesion Molecule 1
VSMCs	Vascular Smooth Muscle Cells
VEGF	Vascular Endothelial Growth Factor
XDH	Xanthine Dehydrogenase
XO	Xanthine Oxidase
XOR	Xanthine Oxidoreductase

SUMMARY

As an important endogenous source of reactive oxygen species (ROS), NADPH oxidase 1 (Nox1) has received tremendous attention in the past few decades. It has been identified to play a key role as the initial "kindle," whose activation is crucial for amplifying ROS production through several propagation mechanisms in the vascular system. As a consequence, Nox1 has been implicated in the initiation and genesis of many cardiovascular diseases and has therefore been the subject of detailed investigations.

The literature on experimental studies of the Nox1 system is extensive. Numerous investigations have identified essential features of the Nox1 system in vasculature and characterized key components, possible regulatory signals and/or signaling pathways, potential activation mechanisms, a variety of Nox1 stimuli, and its potential physiological and pathophysiological functions. While these experimental studies have greatly enhanced our understanding of the Nox1 system, many open questions remain regarding the overall functionality and dynamic behavior of Nox1 in response to specific stimuli. Such questions include the following. What are the main regulatory and/or activation mechanisms of Nox1 systems in different types of vascular cells? Once Nox1 is activated, how does the system return to its original, unstimulated state, and how will its subunits be recycled? What are the potential disassembly pathways of Nox1? Are these pathways equally important for effectively reutilizing Nox1 subunits? How does Nox1 activity change in response to dynamic signals? Are there generic features or principles within the Nox1 system that permit optimal performance?

These types of questions have not been answered by experiments, and they are indeed quite difficult to address with experiments. I demonstrate in this dissertation that one can pose such questions and at least partially answer them with mathematical and computational methods. Two specific cell types, namely endothelial cells (ECs) and vascular smooth muscle cells (VSMCs), are used as "templates" to investigate distinct modes of regulation of Nox1 in different vascular cells. By using a diverse array of modeling methods and computer simulations, this research identifies different types of regulation and their distinct roles in the activation process of Nox1. In the first study, I analyze ECs stimulated by mechanical stimuli, namely shear stresses of different types. The second study uses different analytical and simulation methods to reveal generic features of alternative disassembly mechanisms of Nox1 in VSMCs. This study leads to predictions of the overall dynamic behavior of the Nox1 system in VSMCs as it responds to extracellular stimuli, such as the hormone angiotensin II. The studies and investigations presented here improve our current understanding of the Nox1 system in the vascular system and might help us to develop potential strategies for manipulation and controlling Nox1 activity, which in turn will benefit future experimental and clinical studies.

CHAPTER 1

INTRODUCTION

1.1 Overview

In the past decades, considerable research efforts have focused on studies of reactive oxygen species (ROS) and elucidated various aspects of their dynamics, including their possible endogenous sources, consuming pathways, regulatory mechanisms, and potential physiological and pathophysiological functions in different types of cells and tissues [1-6] (*see detailed discussion in section 1.2.1*). These studies have greatly broadened our knowledge about ROS, their specific properties, and features that are important at the molecular and cellular levels, and made us realize the importance of ROS not only as intra- and inter-cellular signaling molecules, but also as potentially contributing to a wide range of diseases [7-10]. Particularly prominent among these diseases are those of the cardiovascular system, such as hypercholesterolemia, cardiac hypertrophy, atherosclerosis, hypertension, heart failure, and, diabetes, which have been demonstrated by many experimental and clinical studies to involve ROS functionally in their initiation and genesis [5, 7-9, 11-15].

Within the healthy cardiovascular system, ROS plays an essential physiological role in maintaining cardiac and vascular integrity. Under physiological conditions, they are produced in a controlled manner at low concentrations and function as signaling molecules that affect specific redox sensitive pathways and genes and coordinate several integrated physiological responses [1, 6, 16-18] (*see detailed review in* [1, 17, 18]). Under pathophysiological conditions, increased ROS production leads to an unbalanced intracellular redox state, called “oxidative stress” [19] , which triggers deleterious processes that can potentially damage cell structures,

including lipids, proteins, and DNA [3, 20, 21]. Thus, ROS become mediators of vascular injury and inflammation in many cardiovascular diseases [22-24] (*see detailed discussion in section 1.2.4*). Further exploration of this increased ROS production revealed the involvement and contributions of several cellular components as potential endogenous sources of ROS, including xanthine oxidase, NADPH oxidase, endothelial nitric oxide synthase (eNOS), and damaged mitochondria [22, 25]. Among them, NADPH oxidase has been identified to play the key role as the initial "kindle," whose activation is crucial for amplifying ROS production by means of several propagation mechanisms [13, 25-28] (*see detailed discussion in section 1.2.5*).

NADPH oxidase (or simply called Nox) constitutes a family of enzymes that use NADPH and molecular oxygen as substrates to generate a specific amount of ROS [29]. Nox was first found in phagocytes of the innate immune system [30], but later also in other types of cells and tissues of vertebrates including humans [31]. To date, seven Nox homologues have been identified. Four are found in vasculature, namely, Nox1, Nox2, Nox4, and Nox5 [31-35]. These four Nox homologues have different vascular distributions, intracellular locations, subunit compositions, activation mechanisms, and thus exert distinct physiological functions [31, 32, 34-36] (*see section 1.2.2 for details*). Among them, Nox1 has received the most attention because it can be activated and regulated by many physiological and pathological stimuli [34, 37, 38], and therefore has been implicated in a number of cardiovascular diseases [27, 31, 34, 39-42].

The reported studies of the Nox1 system are extensive. Using modern techniques in molecular biology, these studies have identified several essential features of the Nox1 system in vasculature, including key molecular components, possible regulatory signals and/or signaling pathways, potential activation mechanisms, and a variety of stimuli to which Nox1 responds [31-

33, 37, 38]. This experimental and clinical information has greatly enhanced our understanding of the Nox1 system and enabled us to sketch a coarse picture of how individual Nox1 subunits are activated, translocate, and assemble into an active Nox1 enzyme. Nevertheless, although the basic components and interactions are known, the overall functionality and dynamic behavior of Nox1 in response to specific stimuli are not clear and neither are they easy to grasp intuitively.

Several reasons contribute to this difficulty. First, the structure of the Nox1 system is rather complicated, as it consists of different types of metabolic and signaling pathways, as well as several proteins and their interactions. These governing pathways and processes often operate at multiple time scales, ranging from seconds up to several hours, or even days, which renders the integration and understanding of overall system behaviors difficult. Second, Nox1 activity is coordinately regulated by different stimuli through distinct mechanisms. These regulatory mechanisms exist and interact with each other at different levels, including transcriptional and translational regulation, as well as signal-based modulation. The possibility that different stimuli can modulate Nox1 activity via distinct and/or shared regulatory pathways makes intuitive interpretations and predictions of the Nox1 dynamics unreliable. Finally, our knowledge about the disassembly mechanisms of Nox1 is scarce. However, as I will show in this dissertation, these mechanisms are crucial, as they reestablish the normal state of the system, which must quickly be ready for new signals.

To exert its proper function in signal transduction, Nox1 needs to reside, under unstimulated condition, in a state that one may call “Ready-to-Respond State” (or “RtRS”). In this state, Nox1 is prepared to receive signals and act on the ROS system in an effective and appropriate manner. After an input signal has triggered the Nox1 system and the system has

served its role as signal transducer, the active complex must be disassembled. , As it turns out (see later), the disassembly mechanisms of Nox1 determine how efficiently the Nox1 system can return to its RtRS and are therefore much more important than previously thought. One possible reason for previously neglecting this important aspect might be due to the limitations of current experimental designs and set-ups. Modern biochemical techniques have helped us to identify many proteins, and sometimes their intracellular concentrations. However, because experiments usually focus on concentration changes after a certain stimulus is added, they usually do not detect the dynamics of the material flux through each individual pathway, thus making the experimental identification of possible disassembly mechanisms difficult.

The limitations of experimental studies as well as the complicated structure of the Nox1 system suggest that we should complement the experimental studies with a different type of approach, which is afforded by mathematical modeling and computational analysis (*see details in section 1.3*). These computational and modeling approaches are designed to help us integrate and predict dynamic responses of complicated biological systems, propose and identify generic principles that are usually difficult to discover by experiments, and analyze and diagnose prominent features of ill-characterized model structures. I will show that, with the aid of these computational approaches, I will be able to answer some of questions regarding the organization of the Nox1 system that have not been answered by experiments and are often difficult to address.

Some unanswered open questions regarding the Nox1 system are the following. How is Nox1 activity differently regulated by distinct extracellular stimuli? What are the main regulatory and/or activation mechanisms of Nox1 systems in different types of vascular cells?

What are the potential disassembly pathways of Nox1? Are these pathways equally important for effectively reutilizing Nox1 subunits? How does the importance or role of individual recycling pathway change in response to different stimuli? How does the dynamics of Nox1 activity change in response to these stimuli? Are there generic features or principles for the Nox1 system that lead to optimal performance?

These types of questions are difficult to address with experiments, but I will demonstrate here that one can pose such questions and at least partially answer them with mathematical and computational methods. The investigation of these questions with computational modeling methods expands our knowledge of the regulatory functions of the Nox1 system in different vascular cells, improves our understanding of potential disassembly mechanisms of Nox1, characterizes the dynamic features of the Nox1 system responding to different extracellular stimuli, and might help us develop strategies of manipulating and controlling Nox1 activity, which in turn will benefit future experiments.

1.2 Biological Background

1.2.1 Reactive Oxygen Species in Vasculature: Introduction and Metabolism

The term "reactive oxygen species" (ROS) collectively refers to chemically-reactive molecules that are formed upon incomplete reduction of oxygen [3]. They are mainly generated as by-products of normal aerobic metabolism and exist in all cellular organisms, including both prokaryotes and eukaryotes. A term that is closely related to ROS is "free radical." Although these two terms are often interchangeably, they are not truly the same. Free radicals are any atoms, molecules, or irons with unpaired electrons on an open shell configuration [21]. Many

ROS, possessing unpaired electron, are thus free radicals. These include molecules such as superoxide anion ($O_2^{\cdot-}$), hydroxyl radicals ($OH^{\cdot}$), nitric oxide ($NO^{\cdot}$), and lipid radicals. By contrast, other molecules, such as hydrogen peroxide (H_2O_2), peroxynitrite ($OONO^-$), and hypochlorous acid (HOCl), are not free radicals but ROS with oxidizing effects.

The cellular production of ROS generally stems from one electron reduction of molecular oxygen, which can lead to the consecutive production of other ROS via a free radical chain reaction [2]. The step-wise reduction of molecular oxygen via 1-electron transfer, producing a derivative ROS associated with this reaction network, is schematically shown in Figure 1.1.

Most ROS are inherently unstable and can readily react with most non-radical bio-molecules and, in particular, biological macromolecules, such as lipids, proteins, nucleic acids, and carbohydrates. Among the various ROS molecules, some are highly reactive, such as the $OH^{\cdot}$ [1], while others are less reactive; examples are $O_2^{\cdot-}$ and H_2O_2, which serve as intracellular second messengers under physiological conditions [3]. In vascular systems, the most important and widely documented ROS molecules include superoxide, hydrogen peroxide, and nitric oxide. These three molecules will be briefly discussed in the following to provide a general overview of their biochemical characteristics and intracellular sources.

Superoxide (anion) is created via one-electron reduction from molecular oxygen; it is produced both in the cytosol and in the mitochondria [2, 43, 44]. Specifically, $O_2^{\cdot-}$ is formed during the process of oxidative phosphorylation in vicinity of the inner mitochondrial membrane. This reaction constitutes the final step of cellular respiration, which generates usable energy in the form of adenosine triphosphate ATP, especially in electron-rich aerobic environments [2, 3]. Due to the escape of electrons from the respiratory chain, molecular oxygen is prematurely and incompletely reduced to give $O_2^{\cdot-}$.

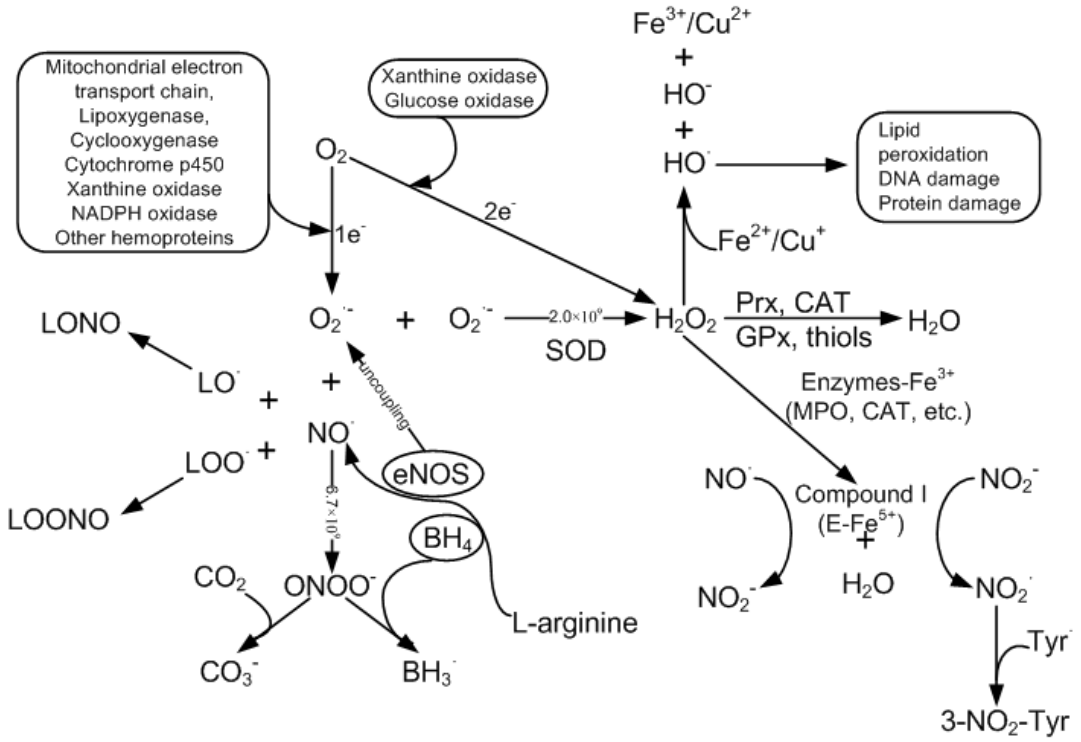

Figure 1.1. Metabolism of reactive oxygen species (ROS).

The one-electron reduction of molecular oxygen into the formation of superoxide ($O_2^{\cdot-}$) can be catalyzed by several enzymes and enzyme systems, including the mitochondrial electron transport chain, lipoxygenase, cyclooxygenase, cytochromeP450, xanthine oxidase, NADPH oxidase, and other hemoproteins. $O_2^{\cdot-}$ can be dismutated into hydrogen peroxide (H_2O_2) spontaneously or in a reaction catalyzed by superoxide dismutase (SOD) (at the reaction speed 2.0×10^9 mol/$L^{-1}s^{-1}$). $O_2^{\cdot-}$ and nitric oxide ($NO^{\cdot}$) react with each other at a rate that is near the diffusion-limit (6.7×10^9 mol/$L^{-1}s^{-1}$) to form peroxynitrite ($ONOO^-$), a potent oxidant. Lipid radicals ($LO^{\cdot}$ and $LOO^{\cdot}$) can also react with $NO^{\cdot}$ to form LONO and LOONO, respectively. $NO^{\cdot}$ is synthesized enzymatically from L-arginine by endothelial $NO^{\cdot}$ synthase (eNOS) with its cofactor BH_4. Oxidation of BH_4, primarily by $ONOO^-$, can lead to eNOS uncoupling and thereby contributes to $O_2^{\cdot-}$ generation. H_2O_2 can also be directly produced from two-electron reduction of molecular oxygen via the reaction catalyzed by xanthine oxidase and glucose oxidase. H_2O_2 can be enzymatically metabolized into water by a number of different enzyme systems, such as catalase (CAT), glutathione peroxidases (GPx), peroxiredoxins (Prx), and small molecules like thiols. H_2O_2 can also be converted to the hydroxyl radical ($HO^{\cdot}$), which is extremely reactive and potentially damages DNA, protein, and lipids. Mammalian peroxidases such as myeloperoxidase (MPO) and the eosinophil peroxidases are activated by H_2O_2 to form highly reactive radicals that can oxidize $NO^{\cdot}$ to NO_2. NO_2 can, in turn, contribute to the formation of nitrotyrosines. Compiled and adapted from reaction mechanisms described in [1, 2, 26, 45].

Because $O_2^{\cdot-}$ is membrane- impermeable (although it can across the cell membrane via anion channels), it is mainly enclosed within the mitochondria until it is converted into a membrane-permeable ROS molecule, namely H_2O_2. The conversion of $O_2^{\cdot-}$ into hydrogen peroxide can take place spontaneously, or more rapidly via an enzymatic reaction catalyzed by a member of the superoxide dismutase (SOD) enzyme family [2, 46, 47], which includes manganese superoxide dismutase in mitochondria and copper and zinc superoxide dismutases in the cytosol of virtually all eukaryotic cells. The SOD-catalyzed dismutation is favored when the concentration of superoxide is low and the concentration of SOD is high, which occurs under physiological conditions.

In spite of being a free radical, $O_2^{\cdot-}$ is surprisingly not very reactive [2]. Together with its inefficiency in penetrating a lipid membrane, superoxide is usually considered a poor signaling molecule [3]. Under physiological conditions in aqueous solutions at a neutral pH, the favored reaction of $O_2^{\cdot-}$ is the dismutation reaction yielding H_2O_2 [2]. However, when produced in excess, a significant amount of $O_2^{\cdot-}$ reacts with $NO^{\cdot}$ with an extremely rapid rate (6.7×10^9 $mol/L^{-1}\cdot s^{-1}$) [48], which is three times faster than the reaction rate for $O_2^{\cdot-}$ with SOD. Given this rapid reaction rate, it is likely that some $O_2^{\cdot-}$ always reacts with $NO^{\cdot}$ within cells as well as in the extracellular space, implicating the importance of $O_2^{\cdot-}$ in the loss of nitric oxide bioavailability.

Hydrogen peroxide is a non-radical molecule It is nevertheless highly important because of its ability of moving freely between intracellular compartments by penetrating biological membranes [3]. By forming radicals, it plays an important intermediate in the production of more reactive ROS. As shown in the schematic of Figure 1.1, H_2O_2 can be further reduced to generate the highly reactive $OH^{\cdot}$ (in the so-called Haber-Weiss or Fenton reaction) in the presence of molecules containing metals such as Fe^{2+} and Cu^{+} [3]. Although the majority of H_2O_2 stems from

the conversion of $O_2^{\cdot-}$ in the mitochondria as well as in the cytosol, mammalian cells contain other sources to produce endogenous H_2O_2 independently of $O_2^{\cdot-}$ generation [49]. For instance, xanthine oxidase and glucose oxidase can directly produce H_2O_2 by donating two electrons to oxygen [50]. A more recent study suggests a specific role of Nox4 to directly release H_2O_2 within vascular smooth muscle cells (VSMCs) [51]. Once produced, H_2O_2 can be removed via several antioxidant enzyme systems [2, 3, 6]. These enzymatic antioxidants include, but are not limited to, catalases (CAT, predominantly residing within the peroxisome), glutathione peroxidases (GPx), and peroxiredoxins (Prx).

Although hydrogen peroxide is much less reactive than other ROS (*e.g.*, the hydroxyl radical), its reactivity with intracellular thiol group is significant [3]. Thiol oxidation of H_2O_2 has been shown to inhibit protein tyrosine phosphatase (PTP) activity [18]. Considering its oxidative effect, free moving capability, and relatively long half-life, H_2O_2 is often believed to be an ideal candidate for a signaling molecule.

Nitric oxide ($NO^{\cdot}$ or, more often, NO) is an odd free radical that does not readily react with most biological molecules despite its unpaired electrons [1]. Instead, it easily reacts with other free radicals (*e.g.*, peroxyl and alkyl radicals), generating less reactive molecules, thus in fact functioning as a free radical scavenger. As mentioned above, however, if superoxide and NO are produced in parallel in large amounts, the two react with each other to form peroxynitrite ($OONO^-$) [52], which is highly cytotoxic. Under physiological conditions, endogenous antioxidant defenses minimize this interaction and maintain what seems to be a tenuous balance between them. NO is synthesized enzymatically from L-arginine by NO synthase (NOS) [53-55]. There are three main isoforms of this enzyme, *i.e.*, neuronal NOS (nNOS), inducible NOS

(iNOS), and endothelial NOS (eNOS), which differ in their respective expression and activity [53-56].

In endothelium, NO is mainly generated within endothelial cells (ECs), and diffuses across cell membranes into other cells like smooth muscle cells (SMCs). It generally functions as an intracellular messenger stimulating guanylate cyclase and protein kinases, thereby relaxing smooth muscle in blood vessels [2]. A loss of NO biological activity is often observed in a variety of common pathological conditions, including hypercholesterolemia, hypertension, diabetes, and heart failure [22]. Expression of eNOS can be regulated either by H_2O_2 via Ca^{2+}/calmodulin-dependent protein kinase II/janus kinase 2 (JAK2)-dependent pathway [57, 58], or by shear stress through cSrc-dependent pathways [59].

1.2.2 NADPH Oxidases and Other Sources of Vascular Reactive Oxygen Species

Virtually all types of vascular cells produce ROS. In addition to mitochondria, ROS can be potentially derived from xanthine oxidase, lipoxygenase, cyclooxygenase, cytochrome P450, nitrix oxide synthase, peroxidases, heme oxygenases, hemoproteins such as heme and hematin, and NADPH oxidases [22, 60-64]. Over the past twenty years, many investigations have demonstrated that the last enzyme family, the membrane-associated NADPH oxidases, are the primary producer of physiological ROS in vascular tissue [13, 27, 28], and therefore will be introduced in greater details in the following.

NADPH Oxidase

NADPH oxidase (Nox) was first described in phagocytes of the innate immune system [30] (*e.g.*, neutrophils and macrophages) where it is responsible for generating large bursts of $O_2^{\cdot-}$

using NADPH and molecular oxygen as an electron donor and acceptor respectively, during the process of phagocytosis. The significance of phagocytic NADPH oxidase in host defense is clearly demonstrated in a rare disorder known as chronic granulomatous disease (CGD) [65-67], in which genetic defects in essential oxidase components result in an inactive enzyme and a predisposition to recurrent life-threatening infections in affected children. The phagocytic Nox (or classic Nox) is a multimeric enzyme that contains a heterodimeric membrane-bound cytochrome b_{558} complex, which consists of $gp91^{phox}$ (renamed Nox2) and $p22^{phox}$, and three cytosolic subunits, namely, $p47^{phox}$, $p67^{phox}$, and the small G-protein Rac [68, 69]. Upon agonist stimulation, these cytosolic subunits translocate to the cytochrome complex, leading to an increase in enzymatic activity.

It was later found that humans have seven different NADPH oxidase homologues, called Nox1 to Nox5, Duox1 and Duox2, as well as two additional homologues of the cytosolic subunits, NoxO1 and NoxA1 [31]. Structurally, all members of the Nox family contain at least six transmembrane domains and cytosolic FAD and NADPH binding domains [70, 71]. Nox5 contains specific EF-hand Ca^{2+}-binding domains, and Duox1 and Duox2 have an extracellular peroxidases-like domain in addition to the EF-hand domains[71]. Although all Nox enzymes are able to increase intracellular ROS, there are important differences regarding their subunit composition, localization, tissue distribution, activation mechanisms, and possible physiological functions [31, 33].

Compared to their phagocytic counterparts, vascular Nox have a few specific features of importance (*see detailed review in* [33]). First, vascular Nox has low but constitutive activity. In homogenized neutrophils, it is necessary to add a cytosolic fraction of $p47^{phox}$ and $p67^{phox}$ to the membrane fraction containing the cytochrome to observe oxidase activity. In contrast, in

unstimulated vascular cells, oxidase activity was observed in isolated membrane fraction [72-75]. This constitutive activity was explained by the detection of $p47^{phox}$ and $p67^{phox}$ proteins in the membrane fraction [72, 73, 76]. However, the rate of superoxide production in vascular cells is much lower (~1-10%) than that in leukocytes [76-78]. This weak activity of vascular Nox may be due to lower expression of oxidase subunits in vascular cells. It is also possible that oxidase activity is limited in vascular cells by the cytosolic concentrations of NADH and NADPH.

Another specific feature of the vascular enzymes is their intracellular release of ROS, which was described in a number of reports [79-81]. What's more important, in contrast to the cytotoxic amounts of superoxide generated in phagocytes, most vascular Nox produce low amounts of ROS, which usually serve as important signaling molecules and regulate many fundamental processes [33]. In addition, unlike phagocyte oxidase that uses NADPH exclusively as an electron donor [82], vascular Nox is freer in substrate specificity. Many reports have shown that vascular Nox may possibly consume NADH as well as NADPH [83-85].

Another difference between phagocytic and vascular oxidases is their tissue distribution. In phagocytes, only one Nox isoform (Nox2) is predominant. In vascular cells, however, expression levels of Nox homologues and their cytosolic subunits vary between different vascular layers, and may even differ among species [33]. So far, four Nox enzymes, namely, Nox1, Nox2, Nox4, and Nox5, are primarily found in the vasculature, and thereby will be introduced separately in greater detail.

Nox1, the first homologue of Nox2 to be cloned [86, 87], is most highly expressed in colon epithelia [88], but is also expressed at lower levels in vascular cells, including VSMCs and ECs [31]. Recent studies have suggested that Nox1 mainly locates at the plasma membrane, specifically in caveolae on the cell surface in VSMCs [35, 89]. Because Nox1 carries electrons

across membranes, it requires charge compensation. Agonist-induced Nox1 activity is VSMC endosomes is blocked by the deletion of chloride channel 3 (CLC-3) and rescued by transfection with intact channel proteins [90]. By exchanging protons for chloride anions, this CLC-3 antiporter prevents oxidase-induced cytosol acidification and accumulation of endosomal negative charges [91].

At the protein level, Nox1 associates with the membrane subunit $p22^{phox}$ [92, 93], which is necessary for enzymatic activity and protein stabilization. Very similar to its homologue Nox2, Nox1 is activated by forming a complex with cytosolic activators, and can interact with $p47^{phox}$[31, 33, 94], $p67^{phox}$[33], and the small GTPase Rac [95-97]. It is interesting to find that $p47^{phox}$ and $p67^{phox}$ have homologues, namely, NoxO1 [94] and NoxA1 [46, 98, 99], which can very strongly activate Nox1. In contrast to $p47^{phox}$, which requires an additional phosphorylation step for translocation from cytosol to membrane and association with Nox1 [33], NoxO1 lacks the auto-inhibitory region found on $p47^{phox}$, and thereby is constitutively associated with Nox1[71]. The membrane translocation of $p67^{phox}$ and the GTP-bound Rac are also essential for Nox1 activation [33]. Interestingly, in VSMCs, Nox1 is complexed with NoxA1 and $p47^{phox}$ because $p67^{phox}$ exists in ECs and fibroblasts, but not in VSMCs from large vessels [27, 98-100].

Nox1 can be activated by a variety of extracellular stimuli [31, 37, 101, 102], including cytokines, growth factors, hormones, and mechanical forces. Upon stimulation, Nox1 could either be acutely activated within a few seconds or exhibit sustained activity for longer-time exposures (*e.g.*, several hours). The former regulation is usually dependent on signaling responses induced by extracellular stimuli, whereas the latter activation is often due to the up- or down-regulation of Nox1 subunit expression. For example, in VSMCs, the acute activation of Nox1 is mainly caused by angiotensin II (AngII)-stimulated protein kinase C (PKC) [38], and

subsequent ROS-sensitive, Src-mediated epidermal growth factor receptor (EGFR) transactivation [38]. By contrast, the sustained activation of Nox1 is preceded by up-regulation of Nox1 mRNA [37, 103], $p22^{phox}$ mRNA and protein [104, 105], and $p47^{phox}$ protein [105, 106]. In addition, recent a study has identified a novel mechano-sensitive pathway through which both Nox1 mRNA and protein expression are up-regulated upon stimulation by oscillatory shear stress (OSS)[101].

Although Nox1 has a low basal expression in VSMCs, it has been extensively studied, because many experimental and clinical studies have revealed evidence that Nox1 can regulate smooth muscle cell growth, proliferation, contraction, and migration, and therefore has been implicated in AngII-induced hypertension and hypertrophy, vascular inflammation, endothelial dysfunction, and even atherosclerosis [34, 102].

Nox2, the first discovered Nox in leukocytes [30], is expressed in both phagocytic [68, 107, 108] and non-phagocytic cells including all vascular wall cells, except VSMCs from large arteries. It is localized in the membrane of phagosomes in neutrophils, in caveolae on the leading edge of lamellipodia in ECs [109] as well as in endosomes [69, 110] of other non-phagocytic cells.

Very similar to Nox1, activation of Nox2 is a highly controlled process that requires three different elements, including the cytoplamic subunit $p67^{phox}$[111], active Rac [112], and at least *in vivo* free fatty acids. The direct interaction between $p67^{phox}$ and Nox2 is not steadily stable, but instead facilitated by $p47^{phox}$, which acts as an "organizer" [113]. In resting cells, non-phosphorylated $p47^{phox}$ does not interact with the membrane, and other oxidase subunits like its SH3 and PX domains, are governed by an autoinhibitory loop [114]. Serine phosphorylation of $p47^{phox}$ results in its conformational change and the exposure of the interacting domain. In

addition, Nox2 has been found to complex with $p40^{phox}$, but the functional consequences of this interaction are controversial [33].

In vascular cells, Nox2 is activated by angiopoietin-1 [115], endothelin-1 [116], vascular endothelial growth factor (VEGF) [117], thrombin [118], and mechanical forces [34]. For example, Nox2 mRNA is increased by oscillatory shear stress (OSS) in ECs [101]. Because $O_2^{\cdot-}$ produced by Nox2 can rapidly neutralize vasodilator NO, Nox2 is expected to induce contraction, and Nox2 expression was shown to correlate well with hypertension [119]. Moreover, Nox2 promotes EC proliferation by p38MAPK and Akt stimulation [34]. Besides, accumulating evidence suggests Nox2 promotes inflammation and atherosclerosis in resident ECs, adventitial fibroblasts, as well as recruited macrophages [34].

Nox4 is highly expressed in the kidney [120], but has been found to be expressed and functionally important in many other cell types including all vascular cells [27, 34, 121]. In general, Nox4 is highly expressed compared to other Nox homologues [121]. In VSMCs, Nox4 has been identified in focal adhesions [35], the nucleus [122], and the endoplasmic reticulum [93]. Nuclear and endoplasmic reticular localizations have been confirmed in other cell types.

Unlike other Nox homologues, Nox4 only requires the membrane subunit $p22^{phox}$ for enzymatic activity, and appears to be constitutively active [123]. This observation has led to the proposal that Nox4 is an inducible Nox with an activity proportional to protein expression. A recent paper identified a $p22^{phox}$-interacting protein, polymerase delta-interacting protein (Poldip2), which increases the activity of Nox4 and participates in its regulation of cytoskeleton in VSMCs [124]. At the mRNA level, Nox4 is up-regulated by serum withdrawal in VSMCs and ECs [33, 125], but down-regulated by growth-promoting agents such as AngII, platelet-derived growth factor (PDGF), interleukin-1 beta (IL-1β), transforming growth factor-β (TGF-β), and

thrombin in VSMCs and fibroblasts [33, 123, 126]. However, these results may need to be re-evaluated since a recent study showed that Nox4 mRNA and protein expression are not always correlated [127]. In addition, Nox4 in ECs is upregulated by physiological shear stress and down-regulated by pathological stress (*e.g.*, high intensity laminar shear stress) and oscillatory shear stress [128].

The physiological function of Nox4 is often cell-specific. For example, Nox4 is required to maintain the quiescent VSMCs phenotype and tumor necrosis factor-α (TNF-α) induced apoptosis in ECs [129-131]. In contrast, proliferation induced by urotensin or hypoxia in pulmonary VSMCs requires Nox4 [132, 133]. Nox4-derived ROS have been implicated in a variety of physiological processes, including cellular senescence, apoptosis, survival, insulin signaling, migration, the unfolded protein response, and differentiation [34].

Nox5 is expressed in lymphatic tissue [134], testis [135], VSMCs [136], ECs [134], spleen, uterus [137], and prostate cancer cells [138]. However, little information is available about the subcellular localization of endogenous Nox5. Recent studies detected that over-expressed Nox5 locates at the plasma membrane in HEK293 cells, and phosphatidylinositol 4, 5-bisphosphate (PIP_2) causes Nox5 to localize in this region [139, 140]. Nox5 has several isoforms, including Nox5-L (α, β, δ, and γ) and a short form, Nox5-S. Nox5-L contains specific EF-hand Ca^{2+}-binding domains, which is absent for Nox1 to Nox4 [141, 142]. Nox5-S lacks EF-hand motifs at the N-terminus [134].

Nox5 differs from other Nox enzymes in its molecular composition as well we its activation by calcium and possibly calmodulin-based mechanisms. Phosphorylation of Nox5 at residues Thr^{494} and Ser^{498} can increase the sensitivity of Nox5 to calcium, and result in activation of Nox5 at lower calcium concentrations [143]. Nox5 is not found in rodents, a model that has been

commonly used to study other Nox proteins, thereby presenting a severe limitation for physiological and pathophysiological studies of Nox5.

Other Sources of Reactive Oxygen Species

In addition to NADPH oxidase, xanthine oxidase and endothelial nitric oxide synthase, although contributing less to vascular ROS formation, have also been extensively studied, and therefore will be briefly introduced in the following paragraphs.

Xanthine oxidase (XO), an enzyme found in abundant amounts mainly in ECs and epithelial cells [144] but absent from SMCs, is a molybdoenzyme that uses xanthine and hypoxanthine as reducing substrates and yields both superoxide and hydrogen via 1- and 2-eletron reduction of molecular oxygen [145]. XO and xanthine dehydrogenase (XDH) are often collectively referred to as xanthine oxidoreductase (XOR). XDH is initially synthesized as a 150-kDa protein from which XO is derived, either reversibly by conformational changes or irreversibly by proteolysis [146]. Under basal conditions, the majority of 150-kDa protein contains XDH activity. Reversible formation of XO from XDH is achieved by the oxidation of cysteine 535 and 992, a process that changes enzymatic function but not molecular weight [147]. The irreversible proteolysis of XDH occurs at a specific site, leading to the formation of a 130-kDa form of XO, which can be further proteolyzed into smaller proteins with XO activity. However, the mechanisms responsible for either the irreversible or the reversible conversions of XDH to XO remain incompletely understood. A recent study shows that hydrogen peroxide may modulate the irreversible conversion of XDH to XO in a calcium-dependent manner, suggesting that stimulation of XDH to XO may represent a feed-forward mechanism for ROS self-propagation [144].

The second source of vascular ROS production that has received substantial attention is **endothelial nitric oxide synthase** (eNOS), which is the enzyme primarily responsible for NO production. eNOS is a cytochrome p450 reductase-like enzyme that requires tetrahydrobiopterin (BH_4) as cofactor to transfer an electron to L-arginine to generate NO under normal physiological conditions [22]. However, in the absence of either L-arginine or BH_4, eNOS can produce superoxide and hydrogen peroxide [148]. This phenomenon has been referred to as "NOS uncoupling", and has been demonstrated in several studies with the purified enzyme as well as *in vivo* experiments [149-151]. The mechanisms of eNOS uncoupling *in vivo* remain unclear. One possibility is via peroxynitrite, the product of the reaction between nitric oxide and superoxide, since peroxynitrite has been shown to be able to oxidize BH_4, thus leading to uncoupling of eNOS *in vivo* [152].

1.2.3 Oxidative Stress and Vascular Diseases

Oxidative stress is a condition characterized by an imbalance in redox state where pro-oxidants overwhelm anti-oxidant capability [19]. Overproduction of ROS (arising either from mitochondria or excessive stimulation of NADPH oxidase) can result in oxidative stress, a deleterious process that can damage cell structures, including lipids, proteins, and DNA [3, 20, 22]. An increasing body of evidence suggests that oxidative stress and associated oxidative damage are mediators of vascular injury and inflammation in many cardiovascular diseases [22-24], including hypertension, hypercholesterolemia, atherosclerosis, and heart failure. Two of them, namely, hypertension and atherosclerosis, are discussed in greater detail as examples in the following.

Hypertension is a chronic cardiac condition in which the systemic arterial blood pressure is elevated [153]. Persistent hypertension is a leading risk factor for stroke, myocardial infarction, heart failure and arterial aneurysms, and a significant cause of chronic kidney failure. Evidence in animal models suggests that oxidative stress is increased in hypertension and that treatment with antioxidants or agents that inhibit NADPH oxidase-driven generation of ROS reduces, and may even prevent, blood pressure elevation in hypertensive animals [26, 154, 155]. A characteristic of hypertension is hypertrophy of large vessels [153]. Several studies have demonstrated that AngII-induced hypertrophy of SMCs is dependent on intracellularly produced H_2O_2, which is derived, at least partially, from a Nox enzyme [84, 156, 157]. AngII-induced hypertrophy can be inhibited by diphenyleneiodonium (DPI), a NADPH oxidase inhibitor [84], attenuation of Nox activity by transfection of antisense $p22^{phox}$ [156], and catalase over-expression [157].

Atherosclerosis is a chronic inflammatory syndrome of large- and medium-sized arteries that is characterized by a formation of atherosclerotic plaques consisting of necrotic cores, calcified regions, accumulated modified lipids, inflamed SMCs, ECs, leukocytes, and foam cells [158, 159]. These features of atherosclerotic plaques illustrate that atherosclerosis is a complex disease, and many components of the vascular, metabolic, and immune systems are involved in this process. Experiments and clinical studies have shown accumulated evidence for the fact that many aspects of this process are known to be redox sensitive; examples include endothelial activation, oxidative modification of lipids, the recruitment of leukocyte, macrophage and VSMCs into atherosclerotic plaques, and VSMCs proliferation. In humans, higher expression of NADPH oxidase subunit proteins is associated with increased superoxide production and severity of atherosclerosis [24].

Disturbed blood flow dynamics is believed to be one of the pertinent factors determining the localization of developing plaques, which preferentially occur in the branched or curved regions of arteries [160]. Emerging evidence suggests that oscillatory shear stress (OSS), which is usually generated on ECs in these branched or curved regions of arteries, is an essential regulator [158, 161, 162]. OSS, as a potent pro-atherogenic factor, can stimulate monocyte adhesion by inducing one of the earliest measurable markers of atherogenesis, namely, intercellular adhesion molecule 1 (ICAM-1). Both *in vitro* and *in vivo* experiments have suggested the same underlying mechanism with which OSS induces inflammation, namely by activating endothelial NADPH oxidase and enhancing endothelial ROS production [101, 163]. This mechanism points to the specific and important role of OSS in leading to rapid and robust atherosclerosis development.

Based on experimental evidence and clinical studies that oxidative stress plays a key role in vascular damage, there has been great interest in developing strategies that target ROS in the treatment of hypertension and other cardiovascular diseases. However, although treatment with antioxidants has been found to be effective in experimental models of hypertension as well as in small clinical studies [164, 165], data from large clinical trials have been disappointing [166, 167]. One possible reason for this poor response to antioxidant vitamins may be related to the low doses of the compounds reaching the sites in which they are needed at the appropriate moment. An alternative potential therapeutic target to ROS is its primary vascular source - NADPH oxidase. Although interesting studies of using peptide-based inhibitors (like PR-39) of NADPH oxidase have shown to be useful for experimental interventions [168, 169], utilization of these peptides as clinical therapeutics still has a long way to go because the peptides cannot be effectively administered orally, and therefore, may have limited efficacy.

1.2.4 Regulatory Mechanisms of Vascular Reactive Oxygen Species and Implications

Under normal physiological condition, ROS molecules operate at low, but measurable concentrations in the cell [1]. Their steady-state concentrations are determined by the balance between their production rates and the rates of removal by various antioxidants. In recent years, the term "redox state" has not only been used to describe the state of a redox pair, *e.g.*, glutathione disulfide (GSSG)/2 glutathione (GSH), but also to describe more generally the redox environment of a cell [170, 171]. Usually, the redox state of a cell is kept within a narrow range under normal conditions. Any significant disturbance of the current "redox balance" may lead to small and temporary "oxidative bursts," which in turn may activate intracellular redox sensitive signaling cascades [21]. This disturbance can be caused either by an increase in ROS formation upon stimulation of extracellular cytokines, growth factors, and hormones, or by a decrease in the activity of antioxidant systems. The literature concerning the latter mechanisms is outside the scope of this dissertation and has been reviewed by others in detail [1-3]. The aim of the following brief review is to provide insights into the mechanisms associated with regulating ROS production.

Regulation of endogenous ROS formation occurs in multiple levels and through different mechanisms. First, NADPH oxidase, a primary source of endogenous ROS, is itself subject to feedforward and feedback regulation. In VSMCs, NADPH oxidase-derived H_2O_2 is capable of activating NADPH oxidase via a cSrc-dependent signaling pathway, thereby amplifying ROS production and contributing to its long-lasting pathological effects [38]. In contrast, Rac1-dependent NADPH oxidase activation and subsequent $O_2^{\cdot-}$ production in ECs mediates a negative feedback loop leading to increased proteosomal degradation of Rac1, which may then down-regulate Nox enzyme activity [172].

Except for signaling-based regulatory mechanisms, ROS can also amplify its production via modulating protein expression on a longer time scale. In endothelial cells, H_2O_2 was found capable of up-regulating $p22^{phox}$ expression, an essential component for NADPH oxidase activation [173]. In VSMCs, AngII-induced ROS increases occur in two phases. The first phase is transient and due to an acute activation of NADPH oxidase by AngII, while the second depends on the initial burst and is a consequence of upregulation of different NADPH oxidase subunits. For example, in VSMC, the sustained phase of ROS production is preceded by upregulation of Nox1 mRNA [37, 103], $p22^{phox}$mRNA and protein [104, 105], and $p47^{phox}$ protein.

NADPH oxidase-derived ROS can also promote their own production from other sources, thereby further amplifying total production. First, several studies have found that NADPH oxidase-derived ROS can promote the oxidative degradation of the essential eNOS cofactor BH_4, thus leading to eNOS uncoupling and superoxide (rather than NO) generation [174]. The potential role of eNOS uncoupling has been supported by *in vitro* BH_4 restoration experiments, as well as in human studies with BH_4 precursor treatment [152, 175]. Second, in ECs, oscillatory shear stress (OSS) induced activation of NADPH oxidase lies upstream of xanthine oxidase-dependent production of H_2O_2, which has been shown to modulate the irreversible conversion (oxidative conversion) of XDH to XO [60]. Third, extra-mitochondrial H_2O_2 can induce mitochondrial DNA damage, destroying respiratory enzymes to produce ROS [176]. Finally, transferrin receptor-dependent endothelial iron uptake is augmentable by H_2O_2, amplifying intracellular H_2O_2 formation to induce apoptosis [177]. Mitochondrial iron uptake can also be upregulated by H_2O_2 [178].

Thus, ROS, originally generated by vascular NADPH oxidase, can propagate their own production via enhanced NADPH oxidase activity and subunit protein expression, intracellular iron uptake, formation of xanthine oxidase, uncoupled eNOS, and damaged mitochondria; the mechanisms are schematically depicted in Figure 1.2. These feedforward mechanisms form a vicious cycle that amplifies and sustains endogenous ROS production in large quantities, contributing to pathological signaling. All these mechanisms together render the generation of any initial burst of ROS, mainly due to vascular NAPHD oxidase activation upon extracellular stimuli, extremely important and worthy of further investigation.

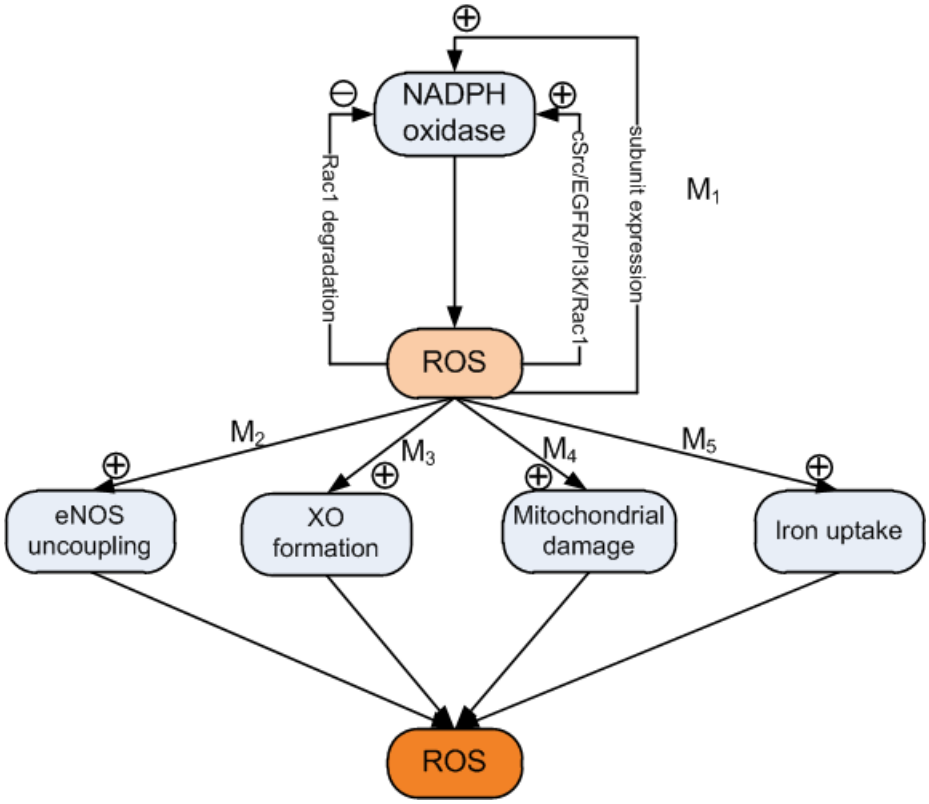

Figure 1.2 Schematic representations of regulatory mechanisms affecting vascular ROS.
Regulation of vascular ROS formation occurs in multiple levels and through different mechanisms. M_1: NADPH oxidase self-regulation through either signaling-based mechanisms or modulation of gene or protein expression; M_2: NADPH oxidase-based ROS propagation through eNOS uncoupling; M_3: NADPH oxidase-based ROS propagation through XO formation; M_4: NADPH oxidase-based ROS propagation through mitochondrial damage; M_5: NADPH oxidase-based ROS propagation through iron uptake.

1.3 Modeling Approaches

Modern techniques in molecular biology have enabled the generation of comprehensive data sets that have greatly benefited the field of computational system biology. With the availability of various kinds of experimental data, qualitative or quantitative, static or dynamic, at multiple time and organizational scales, numerous computational and mathematical modeling approaches have been proposed, developed, and applied to a variety of aspects of biological systems. Some of these have proved to be very successful and thus been widely utilized to different biological systems. These approaches include stoichiometric models [179-182], which describe metabolic pathway systems with a focus on their time-invariant stoichiometry and are frequently used to determine the flux rates throughout a network. Among these approaches, flux balance analysis (FBA) uses the property of stoichiometry but adds constraints that permit the identification of feasible or optimal flux distributions [182].

Another class of successful models contains kinetic models. In contrast to stoichiometric representations, these kinetic models require detailed information about the biochemical features of the metabolic reactions of interest. The best-known representative models in this category include the Michaelis-Menten and Hill rate laws and the mass action rate law.

Between stoichiometric and kinetic models, canonical models are a good compromise, especially as a default for setting up models for ill-characterized systems. Canonical models capture the system dynamics with sufficient kinetic information while keeping the mathematics simple. Therefore, it is often beneficial, especially at the beginning of a modeling effort, to search for a canonical nonlinear model whose structure is fixed and whose individuality comes from its parameter values. Arguably the most promising canonical nonlinear models in

computational system biology are S-systems and Generalized Mass Action (GMA) systems within the Biochemical Systems Theory (BST) [183-187], which will be introduced in detail in the following.

1.3.1 Biochemical Systems Theory (BST)

Biochemical Systems Theory (BST) was originally designed for studying the dynamics and other features of biochemical and gene regulatory systems, but is not restricted to these application areas in terms of its mathematical foundation. The basic tenets of BST are quite simple. In a nutshell, the dynamics of each dependent variable is given by an ordinary differential equation (ODE), which describes the change over time as it is governed by processes that affect this variable. The mathematical descriptions of these processes are constructed by approximating their associated fluxes with products of power-law functions. In the S-system formalism, each ODE has a particularly simple format: The change in a dependent variable is given as one set of influxes (called α-term) minus one set of effluxes (called β-term), and each set is collectively written as one production of power-law function. As the result, the ODE for a specific dependent variable X_i is given as follows:

$$\dot{X}_i = \alpha_i \prod_{j=1}^{n+m} X_j^{g_{ij}} - \beta_i \prod_{j=1}^{n+m} X_j^{h_{ij}} . \qquad (1.1)$$

Here, X_i is the dependent system variable, and $\dot{X}_i$ is its derivative. The products generically run to $n+m$. The first n variables refer to dependent variables, whereas the remaining m variables are independent variables, which have an effect on the system but are not affected by the system. A typical example is a constant enzyme activity. The non-negative number α_i and β_i are rate constants, which quantify the turnover rate of the production or degradation, respectively. The

real-valued numbers g_{ij}, and h_{ij} are kinetic orders that reflect the strengths of the effects that the corresponding variable X_j have on a given flux term. A positive value signifies an activating or augmenting effect exerted by X_j, a negative value indicates an inhibitory effect, and a zero value implies that the corresponding variable X_j has no effect on a given flux.

In the GMA format, instead of aggregating all influxes and all effluxes into one term, each flux is approximated individually with one power-law term such that the derivative of a specific dependent variable X_i is given as follows:

$$\dot{X}_i = \gamma_{i1}\prod_{j=1}^{n+m} X_j^{f_{ij1}} + \gamma_{i2}\prod_{j=1}^{n+m} X_j^{f_{ij2}} + \cdots + \gamma_{ik}\prod_{j=1}^{n+m} X_j^{f_{ijk}} + \cdots . \tag{1.2}$$

Here, the rate constants γ_{ik} are non-negative and the kinetic orders f_{ijk} are real-valued as in the S-system format. It should be noted that differences between these two formulations only exist at branch points, whereas all other steps are represented identically.

BST models have a number of important advantages that have been discussed in detail [183-186]. Among the beneficial features, four particularly useful properties are summarized here: First, BST models are rich enough in structure to capture any nonlinearity including complex oscillations and chaos. Second, the highly structured format of BST models facilitates mathematical, computational, and simulation-aided analyses. These analyses include computations associated with steady states, sensitivity, stability, as well as dynamic features. Third, BST models are characterized by a one-to-one relationship between parameters and structural features. Thus, the interpretation of identified parameters is explicit and immediate. Finally, the homogenous structures of BST models are more or less size independent, and therefore allow the same type of analyses and diagnostics. These models have been shown to be

successfully applicable not only in the context of metabolic pathways, but also in modeling numerous other kinds of biological systems, including genetic networks, multi-level systems, and cell signaling [188-190].

1.4 Dissertation Overview

In spite of the considerable amount of experimental studies that have been conducted in the field, the exploration of the underlying regulatory mechanisms of the Nox1 system and its subsequent ROS formation in vascular cells is incomplete and unclear. Many open questions remain that have not been addressed, and it will be hard to answer them with purely experimental methods. Therefore, in order to improve our understanding, the ***objective of this research is to investigate how Nox1 activity and its subsequent reactive oxygen species (ROS) production are differently and dynamically regulated by distinct extracellular stimuli in vascular system*** by using computational and modeling methods. Two specific cell types, namely endothelial cells (ECs) and vascular smooth muscle cells (VSMCs), are used as "templates" to demonstrate and compare the differences in Nox1 regulatory mechanisms. Furthermore, two distinct extracellular stimuli, namely mechanical shear stresses and hormones like angiotensin II (AngII), are respectively treated as representative Nox1 activators in each cell. In Chapter 2, the shear stress-induced and Nox1-mediated mechanotransduction system in ECs is investigated in detail (as proposed in ***Specific Aim 1***). In Chapter 3, the function and design of the Nox1 system in VSMCs is explored and four potential disassembly mechanisms of Nox1 are proposed and analyzed according to different user-defined criteria (as proposed in ***Specific Aim 2***). In Chapter 4, the AngII-stimulated Nox1 activation and its subsequent ROS production in VSMCs are studied and the features of Nox1 disassembly mechanisms in stimulated cells and overall system

dynamic responses are discussed (as proposed in ***Specific Aim 3***). An overview of chapters and appendixes is shown in Table 1.1. Chapter 5 contains conclusions and suggestions for future work.

Table 1.1 Dissertation overview.

Chapter	Content	Related Appendixes
2[i]	System Analysis of the Role of Bone Morphogenic Protein 4 in Endothelial Inflammation	APPENDIX A
3[ii]	Function and Design of the Nox1 System in Vascular Smooth Muscle Cells	APPENDIX B
4[iii]	Dynamic Analysis of Angiotensin II-Induced Nox1 Activation in Vascular Smooth Muscle Cells	APPENDIX C
5	Conclusions and Future Work	

i. Adapted from: *Yin, W., Jo, H., Voit, E.O. "Systems Analysis of the Role of Bone Morphogenic Protein 4 in Endothelial Inflammation", Annals of Biomedical Engineering, 38:2, 291-307, 2010.*

ii. Adapted from: *Yin, W., Voit, E.O. "Function and Design of the Nox1 System in Vascular Smooth Muscle Cells", (submitted), 2012.*

iii. Adapted from: *Yin, W., Voit, E.O. "Dynamic Analysis of Angiotensin II-Induced Nox1 Activation in Vascular Smooth Muscle Cells", (being submitted), 2012.*

CHAPTER 2

SYSTEMS ANALYSIS OF THE ROLE OF BONE MORPHOGENIC PROTEIN 4 IN ENDOTHELIAL INFLAMMATION[1]

2.1 Introduction

Atherosclerosis is a chronic inflammatory response that is characterized by the hardening of arteries and loss of their elasticity [158, 159]. Its hallmark is the formation of atheromatous plaques consisting of macrophages, smooth muscle cells, cholesterol crystals and calcification within vascular smooth muscle cells. Disturbed blood flow dynamics is believed to be one of the pertinent factors determining the localization of developing plaques, which preferentially occur in the branched or curved regions of arteries[160]. When blood flows through an artery, endothelial cells are subjected to several mechanical forces. Among these, shear stress is believed to be the most important. This tangential frictional force is caused by blood flowing along the walls of the vessel and constitutes an important signal to the endothelial cells lining the arterial wall [191, 192]. Straight sections of the arteries are exposed to relatively unidirectional, high-level laminar shear stress (ULS) and are typically lesion-free. By contrast, the complex arterial geometry and pulsatile blood flow during the cardiac cycle cause disturbed, turbulent flow conditions with low shear in branched and curved regions of the arteries, and these tend to be lesion-prone [191, 192]. For investigations *in vitro*, these complicated flow patterns at arterial

---

[1] Adapted from: *Yin, W., Jo, H., Voit, E.O. "Systems Analysis of the Role of Bone Morphogenic Protein 4 in Endothelial Inflammation", Annals of Biomedical Engineering, 38:2, 291-307, 2010.*

branches are mimicked with experimental set-ups that repeatedly change the direction of blood flow, thus yielding oscillatory shear stress (OSS) [193-195].

Emerging evidence suggests that shear stress is an essential regulator of inflammatory responses in endothelial cells, and thus in the critical early phase of atherogenesis [158, 161, 162]. OSS is a potent pro-atherogenic factor that can stimulate monocyte adhesion by inducing one of the earliest measurable markers of atherogenesis, namely expression of the *Inter-Cellular Adhesion Molecule*-1 (ICAM1) [162, 196]. In contrast, ULS is atheroprotective and has been shown to suppress ICAM1 as well as *Vascular Cell Adhesion Molecule-1* (VCAM1) expression. The mechanisms with which OSS and ULS exert opposite roles in inflammation and atherosclerosis have so far remained unclear, even though they have received intense attention. Some studies suggest that the opposite effects of OSS and ULS are likely mediated through differential expression of several specific genes and proteins in each condition [193, 195, 197, 198]. Among these, DNA microarray studies and subsequent functional studies have identified the recently discovered mechanosensitive gene product *Bone Morphogenic Protein 4* (BMP4) as a potent inflammatory cytokine[195].

The role of BMP4 in mechanosensing is complicated, as the protein acts in concert with numerous other known components of the inflammatory response, including reactive oxygen species, NADPH oxidase, and the signaling molecule NFκB. These components interact in a complicated fashion and on different time scales, which renders intuitive cause-and-effect argumentation problematic. To shed light on the systemic nature of the mechanosensitive response to different stresses, we have in the present work developed a dynamic mathematical model that allows us to merge all pertinent information into a computational structure that permits easy interrogation, analysis, diagnostics, scenario simulations, and analyses that are

different and complementary to experimental approaches. The model is the first of its kind. It is mainly constructed within the framework of *Biochemical System Theory* (BST) [184-186, 199], but extended to permit the account for time delays. At this point, the model is obviously not complete but captures experimental findings quite well qualitatively and semi-quantitatively.

2.2 Materials and Methods

2.2.1 Overview of Model Structure

The shear stress response system consists of numerous genes, proteins and biochemical molecules. Those believed to be most important are reviewed in this section.

BMP4

Bone morphogenic protein 4 (BMP4) is a potent inflammatory cytokine that is synthesized from a 408 amino acid precursor, proteolytically cleaved in the Golgi apparatus, and secreted as active protein [200]. Its activity is counterbalanced by secreted antagonists, such as noggin, follistatin and matrix Gla protein (MGP), which have been found to be co-expressed with BMP4 in cultured endothelial cells [201, 202]. Binding of BMP4 to its antagonists prevents it from binding to the cognate receptor and thus blocks BMP4 induced signaling. Cell culture studies have shown that BMP4 expression is stimulated by OSS and inhibited by ULS [101, 195]. Treatment of cultured endothelial cells with BMP4 alone leads to similar responses as OSS, including increased ICAM1 expression and monocyte adhesion [195]. Furthermore, OSS-induced endothelial inflammatory responses can be completely blocked by treating the cell with sufficient amounts of the BMP4 antagonist noggin or upon administration of BMP4-siRNA [195]. Opposite to our initial expectation, however, ULS tends to decrease BMP4 antagonist

expression, while OSS up-regulates it [201]. This up-regulation may be accomplished through both BMP4–dependent and –independent mechanisms, which would reveal a novel negative feedback regulation of the action of BMP4 under shear stress. These and other studies strongly indicate the important, essential, and specific role of BMP4 in shear-dependent inflammation, which is a key feature of atherosclerosis.

Reactive Oxygen Species

Reactive oxygen species (ROS) have been implicated in many cardiovascular diseases including atherosclerosis and hypertension and play an essential role in many intracellular signaling pathways that ultimately lead to changes in gene transcription, protein synthesis and, consequently, cell function [5, 11, 12, 203]. Under physiological conditions, ambient production of ROS occurs at low concentrations, which are necessary for endothelial cell growth and proliferation [18, 204]. However, under pathological conditions, large quantities of ROS are produced, resulting in a mismatch between ROS formation and the ability of antioxidants to degrade them, which subsequently leads to a state of oxidative stress [11]. ROS were discussed in Chapter 1 of this dissertation.

NADPH Oxidase

NADPH oxidase has been identified as an important player in the shear-induced inflammation in endothelial cells [42, 80, 196]. Its chemical and function features were already discussed in Chapter 1 of this dissertation.

Of note here is that, in addition to humoral factors, which were discussed before, physical factors like shear stress and pulsatile stretch can stimulate NADPH oxidase activation as well [42, 80].

Specifically, shear stress has been shown to be able to stimulate endothelial NADPH oxidase activation by quickly enhancing the amount of phosphorylated $p47^{phox}$ through a PKC-dependent pathway [205]. A recent study *in vitro* furthermore suggests that shear stress can regulate the activity of NADPH oxidase via a BMP4-dependent mechanism [101, 196]. Short-term (1h) and long-term (18~24h) exposures to OSS have been shown to increase O_2^- production in cultured endothelial cells to a similar level. Compared with OSS, ULS induces a similar transient increase in the short term but the opposite long-term effect in terms of superoxide production. While both Nox1 and Nox2 are activated by OSS, only Nox1 expression was shown to be induced by BMP4[101, 128], suggesting that Nox1 may be the NADPH oxidase that mediates the OSS- and BMP4-dependent response.

NFκB

As a downstream signaling target and very important transcription factor, *Nuclear Factor κB* (NFκB) has been suggested to participate and play an essential role in OSS-induced monocyte adhesion [195, 206]. Although the mechanism is not completely clear, hydrogen peroxide is believed to be the upstream molecule that initiates the signal to degrade the inhibitors of NFκB (IκB) and release active NFκB, which can then translocate to the nucleus to mediate expression of a wide array of genes that participate in inflammation and immune processes[101]. ICAM1 has been shown to be one of these targets[207].

Interactions within the Mechanosensitive Response System

The collection and interpretation of numerous results and observations, obtained with extensive series of experiments, have suggested the following mechanism for BMP4-triggered mechanotransduction [42, 80, 101, 195, 196]. OSS induces inflammation and early markers of atherosclerosis in endothelial cells by triggering mechanisms that involve the stimulation of

BMP4 expression, which in turn enhances the activity and expression of $p47^{phox}$-dependent NADPH oxidases, including Nox1, in an autocrine-like manner. The OSS induced activation of NADPH oxidase enhances the production of reactive oxygen species (ROS), up-regulates ICAM1 expression and activation of the transcription factor NFκB, and strengthens monocyte adhesion to endothelial cells, a critical step in atherogenesis. In contrast to OSS, ULS was shown to inhibit BMP4 expression, thus inducing the opposite effect. Intriguingly, both types of shear stress are able to induce an acute increase in superoxide production during an exposure of one hour, but induce opposite effects on superoxide production for much longer exposure [196]. The processes constituting BMP4-triggered mechanotransduction are schematically presented in Figure 2.1.

Although this pathway has been well characterized and tested experimentally [101, 195], several questions remain unanswered. For instance, why do OSS and ULS induce similar short-term effects but different long-term effects with regard to superoxide production? How does the activity of NADPH oxidase dynamically change in response to a specific external stimulus such as shear stress? And how do the various regulatory mechanisms, which govern the expression of all subunits, dynamically cooperate to effect the overall changes in NADPH oxidase activity and the subsequent production of ROS? These types of questions are difficult to answer solely with experimental means and are addressed here with computational methods.

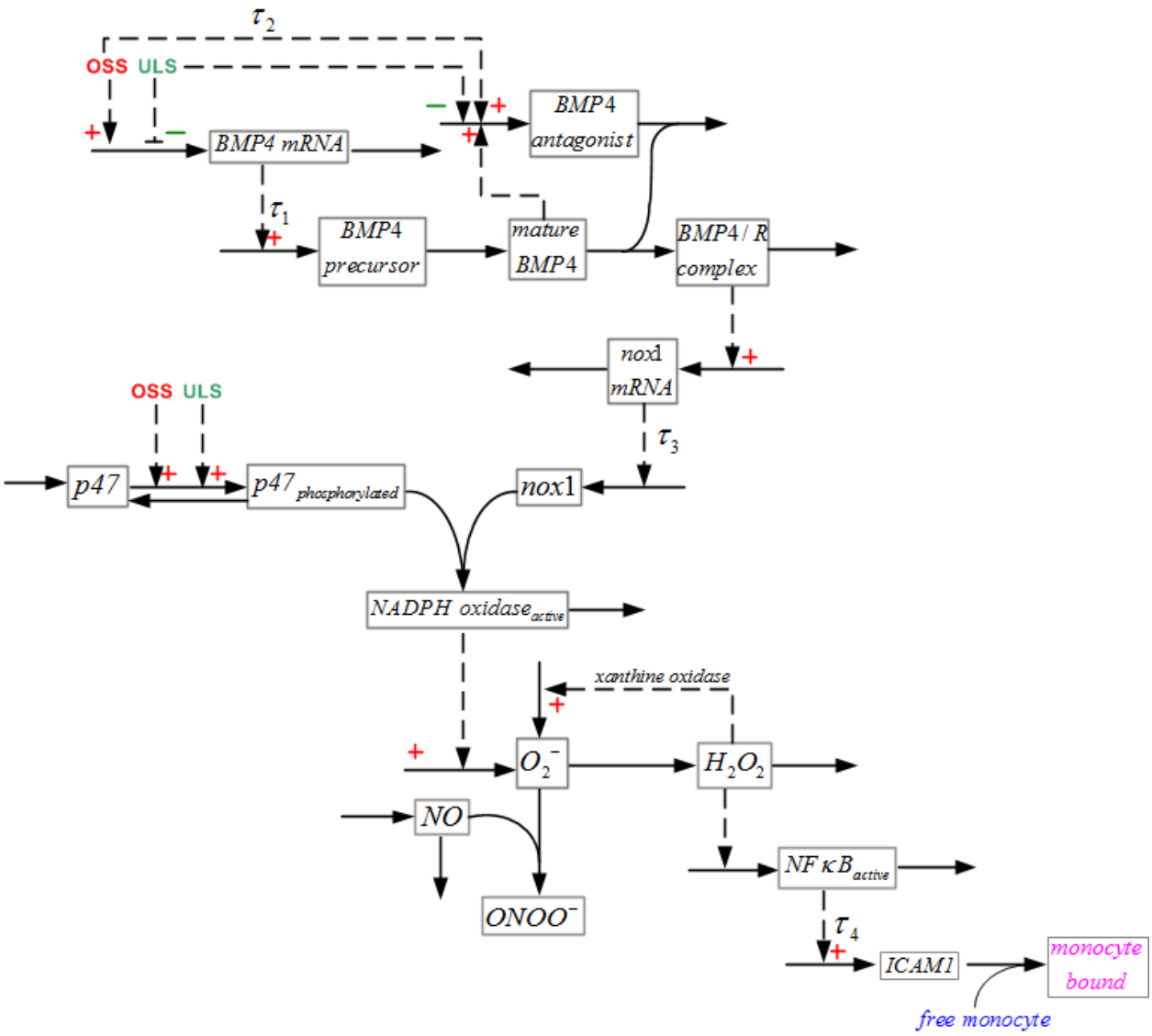

Figure 2.1 Simplified schematic representation of the BMP4-triggered system of shear-dependent inflammation in endothelial cells.

2.2.2 Modeling Framework

The work presented here consists purely of mathematical and computational modeling. The primary goal of the modeling effort is to translate the BMP4-dependent inflammatory pathway (Figure 2.1), triggered by shear stress, into a mathematical structure that permits

diagnoses and analyses and yields insights into the cooperation among the different components of the system.

Very few, if any, of the processes governing the mechanotransduction system in Figure 2.1 are known in sufficient depth to allow the formulation of mechanistic, mathematical representations. This situation is quite typical for biological phenomena that include gene expression, signaling, and metabolic conversion and suggests the use of concept modeling [208] with canonical models that are well suited as default representations of systems composed of ill-characterized components. Specifically, we use the modeling framework of *Biochemical Systems Theory* (BST; [184-187, 199]), which was discussed in Chapter 1 of this dissertation. A particular advantage of BST is a set of guidelines for setting up models for diagrams as the one shown in Figure 2.1. Namely, a differential equation is formulated for each component (dependent variable) that varies over time. This equation consists of all processes or fluxes producing or degrading this component. The processes are modeled as products of power-law functions, which are based on the rigorous foundation provided by Taylor's theory of numerical analysis [209].

While the translation of a diagram such as Figure 2.1 into model equations is straightforward, the severe difficulty of the model design step is the identification of appropriate numerical values for all rate constants and kinetic orders. This parameter identification heavily depends on the availability and quality of the supporting data, other biological information, and on educated assumptions. Particularly useful for these estimation purposes are time series data, for instance, of metabolite concentrations or the abundance of signaling proteins.

2.2.3 Available Data and Model Assumptions

Data

Few of the data are available as time-series or even truly quantitative. Instead, most are given as singular values or extents that are relative to a control level, which is usually assumed to be measured under static no-flow conditions. Much information is semi-qualitative and of the type "24 hours after onset of OSS variable *X* increases several fold over control." Variables like mature BMP4, Nox1, active NFκB and ICAM1 have been characterized through these types of data [101, 195]. Measurements of superoxide and hydrogen peroxide are given by their specific product concentrations, which can be recalculated into ratios over control [60, 101, 196]. Additional information extracted from $p47^{phox}$ knockout experiments [196] and treatments with BMP4 or BMP4 antagonist [195] is qualitative and of the type "variable *X* significantly increases/decreases in comparison with the control under this specific treatment". Shear stresses with different patterns and intensities are added to the system as external stimuli. Among these, ULS typically has a range of 5~15 dyn/cm^2, while OSS has been investigated at only one intensity of ± 5 dyn/cm^2.

Accounting for the primarily semi-qualitative nature of the available data, most model variables are assumed to have their steady state at the "normal" numerical value of 1 (100%). Phosphorylated $p47^{phox}$ is assumed to have a steady state of 0.2, which corresponds to one fifth of the available Nox1 at steady state under control conditions. Obviously, these numerical values are quite crude. However, since essentially all model results are expressed as relative results, the numerical values are not as influential as one might think.

Assumptions

By design, the proposed GMA model of the diagram in Figure 2.1, which was constructed under the guidelines of *BST* [210], includes the following key components: BMP4-mRNA, BMP4-precursor, mature BMP4 protein, BMP4 antagonist, BMP4 and BMP4 receptor (BMP4/R) complex, Nox1-mRNA, Nox1-protein, the free phosphorylated form of $p47^{phox}$, active NADPH oxidase, superoxide, hydrogen peroxide, nitric oxide, active NFκB and ICAM1 expression. Shear stress is treated as an independent variable; *i.e.*, it affects the system but is not affected by it. Interactions and connections between variables are entered into the model equations according to the biological observations as they are diagrammed in Figure 2.1. Thus, two major assumptions for this prototype model are that Figure 2.1 is sufficiently comprehensive to gain interesting insights and that the power-law representation is sufficiently adequate for semi-quantitative explanations and predictions.

As an initial simplification, we do not consider all known subunits of NADPH oxidase individually, but focus on the two most pertinent subunits, namely Nox1 as the representative of the transmembrane form and $p47^{phox}$ as the representative of the cytosolic form. This assumption appears to be reasonable because other subunits are either not significantly regulated by shear stress or do not strongly affect the pathways of interest here [101]. Furthermore, the total amount of free unphosphorylated and phosphorylated forms of $p47^{phox}$ is assumed to be constant due the fact that the amount of the cytosolic component should be of the same or similar magnitude as the amount of the transmembrane component under normal conditions (without external stimulus).

NADPH oxidase and xanthine oxidase are considered to be the only representatives of sources for superoxide production. This assumption ignores the contributions of other sources

that were discussed in Chapter 1 [5, 11], like mitochondrial, cytochrome P450 and uncoupled eNOS, presuming their expression and contribution to superoxide production to remain unchanged or to change only insignificantly in response to shear stress. Furthermore, we presume that the substrate NADPH is not limiting the enzymatic reaction rate and that the concentration of NADPH is about the same under different shear stress conditions. As a consequence, NADPH can be treated as a constant, independent variable that can be merged mathematically with the appropriate rate constants.

Some experiments have suggested that long exposure of endothelial cells to shear stress could possibly affect the expression of relevant enzymes [80, 197, 211-214], including the enzymes catalyzing the conversion of superoxide to hydrogen peroxide (*e.g.*, SOD) and the degradation of hydrogen peroxide (*e.g.*, catalase, glutathione peroxidase, thiol peroxidase). In this initial phase of model development, we assume that the expression and activities of all enzymes in the corresponding reactions remain constant. We plan to consider their effect and regulation by shear stress in the future (see Discussion in section 2.4).

The system under investigation contains several organizational levels, including gene transcription, translation into protein, and enzyme-catalyzed biochemical reactions. These processes operate at distinct time scales, which are at the order of minutes, seconds or even less for biochemical reactions, but hours for gene transcription and protein synthesis. As an indication of these differences, the level of BMP4-mRNA was significantly decreased after ~2h exposure to ULS, but protein expression of BMP4 was first observed ~10h after oscillatory shear stress applied [195], thus suggesting a significant time delay during protein synthesis. At the other end of the spectrum, the reaction rate of nitric oxide and superoxide has been measured to be approaching the diffusion limit [7]. Since we are primarily interested in the activity of the

system as a whole, which occurs at a relatively slow time scale of hours, we initially ignore dynamic changes happening at much faster time scales (of minutes, seconds, or faster). This separation of time scales is a common strategy in modeling [215] and allows us to consider fast reactions, like conversions between superoxide and nitric oxide, and between superoxide and hydrogen peroxide, always to be in a steady state and therefore constant. To address the relatively slow generation of new proteins, the *de novo* appearance of BMP4 precursor, BMP4 antagonist, Nox1, and ICAM1 is modeled with appropriate time delays.

As indicated in the system diagram (Figure 2.1), shear stress affects the system simultaneously through two distinct pathways. One is mediated through the delayed BMP4- and BMP4 antagonist-associated pathway, while the other is hypothesized to occur through phosphorylation of $p47^{phox}$. Details and specifics of the signaling pathway with which shear stress regulates BMP4-mRNA and BMP4 antagonist are still unclear. Therefore, we simply use a power law function with the format S^{f_i} to represent the strength of the signal. S represents the shear stress intensity and $f_i = 1, 2$ represents the effects of shear stress on BMP4 mRNA and BMP4 antagonist expression separately, namely:

$$f_i = \begin{cases} positive, & OSS \\ negative, & ULS \\ 0, & STATIC \end{cases} . \qquad (2.2)$$

Moreover, in order to indicate the protein synthesis of BMP4 antagonist, one time delay is artificially added to the corresponding pathway.

The effect of the signal for the second pathway is assumed to decay exponentially, because of two reasons. One is that the amount of phosphorylated $p47^{phox}$ was detected to increase significantly at time t=2 min (2 min can be ignored in our slow time-scale system) after high fluid shear stress is applied [205]. The other is that among three types of representative

functions (constant, exponentially decaying function, burst signal function) that we explored in simulations (results not shown), the simulation results for an exponentially decaying function best matched the experimental observations. Therefore, an exponentially decaying function is used in the current simulations until more experimental measurements are available.

2.2.4 Model Design

Model Equations

Based on Figure 2.1 and incorporating the assumptions outlined above, we constructed a set of ordinary differential equations in GMA format and extended it by accounting for four time delays (τ_1, τ_2, τ_3 and τ_4) associated with the synthesis of BMP4 precursor, BMP4 antagonist, Nox1 and ICAM1. The time delays were modeled as shown in [216]. The resulting equations are shown in Eq. (2.3):

$$
\begin{aligned}
\dot{X}_1 &= \gamma_1 S^{f_1} - \gamma_2 X_1^{g_1} \\
\dot{X}_2 &= \gamma_3 X_1(t-\tau_1)^{g_2} - \gamma_4 X_2^{g_3} \\
\dot{X}_3 &= \gamma_4 X_2^{g_3} - \gamma_5 X_3^{g_4} - \gamma_6 X_3^{g_5} X_5^{g_6} \\
\dot{X}_4 &= \gamma_5 X_3^{g_4} - \gamma_7 X_4^{g_7} \\
\dot{X}_5 &= \gamma_8 X_3^{g_4} S(t-\tau_2)^{f_2} - \gamma_6 X_3^{g_5} X_5^{g_6} \\
\dot{X}_6 &= \gamma_9 X_4^{g_9} - \gamma_{10} X_6^{g_{10}} \\
\dot{X}_7 &= \gamma_{11}(C - X_7)P - \gamma_{12} X_7^{g_{11}} - \gamma_{13} X_7^{g_{12}} X_8^{g_{13}} \\
\dot{X}_8 &= \gamma_{14} X_6(t-\tau_3)^{g_{14}} - \gamma_{13} X_7^{g_{12}} X_8^{g_{13}} \\
\dot{X}_9 &= \gamma_{13} X_7^{g_{12}} X_8^{g_{13}} - \gamma_{15} X_9^{g_{15}} \\
\dot{X}_{10} &= \gamma_{16} X_9^{g_{16}} + \gamma_{17} X_{11}^{g_{17}} - \gamma_{18} X_{10}^{g_{18}} X_{12}^{g_{19}} - \gamma_{19} X_{10}^{g_{20}} \\
\dot{X}_{11} &= 0.5\gamma_{19} X_{10}^{g_{20}} - \gamma_{20} X_{11}^{g_{21}} \\
\dot{X}_{12} &= \gamma_{21} - \gamma_{18} X_{10}^{g_{18}} X_{12}^{g_{19}} - \gamma_{22} X_{12}^{g_{22}} \\
\dot{X}_{13} &= \gamma_{23} X_{11}^{g_{23}} - \gamma_{24} X_{13}^{g_{24}} \\
\dot{X}_{14} &= \gamma_{25} X_{13}(t-\tau_4)^{g_{25}} - \gamma_{26} X_{14}^{g_{26}}
\end{aligned}
$$

X_1 - $BMP4\ mRNA$
X_2 - $BMP4\ precursor$
X_3 - $mature\ BMP4$
X_4 - $BMP4 / R\ complex$
X_5 - $BMP4\ antagonist$
X_6 - $Nox1\ mRNA$
X_7 - $p47^{phox}_{phosphorylated}$
X_8 - $Nox1$
X_9 - $NADPH\ oxidase_{active}$
X_{10} - $superoxide(O_2^-)$
X_{11} – $hydrogen\ peroxide(H_2O_2)$
X_{12} – $nitric\ oxide(NO)$
X_{13} – $NF\kappa B_{active}$
X_{14} – $ICAM1$

(2.3)

Here, S and P represent the intensity of shear stress and the signal of shear stress acting on the phosphorylation of $p47^{phox}$, respectively. The constant C represents the total amount of free unphosphorylated and phosphorylated forms of $p47^{phox}$. The parameters γ_i and g_i are rate constants and kinetic orders, respectively. The ultimate output of the system is formulated in the following equation:

$$[monocyte\ adhesion] = \kappa \cdot X_{14}^{\ g_{26}}, \tag{2.4}$$

where κ is a constant coefficient, representing the binding ratio of free monocyte to ICAM1.

Parameter Estimation

Many methods have been developed for the estimation of parameters in BST systems [217-219]. Some of them are based on computing kinetic orders and rate constants from information on traditional Michaelis–Menten functions while others use techniques of estimation from time-series data. In our case, neither mechanistic information nor time series data are available, thus forcing us to develop *ad hoc* methods of parameter estimation.

We are primarily interested in system behaviors on a time scale of hours, rather than questions of what exactly happen in the system within seconds or minutes. This strategy implies that most fast processes will be in a steady state, which permits the exploitation of genuine benefits of the BST format. As an example, consider variable X_3, which is modeled with the equation

$$\dot{X}_3 = \gamma_4 X_2^{\ g_3} - \gamma_5 X_3^{\ g_4}, \tag{2.5}$$

in which the quantities γ_5, γ_7, g_4 and g_7 are the parameters that need to be estimated. If the variable is in a steady state, its derivative on the left-hand side of the equation is equal to zero by definition, which leads to the simpler algebraic equation

$$\gamma_4 X_2^{\,g_3} = \gamma_5 X_3^{\,g_4}. \tag{2.6}$$

Logarithmic transformation of this nonlinear equation yields a linear equation in terms of the parameters:

$$g_3 \log(X_2) - g_4 \log(X_3) = \log(\frac{\gamma_5}{\gamma_4}). \tag{2.7}$$

Suppose three scenarios have been assessed experimentally. The first may be a control condition S_0 with no stimulus, while conditions S_1 and S_2 refer to external stimuli 1 and 2. If so, X_3 may assume three distinct (or similar) steady states, each of which is characterized by the same linear Eq. (2.7). These three equations

$$\begin{cases} g_4 \log(X_{3S_S}) - g_7 \log(X_{4S_S}) = \log(\frac{\gamma_7}{\gamma_5}) \\ g_4 \log(X_{3S_O}) - g_7 \log(X_{4S_O}) = \log(\frac{\gamma_7}{\gamma_5}) \\ g_4 \log(X_{3S_L}) - g_7 \log(X_{4S_L}) = \log(\frac{\gamma_7}{\gamma_5}) \end{cases} \tag{2.8}$$

form a linear system where X_{iS_S}, X_{iS_O} and X_{iS_L} represent the steady-state values of variable X_i under the Static control, Oscillatory (OSS) and Laminar (ULS) stress conditions. These equations may be converted into the condition

$$\frac{g_4}{g_7} = \frac{\log(M_{4S_O})}{\log(M_{3S_O})} = \frac{\log(M_{4S_L})}{\log(M_{3S_L})}, \tag{2.9}$$

where $M_{iS_j} = \frac{X_{iS_j}}{X_{iS_S}}$, i = 3, *4* and j = *O, L* represents the ratio of the steady-state values under OSS and ULS in relation to the control condition. Thus, even if we do not know the absolute values at the steady states, we can still derive a linear relationship between g_4 and g_7 if we have information on how the steady-state value of this variable changes for different stimuli.

Consequently, given some positive value for either g_4 or g_7, we can easily calculate the value of the other kinetic order to satisfy all three scenarios. Therefore, for all equations with only two terms, we can derive constraint equations (like Eq. (2.9)), assign experience-based default values of some parameters [186], and then infer the values of the others through linear constraints. Similarly, Eq. (2.7) involves a relationship between γ_5 and γ_7, which is deduced secondarily from g_4 and g_7. All constraint equations for rate constants and kinetic orders are presented in the APPENDIX A. The free choice of a kinetic order may seem to insert undue degrees of freedom, but experience with BST systems severely limits the likely values of kinetic orders, which are usually in ranges of [0, 2] if they are positive, or [-1, 0] if they are negative [186]. Equations with more than two terms or several modulators require similar, but more extensive effort of tuning and validating parameter values.

2.3 Results

The results fall into two categories. The first group describes simulations representing observed scenarios. These simulations functionally connect known inputs and outputs and have explanatory character by allowing the detailed tracing of events between stress and response. By contrast, the second group of simulations consists of analyses that do not directly correspond to existing experimental data and characterize the roles of some of the model components on the dynamics of the system. These simulations lead to predictions regarding not yet observed scenarios and to novel hypotheses.

Due to the paucity of quantitative data, all results are presented in relative units, which measure the ratio of each variable under different stimulus conditions in comparison to a control scenario. This type of assessment is actually directly in line with most observations.

All simulations and diagnoses were executed in MATLABR2007a. Parameter values, including γ_i, g_i and f_i, constants and initial conditions (see details in APPENDIX A) are always the same except if indicated differently in the corresponding text or figure legend.

2.3.1 Simulation of Three Experimentally Investigated Scenarios

In order to elucidate the distinct roles of OSS and ULS, we implemented three scenarios that had been investigated experimentally. The general starting point for the simulations was the mechanosensitive response system at its control steady state, characterized by static blood overlay without shear, and the simulations consisted of applying ULS (15 dyn/cm^2) and OSS (± 5 dyn/cm^2), which caused the system to assume different (quasi) steady states. The results are shown in the Figure 2.2. The panels in the two top rows show model results (lines) for which corresponding experimental data (circles) are available, except for the BMP4/R complex. The panels in the bottom row show model results for which no data are available.

The levels of BMP4 mRNA, BMP4 precursor, mature BMP4, BMP4 antagonist, and Nox1-mRNA increase under OSS and decrease under ULS. Simulations are well consistent with time series measurements for mature BMP4 under ULS and for other measurements at t=24h [101, 195, 196, 201]. An exception is Nox1-mRNA under ULS: The experimental result indicates a non-significant increase of Nox1-mRNA level when ULS is applied, compared with the static control level, while the simulation shows a noticeable decrease. The logic of the model seems to suggest that the singular available data point might not be correct.

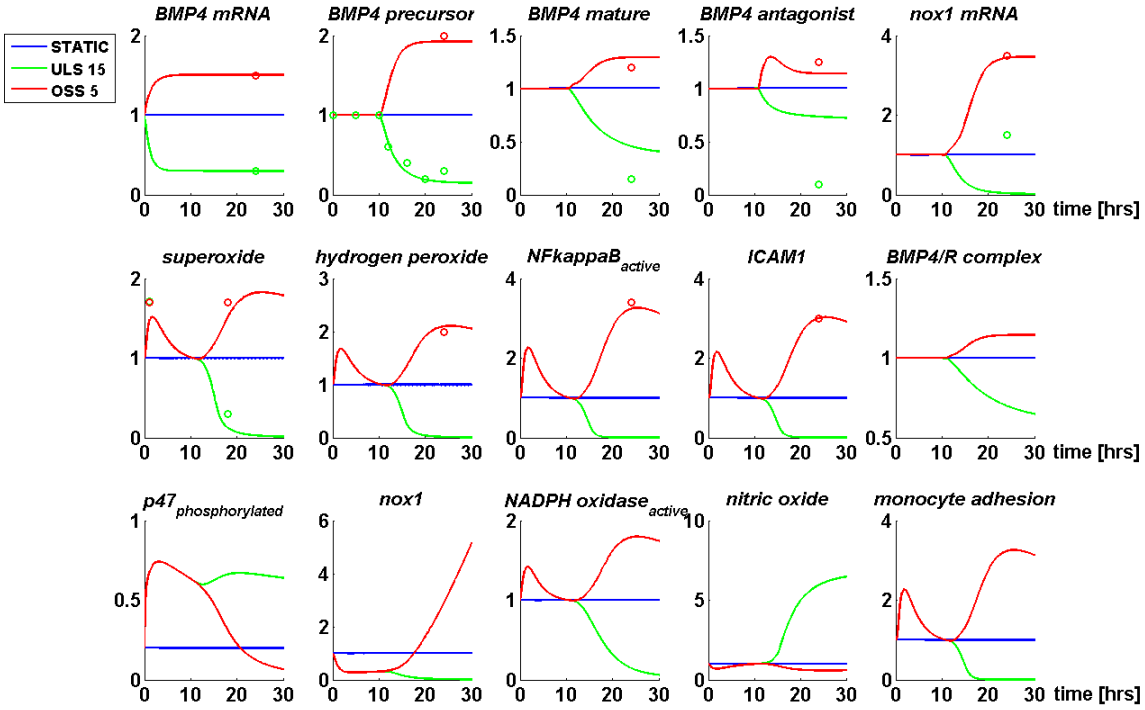

Figure 2.2. Simulation results of three scenarios.

Blue Line: static control; Red line: OSS ($\pm$ 5 dyn/cm^2); Green line: ULS (15 dyn/cm^2). Lines indicate simulation results; dots are experimental measurements.

The processes leading to the production of superoxide appear to be adequately simulated as well. Although we have no experimental data for direct comparisons, we can infer their performance by investigating the intriguing dynamics of superoxide. After shear stress was applied at time t = 0, the amount of superoxide was observed to increase to a similar level for a short-time exposure (~1.7 fold of the static level at time $t = 1h$ [196]) under both shear stresses, but to reach quite different levels for a longer exposures (~1.7 fold under OSS and about one third under ULS at time $t = 18h$ [196]). The simulation results of superoxide clearly reflect the observed similarity in short-term effect and the subsequent discrepancy in long-term effect for the two shear stresses. The amounts of superoxide between $1h$ and $18h$ were not experimentally measured and are therefore unknown. Nonetheless, the simulation offers a possible explanation,

suggesting a quick drop of superoxide after the initial peak, which may be interpreted as the result of fast depletion of the available Nox1 protein. The subsequent climb of superoxide is then caused by the increased amount of Nox1 protein, which is induced by OSS through a delayed BMP4-dependent pathway. As a consequence, the relative ratio of the initial condition of Nox1 to $p47^{phox}$ has an effect on the systemic response, and especially on the dynamics of superoxide production. Opposite to the OSS situation, superoxide production under ULS drops below the control level, although the amount of phosphorylated $p47^{phox}$ stays high. This finding is primarily due to the suppression of Nox1 protein by ULS through the same pathway. By varying the corresponding parameter values, we could easily change the shape of the dynamic transient to some extent. These simulations are, however, futile until more biological observations at intermediate time points become available that would allow us to determine parameter values with greater precision and reliability.

The second ROS, H_2O_2, is also simulated well. As discussed in the Materials and Methods section, we assume no self-propagation or complex signaling mechanisms to be involved in the model. Instead, the activity of H_2O_2 is mainly affected by its precursor, superoxide, and its own degradation. The kinetics of H_2O_2 elimination has been investigated in endothelial cells of the human umbilical vein in culture [220], where it was shown to be composed of two different types of reactions exhibiting a linear and nonlinear dependence on the H_2O_2 concentration. In our simulation, one single degradation term is used instead of two, and the corresponding model parameter ($g_{21}=1.615$) is set between 1 and 2 as a compromise between linearity and second-order non-linearity. Similar to superoxide, hydrogen peroxide in the simulation is up-regulated roughly two-fold under OSS, but greatly down-regulated under ULS.

Nitric oxide, an important antioxidant component, is regulated by shear stress in the opposite direction compared with superoxide and hydrogen peroxide.

As the downstream signal receiver and target gene respectively, NFκB activity and ICAM1 are also simulated well. Consistent with experimental observations [195], a long-term (~24h) simulation reflects an increasing trend for both variables under OSS and a decreasing trend under ULS. Experiments seem to indicate no change in ICAM1 expression for the first few hours, while the corresponding simulation result suggests an immediate increase in ICAM1. The reason for this inconsistency can be traced back to the dynamics of hydrogen peroxide. The current model simplifies both the production and degradation processes of hydrogen peroxide, in line with the primary purposes of this preliminary model. Therefore, the level of hydrogen peroxide increases right after superoxide is increased at the very beginning. As a consequence, the quick increase of hydrogen peroxide leads to the increase of NFKB activity and ICAM1 expression.

No quantitative data are available for comparisons of results of the BMP4/R complex and the variables in the bottom row of Figure 2.2. Active NADPH oxidase and Nox1 protein appear to be reasonable, at least at later times. The simulated concentrations of nitric oxide (NO) also reach reasonable levels after some while, although the initial dynamics may not be correct. Experimental results [221] seem to indicate that NO production begins to increases quickly upon ULS and remains elevated as long as the stress is maintained, whereas the simulation exhibits a temporary undershoot. The reason for this initial discrepancy is that the current model assumes constant NO production and only a single degradation reaction with superoxide. In reality, NO production is subject to genetic and metabolic regulation, as well as various signaling events, which are presently not modeled due to the lack of specific data. As a consequence of the

simplifications, NO initially decreases in the model under ULS, because ULS induces acute O_2^- production, which consumes more NO than under static control. In a similar fashion, the phosphorylated form of $p47^{phox}$ remains high under ULS, because Nox1 is depleted by ULS in the model.

The number of monocytes bound is simulated as the overall output of the system according to Eq. (2.4). As shown in the right lower corner in Figure 2.2, long exposure to shear stress (for about one day) increases the number of bound monocytes to ~3 fold over control during OSS (~3 fold according to experimental measurements[196]) and decreases the number to ~10% of control during ULS (~50% according to experimental measurements [195]). Given the preliminary nature of the model, these results can be considered both qualitatively and semi-quantitatively consistent with the experimental findings.

To elucidate the relevance of the shear stress and the BMP4-depdendant mechanosensing system further, we applied external shear stress with different intensities and patterns to the targeting system. As Figure 2.3 shows, the simulation results for BMP4 mRNA, BMP4 precursor, mature BMP4 and Nox1 mRNA are well consistent with both the available time series and experimental measurements at one time point (t=24h) [101, 195, 222]. Although the simulated results for mature BMP4 under ULS with different intensities are a little bit higher than the experimental measurements (comparing the model results and experimental measurements for ULS at 5 dyn/cm^2 and 15 dyn/cm^2), we still can clearly see the trend that ULS with higher intensity further suppresses the BMP4 expression.

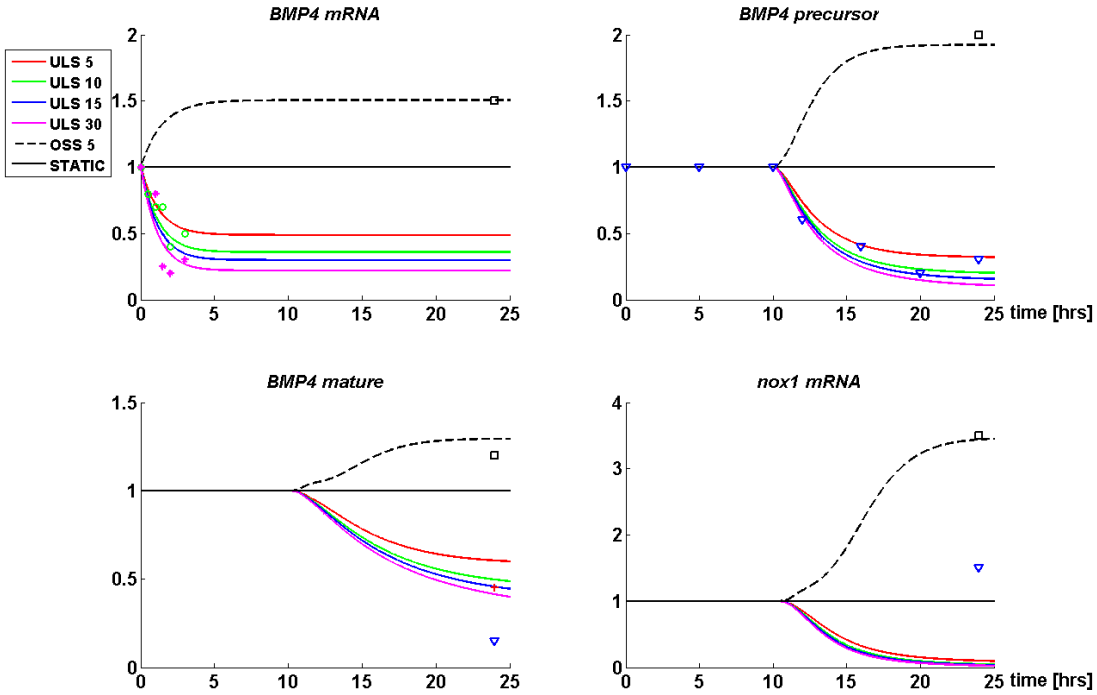

Figure 2.3. Simulation results of shear stress with different intensities and modalities.

Lines indicate simulation results; dots are experimental measurements. Black: static control; Red: ULS (5 dyn/cm^2); Green: ULS (10 dyn/cm^2); Blue: ULS (15 dyn/cm^2); Magenta: ULS (30 dyn/cm^2); Dashed black line: OSS ($\pm$ 5 dyn/cm^2).

2.3.2 Validation Simulations Characterizing the Role of BMP4 under OSS

Experiments *in vitro* [195] have shown that BMP4 alone stimulates monocyte binding in a dose-dependent manner with a maximal activation of 4 to 7 fold over control. In order to test our model by investigating the role of BMP4, we added at time $t = 0$ a bolus of BMP4 to the system, which was initiated at the static control steady state. In a series of simulation experiments, the size of the BMP4 bolus was varied. The combined results are shown in Figure 2.4. They suggest that the number of bound monocytes increases in a dose-dependent manner compared with static control level. The maximal activation achieved in the simulation is ~2.5

fold, which is somewhat smaller than indicated by the experiments. Nonetheless, the qualitative trend in this positive correlation is consistent and supports the hypothesis of a strong effect of BMP4 on the regulation of monocyte adhesion in endothelial cells. Retro-fitting of the model parameter values would make the numerical values more similar, but it is not pursued here in light of the preliminary nature of the model and the scarcity of data.

To elucidate the role of BMP4 in OSS-induced monocyte adhesion further, we added at time t=0 a bolus of BMP4 antagonist to the system, which was initiated under static or OSS condition. Experimental results [195] have shown that treating cells with a sufficient amount of noggin (as a BMP4 antagonist) will completely block OSS-induced monocyte adhesion. As shown in Figure 2.5, BMP4 antagonist treatment in the model simulation with OSS greatly reduces the number of monocytes bound at time t=24h. Even in the static control scenario, treating the system with enough BMP4 antagonist reduces monocyte adhesion, which from a different angle illustrates the important role of BMP4 in OSS-induced monocyte adhesion.

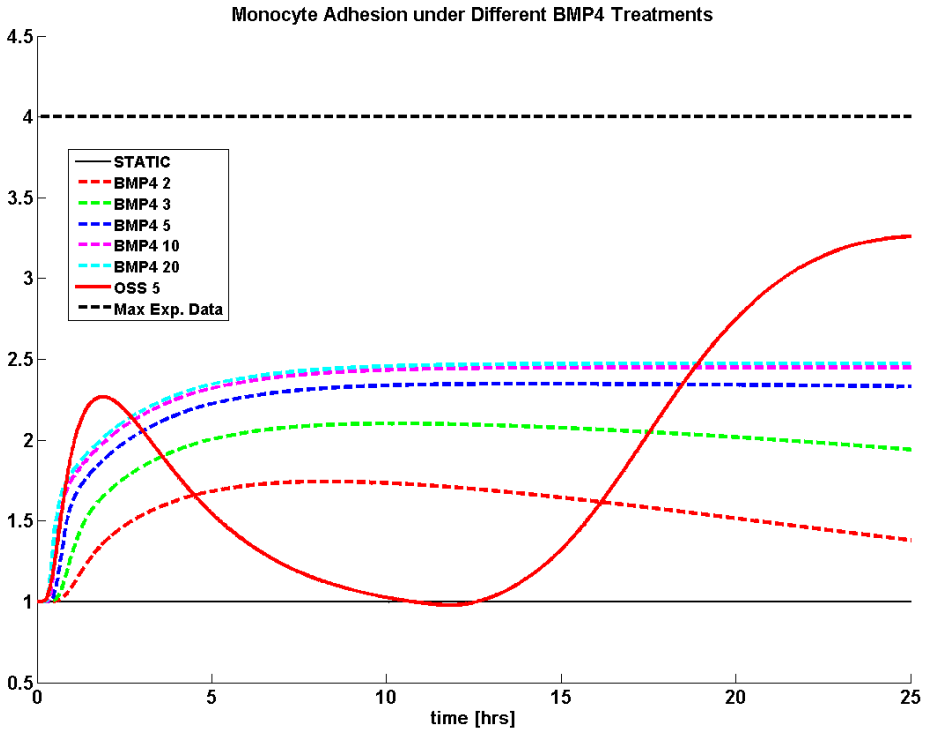

Figure 2.4. Simulated number of bound monocytes under different BMP4 treatments.

Solid black line: static control; solid red line: OSS ($\pm$ 5 dyn/cm^2); dashed red line: treatment with BMP4 bolus of 1 at time t = 0; dashed green line: treatment with BMP4 bolus of 2 at time t = 0; dashed blue line: treatment with BMP4 bolus of 4 at time t = 0; dashed magenta line: treatment with BMP4 bolus of 9 at time t = 0; dashed cyan line: treatment with BMP4 bolus of 19 at time t = 0; dashed black line: experimentally measured maximum increase (in relation to control with BMP4 treatment).

2.3.3 Role of p47^{phox} in the Regulation of NADPH Oxidase Activation by Shear Stress

As a requisite subunit for Nox1- and Nox2-based NADPH oxidase activation, p47^{phox} plays an important role in the regulation of enzyme activity in response to various agonists[205, 223]. In order to clarify the specific role of p47^{phox} in shear stress-induced NADPH oxidase activation, we artificially blocked the signaling pathway through which shear stress stimulates the phosphorylation of p47^{phox} and compared superoxide production with the control case. As shown in Figure 2.6 (dashed lines), the normally quick increase of superoxide production during the first few hours after induction by ULS or OSS is totally blocked, while the production over a

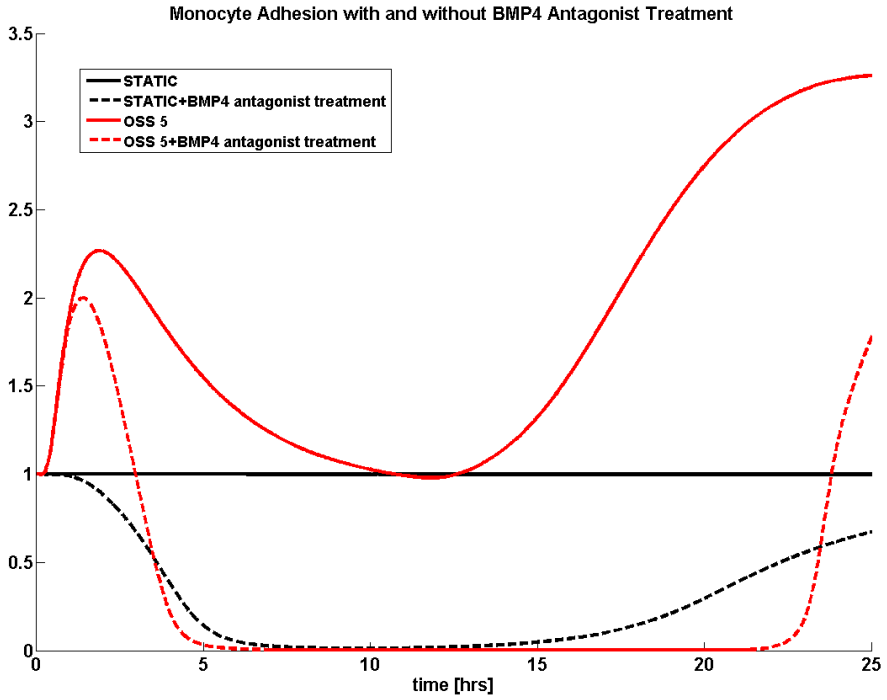

Figure 2.5. Simulated number of bound monocytes with and without BMP4 antagonist treatment.
Solid black line: static control; solid read line: OSS (±5 dyn/cm^2); dashed black line: static control with a BMP4 antagonist bolus of 2 at time t = 0; dashed red line: OSS (±5 dyn/cm^2) with a BMP4 antagonist bolus of 9 at time t = 0.

longer time horizon remains similar. This finding indicates the potential role of p47^{phox} in the quick increase of superoxide production for the first few hours and also provides a possible explanation for why both shear stresses seem capable of stimulating superoxide production during acute exposure.

Finally, the system model represents a p47^{phox} knockout quite well. When the p47^{phox} gene is knocked out, the amount of its corresponding protein becomes extremely small and undetectable by experimental measurements [196]. Obviously, if the available p47^{phox} is entirely depleted, the amount of active p47^{phox} -dependent NADPH oxidase approaches zero, and all subsequent reactions will stop. However, if the amount of p47^{phox} is not completely zero, but drastically reduced (*e.g.*, 30% of the control case), the simulation demonstrates that both

superoxide production and monocyte adhesion become very low with an indistinguishable amount for OSS, ULS and static control conditions (shown in Figure 2.7), even for exactly the same set of parameters. Although OSS and ULS can respectively up-regulate or down-regulate the Nox1 subunit through the BMP4-dependent pathway, the integrative effect of shear stress acting on the activity of NADPH oxidase is limited, or even blocked, if not enough $p47^{phox}$ is available, and this strongly implies the mandatory role of $p47^{phox}$ in the activation of NADPH oxidase. Experimental observations [196] indicate that superoxide produced in endothelial cells obtained from $p47^{phox}$-deficient mouse aortas ($p47^{-/-}$ system) is about 50% or less of the amount produced by the corresponding $p47^{+/+}$ system under static condition. Our simulation results (Figure 2.7 left panel) point in the same direction but indicate a greater reduction (~20% or less of the amount produced by the $p47^{+/+}$ system) in superoxide. This difference in extent is possibly due to the omission of other contributing sources for superoxide production in the current model.

2.4 Discussion

Shear stress has been identified as one of the most important factors for the location of inflammation and subsequent atherosclerosis [42, 158, 161, 162]. *In vitro* experiments have identified an important cytokine, BMP4, which is involved in shear-induced inflammation in endothelial cells and capable of activating endothelial NADPH oxidase, and thus inducing ICAM1 expression [42, 101, 195]. In order to investigate the role of BMP4 in the mechanotransduction system in greater detail, we have in the present work developed a prototype mathematical model. The model was constructed in the GMA format of *Biochemical Systems Theory* [184-187, 199].

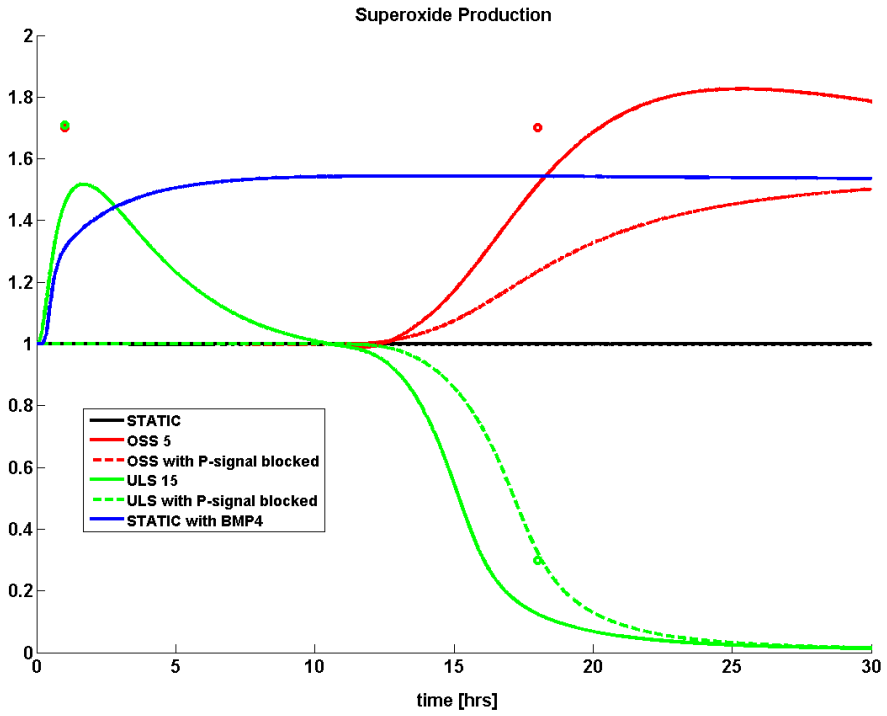

Figure 2.6. Simulated superoxide production under different conditions.

Lines indicate simulation results; dots are experimental measurements. Black line: static control; solid red line: OSS (±dyn/cm^2); dashed red line: OSS (±5 dyn/cm^2) with blocked signal pathway through which OSS otherwise stimulates the phosphorylation rate of p47^{phox}; solid green line: ULS (15 dyn/cm^2); dashed green line: ULS (15 dyn/cm^2) with blocked signal pathway through which OSS otherwise stimulates the phosphorylation rate of p47^{phox}.

As an important initial step, we focused on the key components and processes of the targeted pathway as they are described in Figure 2.1. Due to the paucity (or entire lack) of available time-series data and kinetic characterizations of the processes within the system, we resorted to a novel *ad hoc* method of identifying suitable parameter values that was consistent with the nature of most of the available data, which report responses in relation to a "normal" state. A few assumptions and simplifications (see details in Materials and Methods section) were made to permit a first grasp of the complexity of the mechanosensing system and to allow numerical implementation. Time delays accounting for protein synthesis were added to the GMA model as a means of handling different time scales. Indeed, it turned out that these delays

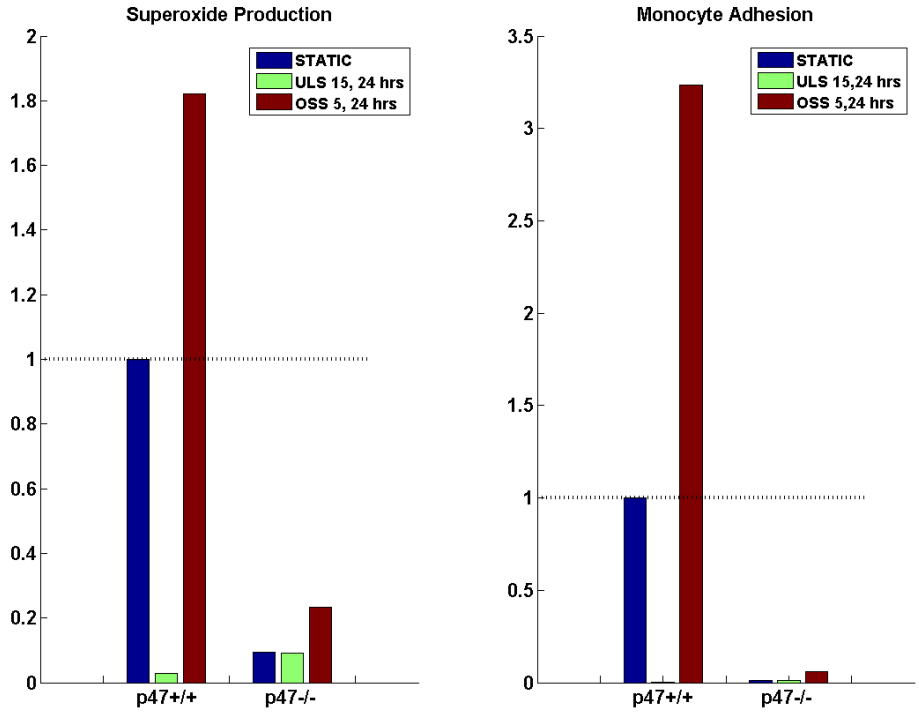

Figure 2.7. Comparison of selected simulation results investigating the $p47^{+/+}$ and $p47^{-/-}$ systems under different shear stress conditions.

In the $p47^{+/+}$ system, $C = 1$ and initial condition of $p47_{phosphorylated} = 0.2$; in the $p47^{-/-}$ system, $C = 0.3$ and initial condition of $p47_{phosphorylated} = 0.06$.

were crucial because their removal led to irreconcilable inconsistencies between model and data (results not shown).

Three scenarios, namely static control, OSS and ULS, were simulated with the model. Most simulation results were found to be consistent with experimental measurements and permitted additional dynamical predictions that have not yet been assessed experimentally. The analysis led to two slight discrepancies between simulation results and experimental observations. One is associated with the steady-state level of Nox1-mRNA under ULS condition, which seemed not to change significantly over static control in experiments, but exhibited a significant reduction in the simulation. A possible explanation may be that the static flow control

is not a physiologically relevant condition for comparison, because the complete lack of blood flow only occurs in extreme pathological conditions. Excluding the static condition, one could simply compare Nox1 mRNA levels under ULS and OSS. In this comparison, the simulation result indicates a significant decrease, which is consistent with the experimental observation. A second discrepancy is the increased ICAM1 expression in the first few hours under ULS, which was not observed *in vitro*. One possible reason for this difference may be that the degradation processes of hydrogen peroxide are extremely simplified at this step, which leads to a direct correlation between the concentration of hydrogen peroxide and ICAM expression. Besides, it is possible that ICAM1 increases as a part of the adaptation response to a sudden change from static to shear conditions (either ULS or OSS). However, it is important to note that ULS inhibits, whereas OSS stimulates, monocyte adhesion to endothelial cells [101, 195], suggesting that there are additional shear-sensitive changes, including an increase in ROS, that regulate the inflammatory response.

Although it is generally agreed that OSS is a critical pro-inflammatory factor that increases ROS production during long exposure (~ one day), different research groups generated distinct transient dynamics and quantitative measurements. For example, studies conducted by Griendling and her colleagues [80] suggested that endothelial cells gradually increase their superoxide production in response to OSS, which is different from our experimental findings [101]. This discrepancy in short-time effect may be caused by the different experimental set-up between the two groups. The model is presently too coarse to identify the "correct" response because changes in parameter values permit reproducing both types of observations (results not shown).

In order to illustrate the specific roles of BMP4 and $p47^{phox}$, additional simulations were implemented to mimic special experimental treatments, like BMP4/BMP4-antagonist treatments and a $p47^{phox}$ knockout model. The results of these simulations unequivocally pointed to the necessity of BMP4 and $p47^{phox}$ in OSS-induced inflammation, suggesting that BMP4 might indeed be a crucial and potent component in the regulation of distinct long-term effects of OSS and ULS, and that $p47^{phox}$ might be a critical factor inducing similar short-effects for OSS and ULS.

Of course, the mechanosensing system *in vivo* is much more complicated than our current model. It consists not only of the single pathway targeted here, but is tied to uncounted other pathways that could have direct or indirect, weak or strong influences on its genomic or metabolic regulation, on important intra- or extra-cellular signals, and on the production or degradation of some of the key compounds that govern our coarse model system. For instance, a recent study suggests that a cAMP/PKA-dependent pathway plays an essential role in the down-regulation of BMP4 under ULS [222]. Furthermore, as stated in the Materials and Methods section, the activities and expressions of some critical antioxidant enzymes, like superoxide dismutase, endothelial nitric oxide synthase and peroxiredoxin 1, have been shown to be regulated by long exposure (~one day) to shear stress, thereby providing a cellular defense mechanism counteracting oxidative stress [211, 213, 214]. These regulations were not incorporated in current model. However, we performed sensitivity analyses of the corresponding parameters (like $\gamma_{19}, \gamma_{21}, g_{20}$), which pointed towards reduced quantities of ROS and increased availability of nitric oxide (data not shown). These results may be interpreted as a self-regulatory defense, which further supports the reasonableness of the current model structure.

To grasp the overall response of endothelial cells to shear stress, these potentially important pathways and mechanisms must ultimately be integrated into a single conceptual framework. It is clear that the increasing scope of such extensions and their explorations will overwhelm the linear cause-and-effect thinking that our human mind likes best, and that the only possible remedy will be a sequence of ever more detailed and fine tuned systematic computational representations. As it stands, the model proposed here is coarse and quite primitive. However, once this prototype model is validated, it can be expanded toward the investigation of other external stimuli like angiotensin II and TNF-α, which also stimulate NADPH oxidase activation and mediate endothelial function in inflammation [13, 224]. The step-wise extension of the model will permit investigations of a growing network of reactions and processes, which might eventually cover the entire dynamic stress response of the endothelial cell.

CHAPTER 3

FUNCTION AND DESIGN OF THE NOX1 SYSTEM IN VASCULAR SMOOTH MUSCLE CELLS[2]

3.1 Introduction

Reactive oxygen species (ROS) play crucial roles as signaling molecules in vascular physiology [16, 17], and aberrations in their profiles or function can lead to a wide spectrum of diseases [5, 9-12, 45]. Under normal physiological conditions, ROS are produced in a controlled manner and found in low concentrations [1]. They exert much of their signaling functions by influencing the activities of specific redox-sensitive genes, proteins, and pathways [1, 16]. Under pathological conditions, ROS production is often increased. This increase leads to an unbalanced redox state, which is generically referred to as "oxidative stress" [19] and often involves deleterious processes that can damage cell structures and negatively alter lipids, proteins, and DNA [3, 20, 21]. Indeed, extended periods of oxidative stress have been shown, both with experimental and clinical evidence, to associate with a wide variety of cardiovascular and metabolic diseases [24, 225], including hypertension, endothelial inflammation, diabetes, and atherosclerosis.

Elevated levels of ROS in the vascular system are often the result of several contributing factors at the production and removal side, but they are generally associated with the activation of vascular NADPH oxidase (Nox) [13, 27, 28], which responds to extracellular stimuli [32, 33]. Once the production of ROS is initially triggered through reactions catalyzed by Nox, ROS can

---

[2] Adapted from: *Yin, W., Voit, E.O. "Function and Design of the Nox1 System in Vascular Smooth Muscle Cells", (submitted), 2012*.

propagate their own production by enhancing activities of other ROS sources [25, 29, 226], including intracellular iron uptake, xanthine oxidase, uncoupled endothelial nitric oxide synthase (eNOS), and damaged mitochondria. This type of propagation constitutes a feedforward mechanism that can lead to a vicious cycle of amplification and the maintenance of endogenous ROS in large quantities, which in turn contribute to pathological signaling. Because vascular NADPH oxidase is at the center of this deleterious process, it has become the subject of extensive investigation.

NADPH oxidase is a member of a family of enzymes that transfer electrons from NADPH to molecular oxygen [29], thus producing specific amounts of superoxide ($O_2^{\cdot-}$), one of the major ROS in vessel walls. The Nox family consists of seven catalytic homologues, four of which (Nox1, Nox2, Nox4, and Nox5) are found in the vasculature [34]. These Nox subtypes present in distinct subcellular compartments, respond to different agonists, and often mediate specific cellular functions [32-36]. Among them, Nox1 has received the most attention mainly because it can be triggered by many physiological or pathological stimuli [34], such as angiotensin II (AngII), a hormone that activates Nox1 in vascular smooth muscle cells (VSMCs) [37, 38], and platelet derived growth factor (PDGF) [37]. Many experimental studies have pointed out that Nox1 is clearly implicated in vascular pathologies [27, 34], including AngII-induced hypertension and hypertrophy [39], serum-induced proliferation and PDGF-induced migration in VSMCs [40, 41], abnormal vascular growth and inflammation [34], and atherosclerosis [28, 42].

Under normal physiological condition, Nox1 serves several beneficial purposes. Importantly, it is a crucial component in several signal transduction pathways [31], and extracellular activators, such as AngII [17] and PDGF [17], typically use Nox1-catalyzed ROS as

specific intracellular signaling molecules to transduce information to downstream signals [227]. If Nox1 does not respond to these extracellular activators efficiently, the ROS it generates are unable to exert their proper signaling function. As a consequence, extracellular signaling information may be lost, along with the intracellular processes or events that were to be triggered. Thus, for proper functioning, Nox1 needs to be maintained in an optimal state, where it is ready to respond appropriately to upstream signals by producing enough ROS to transduce the signal. By the same token, as soon as the input signal disappears, Nox1 must quickly return to its optimal state, where ROS production is low and the machinery for generating new ROS is ready for new upstream signals. In this sense, one may define the optimal state and dynamics for Nox1 under normal physiological condition by two demands. First, Nox1 needs be responsive to input signals. And second, once an input signal ceases, Nox1 must return to its normal state as soon as possible.

The control of Nox1 activity is quite complex, as it is associated with the assembly and disassembly of several components, and in order to understand Nox1 and its regulatory function, it is necessary to discuss its components in some detail. Owing to the large body of experimental studies, we have substantial information about Nox1's molecular composition, intracellular compartmentalization, activation mechanisms, and possible physiological functions [31, 33, 34]. Generally, Nox1 becomes functionally active when it is complexed with several cytosolic subunits and regulators, including an "organizer" [33], an "activator" [33], and the small GTPase Rac [95]. Both the organizer and the activator exist in two homologues, namely, $p47^{phox}$ or NoxO1 [94, 228], and $p67^{phox}$ or NoxA1 [94, 228], respectively. These homologues have different, cell-specific spatial distributions, and their regulatory mechanisms are somewhat different [229]. The specific identity of the Nox1 regulatory subunits is not completely known in

all vascular cells. A notable exception is the case of VSMCs, where Nox1 is complexed with the activator NoxA1 [98, 99] and the organizer $p47^{phox}$ [27, 99, 100]. In this paper, we focus specifically on this very pertinent cell type.

While we have learned much about the assembly and activation of Nox1, the equally important disassembly and recovery of subunits have received much less attentions. One possible reason for neglecting this important aspect might be due to the limitations of current experimental set-ups. Modern biochemical techniques have helped us to identify many proteins, and sometimes their intracellular concentrations. However, because experiments often focus on their concentration changes after a certain stimulus is added, they usually cannot detect the dynamics of material flowing through each individual pathway, thus making the identification of possible disassembly mechanisms difficult. For instance, it is still unclear whether the active Nox1 complex will disassociate into individual subunits or directly degrade via proteolysis once it is no longer needed. It is also unknown in which fashion the disassociation happens and, in fact, whether the order of disassembly is of any importance.

Given the key role of active and inactive Nox1 in normal physiology and in pathophysiology, it is necessary to improve our understanding of Nox1 regulation with respect to both, assembly and disassembly. However, developing deeper insights poses a problem, as subtle differences in the rates of the various assembly and disassembly steps can have consequences that we are unable to quantify and interpret with intuition alone. We are therefore proposing in this work a computational modeling approach that allows us to answer questions about the complex dynamics of Nox1 under normal and pathological conditions.

The model we propose is directly based on the current understanding of the topology of the different, potentially simultaneous activation and disassembly pathways for Nox1 in VSMCs,

as they are shown in Figure 3.1. The disassembly dynamics of the Nox1 system contains four pathways, namely, one direct degradation pathway via proteolysis (marked with f_{14} in Figure 3.1) and three independent recovery pathways (marked as f_2, f_3, and f_4), which differ in a subtle manner: f_2 is the only pathway that directly recoups the subunit NoxA1p; f_3 is the only pathway that directly recoups $p47^{phox}$; and f_4 is the only pathway that directly leads to $Rac1_{GDP}$.

We allow for the flexibility that these disassembly and recovery pathways may be triggered separately or concomitantly by different signals that lead to Nox1 disassembly via dephosphorylation of $p47^{phox}$, via phosphorylation of NoxA1, or via deactivation of Rac1. While these individual pathways have not been experimentally verified specifically in VSMCs, they have been reported to play important roles in the disassembly of Nox1 [230] or its closest homologue, Nox2, in other types of cells [231, 232]. They are therefore reasonable candidates for the so-far ill-characterized disassembly of Nox1.

The proposed system of recovery pathways raises several questions, which have not been answered experimentally, and which are in fact difficult to assess with purely experimental means. Such questions include the following: Are all four pathways active? Are they active simultaneously? Are they all equally important for the effective reestablishment of an appropriate profile of Nox1 subunits? Is one, or are several of the pathways, more effective than others? Do any of them dominate the disassembly process? Does the importance of each pathway change with particular cellular demands? Are the role and importance of each pathway driven by external or intracellular factors, such as initial protein concentrations, necessary response speeds, and the net directions of some of the involved reactions?

These types of questions are difficult to address with experiments, but we will demonstrate here that we can pose such questions and at least partially answer them with

mathematical and computational methods. Indeed, the mathematical model we develop here not only integrates all available biological information and addresses specific questions, but also answers a number of generic questions that target the principles governing the natural design of the Nox1 system. They are of the type "why is this system organized in the fashion we see it, and not in an alternative fashion that appears to be just as reasonable"? To achieve this level of generality, we will construct models in a fashion that is only very mildly dependent on parameter values. Expressed differently, we will develop an entire ensemble of models and distill those with superior features. The initial target is the special case of Nox1 in VSMCs, but features of this representative template are likely to have relevance for other members of the Nox family as well. The model will offer new insights into the possible deactivation mechanisms of Nox1 under normal physiological conditions and allow us to explore generic features that make the observed design superior to imaginable alternatives.

3.2 Materials and Methods

3.2.1 Features of Nox1 in VSMCs

NADPH oxidase 1 (Nox1) is expressed at the plasma membrane [35, 89] and in endosomes [90] of VSMCs of large vessels. For protein stabilization and enzymatic activity, Nox1 needs to associate with the membrane subunit $p22^{phox}$ [92, 93], thereby forming a transmembrane complex. Nox1 is activated when it is complexed with the cytosolic regulators $p47^{phox}$ [31, 94] and NoxA1[98, 99], and the small GTPase Rac1[95-97]; the process is denoted with f_1 in Figure 3.1. Activation of Nox1 is usually preceded by the activation of its cytosolic regulators. Activation of $p47^{phox}$ and Rac1 by certain upstream signals is essential for obtaining full enzymatic activity of Nox1 in VSMCs. In unstimulated cells, $p47^{phox}$ mainly resides in the cytosol [100, 233]. It requires additional phosphorylation in several positions to open its auto-

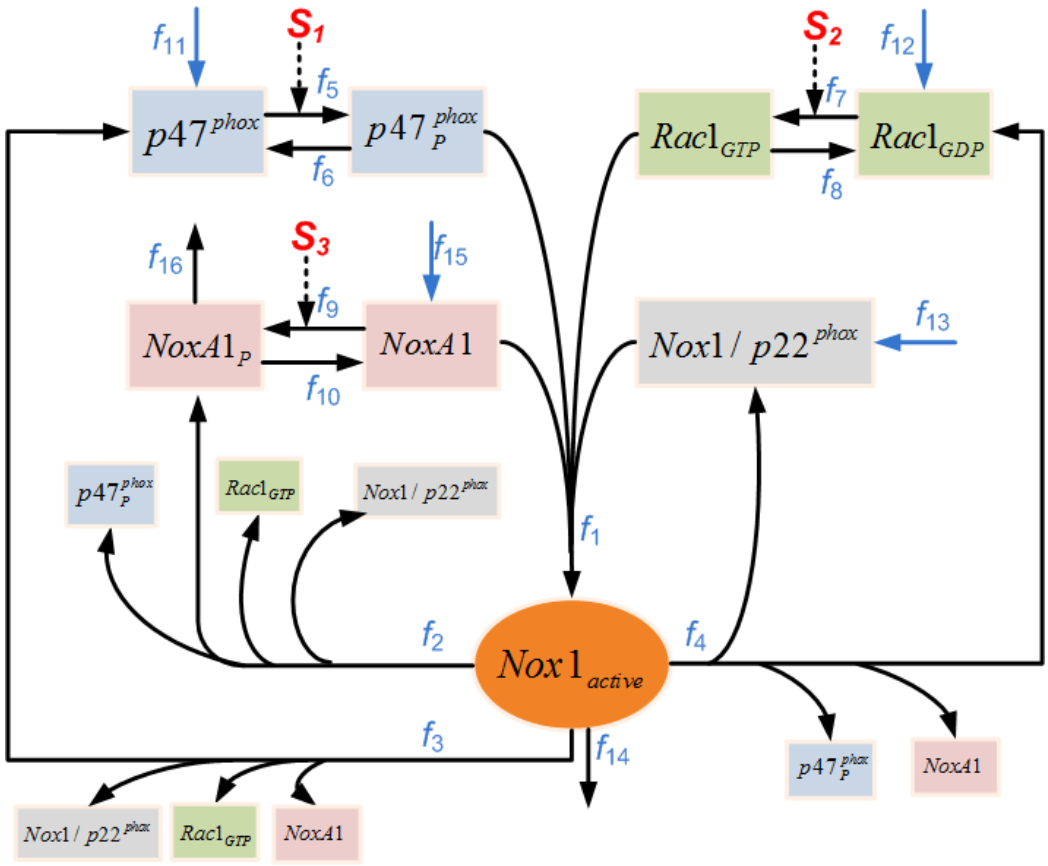

Figure 3.1. Schematic representation of the Nox1 activation-disassembly system in VSMCs.
Note the subtle differences among the three recycling fluxes, which lead to differently phosphorylated or unphosphorylated products. For instance, only the pathway marked f_3 directly produces the unphosphorylated form of $p47^{phox}$ and only f_4 leads directly to $Rac1_{GDP}$.

inhibitory region and to turn it into its active form [33, 70], which then enables it to translocate from the cytosol to the membrane where it associates with the Nox1/p22^{phox} complex. The translocation of phosphorylated p47^{phox} often occurs together with the activator subunit NoxA1 [33, 99]. This phosphorylation of p47^{phox} is mainly catalyzed by protein kinase C (PKC) [38, 105] (marked f_5 in Figure 3.1), which may be stimulated by AngII, typically in association with three different phospholipases [234-236]. However, there are exceptions. For instance, the strong PKC activator phorbol-12-myristate-13-acetate (PMA) alone was shown to increase Nox1 activity in VSMCs [27]. Similar to the activation of p47^{phox}, the small GTPase Rac1 also

requires activation by certain upstream signals. Also like $p47^{phox}$, Rac1 can exist in two inter-convertible forms: GTP-bound (active) and GDP-bound (inactive). Activation of Rac1from its inactive form is facilitated by a family of enzymes called Guanine Exchange Factors (GEFs) [112] (associated with f_7 in Figure 3.1). GEFs render Rac1 capable of associating with the $Nox1/p22^{phox}$ complex, which is another indispensable step for achieving enzymatic activity in Nox1 [95]. Interestingly, the action of GEFs on Rac1 is usually independent of the translocation of $p47^{phox}$ [112]. As an alternative, recent studies suggest that the second cytosolic subunit NoxA1 can be phosphorylated by protein kinase A (PKA) [230, 237] (process f_9 in Figure 3.1). The phosphorylation of NoxA1 greatly enhances its binding affinity to 14-3-3 proteins, thus preventing its association with other Nox1 subunits. Although this mechanism has not directly been verified in VSMCs, it has been suggested as a possible negative regulatory mechanism of Nox1 since both the signal (PKA) and the substrate (NoxA1) co-exist in this type of cell.

Many experimental studies have investigated Nox1-induced ROS production in different cells and under various conditions. By comparing the system responses to certain stimuli with the control system, several Nox1 activators and regulators have been identified. For instance, Nox1 can be directly activated by PDGF [37], AngII [37, 38], thrombin [33], tumor necrosis factor-alpha **(**TNF-α) [90], and many others (for details see [31, 34]). In these experiments, the measured output variables are usually intra- or extra-cellular ROS concentrations or production rates under different conditions. For example, AngII (100nmol/L) has been shown to increase Nox1-catalyzed ROS significantly [38, 235] and is therefore considered an effective activator of Nox1 enzyme. However, due to differences in experimental settings, the measured ROS concentration or production might be found in different magnitudes, and it is possible to encounter slightly different transient behaviors even in response to the same stimulus. As an

example, two experimental groups treated cells with AngII and measured the response over a period of 30 minutes. In both cases, the ROS concentration eventually reached a higher plateau (~2 fold), but in one case the transient was found to be biphasic [38], whereas the other group indicated a continuous and gradual increase in ROS concentration to the same plateau [235]. In both cases, the plateau was sustained for a long time indicating that the levels of ROS and of the corresponding active Nox1 complex assume an up-regulated steady state in response to AngII treatment that is higher than in controls. Western blot analysis did not show any significant effect of AngII on the total Nox1 protein level over 4 hours after AngII treatment [36], which implies that ROS production is likely due to AngII-induced signal activation of Nox1 activity rather than to an increase in the Nox1 protein level.

3.2.2 Variables, Assumptions, Simplifications, and Model Settings

The Nox1 activation-deactivation system has been investigated in numerous studies, and the pathway structure, key components, and a variety of other biological data are available in the literature. The model we propose is based on this information and directly reflects the pathway structure shown in Figure 3.1. The most pertinent information about the model is summarized in Table 3.1. The dependent variables, whose concentrations are affected by the system, include active Nox1 complex ($Nox1_{active}$), $Nox1/p22^{phox}$, $p47^{phox}$, phosphorylated $p47^{phox}$ ($p47_P^{phox}$), GDP-bound Rac1 ($Rac1_{GDP}$), GTP-bound Rac1 ($Rac1_{GTP}$), NoxA1, and phosphorylated NoxA1 ($NoxA1_P$). Input signals, including those leading to $p47^{phox}$ phosphorylation, those effecting Rac1 activation, and those responsible for NoxA1 phosphorylation, are represented by S_1, S_2, and S_3, respectively. They are treated as independent variables, which nominally stay at "1" for

control conditions and are changed to a value above "1" when a relevant extracellular stimulus is applied.

In a VSMC system residing in its control state and exposed to basal input signals, one detects a continuous, low production of ROS [33, 36]. This ROS production does not significantly decrease even if Nox4, a Nox homologue, is significantly knocked down [36]. Combining these two observations suggests the sustained existence of $\mathrm{Nox1}_{\mathrm{active}}$ even if it might have a low concentration. It also indicates that the target system at the ready-to-respond state (RtRS) dynamically maintains a fine-tuned balance of fluxes. As an illustration, consider $\mathrm{Nox1}_{\mathrm{active}}$ (X_1). Basal signals enable continuous formation of X_1 by depleting the pool of $\mathrm{Nox1/p22}^{\mathrm{phox}}$, $p47_P^{phox}$, $\mathrm{Rac1}_{\mathrm{GTP}}$, and $\mathrm{NoxA1}_{\mathrm{P}}$. This formation continues to exist as long as the basal signals are present and the pool of free subunits is not depleted. Thus, in order to maintain X_1 at a stable level, there must be additional pathways (generically referred to as disassembly pathways) that disassociate X_1.

Four alleged disassembly pathways are incorporated in the current model. They include one direct degradation pathway via proteolysis (associated with f_{14} in Figure 3.1) and three independent recycling pathways that recoup subunits of Nox1 (associated with f_2, f_3, and f_4 in Figure 3.1). Because the exact enzymes that catalyze these disassembly reactions of $\mathrm{Nox1}_{\mathrm{active}}$ have not been clearly identified in VSMCs, and their responses to extracellular stimuli are ill characterized, these enzymes are modeled with a nominal activity level of 1. The same strategy is applied to partial or more complicated disassociation mechanisms of $\mathrm{Nox1}_{\mathrm{active}}$, which might exist to serve as effective disassembly mechanisms.

Table 3.1. System variables

Variable	Biological Component
X_1	active Nox1 complex ($Nox1_{active}$)
X_2	$Nox1/p22^{phox}$
X_3	$p47^{phox}$
X_4	phosphorylated $p47^{phox}$ ($p47_P^{phox}$)
X_5	GDP-bound Rac1 ($Rac1_{GDP}$)
X_6	GTP-bound Rac1 ($Rac1_{GTP}$)
X_7	NoxA1
X_8	phosphorylated NoxA1 ($NoxA1_P$)
S_1^*	Signals that phosphorylate $p47^{phox}$ (such as PKC)
S_2^*	Signals that activate Rac1
S_3^*	Signals that phosphorylate NoxA1 (such as PKA)

* indicates independent variable; others are dependent variables.

3.2.3 Model Structure

Based on the model assumptions and the simplifications described above, we propose a model structure, which directly corresponds to the scheme in Figure 3.1, to represent the dynamics of Nox1 in VSMCs. In order to balance the loss of material leaving the system via the proteolytic pathway of $Nox1_{active}$, the model accounts for several processes entering the system, including the influxes of $Nox1/p22^{phox}$, $p47^{phox}$, $Rac1_{GDP}$, and NoxA1 (blue arrows marked f_{11}, f_{12}, f_{13}, and f_{15} in Figure 3.1, respectively). Because the PKA-phosphorylated NoxA1 ($NoxA1_P$) has been shown to bind with 14-3-3 protein to form a complex [237], which could be directly degraded, one additional degradation pathway of $NoxA1_P$ (associated with f_{16} in Figure 3.1) is added to the system. All reactions between active and inactive forms of individual subunits

(marked f_6, f_8, and f_{10} in Figure 3.1), such as dephosphorylation of $p47^{phox}$ and NoxA1, association of GDP to inactivate Rac1, are considered to be reversible, which is supported by experimental observations [33, 112, 230]. By accounting for these various influxes and effluxes, the pathway constitutes an open system that operates at a dynamic steady state, with small amounts of material continuously flowing in and out of the system.

3.2.4 Mathematical Description

The first and arguably most critical step of model design is the translation of the biological system diagram into an appropriate mathematical structure that permits analytical or simulation-supported diagnosis [238]. We use here ordinary differential equations in mass action format that describe how each component in the system varies over time.

The Nox1 system represented in Figure 3.1 can be expressed succinctly in matrix format:

$$\dot{X} = N \cdot F, \tag{3.1}$$

where $X_{8\times1}$ is the dependent variable vector, $\dot{X}$ denotes its derivative, $F_{16\times1}$ is the flux vector, and $N_{8\times16}$ is the stoichiometric matrix, which quantifies the relationships between dependent variables and corresponding fluxes (see details of N in APPENDIX B.1). The fluxes are given in mass action format as

$$\begin{array}{llll} f_1 = \gamma_1 X_2 X_4 X_6 X_7 & f_5 = \gamma_5 X_3 S_1 & f_9 = \gamma_9 X_7 S_3 & f_{13} = \gamma_{13} \\ f_2 = \gamma_2 X_1 & f_6 = \gamma_6 X_4 & f_{10} = \gamma_{10} X_8 & f_{14} = \gamma_{14} X_1 \\ f_3 = \gamma_3 X_1 & f_7 = \gamma_7 X_5 S_2 & f_{11} = \gamma_{11} & f_{15} = \gamma_{15} \\ f_4 = \gamma_4 X_1 & f_8 = \gamma_8 X_6 & f_{12} = \gamma_{12} & f_{16} = \gamma_{16} X_8 \end{array} \tag{3.2}$$

3.2.5 Parameter Estimation

Model simulations and system diagnosis require the specification of numerical values for all parameters from experimental observations. This step is often challenging, for a wide variety of reasons (*e.g.*, see [217]). In the present case, the Nox1 system is at first assumed to operate at its nominal, stable steady state (RtRS), which corresponds to unstimulated control conditions. The concentrations of all dependent variables remain unchanged in this state, which allows the formulation of linear constraints that the fluxes must satisfy Eq. (3.3).

$$\begin{cases} f_{1SS} = f_{2SS} + f_{3SS} + f_{4SS} + f_{14SS} \\ f_{5SS} = f_{3SS} + f_{6SS} + f_{11SS} \\ f_{7SS} = f_{4SS} + f_{8SS} + f_{12SS} \\ f_{9SS} + f_{2SS} = f_{10SS} + f_{16SS} \\ f_{11SS} = f_{14SS} \\ f_{12SS} = f_{14SS} \\ f_{13SS} = f_{14SS} \\ f_{15SS} = f_{14SS} + f_{16SS} \end{cases} \tag{3.3}$$

This set of constraints has an eight-dimensional basis, indicating that only eight linearly independent fluxes need to be characterized from data instead of sixteen. In addition, the fluxes are naturally non-negative, which imposes a set of inequality constraints that confine the search space for feasible parameter values further.

Linear algebra assures us that it ultimately does not matter which basis of flux vectors in Eq. (3.3) is chosen. For reasons of practicality, we select fluxes $f_{2SS}, f_{3SS}, f_{4SS}, f_{6SS}, f_{8SS}, f_{14SS}$, and f_{16SS}, as independent fluxes. As the eighth independent flux, we choose f_{9SS} or f_{10SS}, depending on the relative sizes of f_{2SS} and f_{16SS}. Two reasons support this particular selection. First, f_{2SS}, f_{3SS}, f_{4SS}, and f_{14SS} each represent one disassembly mechanism of $Nox1_{active}$; these fluxes are therefore

of particular interest. Their characterization will enable us to identify the most effective strategies of degrading $Nox1_{active}$. Second, once these selected fluxes are numerically quantified by their rate constants, the remaining fluxes are guaranteed to be non-negative because of their relatively larger magnitudes.

Since little experimental information is available regarding any of the fluxes or their corresponding rate constants, we use Monte Carlo methods, which permit the exploration of large search spaces with reasonable effort. Specifically, the targeted fluxes are randomly sampled from a uniform distribution over an appropriate non-negative domain. The performance of each sampled set is then evaluated by a series of user-defined criteria.

3.2.6 Criteria for Proper Functioning

The criteria used here consist of two types. The first characterizes how efficiently the system responds to signals and how fast this response can be mounted. The rationale for this criterion is the likely advantage for Nox1 to reside in its "optimal state" as much as possible, while ensuring maximal responsiveness to input signals with a minimal response time. The combination of these two aspects becomes particularly important when the system receives several signals within a relatively short time span: If the system is optimized to be launched most effectively from its nominal state, than the system should return to this state as quickly as possible after a signal has been transduced.

The second criterion reflects experimental measurements and qualitative observations. Based on experimental observation of ROS production at and after 30 minutes in AngII [36, 38, 235] and PMA stimulated VSMCs [27], the following three qualitative conditions constitute of the second criterion: (1) At 4 hours of AngII treatment, the total protein of Nox1 subunit,

including both Nox1/p22^{phox} (X_2) and Nox1$_{active}$(X_1), is not significantly changed [36]; (2) After 30 minutes of AngII treatment, the system reaches a steady state or a quasi-steady state with up-regulated Nox1$_{active}$ (X_1) [38, 235]; (3) At 30 minutes of PMA treatment, Nox1$_{active}$ (X_1) activity is up-regulated since ROS production is increased [27].

3.3 Results

3.3.1 Importance of Fine-Tuned Availability of Nox1 Subunits

Before we discuss the details of our modelling results, it is beneficial to confirm, at least conceptually, that a well-controlled disassembly of Nox1 is indeed important and not at all random. In order to respond to extracellular activators like AngII and PDGF effectively, Nox1 needs to reside in a state that is prepared to receive signals and act on the ROS system in an effective and appropriate manner. As discussed in Chapter 1, we call this state the "Ready-to-Respond State" or "RtRS." As soon as an input signal has been processed, Nox1 must quickly return to RtRS, where ROS production is low and the machinery for generating new ROS is ready for new upstream signals. Thus, RtRS and the dynamics with which Nox1 returns to this state must satisfy two demands, as discussed before. Nox1 needs to be maximally responsive to input signals, and, once these cease, return to RtRS as soon as possible.

While many factors affect Nox1's performance, the availability of its subunits in specific proportions is of particular importance for RtRS to be effective. The impact of such a profile can be demonstrated most clearly with a few extreme thought experiments. As an example, suppose that only two subunits (p47^{phox} and Rac1) are involved in the activity of Nox1 and that they are either totally absent (coded as "0") or maximally available and active (coded as "1"), which

simplifies the discussion to four possible states (Table 3.2). Let's furthermore assume that Nox1 must respond to two possible signals (S_1 and S_2) and assess its responsiveness to arbitrary combinations of incoming signal trains of S_1, S_2, or S_1 & S_2. It is not difficult to see that the responsiveness of the Nox1 system is severely limited, no matter in what state Nox1 resides. In reality, the states are somewhere between 0 and 1, but the very much simplified examples already indicate that their distribution is important. Similar thought experiments may be constructed if three subunits are involved in the Nox1 dynamics.

A second factor influencing the responsiveness of Nox1 at RtRS is the relative speed of the rates in reversible reactions, namely the phosphorylation and dephosphorylation of $p47^{phox}$, the activation and deactivation of $Rac1_{GDP}$, and the phosphorylation and dephosphorylation of NoxA1. Again, a thought experiment demonstrates the effects of such rates most easily. Suppose the phosphorylation of $p47^{phox}$ is extremely slow, while dephosphorylation is very fast in comparison, so that $p47^{phox}$ will essentially always be dephosphorylated. An immediate consequence is that no signals of type S_1 have the capacity to trigger the system, because any newly formed phosphorylated $p47^{phox}$ is rapidly deactivated and essentially no additional active $p47^{phox}$ is formed (see Figure 3.1). In the opposite case, if the phosphorylation of $p47^{phox}$ is fast, while dephosphorylation is very slow in comparison, any free $p47^{phox}$ is immediately activated. Thus, even without incoming signals of type S_1, any further addition of S_1 will have little effect on this process, and the Nox1 system is again not responsive to S_1. Similar arguments hold for the other two reversible reactions.

As a conclusion from these thought experiments, optimality of Nox1's RtRS critically depends on the material distribution of subunits and on a fine-tuned balance between the rates in the reversible reactions of the system. In fact, it is not difficult to realize that these two aspects

are correlated with each other. Thus, to maintain or regain an effective RtRS, the Nox1 system must finely tune the balance of fluxes, and the control of this fine-tuning must be dynamic and adaptive.

Table 3.2. Simplified examples illustrating the need for a proper distribution of Nox1 subunits.

Subunit Distribution in RtRs	Responsiveness to Representative Signals
$[p47^{phox}] = 0$; $[Rac1_{GDP}] = 0$;	No response to S_1, S_2, or S_1 & S_2
$[p47^{phox}] = 0$; $[Rac1_{GDP}] = 1$;	Response to S_2, and S_1&S_2, but no response to S_1
$[p47^{phox}] = 1$; $[Rac1_{GDP}] = 0$;	Response to S_1, and S_1&S_2, but no response to S_2
$[p47^{phox}] = 1$; $[Rac1_{GDP}] = 1$;	Response only to S_1&S_2, but not to S_1 or S_2

The computational results fall into two categories. The first category evaluates the four disassembly mechanisms of Nox1 against different, objective criteria of functional effectiveness, which are described in detail in the section 3.2 (Materials and Methods). The second category explores the functional importance of the relevant disassembly and recovery pathways, and their relationships to details of the intracellular milieu, such as initial protein concentrations, the relative magnitudes of different pathway rates, and balances between forward and reverse reactions.

3.3.2 Assessment of Nox1 Disassembly Mechanisms According to the First Criterion

In order to evaluate the system's responsiveness to different signals and signal combinations, we investigate four distinct sets of input signals, namely strong individual signals S_1, S_2, or S_3, as well as simultaneous S_1 and S_2 signals. Among these, three signal sets have been

experimentally shown to possess the capacity of activating Nox1 in VSMCs [27, 38]. The exception, and thus a prediction of the model, is the response to an individual S_3 signal, which is likely to inhibit Nox1 activity, although this has not been directly verified yet in VSMCs.

A factor that could possibly affect the system's responsiveness is the set of initial concentrations of the system components, especially for the cytosolic subunits $p47^{phox}$, Rac1, and NoxA1. Indeed, two questions that need to be investigated are whether their active or inactive forms are dominant under control conditions and how different distributions between these states affect the system's responsiveness to input signals. Because no experimental information is available to address these questions, we explore a large space of possible combinations for initial distributions of the cytosolic components. In order to facilitate this comparative analysis, we assume that the sum of each quantity in its active plus its inactive form is constant, with an arbitrary default value of 100. The initial quantity of a component in active form is assigned by sampling a truncated Gaussian distribution with either a higher mean or a lower mean, as formulated in Eq. (3.4).

$$X_i \in \text{"0"}: \begin{cases} X_i = 5, & X_i \le 5 \\ X_i \in N(25,5), & 5 < X_i \le 50 \\ X_i = 50, & X_i > 50 \end{cases}; \qquad X_i \in \text{"1"}: \begin{cases} X_i = 50, & X_i \le 50 \\ X_i \in N(75,5), & 50 < X_i \le 95 \\ X_i = 95, & X_i > 95 \end{cases} \tag{3.4}$$

Here, "0" and "1" represent truncated Gaussian distributions with a lower and higher means, respectively. This strategy yields a total of 8 combinations of initial condition (Table 3.3). For instance, index 4 in Table 3.3 codes for the vector [0 1 1] and represents the specific situation where the states of phosphorylated NoxA1, $Rac1_{GTP}$, and free $p47^{phox}$ are initially dominant.

Once the initial conditions and input signals are specified, the independent fluxes f_{2SS}, $f_{3SS}, f_{4SS}, f_{6SS}, f_{8SS}, f_{9SS}$ (or f_{10SS}), f_{14SS}, and f_{16SS} are randomly sampled between 1 and 100 with the same uniform distribution $U(0, 2)$ in $\log_{10}$ space, which ensures an appropriate spread of probabilities, and the system's response is evaluated by the new steady state of $\text{Nox1}_{\text{active}}$ (X_1) under different input signals. Intriguingly, the averages of the new steady state of X_1 are essentially unchanged among any of the four sets of input signals and for all initial condition combinations (Figure 3.2(a)).

Table 3.3. Combinations of initial conditions for the three cytosolic subunits contributing to Nox1 assembly.

Index	$p47_P^{phox}$ (X_4)	Rac1_{GTP} (X_6)	NoxA1_{P} (X_8)
1	0*	0	0
2	0	0	1
3	0	1	0
4	0	1	1
5	1	0	0
6	1	0	1
7	1	1	0
8	1	1	1

*: "0" represents a truncated Gaussian distribution with a lower mean, while "1" represents a truncated Gaussian distribution with a higher mean, as described in the Text.

The situation is different for the flux representing the amount of $\text{Nox1}_{\text{active}}$ that is being degraded via direct proteolysis pathway (f_{14SS}). If the numerical sampling range for this flux is gradually decreased, the system responses to input signals, given as the averages of new steady states of X_1, gradually increase or decrease under different input signals. An illustration is given in Figure 3.2 (b). Here, all independent fluxes are sampled with the same distribution $U(0, 2)$ in $\log_{10}$ space, except for f_{14SS}, which is sampled between 0.001 and 0.1 from $U(-3, -1)$ in $\log_{10}$ space. As a consequence of the low magnitude of this flux, in comparison to the other fluxes, the

steady state of X_1 is enabled to increase or decrease greatly in response to different input signals. Expressed differently, a low flux f_{14SS} "sensitizes" X_1. For the extreme case of $f_{14SS} = 0$ (Figure 3.2 (c)), the system has the most effective responses, and it behaves quite similarly when f_{14SS} is very small. This result clearly shows that a relative low magnitude of f_{14SS} is important for the system's responsiveness to input signals.

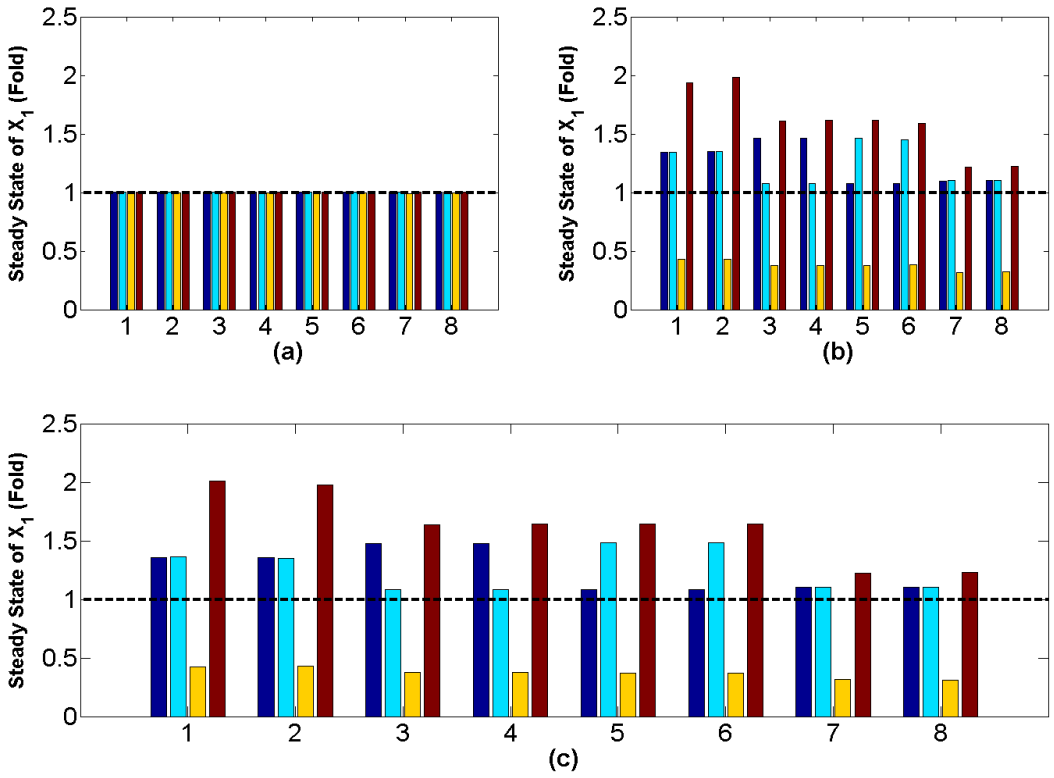

Figure 3.2. Monte-Carlo simulation results for evaluating the performance of the system against the first criterion.

(a) All independent fluxes are sampled from $U(0, 2)$ in $\log_{10}$ space; (b) All independent fluxes are sampled from $U(0, 2)$ except that f_{14SS} is sampled from $U(-3, -1)$ in $\log_{10}$ space; (c) All independent fluxes are sampled from $U(0, 2)$ in $\log_{10}$ space except for f_{14SS}, which equals zero. Colors indicate different input signals. Dark Blue: S_1 signal; Light Blue: S_2 signal; Yellow: S_3 signal; Brown: Combined S_1 and S_2 signal. Numbers indicate index in Table 3.2 for representing different initial distributions. The sampling size for each bar is 2,000 points. Details of simulation settings are given in the APPENDIX B Table B.1.

The same simulation results demonstrate that different combinations of initial conditions affect system performance and can lead to distinct responding patterns. For instance, consider the situation where $p47^{phox}$ and Rac1 are dominant in their active forms. The system readily responds to S_3 signals, but exhibits the most inefficient responses to input signals S_1, S_2 and their combination (Figure 3.2 (c; bars 7 and 8)). Thus, maintaining both $p47^{phox}$ and Rac1 dominant in their active states appears to be an inferior strategy. By contrast, if both $p47^{phox}$ and Rac1 are dominant in their inactive forms, the system is most responsive among all the simulations (Figure 3.2 (c; bars 1 and 2)), suggesting that this state is to be preferred for effective responses. Other sets of initial distributions (Figure 3.2 (c; bars 3 through 6)) are either not responsive to S_1 or S_2 signals, respectively. This computational result correlates well with the previous, and so far unexplained, observation that a system with components in their active forms is generally less responsive than if the components are in their inactive forms.

3.3.3 Assessment of Nox1 Disassembly Mechanisms According to the Second Criterion

Similar to the analysis in the previous section, input signals and initial conditions need to be specified before simulations can be performed. Here the situation is slightly different, because the second criterion is associated with quantitative experimental observations, which allows us to replace the sampling scheme with direct experimental information about input signals and initial conditions. Details of the correspondence between the experimental, extracellular treatments and the numerical characteristics of the input signals and initial conditions for the model are summarized in APPENDIX B.3 and Table B.2.

While valuable, the data are not sufficient to determine specific parameter values and it is still necessary to sample the independent fluxes. They are randomly selected between 0.01 and

100 from the uniform distribution $U(-2, 2)$ in $\log_{10}$ space, and each sampled set is screened against three qualitative criteria as described in the section Materials and Methods. The wide range is expected to cover all pertinent combinations of fluxes, and therefore appears to be adequate for the initial sampling. Ratios beyond this range would result in either very fast or very small reactions, which would ultimately render a dependent variable static.

With these settings, we can now examine combinations of fluxes of the proteolytic pathway (f_{14SS}) and the total recycling pathways (summations of f_{2SS}, f_{3SS}, and f_{4SS}) by screening preliminarily sampled points (APPENDIX B Figure B.1) against different criteria (Figure 3.3). We begin by testing flux combinations against our first criterion of a Nox1 protein level that is sustained for 4 hours of AngII treatment. Interestingly, forcing all admissible flux combinations to match this criterion filters out almost all sampling points located in the lower-right region of the plot, where the proteolytic flux is large and the recycling flux is small. In other words, the combination of a large proteolytic flux and a small recycling flux is inefficient, and this finding directly and independently confirms the results presented before. Next we screen the flux combinations against the second criterion of an up-regulated (quasi-) steady state of $\text{Nox1}_{\text{active}}$ (X_1) at 30 minutes of AngII treatment. This screen filters out different combinations of fluxes, and the remaining, successful combinations locate mainly in the upper-left region of the plot where the proteolytic flux is smaller than 1 while the recycling flux is larger than 1. Finally, filtering the flux combinations against the third criterion, namely up-regulated $\text{Nox1}_{\text{active}}$ (X_1) under phorbol-12-myristate-13-acetate (PMA) treatment, effectively excludes essentially all combinations that are located to the very right, where the numerical value of the proteolytic flux is usually larger than ~ 3, which corresponds to about 0.5 in $\log_{10}$ space.

Valid combinations of flux magnitudes should satisfy all three criteria. Thus, when we sequentially screen against all three criteria, we obtain the result in the lower-right panel of Figure 3.3: the remaining flux combinations are compactly located in a well-defined region where the numerical value of the proteolytic flux is less than ~0.3 (corresponding to about -0.5 in $\log_{10}$ space) while the recycling flux is larger than 1. An extended flux distribution analysis (discussed below; see Figure 3.4) of these remaining points confirms this result. To summarize

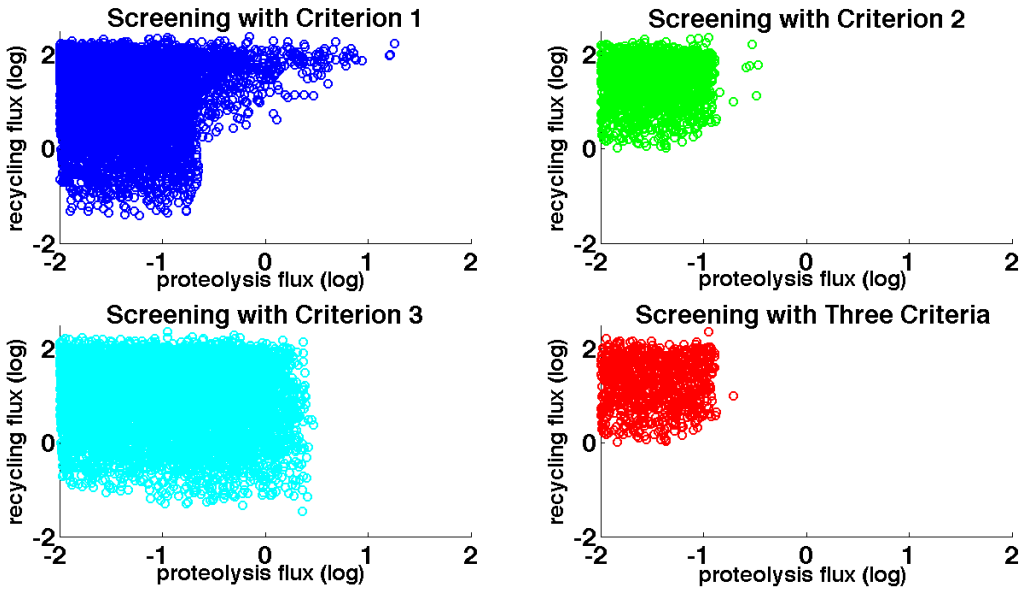

Figure 3.3. Results of a Monte-Carlo simulation with an initial sample of 20,000 points, used to evaluate the performance of the Nox1 system.

Top-left: 7,040 points (combinations of proteolytic and recycling flux magnitudes) are retained after screening against the first criterion. Top-right: 1,473 points are retained after screening against the second criterion; Bottom-left: 6,471 points are retained after screening against the third criterion; Bottom-right: 843 points are retained after screening against all three criteria.

this section, the fluxes were originally sampled with the same probability distribution. Filtering according to the three criteria discussed before yields proteolytic and recycling fluxes that have distinctly separated distributions, with the average recycling flux exceeding the average

proteolytic flux by almost 3 magnitudes in log space, which corresponds to a ratio of about ~ 500 fold.

The combined criteria-driven identification of suitable parameter ranges clearly suggests that the admissible flux candidates satisfying all three criteria tend to reside in the region where much more flux runs through the recycling pathway than through proteolysis. In other words, we can say that under control conditions (unstimulated cells) the dissociation of $Nox1_{active}$ into recycled subunits plays a dominant role in lowering enzyme activity, thus serving as the primary disassembly mechanism. Beyond this conclusion, the flux distribution analysis of the recycling pathways f_{2SS}, f_{3SS}, and f_{4SS} does not reveal a clear activity pattern (lower panels in Figure 3.4). The identification and analysis of such patterns are discussed below.

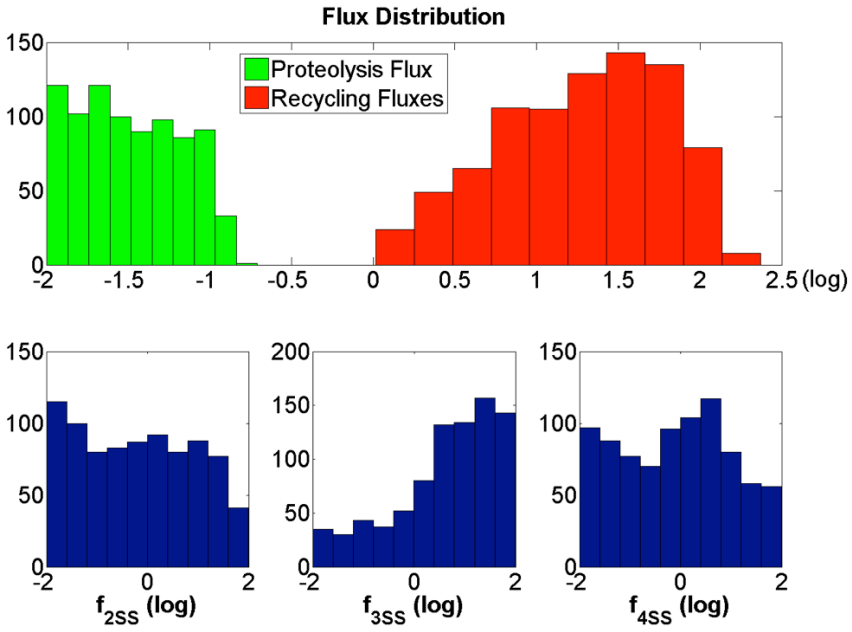

Figure 3.4. Distributions of flux magnitudes in samples filtered with the second criterion.
Upper panel: flux distributions of proteolytic and recycling fluxes. Lower panel: distributions of magnitudes of individual recycling fluxes.

3.3.4 Patterns of Nox1 Recycling Mechanisms

As suggested by the results in previous sections, the three recycling pathways appear to play more important roles for the disassembly of $Nox1_{active}$ than proteolysis. In fact, the fluxes going through these pathways are at least 2 magnitudes (~100 fold) larger, a conclusion that is consistent no matter which of the criteria are used. It is now of interest to explore whether any of the recycling fluxes is more effective than the others. For this analysis, we temporarily ignore the small contribution of proteolysis and set its flux f_{14SS} equal to zero. To balance this missing efflux from the system, the alleged input influxes f_{11SS}, f_{12SS}, and f_{13SS} are also set to zero, so that the constraints in Eq. (3.3) of the Materials and Methods section are again satisfied.

The steady-state fluxes through the three recycling pathways of $Nox1_{active}$ are f_{2SS}, f_{3SS}, and f_{4SS}. *A priori* we do not have any information regarding the relative importance of each of these fluxes or their combinations. Accounting for all possibilities, seven disassembling modules are considered (Figure 3.5). In order to explore the effectiveness of these distinct modules, we again use Monte-Carlo simulations, which allow us to screen for very many combinations of flux magnitudes and to examine their responsiveness and response times to treatment with AngII (represented by a combined S_1 and S_2 signal).

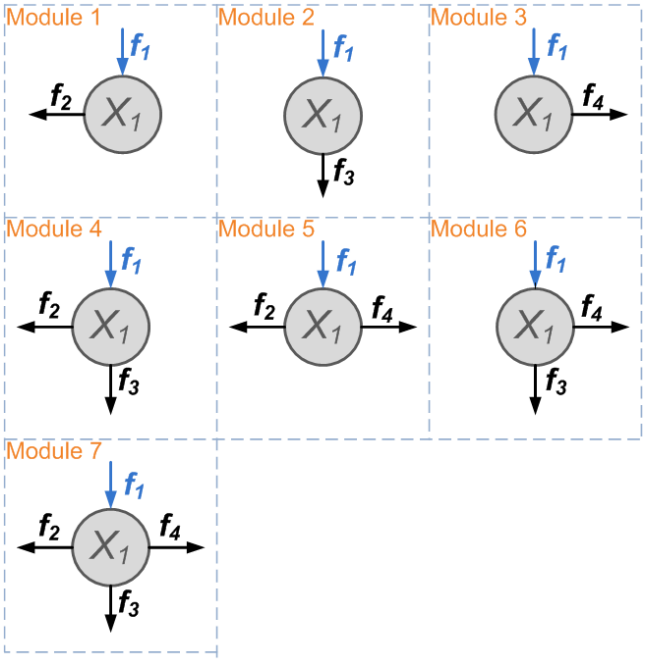

Figure 3.5. Schematic representation of seven possible Nox1 recycling modules.
The proteolytic flux f_{14SS} is assumed to be negligible, as suggested by simulation results in previous sections.

We begin with a closed Nox1 system (for the model structure see APPENDIX B Figure B.2), where the efflux f_{16SS} has a very small magnitude and can be omitted. We analyze the system's response to the pertinent input signal (combined S_1 and S_2) and also track how the active Nox1 complex behaves when the input signal is removed.

In order to keep the initial flux distribution consistent with observations in AngII treatment experiments, we set the control condition such that free $p47^{phox}$, GDP-bound Rac1, and NoxA1 are dominant; in earlier notation, this setting corresponds to the index [0 0 0] in Table 3.3. For fair comparisons among the different flux modules, we always set the flux of active Nox1 production (f_{1SS}) constant (at the numerical value of 100), which ensures that differences in system performance are due to the module structure at hand, rather than differences in flux magnitudes in a given Monte Carlo sample. Within this constraint, the remaining independent

fluxes (f_{6SS}, f_{8SS}, and f_{9SS}) are calculated from (uniformly) randomly sampled rate constants γ_6, γ_8, and γ_9. Sampling rate constants rather than fluxes allows us to inspect the effect of the different reaction rates, especially those associated with reversible reactions, on the performance of the system.

The rate constants, which represent the reversible reactions for activation and deactivation of subunits $p47^{phox}$, Rac1, and NoxA1, respectively, are either sampled as "slow" from the uniform distribution $U(0, 1)$, or as "fast" from the uniform distribution $U(10, 100)$. The simulation results (Figure 3.6 (a)) indicate that when the reversible reaction rates are "slow", all seven deactivation modules tend to exhibit similar behaviors in response to the input signal. Namely, the steady state value of X_1 (in the "on" response) is up-regulated to about the same level between 2.5 ~ 3 fold in all simulations. When the input signal is removed (in the "off" response), X_1 returns to the control level for all seven modules. However, the response times for the "on" and "off" responses are quite different among the modules. Module 1, which has only one recycling pathway specifically associated with f_{2SS}, has the longest response time in both the "on" and "off" responses. In contrast, modules 6 and 7, which contain both recycling pathways (f_{3SS} and f_{4SS}) have much shorter response times (less than half of other response times). The response time is an important feature of a signaling system, because it determines its refractory period. Thus, the latter modules are to be considered more efficient than the former. By the same token, the differences in response times have to be significant to allow the identification of superior and inferior designs. In the present case, the differences among all seven modules are insignificant in terms of responsiveness and response times, as long as the reversible reaction rates are fast in both directions (Figure 3.6 (b)). Thus, these simulations clearly demonstrate how relative reaction rates for the reversible processes in the system affect performance.

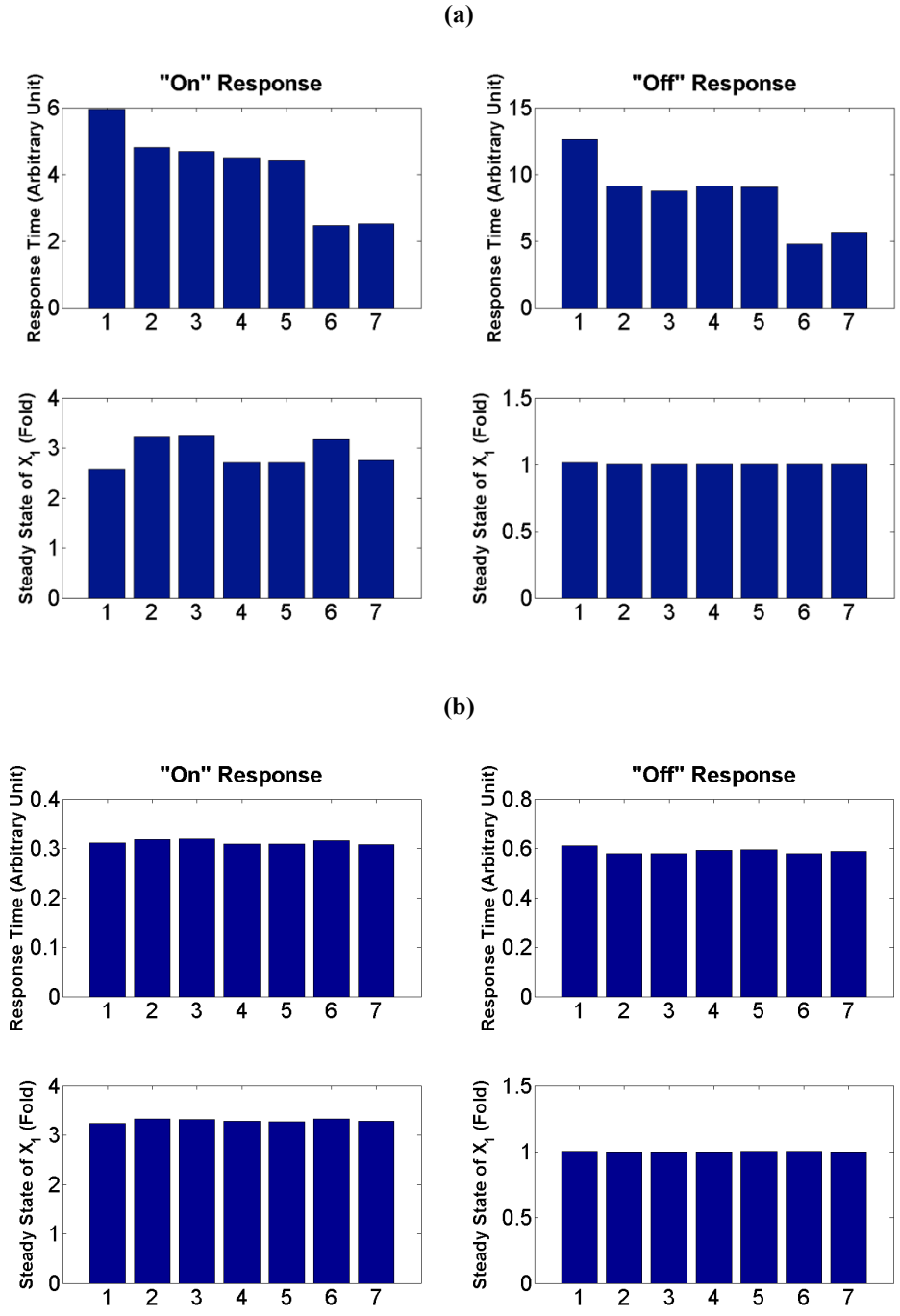

Figure 3.6. Results of Monte-Carlo simulations evaluating the responsiveness and response time of a closed Nox1 activation-deactivation system (f_{16SS} = 0).

(a) Slow rates for reversible reactions with $\gamma_i \in U(0, 1)$, i = 6, 8, 9. (b) Fast rates for reversible reactions with $\gamma_i \in U(10, 100)$, i = 6, 8, 9. Integer numbers indicate the index of the deactivation module. The sampling size for each bar is 2,000 points. Note different y-axes.

In reality, the system is open, and the efflux f_{16SS} may affect the disassembly of Nox1. The analysis of this case is complicated by the fact that we have no information regarding the relative magnitudes of the input fluxes and only know that the constraint $f_{2SS} + f_{9SS} = f_{10SS} + f_{16SS}$ must be true. We study two scenarios. In the first, f_{9SS} is larger than f_{10SS}, which tips the balance from NoxA1 to NoxA1_p, while in the second scenario the opposite is true.

Intriguingly, the system performance is strongly affected by the transition from a closed to an open system, even though the efflux f_{16SS} is not substantial (compare Figures 3.6 and 3.7). In particular, the magnitudes of the reversible reaction rates affect the performance of the system differently for the various deactivation modules. When the reversible reaction rates are slow (Figure panels 3.7(a) and (b)), different disassembly modules exhibit distinct responses, depending on the direction of the net flux between f_{9SS} and f_{10SS}. For instance, in modules 2, 3, and 6, which do not contain the recycling pathway f_{2SS}, the steady states of X_1 in the "on" response are up-regulated to above 3 fold. By contrast, the steady state of X_1 for the other modules (1, 4, 5, and 7) is only modestly up-regulated (less than 2 fold). Moreover, the stronger responders (modules 2, 3, and 6) exhibit much shorter response times. In particular, module 6 has a response time that is almost one third of the other response times, as long as $f_{9SS} \leq f_{10SS}$ (Figure 3.7(b)). By contrast, if $f_{9SS} > f_{10SS}$, the differences in response times for the various modules are insignificant.

(a)

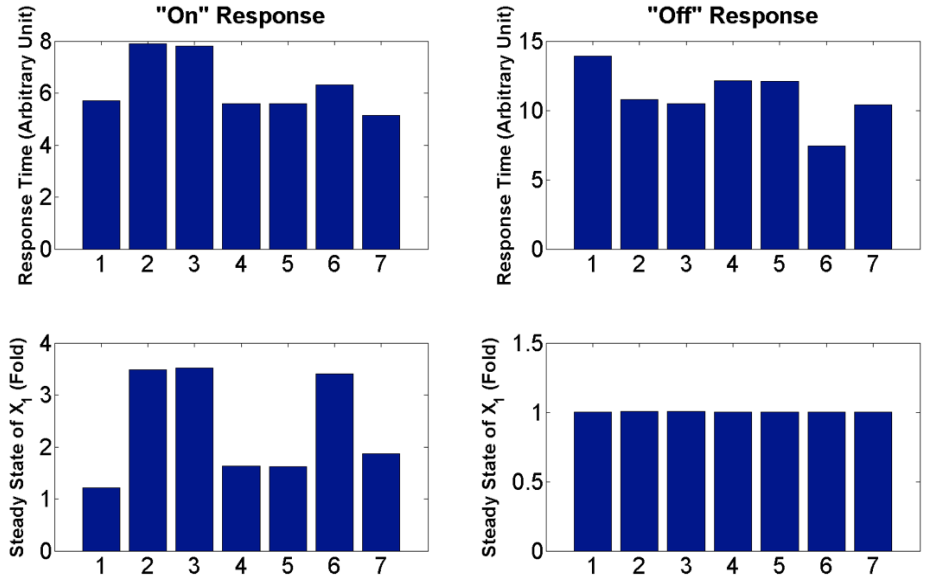

(b)

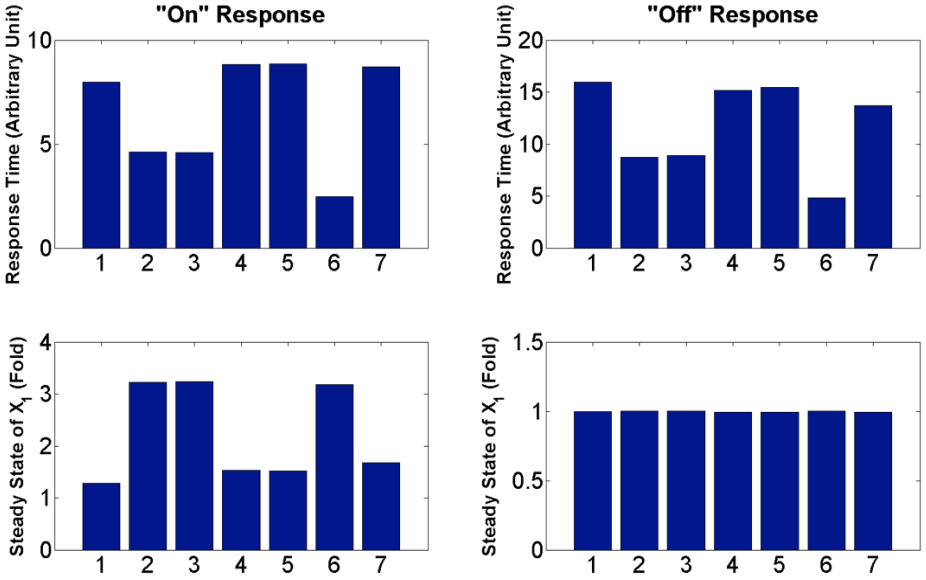

Figure 3.7. Results of Monte-Carlo simulations evaluating the responsiveness and response times of an open Nox1 activation-deactivation systems ($f_{16SS} \neq 0$) with slow reversible reaction rates ($\gamma_i \in U(0, 1)$, $i = 6, 8, 9$). (a) Scenario 1: $f_{9SS} > f_{10SS}$; (b) Scenario 2: $f_{9SS} \leqslant f_{10SS}$. Integer numbers indicate the index of the deactivation module. The sample size for each bar is 2,000 points.

When all reversible reaction rates are fast, the seven disassembly modules tend to perform similarly in terms of responsiveness as well as response time (Figure panels 3.8 (a) and (b)). However, the response times of modules 2, 3, and 6 are much shorter than the others if $f_{9SS} \leq f_{10SS}$ (Figure 3.8 (b)), indicating that this constraint renders these three modules particularly efficient.

3.4 Discussion

Although Nox1 exhibits relatively low basal expression in VSMCs [37], it has been extensively studied. Nox1-induced ROS often serve as important intracellular signaling molecules, transducing extracellular signals into intracellular targets. This process can be activated by numerous physiological and pathological stimuli [37, 38, 239] and has therefore been implicated in a variety of cardiovascular diseases [31, 34]. As a consequence, Nox1 must function properly and efficiently. It must be able to respond quickly and strongly. It is similarly important for Nox1 to return to its normal state fast, lest it is unable to respond to further stimuli.

The activation and disassembly processes of Nox1 in VSMCs constitute a system of pathways whose components have been identified and characterized to some degree over the past decades [33, 37, 38, 93, 95, 99]. In particular, the scientific community has assembled quite a detailed picture of how individual subunits of Nox1 are organized to form an active enzyme complex. While the components and basic interactions are known, the overall functionality of the Nox1 system is not easy to intuit. For instance, the balance between phosphorylated and dephosphorylated states under nominal, unstimulated conditions, as well as the reaction rates of the system's governing processes, might appear to be accidents of evolution: After all, why

(a)

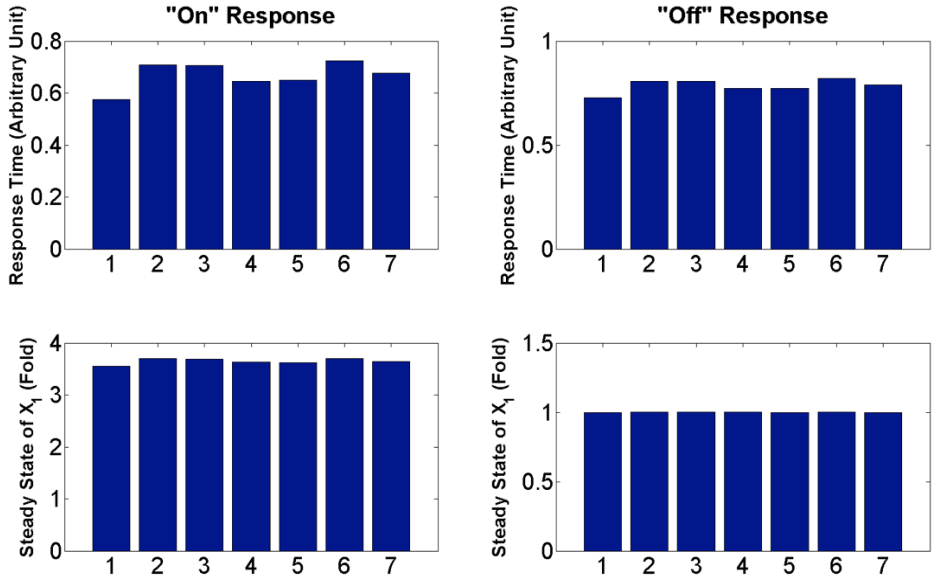

(b)

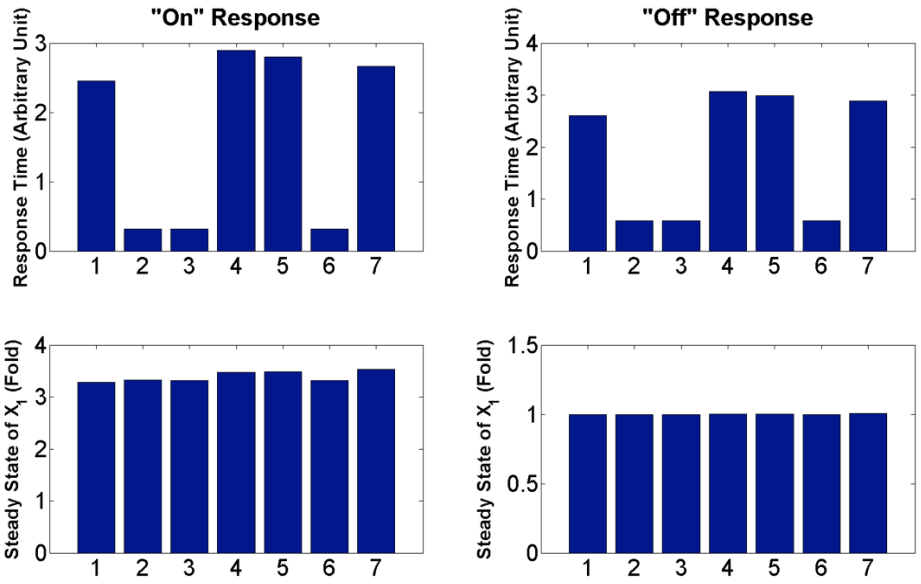

Figure 3.8. Results of Monte-Carlo simulations evaluating the responsiveness and response times for an open Nox1 activation-deactivation system ($f_{16SS} \neq 0$) with fast reversible reaction rates ($\gamma_i \in U(10, 100)$, $i = 6, 8, 9$). (a) Scenario 1: $f_{9SS} > f_{10SS}$; (b) Scenario 2: $f_{9SS} \leq f_{10SS}$. Integer numbers indicate the index of the deactivation module. The sample size for each bar is 2,000 points.

should it matter in which order the Nox1 complex is disassembled? As we have shown with our computational analysis here, specific routes of disassembly and proper characteristics of the unstimulated RtRS are crucial for optimal performance. To arrive at this insight, we set up a rather generic pathway model and analyzed it in a fashion that is only minimally affected by the choice of particular parameter values.

The model accounts for four potential Nox1 disassembly pathways, which include one direct degradation pathway of $Nox1_{active}$ via proteolysis and three independent recovery pathways for subunits (see fluxes f_{14}, f_2, f_3, and f_4 in Figure 3.1). Investigations of these fluxes at a nominal, unstimulated steady state were performed with Monte-Carlo simulations. For these analyses, the magnitudes of fluxes were classified as fast or slow, and the relatively effectiveness of the four disassembly pathways was assessed in terms of different criteria, namely, the strength and speed of system responses to input signals, and their consistency with experimental and clinical data.

Assessments with respect to the different criteria led to similar results. First, for effective functioning, the flux associated with proteolysis (f_{14SS}) must be much smaller (by at least two orders of magnitude) than the fluxes associated with recycling pathways (Figures 3.2 – 3.4), indicating the relative inefficiency of proteolysis for the disassembly of $Nox1_{active}$ under normal physiological conditions. Expressed differently, the disassociation of the active Nox1 complex and recycling into subunits plays the dominant role, which is seen in the relatively large magnitudes of these fluxes. This result is not too surprising, because proteolysis requires total *de novo* assembly of Nox1 before new signals can be transduced.

Less predictable, the optimal unstimulated state (RtRS) is characterized by specific balances between phosphorylated and dephosphorylated forms of the subunits. These proper balances are critical for efficiency. As consistently shown by the results of different scenario simulations (Figures 3.2 (b) and (c)), the initial states with indices [0 0 0] and [0 0 1] exhibit the most effective responses to external signals, while systems with indices [1 1 0] and [1 1 1] are the least efficient. These results imply that both $p47^{phox}$ and Rac1 should reside in their inactive forms when the system is at rest. This inference from the computational analysis, while difficult to predict from the topology of the pathway, is well consistent with experimental observations [100, 112, 233] and offers an unbiased rationale and explanation. As an interesting side effect, this state equips the Nox1 system with a certain degree of noise tolerance: Residing in the inactive forms, any spurious formation of Nox1 in the absence of true signals, followed by an erroneous signal transduction, is much less likely than if the system maintained the active forms, which are the direct precursors of the active Nox1 enzyme. Thus, to avoid spurious signaling events, the system is "parked" in its inactive form and requires external stimuli to trigger a signal transduction event. In contrast to $p47^{phox}$ and Rac1, the unphosphorylated form of the Nox1 activator unit NoxA1 is the direct precursor component of active Nox1, and the current analysis has not revealed whether the balance is tilted toward the precursor or its complement.

One should note that although the three disassociation and recycling pathways apparently play interchangeable roles in disassembling $Nox1_{active}$, they actually guide the system to different states. It is instructive to perform another thought experiment to study the resulting consequences. Suppose the system receives a strong signal S_1. Depending on the different combinations or flux distribution patterns among the three recycling pathways f_2, f_3 and f_4, the enzymatic profiles of $Nox1_{active}$ generation can vary substantially. Let's first consider the extreme

case where only f_3 is present as the recycling pathway (cf. Figure 3.1). In the presence of S_1, $p47^{phox}$ becomes depleted, and formation of active Nox1 subsequently depletes the other active precursors $Rac1_{GTP}$ and NoxA1. Disassociation of the Nox1 complex through pathway f_3 restores $p47^{phox}$ and, more importantly, $Rac1_{GTP}$ and NoxA1, which enable sustained formation of new active Nox1 as long as S_1 is present. In other words, if S_1 is persistent and f_3 is the only recycling pathway, Nox1 will be highly and continuously activated. By contrast, if S_1 is persistent and the system does not use f_3, but instead f_2 or f_4, the situation is very different. Because f_2 and f_4 respectively restore NoxA1p and $Rac1_{GDP}$, but not NoxA1 and $Rac1_{GTP}$, the restoration of these two active precursors depends mainly on the reverse reactions f_7 and f_{10}. As a consequence, the formation of new active Nox1 is now limited by the availability of NoxA1 or $Rac1_{GTP}$ even if there are significant residual amounts of phosphorylated $p47^{phox}$. Thus, the refraction period of the Nox1 system is driven by the slower rates of f_7 and f_{10}. As a result, one should expect a much lower activity of Nox1, compared to the previous case, even under the same input signal S_1. In other words, in the presence of all three pathways, the system can lower Nox1 activity by either inhibiting f_3 or decreasing its flux distribution ratio in the presence of input signal S_1.

The analogous arguments hold for an input signal of type S_2. By contrast, signal S_3 is a "negative" signal that effectively shuts down the entire system as it decreases the availability of NoxA1. The presence of pathway f_2 can further exacerbate this situation, while the presence of f_3 or f_4 may counteract this negative effect by releasing more active NoxA1. However, the situation under this scenario is more complicated because f_3 or f_4 also restore the inactive form of $p47^{phox}$ or $Rac1_{GDP}$, which might need additional activation signals.

Nothing is truly known about the internal regulation of the Nox1 system, but our analysis implies that the three disassembly and recycling pathways may not just be redundant variants,

but that they may permit specific control mechanisms that allow the system to habituate, adjust to persistent signals, and control its refractory period under repeated signals of the same or different types. An example is given by a system exposed to a persistent signal S_1, and comparative simulation results for three distinct scenarios with only one recycling pathway each are presented in Figure B.3 (for details, see APPENDIX B.4). Although the responsiveness of the Nox1 system is affected by a number of factors, such as the relative rates of the reversible reactions and the magnitude of efflux, recycling via dephosphorylation of $p47^{phox}$ consistently tends to lead to as high, and usually higher, a steady state of X_1 than the other two recycling mechanisms. Therefore, to achieve enhanced responsiveness to persistent signals of type S_1, the most efficient regulatory mechanism would appear to be the activation of the corresponding recycling pathway via dephosphorylation of $p47^{phox}$. This activation could be triggered directly by signals of type S_1 or by an indirect mechanism. Particular responsiveness to other signals would require different control strategies.

In order to explore the relative effectiveness of the three recycling pathways, we used Monte-Carlo simulations to test the performance of seven distinct disassembly modules. These modules accounted for scenarios with only one, two or all three recycling pathways. Initially, we tested the case where the basal flux through the proteolytic pathway (f_{14}) is so small that it can be omitted. Several cases were explored. When the independent efflux f_{16} is also small enough to be ignored, the simulation results (Figure 3.6) are strongly affected by the relationships between the rate constants for the reversible reactions. When the reversible reactions are slow, modules 6 and 7 (see Figure 3.5), have the shortest response time. These modules contain both disassociation pathways f_3 and f_4, which directly restore inactive $p47^{phox}$ and Rac1. In contrast, if the reversible reactions are fast, all modules exhibit a similar performance in terms of responsiveness as well as

response time. These results are consistent with the arguments from the thought experiment above. They strongly indicate that it is efficient to replenish the subunit pools as quickly as possible. However, this is only possible up to a point. In this case, the distributed disassembly via f_3 and f_4 is a preferred strategy. Recycling through f_2 is particularly effective if the system is to be shut down.

If the efflux f_{16} cannot be ignored, the system performance is strongly influenced by the net balance between the fluxes converting NoxA1 and NoxA1_P into each other. Clearly, tipping the balance toward the phosphorylated form supplies substrate for f_{16}, thereby leading to a depletion of this subunit. This effect is exacerbated by a large apportionment of the deactivation flux toward f_2, which is the only recycling flux generating NoxA1_P. Indeed, supporting this assessment, our model analysis pointed to the importance of a suitable balance between f_9 and f_{10}. Given the potentially detrimental outcome of this scenario, it will be useful to study the magnitudes and regulation of both f_{16} and f_2 experimentally.

We have employed computational methods to investigate the effectiveness of alternative strategies for Nox1 disassembly and the recycling of subunits in VSMCs. The results of the Monte-Carlo simulations, which by and large are independent of specific parameter values, strongly indicate that disassembly through recycling is much more effective than proteolysis. Furthermore, the relative performance of each recycling pathway is affected by the rates and balances of the reversible reactions in the system, and also by quantitative features of the system, such as the magnitude of the efflux of phosphorylated NoxA1 (f_{16}) and the direction of the net flux between NoxA1 and NoxA1_P. These balances are natural targets for internal control mechanisms of Nox1 dynamics, which at this point are unknown. Finally, the analysis revealed

information regarding the refractory period of the signaling system, which is determined by the relative magnitudes of several flux rates.

CHAPTER 4

DYNAMIC ANALYSIS OF ANGIOTENSIN II-INDUCED NOX1 ACTIVATION IN VASCULAR SMOOTH MUSCLE CELLS[3]

4.1 Introduction

All cell types in vasculature have the ability to produce reactive oxygen species (ROS). More and more experimental and clinical evidence indicates that ROS, serving as important inter- and intra-cellular second messengers [3, 16], are involved in numerous fundamental biological processes [5, 10, 17, 45], including growth, proliferation, migration, and apoptosis. By the same token, ROS have been implicated in the genesis of a variety of vascular diseases [1, 7, 11, 12], including atherosclerosis, hypertension, angiogenesis, and heart failure. Given their widespread importance, it becomes imperative to gain a better understanding of the potential endogenous sources of ROS and their regulatory mechanisms in vascular wall.

The physiological generation of ROS often occurs as a by-product of other cellular processes [25]. Prominently, NADPH oxidase (Nox) has been identified as a main source of ROS, when it responds to various extracellular stimuli [13, 27, 28, 33], such as growth factors, hormones, and mechanical forces. Four distinct Nox homologues are found in vasculature, including Nox1, Nox2, Nox4, and Nox5 [33, 34]. The cellular distributions of these different homologues are rather complicated; they may exist in different types of vascular cells, and may also co-express in the same type of cells. For instance, in vascular smooth muscle cells (VSMCs)

---

[3] Adapted from: *Yin, W., Voit, E.O. "The Dynamic Analysis of Angiotensin II-Induced Nox1 Activation in Vascular Smooth Muscle Cells", (in the process of being submitted), 2012.*

of large vessels, which have been extensively used to study the activation and regulation of Nox enzymes, two distinct homologues, namely Nox1 and Nox4, are found to co-exist [35].

Compared to Nox4, which primarily maintains the basal level of ROS under unstimulated cells and is proposed to have enzymatic activity proportional to its protein expression [31, 34], Nox1 is much more active and capable of responding to many extracellular stimuli. It is also regulated through a number of different signaling pathways[31]. Indeed, uncounted experiments have been devoted to exploring the underlying activation and regulatory mechanisms of Nox1 in different types of cells, as well as the responses to different stimuli. Among these stimuli, angiotensin II (AngII)-induced Nox1 activation in VSMCs has received the most attention [36-38]. This system is thus as a good template to explore further details of the dynamics of Nox1.

Regulation of Nox1 occurs at multiple levels, including transcription and translation, as well as through signal-based modulation. The former mechanisms are mainly associated with the long-term, sustained effects of Nox1 activity, while the latter is tightly related to the dynamic and transient responses of the Nox1 system. The signaling molecules that could directly affect Nox1 activity and subsequent ROS production include protein kinase C (PKC) [33], protein kinase A (PKA)[230], and cSrc together with its downstream signaling molecules [38, 233]. The involvement and regulatory functions of these signaling molecules have been identified and validated through various kinds of experiments, such as experiments that add pertinent activators and inhibitors to both unstimulated and stimulated cells [38], and knocked-down or silencing experiments of specific signaling molecules [38]. These carefully designed experiments have greatly enhanced our understanding of Nox1 regulation, and particularly its activating process, and have revealed the important and distinct roles of the involved signaling molecule. For instance, PKC has been shown to be involved in regulating the initial release of ROS in AngII-

induced Nox1 activation in VSMCs; while the cSrc-dependent signaling cascade appears to be more involved with the sustained ROS increase over longer time horizons [38].

Many studies have found that signal-based regulation often operates in a complicated fashion. On the one hand, distinct signals may simultaneously regulate the same process. For the Nox1 system in VSMCs, both PKC [33] and cSrc [233] signals have been reported to be able to enhance the phosphorylation of $p47^{phox}$, an essential step for initiating Nox1 activation. On the other hand, the same signaling molecule may be involved in multiple processes but exert opposite effects. For instance, PKC is not only involved in $p47^{phox}$ phosphorylation [33], but also capable of facilitating the phosphorylation of the subunit NoxA1[230]. The former mechanism tends to activate the Nox1 system, while the latter has the opposite effect of inhibiting Nox1 activity by reducing the availability of active subunit NoxA1. As a consequence of these complex signaling regulation mechanisms, intuition is insufficient for deducing or predicting the ultimate effect or function of a pertinent signal that can potentially play two opposite roles. It is also not easy to infer the dominant signaling player for each pertinent process when multiple signals are involved.

Compared to the activation process, the disassembly mechanisms of Nox1 have received much less attention, and many open questions remain that need to be answered. Some of these questions have already been posed and partially answered in Chapter 3, where we discussed four possible Nox1 disassembly mechanisms, namely one direct degradation pathway via proteolysis and three independent recycling pathways. By using different types of criteria, we inferred that the direct degradation pathway via proteolysis is most inefficient in disassembling the active Nox1 complex under nominal physiological condition, that is, in unstimulated cells. Moreover, we found that the relative importance and performance of each recycling pathway are affected by

the rates and balances of the reversible reactions in the system, and also by other quantitative features of the system (see detailed discussion in section 3.4).

All analyses in Chapter 3 were based on the considerations of constant signals and steady-state values of the Nox1 system under both unstimulated and stimulated conditions. This restriction to the steady state is not sufficient for interpreting the function of the Nox1 system when it is exposed to the dynamic signals whose values continuously change over time. For instance, when the cell is treated with certain doses of Ang II , the Nox1 system is actually regulated by AngII-induced, dynamic signals, rather than constant signals. Dynamic scenarios of this type raise additional questions, including the following. Are the previously proposed disassembly pathways active simultaneously in the presence of dynamic signals? Are they equally important in disassembling Nox1 in stimulated cells? Does the role and importance of each disassembly pathway change in response to AngII-induced dynamic signals? How do AngII-induced signals dynamically regulate Nox1 activity?

These types of questions are difficult to address with experiments, but we demonstrated here that we can at least partially answer and explore them with mathematical and computational methods. Indeed, the mathematical models we propose here not only integrate all available biological information and answer specific questions, but are also capable of reproducing most experimental observations regardless of whether they are static or dynamic, qualitative or quantitative. In fact, these mathematical models help us understand the overall dynamic behavior of the target system and its complicated structure, and enable us to analyze and predict the effects of time-varying responses in all system components.

The design of such models is complicated by the fact that good data are still scarce. Currently, many experiments exclusively measure input-output relationships of some select system components, without however characterizing the intermediate dynamics of the system. While these experiments have offered us many invaluable insights into the target system, including its key components, activators, and inhibitors, they seldom reveal detailed and specific information of each pertinent reaction or process, such as its reaction rate, kinetic properties of enzymes, or flux information. The question thus arises whether sophisticated computational approaches might be able to extract additional insights out of the given body of data, This chapter shows that this is possible, at least to some degree. It uses computational simulation methods to characterize dynamic features of the AngII-induced Nox1 activation system in VSMCs.

4.2 Materials and Methods

4.2.1 Overview of Model Structure

Angiotensin II (AngII)-stimulated ROS production in VSMCs is mediated via Nox1 activation [37]. Typically, this activation occurs in two distinct phases [240]: the first is rapid and transient (with a time scale ranging from seconds up to minutes), whereas the second phase is delayed and sustained (with a time scale ranging between 1 hour and several hours). The early phase of ROS production is due to an acute activation of Nox1 by AngII through different signal regulatory pathways [38], while the second phase is thought to depend mainly on the initial burst and is a consequence of up-regulation of mRNA and/or protein expressions of different Nox subunits, including Nox1 [37, 103], $p22^{phox}$ [104, 105], and $p47^{phox}$ [105, 106]. In order to investigate the regulatory mechanisms of Nox1 activation, we will mainly focus on the first

phase of ROS production with the targeted time interval ranging from the beginning of an AngII stimulus experiment up to 30 minutes.

In the first phase, rapid ROS release requires $p47^{phox}$ phosphorylation by PKC and its subsequent translocation to the membrane [38, 105, 241]. PKC activity is regulated by AngII through three different phospholipases (PLs): PLC [234], PLA_2 [236], and PLD [235]. An additional potential regulator of $p47^{phox}$ phosphorylation is cSrc [233, 242], although its function remains to be determined biochemically. Another indispensible step for Nox1 activation by AngII requires Rac1 [95, 96, 243], whose activation is regulated by some guanine nucleotide exchange factor (GEF), which has not be unambiguously identified in VSMCs. Of importance, the sustained stimulation of Rac1 by AngII depends on the initial burst of Nox1-catalyzed H_2O_2, which in turn activates cSrc and its downstream signaling molecules EGFR and PI3K [38]. As a result, this H_2O_2-induced cSrc activation creates an amplification of oxidase activity by imposing a positive feedback on the system, thereby maintaining the sustained increase of ROS production in cells stimulated with AngII. Moreover, recent studies suggest that the cytosolic subunit NoxA1 can be phosphorylated by some protein kinases, including protein kinase A (PKA) and PKC [230, 237]. This phosphorylation of NoxA1 greatly enhances its binding affinity to 14-3-3 proteins [237], thus preventing its association with other Nox1 subunits. However, compared to other signaling molecules like PKC, AngII-induced PKA activation in VSMCs appears to be negligible (*K. Griendling, pers. comm.*). Therefore, we temporally ignore the regulatory effect of PKA on the process of NoxA1 phosphorylation in the current model and only consider the PKC-mediated NoxA1 phosphorylation.

Based on our current understanding of the activation pathway, its topology, key components, pertinent regulatory signals, and the different, potentially simultaneous disassembly

pathways which have been proposed and discussed in Chapter 3, we propose here a model structure describing AngII-induced Nox1 activation and its subsequent ROS production in VSMCs. The key processes are shown schematically in Figure 4.1. In order to represent the Nox-catalyzed ROS production in VSMCs as faithfully as possible, we consider not only Nox1, but also its homologue Nox4. However, because the enzymatic activity of Nox4 is not acutely affected by AngII treatment within the time interval 0~30 minutes, Nox4 is simply considered as an independent input with constant enzymatic activity under both unstimulated and stimulated conditions.

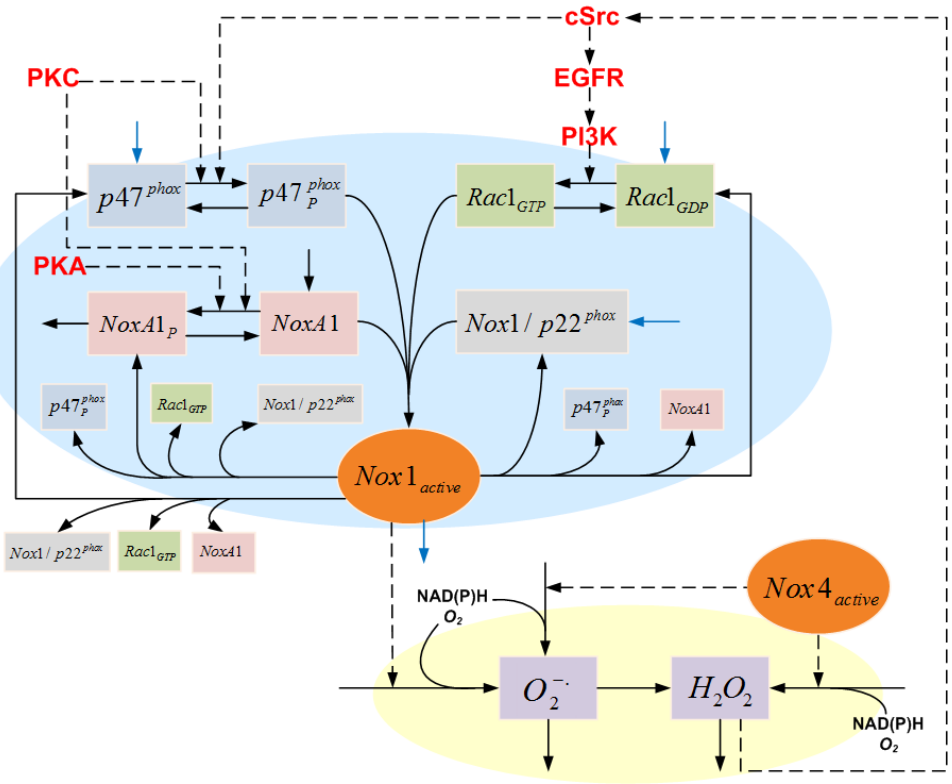

Figure 4.1 Schematic representation of the model structure for AngII-induced Nox1 activation and subsequent ROS production in VSMCs.

Components within the blue ellipse govern the Nox1 activation-disassembly system, while components within the yellow ellipse show a simplified representation of ROS metabolism. Orange ellipses represent two Nox1 homologues that co-exist in VSMCs; the activity of Nox4 is considered constant. Red fonts represent signaling molecules; the effect of PKA is currently ignored because the AngII-induced PKA activation is apparently negligible.

4.2.2 Two-Phase Modeling Strategy

The first step toward the computational analysis is to design a pathway model of the system in Figure 4.1. However, it seems not feasible to estimate parameters and deal with uncertainties regarding the ill-characterized pathway structure in one stroke. Instead, we apply a two-phased strategy: In the first phase, the target system is decomposed into four distinct modules. These modules include: the AngII-induced PKC activation module (shown in red font in Figure 4.1; the detailed structure of this module is given in Figure 4.2); the cSrc/EGFR/PI3K signaling cascade module (also shown in red font in Figure 4.1; the detailed structure of this module is given in Figure 4.3); the module of ROS metabolism (shown in the yellow ellipse in Figure 4.1); and the Nox1 activation-disassembly module (shown in the blue ellipse in Figure 4.1). Each module is separately constructed, and parameters are estimated correspondingly, as far as it is feasible. In the second phase, all individually constructed modules are integrated and the composite model is further modified and analyzed.

Phase I: Model Decomposition

The pathway system depicted in Figure 4.1 is decomposed into four distinct modules, as discussed above, and each individual module is briefly and separately described in the following.

AngII-induced PKC activation module: Protein kinase C (PKC) is a family of protein kinases that are involved in controlling the function of other proteins through the phosphorylation of hydroxyl groups of serine and threonine amino acid residues on these proteins [244, 245]. The PKC family contains fifteen isoforms in human, which can be divided into three subfamilies based on their second messenger requirements [244]. The term "protein kinase C" usually refers to the entire family of isoforms. The PKC enzymes are activated by signals such as increases in the concentration of diacylglycerol (DAG) [244, 246], calcium ions (Ca^{2+}) [244], or arachidonic acid (AA) [247], and therefore play important roles in several signal transduction cascades.

In cultured VSMCs, PKC can be activated by many extracellular stimuli. Among them, the best-studied example is probably AngII [248, 249]. Treatment of VSMCs with AngII induces a series of biochemical events, including sequential phospholipase C (PLC)-mediated hydrolysis of phosphotidylinositol (PI) and polyphosphoinositides (including PIP and PIP_2) [250-252], phospholipase D (PLD)-mediated hydrolysis of phosphatidylcholine (PC) [253, 254], and cytosolic phospholipase A 2 ($cPLA_2$)-mediated hydrolysis of PC and phosphatidylserine (PE) [255]. These coordinated events result in a transient formation of inositol trisphosphate (IP_3) that is associated with calcium (Ca^{2+}) mobilization [256, 257], a biphasic formation of diacylglycerol (DAG) [250, 251], and a rapid and time-dependent release of arachidonic acid (AA) [255]. Through these mechanisms, AngII leads to an increase in the concentrations of Ca^{2+}, DAG, and AA, and thus up-regulates PKC enzymatic activity in VSMCs.

Although several studies have documented that AngII can induce a sustained PKC activation in VSMCs, there few published records directly describe to which level PKC activity is upregulated, let alone its responsive dynamics. Therefore, in order to mimic the dynamic activity of PKC in response to extracellular AngII treatment in VSMCs, we use here computational simulation methods.

The PKC activation system has been investigated in numerous studies, and the pathway structure, key components, and a variety of other biological data are available in the literature. The model we propose is based on this information and directly reflects the pathway structure shown in Figure 4.2. The most pertinent information for the model is summarized in Table 4.1. The dependent variables, whose concentrations are affected by the system, include inactive PKC, active PKC in six distinct forms (PKC alone, AA·PKC complex, Ca^{2+}·PKC complex, AA·Ca^{2+}·PKC complex, Ca^{2+}·PKC·DAG complex, and AA·PKC·DAG complex), and inactive intermediate complexes in four different forms (Ca^{2+}·PKC complex, Ca^{2+}·PKC·DAG complex, DAG·PKC complex, and AA·PKC·DAG complex). The independent variables, whose concentrations are not affected by the system, include DAG, AA, and Ca^{2+}. All biochemical reactions tend to be reversible (denoted by double-headed arrows in Figure 4.2), including

reactions in both "forward" (denoted by the arrow pointing to the right) and "backward" (denoted by the arrow pointing to the left) directions. Since AngII indirectly regulates PKC activity through these three independent variables, it is feasible and reasonable to use their dynamic profiles under AngII treatment as "offline inputs" to the PKC activation system to simulate the dynamic changes of PKC in response to AngII.

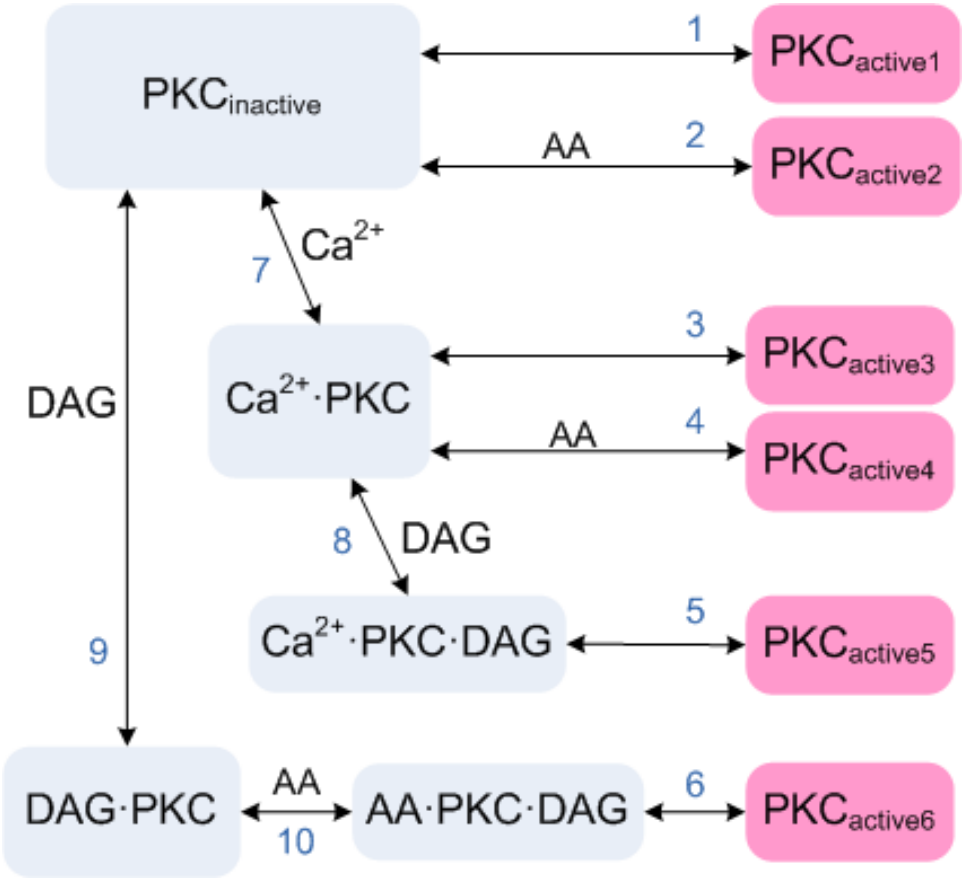

Figure 4.2 Schematic representation of the AngII-induced PKC activation in VSMCs.

Pink boxes represent active PKC in distinct formats; Grey boxes represent inactive PKC in distinct formats. Black Fonts represent independent variables. Blue numbers are indices for the various reactions.

Table 4.1 System variables in PKC activation module.

Variable Index	Variable Name
X_1	$PKC_{inactive}$ (inactive PKC alone)
X_2	$PKC_{active1}$ (active PKC alone)
X_3	$PKC_{active2}$ (active AA·PKC complex)
X_4	$PKC_{active3}$ (active Ca^{2+}·PKC complex)
X_5	$PKC_{active4}$ (active AA·Ca^{2+}·PKC complex)
X_6	$PKC_{active5}$ (active Ca^{2+}·PKC·DAG complex)
X_7	$PKC_{active6}$ (active AA·PKC·DAG complex)
X_8	Inactive Ca^{2+}·PKC complex
X_9	Inactive Ca^{2+}·PKC·DAG complex
X_{10}	Inactive DAG·PKC complex
X_{11}	Inactive AA·PKC·DAG complex
X_{12}^*	AA
X_{13}^*	Ca^{2+}
X_{14}^*	DAG

Symbols with * indicate independent variables; other symbols indicate dependent variables.

To translate the targeted biological system diagram into an appropriate mathematical structure that permits analytical and simulation-supported diagnosis, we use ordinary differential equations in mass action format. The module thus can be expressed as shown in Eq. (4.1):

$$
\begin{aligned}
\dot{X}_1 &= -k_f(1)*X_1 - k_f(2)*X_1*X_{12} - k_f(7)*X_1*X_{13} - k_f(9)*X_1*X_{14} + k_b(1)*X_2 + k_b(2)*X_3 + k_b(7)*X_8 + k_b(9)*X_{10} \\
\dot{X}_2 &= k_f(1)*X_1 - k_b(1)*X_2 \\
\dot{X}_3 &= k_f(2)*X_1*X_{12} - k_b(2)*X_3 \\
\dot{X}_4 &= k_f(3)*X_8 - k_b(3)*X_4 \\
\dot{X}_5 &= k_f(4)*X_8*X_{12} - k_b(4)*X_5 \\
\dot{X}_6 &= k_f(5)*X_9 - k_b(5)*X_6 \\
\dot{X}_7 &= k_f(6)*X_{11} - k_b(6)*X_7 \\
\dot{X}_8 &= -k_f(3)*X_8 - k_f(4)*X_8*X_{12} + k_f(7)*X_1*X_{13} - k_f(8)*X_8*X_{14} + k_b(3)*X_4 + k_b(4)*X_5 - k_b(7)*X_8 + k_b(8)*X_9 \\
\dot{X}_9 &= -k_f(5)*X_9 + k_f(8)*X_8*X_{14} + k_b(5)*X_6 - k_b(8)*X_9 \\
\dot{X}_{10} &= k_f(9)*X_1*X_{14} - k_f(10)*X_{10}*X_{12} - k_b(9)*X_{10} + k_b(10)X_{11} \\
\dot{X}_{11} &= k_f(10)*X_{10}*X_{12} - k_f(6)*X_{11} + k_b(6)*X_7 - k_b(10)X_{11}
\end{aligned}
\tag{4.1}
$$

Here, each X_i, i =1, 2, ⋯, 11, is a dependent variable, while each X_i, i =12, ⋯, 14, is an independent variable (see Table 4.2). The parameters k_f and k_b are rate constants of the corresponding reactions in forward and backward directions, respectively.

cSrc/EGFR/PI3K signaling cascade module: Although experimental studies have revealed that AngII increases ROS levels in VSMCs via a Nox1-mediated mechanism [37], the upstream signaling mechanisms through which AngII stimulates Nox1 activity are still not completely known. It has been suggested that they might include several signaling molecules, including PKC [38, 241], epidermal growth factor receptor (EGFR) [38], cSrc[38, 233], and phosphatidylinositol-3-kinase (PI3K) [38]. These signaling molecules are involved in different phases of ROS production, and thus have distinct functions in regulating Nox1 activity. The suggested mechanism is shown in Figure 4.3 and summarized as ollows. AngII binds to the AngII type 1 receptor (AT1R), leading to acute Nox1 activation, mainly through PKC-regulated $p47^{phox}$ phosphorylation and the release of an initial burst of ROS. This initial increase in ROS (specifically, H_2O_2) then activates the redox-sensitive signaling molecule cSrc, a process which results in the subsequent activation of its down-stream signals, including EGFR and PI3K. The

activation of PI3K enhances the productivity of phosphatidylinositol (3,4,5)-triphosphate (PIP_3), which potentially stimulates Rac1 activation, an essential and indispensable step for gaining Nox1 enzymatic activity. As a result, Nox1 is continuously activated and the increase of ROS continues. Although the regulatory mechanism of PIP_3 on Rac1 activation is not completely understood, it has been suggested that PIP_3 may regulate Rac activation by binding with several Rac-guanine nucleotide exchange factors (Rac-GEF) including Vav and Sos, which enhances their activity [38].

The proposed model structure for the cSrc/EGFR/PI3K signaling cascade is schematically shown in Figure 4.3. All signaling molecules can exist in two interconvertible forms, namely active form (marked with an asterisk in Figure 4.3) and inactive (without asterisk). The levels of all active signaling molecules are defined as "1" (100%) in unstimulated condition, but may increase above "1" (by activation) or decrease below "1" (by inhibition) as their up-stream signals vary. Two further metabolites of the module, phosphatidylinositol (4,5)-bisphosphate (PIP_2) and PIP_3 (denoted with green boxes), are also interconvertible into each other; the reaction from PIP_2 to PIP_3 is regulated by the level of active PI3K.

In order to understand how the Nox1 system is dynamically activated and regulated by the cSrc-dependent signaling cascade, we first need to determine the dynamic response of PIP_3. Unfortunately, this profile cannot be directly found in literature, but needs to be estimated through simulation methods. By contrast, records of the active signaling molecules for cSrc, EGFR, and PI3K under the same experimental condition can be found in literature (see details in section 4.2.3). As a result, the availability of multiple experimental data sets for the same signaling cascade offers several options as we set up the corresponding module to predict the dynamic profile of PIP_3.

For instance, we can use the PI3K data as the only external input and directly predict PIP_3 dynamics, while ignoring the effects of upstream EGFR and cSrc signals. Alternatively, we can use EGFR data as the only external input to predict the dynamics of both PI3K and PIP_3. Finally, we can also use cSrc data as the system input to predict the entire signaling cascade

simultaneously. These options raise several questions: Are the data characterizing different aspects of the same signaling cascade consistent with each other? Do these data have equivalent information content or is one or are several of them more useful for our task?

In order to explore possible answers to these questions, we use three candidate modules by using different data as the external input; the module structures are shown in Figure 4.4, panels (a) to (c). Due to the different input variables, the three candidate modules have distinct structures, and different numbers of system variables and parameters. The most pertinent information of the three module candidates is summarized in Table 4.2. Specifically, the first candidate (Figure 4.4a) uses active PI3K as an input, and contains only one dependent variable, PIP_3. The second candidate (Figure 4.4b) uses active EGFR as input, and contains two dependent variables, namely PIP_3 and PI3K. The last module (Figure 4.4c), takes active cSrc as input and represents the entire signaling cascade; it therefore has the most dependent variables, namely PIP_3, PI3K and EGFR.

The mathematical representation of the pathway structures again uses ordinary differential equations in mass action format, which is extended toward the GMA format (see Chapter 1) in some places to permit the modeling of different signal strengths. Specifically, a real-valued kinetic order g_i is assigned to each regulatory signal. A positive value indicates activation, while a negative value indicates inhibition. Thus, models of the three module candidates are given in Eqs. (4.2), (4.3), and (4.4).

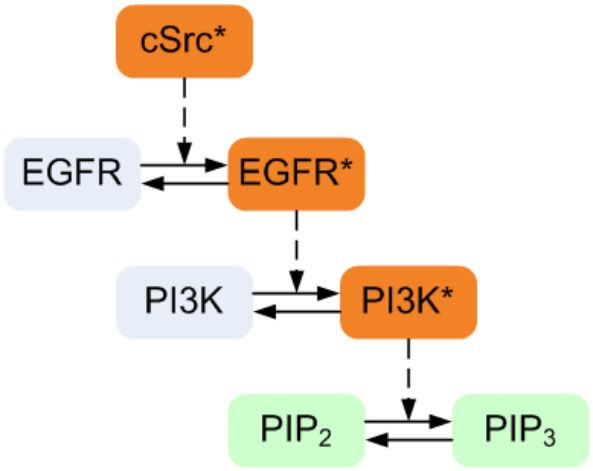

Figure 4.3 Schematic representation of the cSrc/EGFR/PI3K signaling cascade.

Orange boxes with an asterisk represent active signaling molecules. Light blue boxes without an asterisk represent inactive signaling molecules. Green boxes represent metabolites.

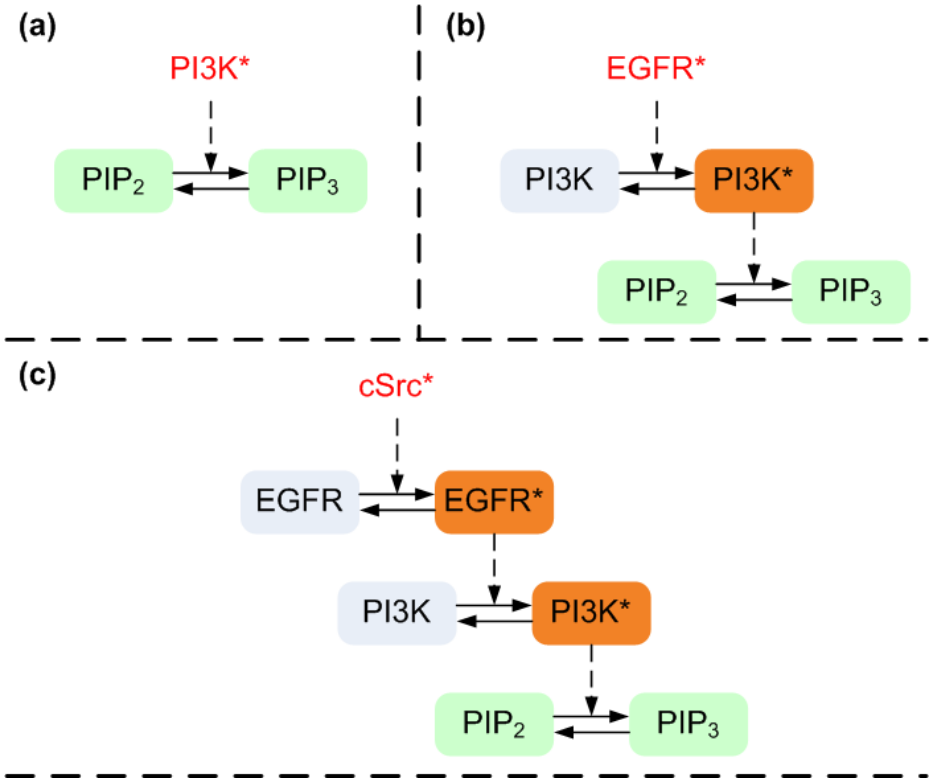

Figure 4.4 Three candidate modules for the cSrc/EGFR/PI3K signaling cascade that use different data as external input.

(a) Active PI3K serves as input signal; (b) Active EGFR serves as input signal; (c) Active cSrc serves as input signal. Orange boxes with asterisk represent active signaling molecules. Light blue boxes without asterisk represent inactive signaling molecules. Green boxes represent metabolites. Red fonts with asterisk represent active input signals.

Table 4.2 System variables in three candidate modules of the cSrc/EGFR/PI3K signaling cascade.

Module Candidate	Input Signal	Variable Index and Name	
1	Active PI3K	X_1	PIP_3
		X_2^*	PIP_2
		X_3^*	Active PI3K
2	Active EGFR	X_1	PIP_3
		X_2	Active PI3K
		X_3^*	PIP_2
		X_4^*	Active EGFR
3	Active cSrc	X_1	PIP_3
		X_2	Active PI3K
		X_3	Active EGFR
		X_4^*	PIP_2
		X_5^*	Active cSrc

Symbols with * indicate the independent variables; Symbols without * indicate the dependent variables.

Candidate Module 1: $$\dot{X}_1 = \gamma_1 * X_2 * X_3^{g_1} - \gamma_2 * X_1 \tag{4.2}$$

Candidate Module 2: $$\begin{cases} \dot{X}_1 = \gamma_1 * X_3 * X_2^{g_1} - \gamma_2 * X_1 \\ \dot{X}_2 = \gamma_3 * (T_{PI3K} - X_2) * X_4^{g_2} - \gamma_4 * X_2 \end{cases} \tag{4.3}$$

Candidate Module 3: $$\begin{cases} \dot{X}_1 = \gamma_1 * X_4 * X_2^{g_1} - \gamma_2 * X_1 \\ \dot{X}_2 = \gamma_3 * (T_{PI3K} - X_2) * X_3^{g_2} - \gamma_4 * X_2 \\ \dot{X}_3 = \gamma_5 * (T_{EGFR} - X_3) * X_5^{g_3} - \gamma_6 * X_3 \end{cases} \tag{4.4}$$

In these representations, the parameters γ_i, $i = 1, \cdots, 6$, represent rate constants, while g_i, $i = 1, 2, 3$, are kinetic orders. These two parameters, whose numerical values need to be estimated, characterize the dynamics of the system. T_{PI3K} and T_{EGFR} respectively represent the total amount of PI3K and EGFR, including both active and inactive forms.

Module of ROS metabolism: VSMCs possess mainly two types of reactive oxygen species (ROS), namely superoxide ($O_2^{\cdot -}$) and hydrogen peroxide (H_2O_2). As stated in the section 1.2.1

(also see Figure 1.1), these two ROS molecules can be generated from a variety of intracellular sources, and also be consumed by different mechanisms. Due to the existence of multiple production and degradation pathways for ROS, the pathway structure of ROS metabolism is complicated, and the experimental identification of ROS from specific sources difficult. A recent study used membrane fractions extracted from cultured rat aortic smooth muscle cells (RASMCs) to measure ROS production [36]. In this study, sources other than Nox1 and Nox4 were excluded, and thus had no measurable contributions to ROS production. Based on this experimental investigation, we limit our analysis here on ROS produced from Nox1- and Nox4-catalyzed biochemical reactions.

Although the main product of Nox is commonly considered to be superoxide (see discussion in section 1.2.2), some Nox is believed to be capable of producing other types of ROS. For instance, in VSMCs, Nox4 is thought to directly release hydrogen peroxide rather than superoxide [36]. Therefore, it is reasonable for the model to consider Nox4 as a constant supply for both superoxide and hydrogen peroxide.

Compared to their production process, the degradation pathways of ROS are more complicated. As a free radical species, superoxide has a surprisingly limited reactivity with intracellular components [3]. As a result, the dominant pathway for superoxide depletion is its conversion to hydrogen peroxide, either spontaneously or enzymatically via superoxide dismutase (SOD) [1, 11, 21]. The fact that the amount of SOD in VSMCs is sufficient to dismutase increased superoxide production rapidly into H_2O_2 further confirms the effectiveness of this pathway. Besides, superoxide can also be consumed by its reactions with other molecules [11], such as NO, although the involved amount might be very limited. With respect to depletion mechanisms, H_2O_2 is far more diverse and complicated than superoxide, because H_2O_2 is more reactive, especially when it reacts with intracellular thiol groups [2, 3]. Once produced, H_2O_2 can be removed via several antioxidant enzyme systems [2], including catalases (CAT), glutathione peroxidases (GPx), and peroxiredoxins (Prx). Since the details of H_2O_2 degradation are not of premier interest here (see the comprehensive and detailed model for H_2O_2 elimination in [258]),

we combine for simplification all H_2O_2 degradation pathways into one pathway. By doing so, we do not necessarily need to know detailed profiles of each involved antioxidant system that could potentially react with H_2O_2, which thus greatly reduces the modeling and computational complexity.

After collecting all available biological information regarding Nox-mediated ROS production and degradation in VSMCs, we propose a simplified model structure for ROS metabolism that is schematically represented in Figure 4.5. The most pertinent information about this module is summarized in Table 4.3. The model contains two dependent variables, namely superoxide and hydrogen peroxide. The active Nox1 enzyme is temporarily considered as an independent variable in this module, although its activity may dynamically change over time in other modules. The active Nox4 enzyme serves as another independent variable, whose value is kept constant for both unstimulated and stimulated conditions (except for Nox4 knock-outs). The concentrations of other involved substrates, such as NADPH and molecular oxygen, are considered to be abundant enough to become constant. Thus, they can ultimately be combined with system parameters, such as rate constants.

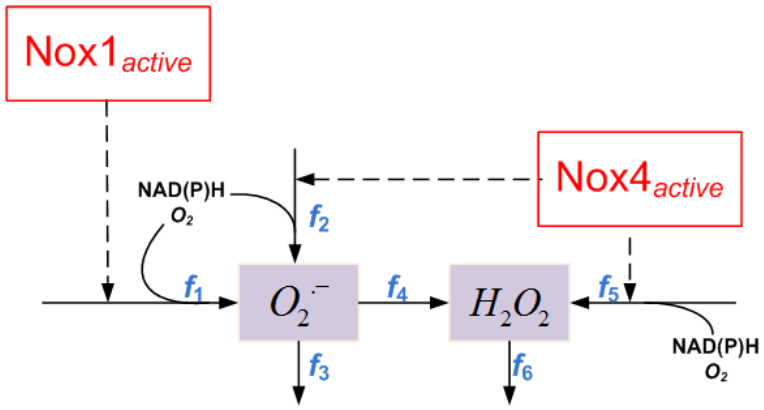

Figure 4.5 Schematic representation of ROS metabolism in VSMCs.

To translate the pathway structure in Figure 4.5 into a model, we again utilize ordinary differential equations in GMA format. Specifically, the targeted module is mathematically represented by Eq. (4.5) in the following manner:

$$\dot{X} = N \cdot F \,. \tag{4.5}$$

Here, $X_{2\times1}$ is th vector of dependent variables, $F_{6\times1}$ is the flux vector, and

$N_{2\times6} = \begin{bmatrix} 1 & 1 & -1 & -1 & 0 & 0 \\ 0 & 0 & 0 & 0.5 & 1 & -1 \end{bmatrix}$ is the stoichiometric matrix, which describes the quantitative relationships between dependent variables and corresponding fluxes. The explicit expression of each individual flux is given in Eq. (4.6). Most fluxes are mathematically expressed with the mass action rate law except for the degradation of H_2O_2, which is modeled in GMA format with a corresponding kinetic order equal to 0.5. This modification is adjusted according to a later parameter estimation process to obtain satisfactory model fits.

$$\begin{cases} f_1 = \gamma_1 * X_3 \\ f_2 = \gamma_2 * X_4 \\ f_3 = \gamma_3 * X_1 \\ f_4 = \gamma_4 * X_1^2 \\ f_5 = \gamma_5 * X_4 \\ f_6 = \gamma_6 * X_2^{0.5} \end{cases} \tag{4.6}$$

Table 4.3 System variables in the ROS metabolism module.

Variable Index	Variable Name
X_1	Superoxide ($O_2^{\cdot-}$)
X_2	Hydrogen Peroxide (H_2O_2)
X_3^*	Active Nox1 ($Nox1_{active}$)
X_4^*	Active Nox4 ($Nox4_{active}$)

Symbols with * indicate independent variables; Symbols without * indicate the dependent variables.

Nox1 activation-disassembly module: To capture all potential activating and disassembly pathways of Nox1 in VSMCs, we already proposed a generic pathway structure and described it in great detail in Chapter 3 (see Figure 3.1). In this Chapter, we will keep the generic pathway

structure that has been proposed before, and only change the static input signals S_1, S_2 into corresponding dynamical signals (PKC and the cSrc-dependent signaling cascade).

Phase II: Model Integration

In order to explore the overall dynamic behaviors of the Nox1 system and its subsequent ROS production in response to AngII, the four modules described above (see Phase I: Model Decomposition) are integrated into one structure, according to the following steps (*cf.* Figure 4.6): First, the AngII-induced PKC activation module is simulated and the dynamic profile of PKC_{active} is predicted. Then, the predicted PKC_{active} and the output of the cSrc/EGFR/PI3K signaling cascade (represented by PIP_3, which cannot be separately predicted like PKC_{active}) are fed into the Nox1 activation-disassembly module as "driving" inputs, regulating the activity of $Nox1_{active}$. Finally, $Nox1_{active}$ is modeled to serve as a dynamic input to the ROS metabolism module, up- or down-regulating ROS production or concentration.

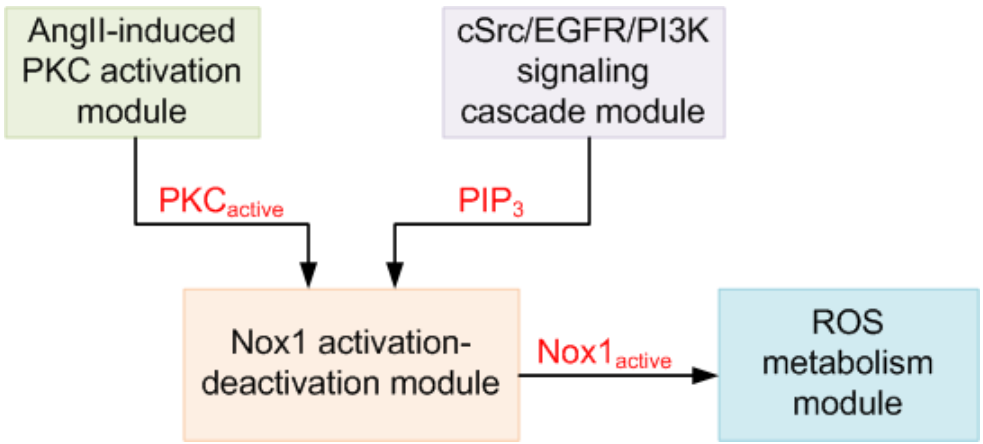

Figure 4.6 Proposed process for integrating the four modules developed before.

The choice between three distinct module candidates for the cSrc/EGFR/PI3K signaling cascade leads to the possibility of three integrated model candidates. Each model candidate

contains different numbers of system variables, fluxes, and pertinent parameters. To translate the model diagrams into a mathematical structure that permits analytical or simulation-aided diagnoses of the integrated system, we combine the mathematical descriptions in Eqs. (4.2) - (4.6) by reassigning the corresponding system variables and parameters. The most pertinent information about the system variables and mathematical description for the three integrated model candidates is summarized in Table 4.4. Eqs. (4.7), (4.8), and (4.9), N_i, i =1, 2, 3, show the stoichiometric matrix (see details of N_i in APPENDIX C.1). It quantifies the relationships between the dependent system variables and corresponding fluxes in each model candidate. F_i, i = 1, 2, 3, is the flux vector for model candidate i; it is explicitly given in Table 4.5.

4.2.3 Data Sources

Over the past decades, NADPH oxidase and its product ROS have received ample attentions, and numerous pertinent experiments have been implemented under different conditions and in various types of cells. These experimental studies not only enhance our biological understanding of the Nox family, but also provide us a considerable amount of qualitative and/or quantitative data in either static or dynamic formats, which can help facilitate many steps of our modeling process, such as parameter estimation and model validation. Since quantitative results of experiments in different cell types, or targeting different Nox homologues, may differ substantially, we focus on experimental results for Nox1 and its subsequent ROS product in one particular cell type – vascular smooth muscle cells (VSMCs). The most relevant experimental data, collected from literature, are summarized in the following.

Experimental Data for AngII-Induced PKC Activation in VSMCs

The dynamic profiles of AA, Ca^{2+}, and DAG under AngII (100nM) treatment in VSMCs are found in literature [250, 255, 257] and correspondingly displayed in Figure 4.7. The solid black line represents the level of each type of molecule in unstimulated cells, which is considered

the control condition and represented as "1". The circles are experimental records, which are recalculated as fold changes compared to the level in the control condition.

Table 4.4 Systematic information of three integrated model candidates.

Index	System Variables				System Equation
Model Candidate 1	X_1	$Nox1_{active}$	X_9	$O_2^{\cdot-}$	$\dot{X} = N_1 \cdot F_1$, (4.7) where $X_{11\times1}$ is the vector of dependent system variables, N_1 is the 11×24 stoichiometric matrix, and F_1 is a 24×1 flux vector.
	X_2	$Nox1/p22^{phox}$	X_{10}	H_2O_2	
	X_3	$p47^{phox}$	X_{11}	PIP_3	
	X_4	$p47^{phox}{}_P$	X_{12}^*	PKC_{active}^*	
	X_5	$Rac1_{GDP}$	X_{13}^*	PIP_2^*	
	X_6	$Rac1_{GTP}$	X_{14}^*	$PI3K_{active}^*$	
	X_7	NoxA1	X_{15}^*	$cSrc_{active}^*$	
	X_8	$NoxA1_P$	X_{16}^*	$Nox4_{active}^*$	
Model Candidate 2	X_1	$Nox1_{active}$	X_{10}	H_2O_2	$\dot{X} = N_2 \cdot F_2$, (4.8) where $X_{12\times1}$ is the vector of dependent system variables, N_2 is the 12×26 stoichiometric matrix, and F_2 is a 26×1 flux vector.
	X_2	$Nox1/p22^{phox}$	X_{11}	PIP_3	
	X_3	$p47^{phox}$	X_{12}	$PI3K_{active}$	
	X_4	$p47^{phox}{}_P$	X_{13}^*	PKC_{active}^*	
	X_5	$Rac1_{GDP}$	X_{14}^*	PIP_2^*	
	X_6	$Rac1_{GTP}$	X_{15}^*	$EGFR_{active}^*$	
	X_7	NoxA1	X_{16}^*	$cSrc_{active}^*$	
	X_8	$NoxA1_P$	X_{17}^*	$Nox4_{active}^*$	
	X_9	$O_2^{\cdot-}$			
Model Candidate 3	X_1	$Nox1_{active}$	X_{10}	H_2O_2	$\dot{X} = N_3 \cdot F_3$, (4.9) where $X_{13\times1}$ is the vector of dependent system variables, N_3 is the 13×28 stoichiometric matrix, and F_3 is a 28×1 flux vector.
	X_2	$Nox1/p22^{phox}$	X_{11}	PIP_3	
	X_3	$p47^{phox}$	X_{12}	$PI3K_{active}$	
	X_4	$p47^{phox}{}_P$	X_{13}	$EGFR_{active}$	
	X_5	$Rac1_{GDP}$	X_{14}^*	PKC_{active}^*	
	X_6	$Rac1_{GTP}$	X_{15}^*	PIP_2^*	
	X_7	NoxA1	X_{16}^*	$cSrc_{active}^*$	
	X_8	$NoxA1_P$	X_{17}^*	$Nox4_{active}^*$	
	X_9	$O_2^{\cdot-}$			

Symbols with * indicate independent variables, and symbols without * indicate dependent variables. The details of N_i, i = 1, 2, 3, are given in the APPENDIX C.1.

Table 4.5 Mathematical descriptions of fluxes in three integrated model candidates.

Index	Mathematical Description of F_i
Model Candidate 1	$F_1 = [f_1\ f_2\ f_3 \cdots f_{23}\ f_{24}]^T$, where each flux is given in the GMA format as: $f_1 = \gamma_1 X_2 X_4 X_6 X_7$ $f_7 = \gamma_7 X_5 X_{11}^{g_3}$ $f_{13} = \gamma_{13}$ $f_{19} = \gamma_{19}^* X_9$ $f_2 = \gamma_2 X_1$ $f_8 = \gamma_8 X_6$ $f_{14} = \gamma_{14} X_1$ $f_{20} = \gamma_{20}^* X_9^2$ $f_3 = \gamma_3 X_1$ $f_9 = \gamma_9 X_7 X_{12}^{g_4}$ $f_{15} = \gamma_{15}$ $f_{21} = \gamma_{21}^* X_{16}$ $f_4 = \gamma_4 X_1$ $f_{10} = \gamma_{10} X_8$ $f_{16} = \gamma_{16} X_8$ $f_{22} = \gamma_{22}^* X_{10}^{0.5}$ $f_5 = \gamma_5 X_3 X_{12}^{g_1} X_{15}^{g_2}$ $f_{11} = \gamma_{11}$ $f_{17} = \gamma_{17}^* X_1$ $f_{23} = \gamma_{23} X_{13} X_{14}^{g_5}$ $f_6 = \gamma_6 X_4$ $f_{12} = \gamma_{12}$ $f_{18} = \gamma_{18}^* X_{16}$ $f_{24} = \gamma_{24} X_{11}$
Model Candidate 2	$F_2 = [f_1\ f_2\ f_3 \cdots f_{24}\ f_{25}\ f_{26}]^T$, where each flux is given in the GMA format as: $f_1 = \gamma_1 X_2 X_4 X_6 X_7$ $f_7 = \gamma_7 X_5 X_{11}^{g_3}$ $f_{13} = \gamma_{13}$ $f_{19} = \gamma_{19}^* X_9$ $f_{25} = \gamma_{25}(T_{PI3K} - X_{12}) X_{15}^{g_6}$ $f_2 = \gamma_2 X_1$ $f_8 = \gamma_8 X_6$ $f_{14} = \gamma_{14} X_1$ $f_{20} = \gamma_{20}^* X_9^2$ $f_{26} = \gamma_{26} X_{12}$ $f_3 = \gamma_3 X_1$ $f_9 = \gamma_9 X_7 X_{13}^{g_4}$ $f_{15} = \gamma_{15}$ $f_{21} = \gamma_{21}^* X_{17}$ $f_4 = \gamma_4 X_1$ $f_{10} = \gamma_{10} X_8$ $f_{16} = \gamma_{16} X_8$ $f_{22} = \gamma_{22}^* X_{10}^{0.5}$ $f_5 = \gamma_5 X_3 X_{13}^{g_1} X_{16}^{g_2}$ $f_{11} = \gamma_{11}$ $f_{17} = \gamma_{17}^* X_1$ $f_{23} = \gamma_{23} X_{14} X_{12}^{g_5}$ $f_6 = \gamma_6 X_4$ $f_{12} = \gamma_{12}$ $f_{18} = \gamma_{18}^* X_{17}$ $f_{24} = \gamma_{24} X_{11}$
Model Candidate 3	$F_3 = [f_1\ f_2\ f_3 \cdots f_{26}\ f_{27}\ f_{28}]^T$, where each flux is given in the GMA format as: $f_1 = \gamma_1 X_2 X_4 X_6 X_7$ $f_7 = \gamma_7 X_5 X_{11}^{g_3}$ $f_{13} = \gamma_{13}$ $f_{19} = \gamma_{19}^* X_9$ $f_{25} = \gamma_{25}(T_{PI3K} - X_{12}) X_{13}^{g_6}$ $f_2 = \gamma_2 X_1$ $f_8 = \gamma_8 X_6$ $f_{14} = \gamma_{14} X_1$ $f_{20} = \gamma_{20}^* X_9^2$ $f_{26} = \gamma_{26} X_{12}$ $f_3 = \gamma_3 X_1$ $f_9 = \gamma_9 X_7 X_{14}^{g_4}$ $f_{15} = \gamma_{15}$ $f_{21} = \gamma_{21}^* X_{17}$ $f_{27} = \gamma_{27}(T_{EGFR} - X_{13}) X_{16}^{g_7}$ $f_4 = \gamma_4 X_1$ $f_{10} = \gamma_{10} X_8$ $f_{16} = \gamma_{16} X_8$ $f_{22} = \gamma_{22}^* X_{10}^{0.5}$ $f_{28} = \gamma_{28} X_{13}$ $f_5 = \gamma_5 X_3 X_{14}^{g_1} X_{16}^{g_2}$ $f_{11} = \gamma_{11}$ $f_{17} = \gamma_{17}^* X_1$ $f_{23} = \gamma_{23} X_{15} X_{12}^{g_5}$ $f_6 = \gamma_6 X_4$ $f_{12} = \gamma_{12}$ $f_{18} = \gamma_{18}^* X_{17}$ $f_{24} = \gamma_{24} X_{11}$

Symbols with * indicate parameters with estimated numerical values, and symbols without * indicate parameters with unknown numerical values. T_{PI3K} and T_{EGFR} respectively represent the total amount of PI3K and EGFR, including both active and inactive forms.

In unstimulated cells, the basal levels of DAG, Ca^{2+}, and AA are found to be ~0.5nmol/10^6 cells, ~150-300 nM, and at the order of μM [236, 253, 257], respectively. These steady state values (marked with subscript $_{SS}$ symbol) are recalculated into a unit of (# molecules/cell) as follows:

$[DAG]_{SS}$ = ~0.5nmol/10^6 cells ≈ $0.5*10^{-9}*6*10^{23}$ molecules/10^6 cells ≈ $3*10^8$ molecules/cell.

$[Ca^{2+}]_{SS}$ = 150~300nM ≈ $150~300*10^{-3}*6*10^5$ molecules/cell ≈ $9~18*10^4$ molecules/cell.

$[AA]_{SS}$ = 1~ 10 μM ≈ 1~10 * 6*105 molecules/cell ≈ $0.6~6*10^6$ molecules/cell.

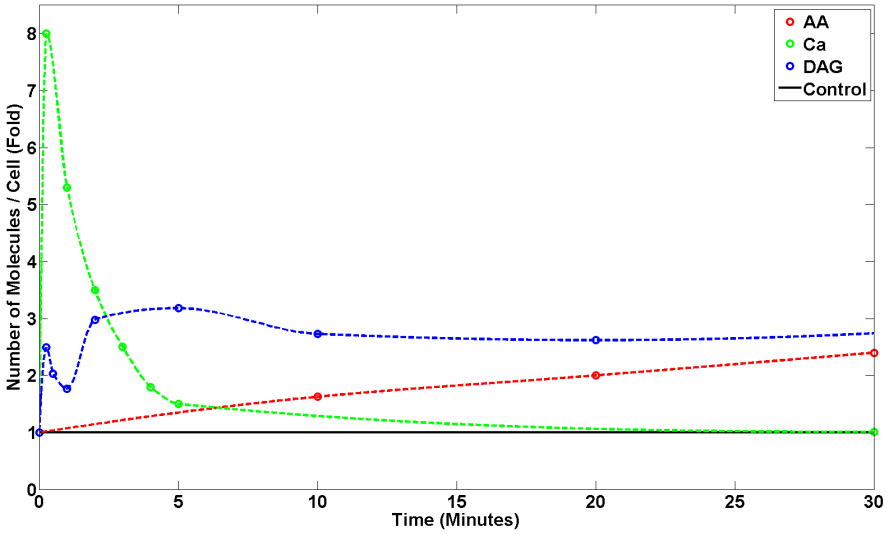

Figure 4.7 Experimental data for AngII-induced PKC activation in VSMCs.

Cells were treated with AngII (100nM) at time $t = 0$. Solid black line indicates the level of each variable in unstimulated cells (or called control condition), which is represented as "1" (100%). Circles are experimental records [236, 253, 257], which were recalculated as fold changes compared to the level in the control condition. Dashed lines were added for easy readability.

Experimental Data for cSrc/EGFR/PI3K Signaling Cascade

The dynamic profiles of cSrc, EGFR, and PI3K under AngII (100nM) treatment in VSMCs are also found in literature [259-261] and correspondingly displayed in Figure 4.8. The solid black line represents the level of active signaling molecules in unstimulated cells (control condition), which is assumed to be at "1". The circles are experimental records that are recalculated in fold.

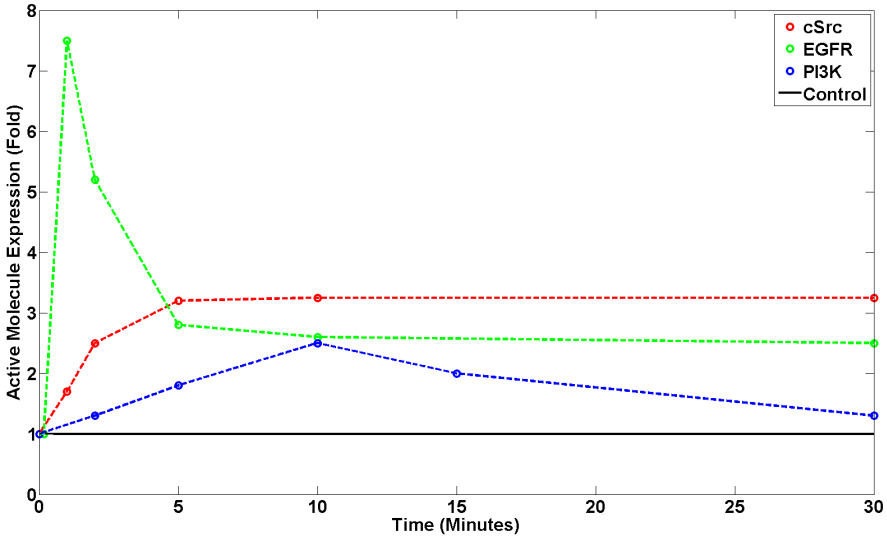

Figure 4.8 Experimental data for AngII-induced cSrc/EGFR/PI3K signaling cascade in VSMCs.
The cells were treated with AngII (100nM) at time $t = 0$. The solid black line represents the level of active signaling molecule, which is represented as "1" (100%). Circles are experimental records [259-261]. Dashed lines were added for easy readability.

Experimental Data for ROS Metabolism Module

There are mainly two types of experimental measurements for NADPH oxidase. One aims to detect the existence and distribution of Nox homologues in different types of cells and tissues by measuring their subunit expression at mRNA and/or protein levels. Although sometimes the expression at the mRNA level does not well correlate with its corresponding protein level [127], these measurements still reveal the relative abundances between measured subunits to some extent. In VSMCs from large arteries, Nox1 and Nox4 mRNA are found to be expressed to a much higher degree than Nox2 (over 10^3 fold) [37], and this observation is further confirmed by very low Nox2 protein detection, using immunoprecipitation and immunoblotting in human aortic smooth muscle cells [105]. In quiescent VSMC, Nox4 mRNA expression is much higher than Nox1 mRNA expression (over 10^3 fold in [36], over 20 fold in [28]). In proliferating VSMC, the number of Nox1 mRNA molecules is significantly increased (~2 fold), but the number of Nox4 mRNA molecules is decreased [36, 37], which effectively reduces the dramatic difference between Nox1 and Nox4 mRNA expression.

The second class of experiments aims to explore the functionality of Nox enzymes. By comparing the control system as it responds to certain stimuli, plenty of Nox activators and regulators have been identified (see detailed reviews in [31, 34]). The conclusions drawn from these comparisons are usually based on experimental measurements of either the intra- or extra-cellular ROS concentration (or production) under different conditions. However, due to differences of experimental set-ups and conditions, the measured ROS concentration (or production) might be found in different magnitudes, or have distinct transient behavioral patterns, even in response to the same stimulus and under the exact same condition. For instance, one research group found that the ROS concentration first increased significantly (~1.6 fold) 30 seconds after AngII (100nM) treatment in VSMCs, but declined after 1 minute due to some unknown reasons, and then increased again to a plateau (~ 2 fold at 30 minutes) [38]. By contrast, another group indicated a continuous and gradual increase in ROS concentration for over 30 minutes for the same dose of angiotensin II treatment in the same type of cell [235]. Although the transient responses of ROS are thus different, they agree that, after 30 minutes of AngII (100nM) treatment, the ROS level is significantly increased, and this increase can last for a long time, indicating that AngII is a strong activator of Nox1 and can enable the ROS concentration to reach a much higher plateau than under unstimulated conditions. Additionally, these two studies suggest that 30 minutes is a time interval that is long enough to allow the system reach a new (quasi-) steady state where the level of ROS increases stably.

Although ROS molecules have multiple intracellular sources, we focus here on Nox-catalyzed ROS production in VSMCs. In well-designed experiments with a membrane fraction model [36], this type of ROS production was well calibrated and accurately measured. In quiescent VSMCs, the measured production rates for superoxide and hydrogen peroxide in unstimulated cells are about 90 pmol/mg/min and 400 pmol/mg/min, respectively [36].

Experimental Data for the Nox1 Activation-Disassembly Module

The structural and regulatory Nox1 subunits, including $p22^{phox}$, $p47^{phox}$, NoxA1 and Rac1, have been shown to co-express in VSMCs [27, 33, 99, 105]. In unstimulated cells, $p47^{phox}$ stays mainly in cytosol, according to results from immunofluorescence confocal microscopy [100]. The small GTPase Rac1 becomes membrane associated in its GTP-bound active form only if the corresponding GEF is activated [112]. In other cells, only ~0.2% endogenous Rac1 was experimentally observed in the GTP-bound form [96]. However, due to the lack of precise measurements at protein level, accurate quantitation of these subunits is not available in literature. Instead, the relative abundances of these subunits, as summarized in Table 4.6 (*in consultation with experimentalists*), will be used in later sections.

Table 4.6 Numerical steady states of system variables in Nox1 activation-disassembly module.

Variable Name	Numerical Steady-State Value
Active Nox1 complex ($Nox1_{active}$)	10^3 (molecules/cell)
$Nox1/p22^{phox}$	$2.4 \cdot 10^4$ (molecules/cell)
$p47^{phox}$	$5.4 \cdot 10^3$ (molecules/cell)
Phosphorylated p47phox ($p47_P^{phox}$)	$1.2 \cdot 10^3$ (molecules/cell)
GDP-bound Rac1 ($Rac1_{GDP}$)	$6 \cdot 10^3$ (molecules/cell)
GTP-bound Rac1 ($Rac1_{GTP}$)	$1.2 \cdot 10^3$ (molecules/cell)
NoxA1	$5.4 \cdot 10^3$ (molecules/cell)
Phosphorylated NoxA1 (NoxA1P)	$0.6 \cdot 10^3$ (molecules/cell)

Combined Static Data for the Integrated Model

In order to explore the possible regulatory mechanisms of the Nox1 system, a variety of scenarios have been experimentally executed in *in vivo* or *in vitro* environments. These scenarios include the knock-out, knock-down, or over-expression of certain Nox1 subunits [36, 37, 39, 98, 262], pre-incubation with activators or inhibitors in both unstimulated and stimulated cells [28, 37, 233, 259], and treatment with different extracellular stimuli [235, 263]. Although many of these kinds of experiments were only executed qualitatively or semi-quantitatively,leading to one "static" data point, they have helped with the identification of a series of key components and pathways involved in Nox1 activation. Specifically, they have provided intrinsic insights of regulatory signals and their potential effects on Nox1 enzymatic activity, and therefore can be used as reasonable criterion to facilitate the parameter estimation process. The most pertinent information regarding static data of the Nox1 system and its subsequent ROS production in VSMCs stimulated by AngII (100nM), as well as other extracellular stimuli,was collected from literature and is summarized in Table 4.7.

Combined Dynamic Data for Integrated Model

Another type of experimental data consists of records at a series of sequential time points (*i.e.*, "time-series" data). Compared to static data, time-series data usually provide more detailed information, especially with respect to the system's dynamic responses. However, this advantage of dynamic data doesn't come for free. It usually requires more complicated experimental set-ups. As a consequence, much fewer dynamic data than static data are available in the literature, especially for complicated signaling systems.

For the AngII-induced Nox1 activation in VSMCs, there are currently only two sets of dynamic data available in literature. The first set describes the dynamic profile of $Rac1_{GTP}$ after AngII (100nM) treatment [38] (displayed in Figure 4.9 *top panel*), while the second set characterizes the changes in ROS concentration (specifically, H_2O_2) under the same treatment [38] (displayed in Figure 4.9 *bottom panel*). These two data sets, although measured at limited time points, provide very useful information about the system's overall dynamic behaviors in response to AngII, and therefore can be utilized as criteria in later parameter estimation processes.

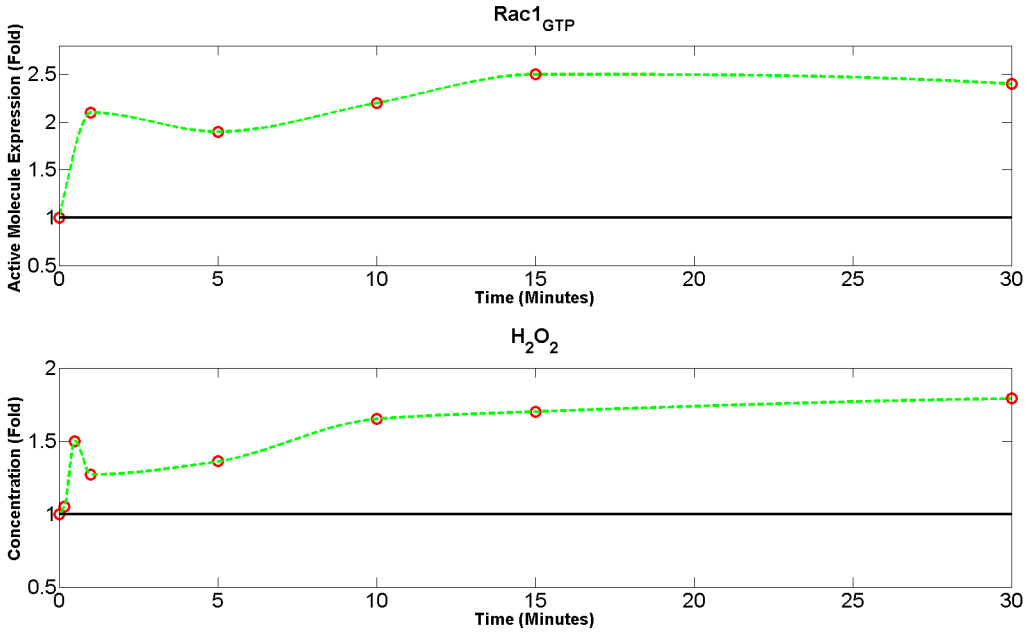

Figure 4.9 Combined dynamic data for integrated model.

Top panel: dynamic profile for Rac1GTP; Bottom panel: dynamic profile for H_2O_2. Solid black lines represent the levels of targeted variables in unstimulated cells, which are assumed as "1". Circles are experimental records [38] that are expressed in fold. Dashed lines are added for readability.

Table 4.7 Static experimental data of Nox1 and ROS production in VSMCs.

Experimental Condition	Scenario Description	Experimental Readout (Fold)	Reference
Control	Unstimulated	1	
AngII*	PKC↑, cSrc/EGFR/PI3K↑	$[V_{O_2^-}]_{30\,min} = 1.8 \sim 2.2$ $[V_{H_2O_2}]_{30\,min} = 1.13 \sim 1.5$ $[Rac1_{GTP}]_{30min} = 2.4$ $[p47^{phox}{}_P]_{30min} = 2$ $[O_2^{\cdot -}]_{30min} = 1.8$	[36, 38, 233]
AdASNox1^	Unstimulated, Nox1 protein is knocked-down to ~1%	$[V_{O_2^-}]_{30\,min} = 0.22$ $[V_{H_2O_2}]_{30\,min} = 0.86$	[36, 37]
AdASNox1^ + AngII*	PKC↑, cSrc/EGFR/PI3K↑, Nox1 protein is knocked-down to ~1%	$[V_{O_2^-}]_{30\,min} = 0.43$ $[V_{H_2O_2}]_{30\,min} = 0.98$	[36, 37]
siNox4&	Unstimulated, Nox4 mRNA is knocked-down to ~50%	$[V_{O_2^-}]_{30\,min} = 0.87$ $[V_{H_2O_2}]_{30\,min} = 0.58$	[36]
siNox4& + AngII*	PKC↑, cSrc/EGFR/PI3K↑, Nox4 mRNA is knocked-down to ~50%	$[V_{O_2^-}]_{30\,min} = 1.8$ $[V_{H_2O_2}]_{30\,min} = 0.87$	[36]
AngII* + AG1478$	PKC↑, cSrc↑, AngII-induced EGFR transactivation is blocked	$[H_2O_2]_{30min} = 1.2$	[38]
AngII* + AdRacN17#	PKC↑, cSrc/EGFR/PI3K↑, AdRacN17 has much lower affinity for GTP than for GDP	$[H_2O_2]_{30min} = 1.14$	[38]
AngII* + PP1~	PKC↑, AngII-induced cSrc activation is blocked	$[H_2O_2]_{30min} = 1.08$	[38]
PMA@	PKC↑↑	ROS ↑	[27]
AngII* + GF 109230X%	cSrc/EGFR/PI3K↑, AngII-induced PKC activation is blocked	$[H_2O_2]_{30sec} = 1.12$ $[H_2O_2]_{30min} = 1.45$	[38]

Scenario conditions: AngII* at 100 nM, AdASNox1^ represents Nox1-depleted cells, siNox4& represents Nox4-depleted cells, AG1478$ represents a EGFR kinase inhibitor, at 250nmol/L, AdRacN17# is a dominant-negative construct of Rac1, PP1~ is a cSrc inhibitor, at 20 μmol/L, PMA@, is a PKC activator, GF 109230X% is a PKC inhibitor, at 10 μmol/L. The symbol *V* in the Readout column indicates production rate, and others are measured at concentration level.

4.2.4 Parameter Estimation

Before running model simulations and various kinds of system diagnosis, a challenging but indispensable step is to specify the numerical values for all parameters according to available experimental observations. According to the specific type of available data (qualitative or quantitative, static or dynamic), an appropriate parameter estimation method needs to be chosen carefully. Based on the currently available data sources introduced in section 4.2.3, different methods will be used here to estimate parameter values for different modules as well as the integrated models.

Parameter Estimation for AngII-Induced PKC Activation Module

The parameters used in the AngII-induced PKC activation module include the rate constants for both forward (k_f) and backward (k_b) reactions for each individual biochemical process. The numerical values of these rate constants are found in the literature [264] and summarized in Table 4.8.

Parameter Estimation for ROS Metabolism Module

Parameters that need to be estimated for the ROS metabolism module include the rate constants γ_1 to γ_6. Due to the particular format of the flux expressions, estimating these rate constants is equivalent to estimating the corresponding fluxes. What's more, in unstimulated cells, the assumption that the system operates at a steady state imposes a set of linear constraints to these fluxes. Specifically, the relevant fluxes need to satisfy Eq. (4.9).

Table 4.8 Parameter values in the AngII-induced PKC activation module.

Reaction Index	k_f	k_b
1	1	50
2	2×10^{-10}	0.1
3	1.2705	3.5026
4	2×10^{-9}	0.1
5	1	0.1
6	2	0.2
7	1×10^{-6}	0.5
8	1.3333×10^{-8}	8.6348
9	1×10^{-9}	0.1
10	3×10^{-8}	2

Parameter values are adapted from[264].

$$\begin{cases} f_1 + f_2 = f_3 + f_4 \\ 0.5 * f_4 + f_5 = f_6 \\ f_i > 0, i = 1,\cdots,6 \end{cases}, \tag{4.9}$$

As stated in section 4.2.3, according to experimental measurements from the membrane fraction model from RASMCs, the measured production rate of $O_2^{\cdot-}$ in a membrane fraction model from RASMCs was about 90 pmol/mg/min [36]. In order to convert this measured production rate into the metrics that we use in our simulation (#molecules/s/cell), the following information needs to be taken into account:

(1) 10^6 smooth muscle cells (SMC) contain 80 ~ 100 mg protein (*information provided by experimentalists*)

(2) The membrane fraction contains much less than 10% protein of whole cell (*estimated by experimentalist, and 1%~2% is used in real calculation*).

With this information, the overall production rate of $O_2^{\cdot-}$ is estimated as follows:

$$\frac{90\,pmol}{\min\cdot mg}=\frac{90*10^{-12}\,molecules}{60*10^{6}/((1\%\sim 2\%)*(80\sim 100))s\cdot cell}\approx 1.5*10^{6}\,molecules/s/cell$$

The production of $O_2^{\cdot-}$ comes from two sources. The predominant one is catalyzed via Nox1 (marked as f_1 in Figure 4.5) [36]. The other, as a minor source, is catalyzed directly by Nox4 (marked as f_2 in Figure 4.5) [51]. Therefore, the calculated overall production rate of $O_2^{\cdot-}$ is split into two parts with the Nox1-catalyzed production being dominant (~80%) and the Nox4-catalyzed production being minor (~20%). Therefore, f_1 and f_2 are respectively estimated as:

$$f_1 =\sim 0.8*1.5*10^{6}\,molecules/s/cell = 1.25*10^{6}\,molecules/s/cell$$
$$f_2 =\sim 0.2*1.5*10^{6}\,molecules/s/cell = 0.25*10^{6}\,molecules/s/cell$$

The degradation of $O_2^{\cdot-}$ can also be divided into two parts. The first part is through the pathway that converts $O_2^{\cdot-}$ into H_2O_2 (marked as f_4 in Figure 4.5). The second part is through the biochemical reaction of $O_2^{\cdot-}$ with other molecules (marked as f_3 in Figure 4.5). Due to the limited reactivity of $O_2^{\cdot-}$ as well as the fact that the SOD enzyme is sufficient to convert $O_2^{\cdot-}$ into H_2O_2 in VSMCs, the former pathway plays a more dominant role in degrading $O_2^{\cdot-}$ (~99%) [21]; the latter pathway consumes much less $O_2^{\cdot-}$ (~1%). Therefore, f_3 and f_4 are respectively estimated as:

$$f_3 = 1\%*1.5*10^{6}\,molecules/s/cell = 0.015*10^{6}\,molecules/s/cell$$
$$f_4 = 99\%*1.5*10^{6}\,molecules/s/cell = 1.485*10^{6}\,molecules/s/cell$$

Using a new state-of-the-art electron spin resonance (ESR) assay for quantitative measurements of both $O_2^{\cdot-}$ and H_2O_2, one research group found that the basal H_2O_2 production

exceeds $O_2^{\cdot -}$ generation by 3 ~ 5 times, and the main production of H_2O_2 is catalyzed by Nox4 [36, 51]; we use 2 to fit measurements in knocked-out experiments. Therefore, the remaining influx and efflux of H_2O_2 (respectively marked as f_5 and f_6 in Figure 4.5) are estimated as:

$$f_5 = (2*1.5*10^6 - 0.5*f_4)molecules/s/cell = 2.2575*10^6\, molecules/s/cell$$
$$f_6 = 2*1.5*10^6\, molecules/s/cell = 3*10^6\, molecules/s/cell$$

After the numerical values of all pertinent fluxes in unstimulated condition are estimated, their corresponding rate constants are calculated given the explicit expressions of fluxes in Eq. (4.6) and the concentrations of $O_2^{\cdot -}$ and H_2O_2, which stay at quite low levels (at nmol/L magnitude). Since the exact values of $O_2^{\cdot -}$ and H_2O_2 in unstimulated condition are hard to measure accurately and may vary in different experimental set-ups, we use 600 molecules/cell (which equals 1 nmol/L) and 3,000 molecules/cell (which equals 5 nmol/L) to represent the $O_2^{\cdot -}$ and H_2O_2 concentrations, respectively. The calculated numerical values of fluxes and rate constants are summarized in Table 4.9.

Table 4.9 Parameter values in ROS metabolism module.

Fluxes	Numerical Value	Rate Constants	Numerical Value
f_1	$1.25*10^6$ (molecules/s/cell)	γ_1	1250
f_2	$0.25*10^6$ (molecules/s/cell)	γ_2	0.2083
f_3	$0.015*10^6$ (molecules/s/cell)	γ_3	25
f_4	$1.48*10^6$ (molecules/s/cell)	γ_4	4.125
f_5	$2.2575*10^6$ (molecules/s/cell)	γ_5	1.8813
f_6	$3*10^6$ (molecules/s/cell)	γ_6	$5.4772*10^4$

The numerical value of $Nox1_{active}$ in unstimulated condition is 10^3 molecules/cell, and the numerical value of $Nox4_{active}$ is estimated to be 50 times the amount of $Nox1_{active}$, which is $50*10^3 = 5*10^4$ molecules/cell.

Parameter Estimation for Other Modules

Unlike the parameters in the AngII-induced PKC activation module and the ROS metabolism module, whose numerical values could be either directly found in literature or estimated from measured experimental data, the parameter values in the other two modules, namely the cSrc/EGFR/PI3K signaling cascade module and the Nox1 activation-disassembly module, are not available in literature. Neither of them could be estimated since there are too many parameters but biological information and available observations are limited. Thus, finding a unique set of numerical values for these parameters is currently unrealistic. Therefore, we use a Monte-Carlo method, which is essentially independent of specific parameter values, to explore the possible ranges or magnitudes of the remaining unknown parameters.

The Monte-Carlo method is a class of computational methods that rely on repeated random sampling and simulation. It comes in various formats, but here follows a particular pattern. First, a possible input domain is defined, and input samples are randomly generated from a probability distribution over the domain. For each sampled input, a deterministic computation is implemented and its performance is evaluated. As a result, these computed results are aggregated and finally analyzed. The Monte-Carlo method is especially useful for simulating systems with many degrees of freedom and often applied to model phenomena with significant uncertainty.

Before implementing Monte-Carlo simulations, we need to consider two aspects. The first pertains to parameters that need to be randomly sampled, while the second pertains to the criteria that are used to evaluate the simulated results. Besides, a few assumptions and simplifications are made in order to simplify the sampling task, and finally there are 48 defined

parameter combinations that are need to be investigated for three integrated model candidates. The details of these aspects as well as the simulation setting are separately discussed in the following.

Pertinent Independent Parameters: As stated in section 4.2.2, we have proposed three integrated model candidates, and each model candidate contains different numbers of parameters (see details in Table 4.5). Among these parameters, some are already known or were estimated from data (marked with * in Table 4.5); the others are unknown (marked without * in Table 4.5) and need to be randomly sampled for their numerical values during Monte-Carlo simulations. In model candidate 1, there are totally 23 unknown parameters, namely γ_1 - γ_{16}, γ_{23}, γ_{24}, and g_1 - g_5. Model candidate 2 contains 27 unknown parameters, including γ_1 -γ_{16}, γ_{23} - γ_{26}, g_1 - g_6, and T_{PI3K}. The third model candidate has 31 unknown parameters, namely γ_1 - γ_{16}, γ_{23} - γ_{28}, g_1 - g_7, T_{PI3K}, and T_{EGFR}.

As stated in section 3.2.5, the Nox1 activation-disassembly system is at first assumed to operate at its nominal, stable steady state, which corresponds to unstimulated control conditions. The concentrations of all pertinent dependent variables remain unchanged in this state, which requires the corresponding fluxes to be dynamically balanced. This stable state of the Nox system (specifically, the stable activity of $Nox1_{active}$) maintains a stable and low level of ROS. As a result, the integrated system is assumed to operate at a stable state in unstimulated control condition, which allows the formulation of a set of linear constraints that the fluxes must satisfy. These linear constraints, as summarized in Table 4.10, have different-dimensional bases, indicating that each model candidate will have different numbers of linearly independent fluxes (or parameters) that need to be characterized. In addition, the fact that all fluxes are naturally

non-negative values further confines the feasible search space by adding more inequality constraints.

There is no unique rule to select the independent target fluxes (or parameters). According to different exploration demands or interests, many possible sets of independent fluxes (or parameters) exist. The pertinent independent fluxes (or parameters) that we select (explicitly shown in Table 4.10) include the common parameters for the Nox1 activation-disassembly module (exactly the same set of independent parameters as we specified in Chapter 3), all kinetic orders, and the specific parameters for each integrated model. The main reason for this selection is that we are interested in exploring two features of the integrated system: one is about the potential disassembly mechanisms of Nox1 (represented by rate constants γ_2 to γ_4), and the other is about the signal-based regulations of Nox1 (represented by kinetic orders).

Evaluation Criteria: The performance of a given Monte-Carlo sample is evaluated through a set of user-defined criteria. To use all available experimental records and observations found in literature (see details in section 4.2.3), a set of comprehensive and strict evaluation criteria is created. It consists of six screening conditions that can be stated as follows:

C1. All rate constants are positive;

C2. Under PMA treatment, the ROS concentration is increased after 30 minutes;

C3. Under AngII treatment, the ROS concentration reaches a new and higher plateau at 30 minutes than under unstimulated conditions;

C4. Simulations show consistency for up- or down- regulations for all static and dynamic data;

C5. The fitting error for the static data should be within a given tolerance;

C6. The fitting error for the dynamic data should be within a given tolerance.

Assumptions and Simplifications: Some of the independent parameters listed in Table 4.10 are common to all three model candidates. These include γ_2, γ_3, γ_4, γ_6, γ_8, γ_9, γ_{14}, and γ_{16}, which are particularly relevant for the Nox1 activation-disassembly module, which has been extensively explored and discussed in Chapter 3. According to the criteria-driven analysis in Chapter 3, the flux associated with the proteolytic pathway (represented by f_{14SS}) is much smaller (at least 100 fold smaller) than the fluxes associated with the three recycling pathways (respectively represented by f_{2SS}, f_{3SS}, and f_{4SS}), indicating the numerical value of γ_{14} should be at least 100 fold smaller than the numerical values of γ_2, γ_3, and γ_4. Therefore, in order to reduce the number of independent parameters and reduce searching space, we temporarily ignore the small contribution of the proteolytic pathway by setting its corresponding rate constant γ_{14} equal to zero.

Each rate constant is associated with a specific biochemical reaction, and its numerical value quantifies the speed of the corresponding biochemical reaction. For the seven remaining common independent rate constants, we find that some are associated with similar biochemical reactions. For instance, γ_2 and γ_9 are respectively associated with biochemical reactions involved in phosphorylation of NoxA1 in its complex or free forms; γ_3 and γ_6 are respectively associated with biochemical reactions involved in dephosphorylation of $p47^{phox}{}_P$ in its complex or free forms; γ_4 and γ_8 are respectively tied to biochemical reactions involved in the hydrolysis of GTP-bound Rac1 into $Rac1_{GDP}$ in its complex or free forma. In order to reduce the number of independent parameters further and shrink the search space, we assume that rate constants that are associated with similar biochemical reactions should have numerical values of similar magnitudes. Thus, the seven remaining independent rate constants are divided into 4 distinct

sets: γ_2 and γ_9; γ_3 and γ_6; γ_4 and γ_8; and γ_{16}. The numerical values of rate constants in each set are assumed to be of the same magnitude.

Definition of 48 Possible Parameter Combinations for Three Integrated Model Candidates: Based on the assumptions and simplifications in the previous section, we are in a position to reduce the original eight common independent parameters to 4 sets. Since little experimental information is available regarding the absolute values or magnitudes of any of these parameters, we use again a Monte-Carlo method, which permits the exploration of large searching spaces with reasonable effort and minimally depends on specific parameter values. Specifically, the parameters in each set are randomly sampled from a uniform distribution within either a "low" range or a "high" velocity range over an appropriate non-negative domain. This sampling strategy leads to two combinations for each set and results in $4^2 = 16$ combinations for each model candidate. As a result, it totally leads to $3 \times 16 = 48$ combinations for all three integrated model candidates. The details of these combinations are summarized in Table 4.11. Each individual combination has a specific designation of the sampling ranges for the investigated parameters, and is also tied to a particular model candidate. For instance, the combination MC2-5 refers to model candidate 2, a sample γ_2/γ_9, γ_4/γ_8, and γ_{16} from the "low" velocity distribution, and a sample γ_3/γ_6 from the "high" velocity distribution.

Monte-Carlo Simulation Settings: All simulations are implemented in MATLABR2010a. The sample size for each combination (totally 48 parameter combination) is ten thousand. The common independent parameters are divided into 4 distinct sets, and each set is randomly sampled from either the uniform distribution with a relatively "low" range $U(10^{-4}, 10^{-3})$ (implemented with $U(-4, -3)$ in $\log_{10}$ space) or the uniform distribution with a relatively "high" range $U(10^{-3}, 10^{-2})$ (implemented with $U(-3, -2)$). Other independent parameters are randomly

sampled according to our empirical experience as the following: the kinetic order g_i is sampled with $U(0, 2)$ for $i = 1, 2, \ldots, 7$; other rate constants γ_i are sampled with $U(0.1, 10)$ (implemented with $U(-1, 1)$ in $\log_{10}$ space) for $i = 23$, 25, and 27; T_{PI3K} and T_{EGFR} are sampled with $U(2, 10)$ when they are needed in corresponding the model candidate.

For each Monte-Carlo sample, several scenarios are simulated, including the unstimulated control condition, treatment of AngII (100nM), a Nox1 knock-down, a Nox4 knock-down, treatments with PP1 (a cSrc inhibitor), PMA (a PKC activator), GF 10923X (a PKC inhibitor), and AdRacN17 (a dominant-negative construct of Rac1). The performance of each sample is evaluated against the set of criteria defined in section 4.2.4. Specifically, this set of criteria is numerically implemented as follows:

*C*1. All rate constants are positive: $\gamma_i > 0$, for $i = 1, 2, \ldots, 28$.

*C*2. Under PMA treatment, the ROS concentration increases at 30 minutes:

$$\left[\frac{X_{10}(t = 30\,\text{min})}{X_{10}(t = 0)}\right]_{PMA} - 1 > 0.1$$

*C*3. Under AngII treatment, the ROS concentration reaches a new plateau at 30 minutes: this condition can be implemented in three different ways:

$$C3\text{-}1: norm(\frac{dY}{dt}|_{t=30\,\text{min}}) < 0.1, \quad Y = [X_9 \; X_{10}]^T.$$

$$C3\text{-}2: norm(\frac{dY}{dt}|_{t=30\,\text{min}}) < 0.5, \quad Y = [X_1 \quad X_2 \quad X_3 \quad X_4 \quad X_5 \quad X_6 \quad X_7 \quad X_8 \quad X_9 \quad X_{10}]^T.$$

*C*3-3: $\left|\frac{dX_6}{dt}|_{t=30\min}\right| < 10^{-3}$, *and* $\left|\frac{dX_{10}}{dt}|_{t=30\min}\right| < 10^{-3}$.

(Derivatives of X_6 and X_{10} at 30 minutes are as close as the estimations of their derivatives from experimental dynamic data (displayed in Figure 4.9). The estimations of derivatives of X_6 and X_{10} at 30 minutes are respectively -3.33*10^{-4} and 5.0*10^{-5}. So, here 10^{-3} is used as a loose cut-off.)

*C*4. (*simulated_data*(*i*) – 1) × (*static_data*(*i*) – 1) > 0, for *i* = 1, 2, …17, and

(*simulated_data*(*i*) – 1) × (*dynamic_data*(*i*) – 1) > 0, for *i* = 1, 2, …12.

(Details of static_data and dynamic_data are summarized in Table 4.12.)

*C*5. $\left|\frac{simulated\_data(i) - static\_data(i)}{static\_data(i)}\right| < 30\%$, for *i* = 1, 2, …, 17.

*C*6. $\left|\frac{simulated\_data(i) - dynamic\_data(i)}{dynamic\_data(i)}\right| < 30\%$, for *i* = 1, 2, …, 12.

Table 4.10 Flux constraints and independent parameters for three integrated model candidates.

Index	Flux Constraints	Independent Fluxes and Parameters
Model Candidate 1	$\begin{cases} f_{1SS} = f_{2SS} + f_{3SS} + f_{4SS} + f_{14SS} \\ f_{5SS} = f_{3SS} + f_{6SS} + f_{11SS} \\ f_{7SS} = f_{4SS} + f_{8SS} + f_{12SS} \\ f_{9SS} + f_{2SS} = f_{10SS} + f_{16SS} \\ f_{11SS} = f_{14SS} \\ f_{12SS} = f_{14SS} \\ f_{13SS} = f_{14SS} \\ f_{15SS} = f_{14SS} + f_{16SS} \\ f_{23SS} = f_{24SS} \end{cases}$	$Flux_{in} = [f_{2SS}, f_{3SS}, f_{4SS}, f_{6SS}, f_{8SS}, f_{9SS}, f_{14SS}, f_{16SS}, f_{23SS}]$ $Para_{in} = [\gamma_2, \gamma_3, \gamma_4, \gamma_6, \gamma_8, \gamma_9, \gamma_{14}, \gamma_{16}, \gamma_{23}, \cdots$ $\cdots, g_1, g_2, g_3, g_4, g_5]$
Model Candidate 2	$\begin{cases} f_{1SS} = f_{2SS} + f_{3SS} + f_{4SS} + f_{14SS} \\ f_{5SS} = f_{3SS} + f_{6SS} + f_{11SS} \\ f_{7SS} = f_{4SS} + f_{8SS} + f_{12SS} \\ f_{9SS} + f_{2SS} = f_{10SS} + f_{16SS} \\ f_{11SS} = f_{14SS} \\ f_{12SS} = f_{14SS} \\ f_{13SS} = f_{14SS} \\ f_{15SS} = f_{14SS} + f_{16SS} \\ f_{23SS} = f_{24SS} \\ f_{25SS} = f_{26SS} \end{cases}$	$Flux_{in} = [f_{2SS}, f_{3SS}, f_{4SS}, f_{6SS}, f_{8SS}, f_{9SS}, f_{14SS}, f_{16SS}, f_{23SS}, f_{25SS}]$ $Para_{in} = [\gamma_2, \gamma_3, \gamma_4, \gamma_6, \gamma_8, \gamma_9, \gamma_{14}, \gamma_{16}, \gamma_{23}, \gamma_{25}, \cdots$ $\cdots, g_1, g_2, g_3, g_4, g_5, g_6, T_{PI3K}]$
Model Candidate 3	$\begin{cases} f_{1SS} = f_{2SS} + f_{3SS} + f_{4SS} + f_{14SS} \\ f_{5SS} = f_{3SS} + f_{6SS} + f_{11SS} \\ f_{7SS} = f_{4SS} + f_{8SS} + f_{12SS} \\ f_{9SS} + f_{2SS} = f_{10SS} + f_{16SS} \\ f_{11SS} = f_{14SS} \\ f_{12SS} = f_{14SS} \\ f_{13SS} = f_{14SS} \\ f_{15SS} = f_{14SS} + f_{16SS} \\ f_{23SS} = f_{24SS} \\ f_{25SS} = f_{26SS} \\ f_{27SS} = f_{28SS} \end{cases}$	$Flux_{in} = [f_{2SS}, f_{3SS}, f_{4SS}, f_{6SS}, f_{8SS}, f_{9SS}, f_{14SS}, f_{16SS}, f_{23SS}, f_{25SS}, f_{27SS}]$ $Para_{in} = [\gamma_2, \gamma_3, \gamma_4, \gamma_6, \gamma_8, \gamma_9, \gamma_{14}, \gamma_{16}, \gamma_{23}, \gamma_{25}, \gamma_{27}, \cdots$ $\cdots, g_1, g_2, g_3, g_4, g_5, g_6, g_7, T_{PI3K}, T_{EGFR}]$

$f_{i\mathrm{SS}}$, i = 1, 2, 3, …, 27, 28, represents the steady state flux value for the i^{th} pathway in unstimulated conditions. $Flux_{in}$ indicates the selected independent flux vector, and $Para_{in}$ indicates the selected independent parameter vector for each model candidate.

Table 4.11 48 possible parameter combinations for three integrated model candidates.

$[\gamma_2/\gamma_9, \gamma_3/\gamma_6, \gamma_4/\gamma_8, \gamma_{16}]$	Model Candidate 1	Model Candidate 2	Model Candidate 3
[0 0 0 0]	MC1-1	MC2-1	MC3-1
[0 0 0 1]	MC1-2	MC2-2	MC3-2
[0 0 1 0]	MC1-3	MC2-3	MC3-3
[0 0 1 1]	MC1-4	MC2-4	MC3-4
[0 1 0 0]	MC1-5	MC2-5	MC3-5
[0 1 0 1]	MC1-6	MC2-6	MC3-6
[0 1 1 0]	MC1-7	MC2-7	MC3-7
[0 1 1 1]	MC1-8	MC2-8	MC3-8
[1 0 0 0]	MC1-9	MC2-9	MC3-9
[1 0 0 1]	MC1-10	MC2-10	MC3-10
[1 0 1 0]	MC1-11	MC2-11	MC3-11
[1 0 1 1]	MC1-12	MC2-12	MC3-12
[1 1 0 0]	MC1-13	MC2-13	MC3-13
[1 1 0 1]	MC1-14	MC2-14	MC3-14
[1 1 1 0]	MC1-15	MC2-15	MC3-15
[1 1 1 1]	MC1-16	MC2-16	MC3-16

"0" represents the uniform distribution with a relatively "low" range; "1" represents the uniform distribution with a relatively "high" range.

Table 4.12 Static and dynamic data structure used in criteria.

Index	Static_Data Structure		Dynamic_Data Structure	
	Scenario	Data	Scenario	Data
1	+AngII	$(f_{17}+f_{18})_{t=30min}/(f_{17}+f_{18})_{t=0} = 2$	+AngII	$X_6(t = 1\ min)/X_6(t = 0) = 2.1$
2	AdASNox1	$(f_{17}+f_{18})_{t=30min}/(f_{17}+f_{18})_{t=0} = 0.22$	+AngII	$X_6(t = 5\ min)/X_6(t = 0) = 1.9$
3	AdASNox1 +AngII	$(f_{17}+f_{18})_{t=30min}/(f_{17}+f_{18})_{t=0} = 0.43$	+AngII	$X_6(t = 10\ min)/X_6(t = 0) = 2.2$
4	siNox4	$(f_{17}+f_{18})_{t=30min}/(f_{17}+f_{18})_{t=0} = 0.87$	+AngII	$X_6(t = 15\ min)/X_6(t = 0) = 2.5$
5	siNox4 +AngII	$(f_{17}+f_{18})_{t=30min}/(f_{17}+f_{18})_{t=0} = 1.8$	+AngII	$X_6(t = 30\ min)/X_6(t = 0) = 2.4$
6	+AngII	$(f_{21}+0.5\times f_{20})_{t=30min}/(f_{21}+0.5\times f_{20})_{t=0} = 1.29$	+AngII	$X_{10}(t = 10sec)/X_{10}(t = 0) = 1.05$
7	AdASNox1	$(f_{21}+0.5\times f_{20})_{t=30min}/(f_{21}+0.5\times f_{20})_{t=0} = 0.86$	+AngII	$X_{10}(t = 30sec)/X_{10}(t = 0) = 1.5$
8	AdASNox1 +AngII	$(f_{21}+0.5\times f_{20})_{t=30min}/(f_{21}+0.5\times f_{20})_{t=0} = 0.98$	+AngII	$X_{10}(t = 1min)/X_{10}(t = 0) = 1.27$
9	siNox4	$(f_{21}+0.5\times f_{20})_{t=30min}/(f_{21}+0.5\times f_{20})_{t=0} = 0.58$	+AngII	$X_{10}(t = 5min)/X_{10}(t = 0) = 1.36$
10	siNox4 +AngII	$(f_{21}+0.5\times f_{20})_{t=30min}/(f_{21}+0.5\times f_{20})_{t=0} = 0.87$	+AngII	$X_{10}(t = 10min)/X_{10}(t = 0) = 1.65$
11	+AngII	$X_4(t = 30min)/X_4(t = 0) = 2$	+AngII	$X_{10}(t = 15min)/X_{10}(t = 0) = 1.7$
12	+AngII	$X_9(t = 30min)/X_9(t = 0) = 1.8$	+AngII	$X_{10}(t = 30min)/X_{10}(t = 0) = 1.79$
13	AngII + AG1478	$X_{10}(t = 30min)/X_{10}(t = 0) = 1.2$		
14	AngII + AdRacN17	$X_{10}(t = 30min)/X_{10}(t = 0) = 1.14$		

15	AngII+PP1	X_{10}(t = 30min)/X_{10}(t = 0) = 1.08		
16	AngII+GF 10923X	X_{10}(t = 30min)/X_{10}(t = 0) = 1.12		
17	AngII + GF 10923X	X_{10}(t = 30min)/X_{10}(t = 0) = 1.45		

4.3 Results

4.3.1 Prediction of AngII-Induced PKC Activation in VSMCs

Two distinct scenarios, respectively representing the unstimulated control condition and the stimulated AngII(100nM) treatment condition, are simulated separately.

Figure 4.10 shows the simulation result for unstimulated control conditions, where no AngII is added to the system, and AA, Ca^{2+}, and DAG constantly stay at their basal levels. The level of total active PKC (the sum of X_2, X_3, X_4, X_5, X_6, and X_7, variables defined in Table 4.1) in the simulation starts from zero and quickly approaches a stable value at ~$1.76*10^5$ molecules/cell (see left panel in Figure 4.10). This value represents the basal level of PKC_{active} and is used as the initial condition for the simulation of AngII treatment scenario. The uneven distribution of active PKC in different forms (see right panel in Figure 4.10) suggests that the active complex AA·PKC·DAG in unstimulated control conditions (marked as index 6) plays a dominant role in maintaining the basal enzymatic activity of PKC.

Figure 4.11 shows the simulation results for the scenario where extracellular AngII (100nM) is added to the system and the levels of AA, Ca^{2+}, and DAG no longer remain constant, but vary dynamically. Compared to the constant PKC_{active} level in unstimulated conditions, the level of PKC_{active} increases in a particular biphasic fashion with AngII treatment (see Figure 4.11 upper panels). The first phase of PKC activation is acute and transient, peaking ~1.5 fold over

the control level at 30 seconds after AngII treatment. The second phase is gradual and sustained, which approaches ~2 fold over control level and can last for at least 30 minutes.

The following PKC_{active} distribution analysis at different time points reveals that the importance and roles of different PKC_{active} forms may vary over time. At 30 seconds, the large amounts of active complex Ca^{2+}·PKC·DAG (marked as index 5) and AA·PKC·DAG (marked as index 6) show the effectiveness of these two active complexes, indicating the equally important roles of all three molecules AA, Ca^{2+}, and DAG in the first phase of PKC activation. By contrast, at 30 minutes, the overwhelming amount of active complex AA·PKC·DAG (marked as index 6) suggests the dominate roles of only two molecules AA and DAG in the second phase of PKC activation.

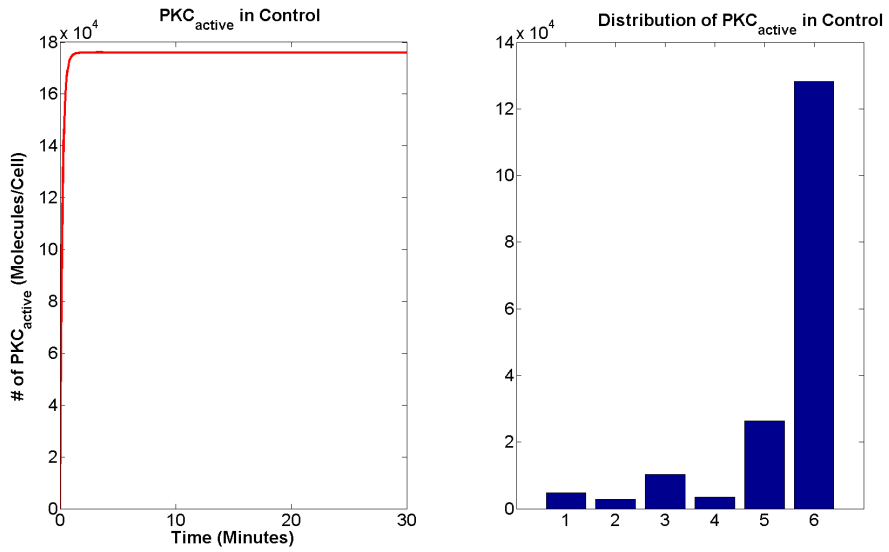

Figure 4.10. Simulation results of PKC_{active} in unstimulated control conditions.
Left panel: the summation of active PKC in unstimulated control condition. Right panel: Distribution of active PKC in different forms in unstimulated control conditions. Numbers along the *x*-axis of the right panel indicate the index of different PKC_{active} forms. The simulation starts with the initial condition X_0 = [$6*10^5$ 0 0 0 0 0 0 0 0 0 0 $6*10^6$ $6*10^4$ $6*10^7$].

4.3.2 Monte-Carlo Simulations for Three Integrated Model Candidates

Monte-Carlo simulations are implemented for 48 possible parameter combinations for three integrated model candidates (see details of simulation settings in section 4.2.4). The simulated results are assessed against different screening criteria. Table 4.13 shows the screening results for 48 possible combinations against each individual criterion from *C*1 through *C*6 as well as their combinations. The original sampling size for each combination is ten thousand, and the numbers in the Table 4.13 indicate the numbers of remaining samples for each combination (represented by rows in Table 4.13) that are satisfying the screening criteria specified in the corresponding column.

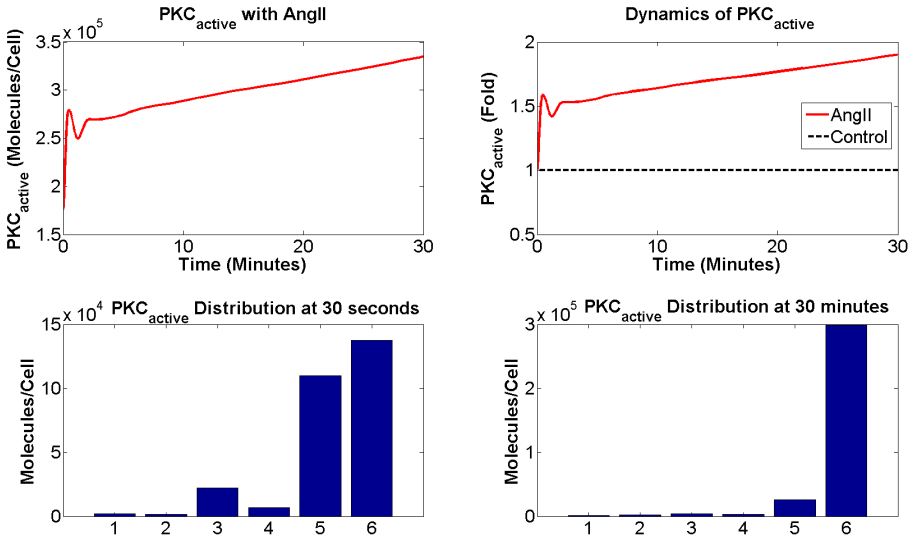

Figure 4.11. Simulation results of PKC_{active} with AngII (100nM) treatment.

Upper-left panel: sum of active PKC forms under AngII treatment. Upper-right panel: Dynamics of PKC_{active} under AngII treatment when the total amount of PKC_{active} under control is assumed to be at "1". Lower-left panel: distribution of active PKC in different forms at 30 seconds. Lower-right panel: distribution of active PKC in different forms at 30 minutes. Numbers along the *x*-axes of the lower panels indicate the index of different PKC_{active} forms. The simulation starts with the initial condition: X_0 =[2.375 0.048 0.029 0.103 0.034 0.264 1.283 0.285 0.026 1.425 0.128 60 0.6 600]*10^5.

We begin the analysis by screening the sampled points against each individual criterion from *C*1 to *C*6, and the numbers of remaining points, compared to the original 10,000, are respectively listed in column 2 to column 9 in Table 4.13. Among them, *C*4, *C*5, and *C*6 appear to be the most stringent criteria, because they exclude numerous random samples, and even result in no admissible candidates for some combinations of parameter settings. There are three options for implementing criterion *C*3. Comparing their screening results, these three conditions have quite similar filtering patterns, but differ in the numbers of remaining admissible sample points. Specifically, for one parameter combination, criterion *C*3-2 tends to allow the largest number of remaining sampling points, while criterion *C*3-3 tends to retain the least number of admissible points, indicating that *C*3-3 and *C*3-2 are respectively the strictest and loosest screening conditions among three options for criterion *C*3.

The originally sampled points are then filtered cumulatively against several criteria. As shown in columns 10 to 20 in Table 4.13, each addition of a criterion further reduces the size of remaining sample for every combination. This situation is particularly obvious when criteria *C*4, *C*5, and *C*6 are gradually added. For instance, studying Model Candidate 1 (MC1), the choice of *C*3-1, *C*3-2 or *C*3-3 is unimportant, when *C*4 is added to the screening conditions: no admissible points are left. In another words, the results suggest that it is impossible to find admissible candidates that simultaneously satisfy the first 4 criteria (from *C*1 to *C*4) when the PI3K data is used as the "offline" input.

An analogous situation holds for Model Candidate 3 (MC3) where almost no parameter combination satisfies the combined screening criteria from *C*1 to *C*5 (with only one exception for using either *C*3-1 or *C*3-2), which illustrates that the integrated model has poor performance of reproducing observed experimental records, when cSrc data are used as input.

Table 4.13 Monte-Carlo simulation results for 48 parameter combinations.

Model Index	C1	C2	C3-1	C3-2	C3-3	C4	C5	C6	C1, C2	C1,C2, C3-1	C1,C2, C3-2	C1,C2, C3-3	C1,C2, C3-1, C4	C1,C2, C3-2, C4	C1,C2, C3-3, C4	C1,C2, C3-1, C4,C5	C1,C2, C3-2, C4,C5	C1,C2, C3-3, C4,C5	C1,C2, C3-*i*, C4, C5, C6 for *i* = 1, 2,3
MC1-1	10000	4411	7924	9379	4781	0	0	0	4411	3380	4105	1868	0	0	0	0	0	0	0
MC1-2	5447	1524	8966	9714	7312	4553	4553	4553	1524	1163	1428	646	0	0	0	0	0	0	0
MC1-3	10000	4291	7831	9739	3130	0	198	0	4291	3270	4155	1203	0	0	0	0	0	0	0
MC1-4	5612	1400	8875	9867	6264	4388	4465	4388	1400	1062	1354	383	0	0	0	0	0	0	0
MC1-5	10000	5568	8591	9688	5780	0	462	0	5568	4757	5401	3298	0	0	0	0	0	0	0
MC1-6	5518	1894	9336	9839	7831	4482	4722	4482	1894	1665	1839	1161	0	0	0	0	0	0	0
MC1-7	10000	5213	7018	9515	2728	0	245	0	5213	3598	4950	1370	0	0	0	0	0	0	0
MC1-8	5609	1754	8312	9715	5927	4391	4499	4391	1754	1199	1677	443	0	0	0	0	0	0	0
MC1-9	10000	4658	7702	9424	4309	0	377	0	4658	3385	4321	1755	0	0	0	0	0	0	0
MC1-10	10000	2507	8126	9545	4721	0	299	0	2507	1866	2331	978	0	0	0	0	0	0	0
MC1-11	10000	4348	7456	9714	2837	0	214	0	4348	3124	4218	1041	0	0	0	0	0	0	0
MC1-12	10000	2230	7646	9702	3250	0	112	0	2230	1579	2137	500	0	0	0	0	0	0	0
MC1-13	10000	5507	8689	9721	5918	0	558	0	5507	4777	5358	3415	0	0	0	0	0	0	0
MC1-14	10000	2970	8832	9749	6063	0	460	0	2970	2577	2874	1769	0	0	0	0	0	0	0
MC1-15	10000	5093	6869	9461	2606	0	226	0	5093	3410	4809	1268	0	0	0	0	0	0	0
MC1-16	10000	2707	6927	9412	2889	0	135	0	2707	1806	2551	669	0	0	0	0	0	0	0
MC2-1	10000	4490	7957	9629	4131	198	0	0	4490	3313	4271	1438	52	115	8	0	0	0	0
MC2-2	5516	1495	9049	9836	6945	4587	4484	4484	1495	1132	1428	502	20	39	2	0	0	0	0
MC2-3	10000	4152	8220	9786	4098	0	445	0	4152	3228	4033	1306	0	0	0	0	0	0	0
MC2-4	5556	1341	9178	9916	6977	4444	4651	4444	1341	1031	1306	410	0	0	0	0	0	0	0
MC2-5	10000	5505	9352	9931	6710	480	313	0	5505	5124	5467	3620	138	207	39	32	47	6	0
MC2-6	5441	1785	9705	9972	8347	4809	4716	4559	1785	1671	1771	1131	45	64	14	8	15	3	0
MC2-7	10000	5227	9727	9983	7659	122	544	0	5227	5046	5216	3868	87	87	71	10	10	7	0
MC2-8	5600	1756	9884	9997	8796	4449	4676	4400	1756	1698	1754	1284	21	21	12	2	2	1	0
MC2-9	10000	4556	7895	9701	3709	27	240	0	4556	3430	4385	1337	8	23	1	2	5	0	0
MC2-10	10000	2331	8358	9774	4336	42	211	0	2331	1767	2246	694	19	26	4	0	0	0	0
MC2-	10000	4149	8256	9798	4118	0	502	0	4149	3177	4039	1291	0	0	0	0	0	0	0
MC2-12	10000	2176	8626	9843	4736	0	398	0	2176	1707	2123	712	0	0	0	0	0	0	0
MC2-13	10000	5508	9508	9955	7084	300	359	0	5508	5207	5479	3846	110	143	32	26	41	7	0
MC2-14	10000	2912	9592	9972	7342	330	284	0	2912	2749	2903	2018	84	98	39	14	21	5	0

Model Index	C1	C2	C3-1	C3-2	C3-3	C4	C5	C6	C1, C2	C1,C2, C3-1	C1,C2, C3-2	C1,C2, C3-3	C1,C2, C3-1, C4	C1,C2, C3-2, C4	C1,C2, C3-3, C4	C1,C2, C3-1, C4,C5	C1,C2, C3-2, C4,C5	C1,C2, C3-3, C4,C5	C1,C2, C3-*i*, C4, C5, C6 for *i* = 1, 2,3
MC2-15	10000	5188	9735	9988	7748	92	519	0	5188	5005	5179	3831	59	63	46	6	6	6	0
MC2-16	10000	2739	9802	9988	7842	98	395	0	2739	2650	2734	2011	46	46	32	4	4	4	0
MC3-1	10000	4412	8130	9668	4271	3	0	0	4412	3392	4226	1440	0	1	0	0	0	0	0
MC3-2	5543	1557	9082	9845	7000	4459	4457	4457	1557	11969	1494	530	0	0	0	0	0	0	0
MC3-3	10000	4227	7355	9452	3586	0	367	0	4227	2852	3937	1160	0	0	0	0	0	0	0
MC3-4	5508	1344	8726	9740	6536	4493	4649	4492	1344	928	1244	350	0	0	0	0	0	0	0
MC3-5	10000	5534	8979	9768	6073	4	227	0	5534	4959	5398	3283	0	1	0	0	0	0	0
MC3-6	5497	1857	9497	9892	8028	4505	4610	4503	1857	1650	1817	1124	0	1	0	0	0	0	0
MC3-7	1000	5128	8864	9782	6106	3	403	0	5128	4473	4991	3033	0	0	0	0	0	0	0
MC3-8	5499	1735	9422	9899	7991	4501	4698	4501	1735	1508	1691	1006	0	0	0	0	0	0	0
MC3-9	10000	4572	7659	9586	3696	1	187	0	4572	3294	4341	1351	0	1	0	0	0	0	0
MC3-10	10000	2353	8122	9679	4211	2	149	0	2353	1740	2241	707	0	0	0	0	0	0	0
MC3-11	10000	4193	7329	9376	3708	0	389	0	4193	2832	3841	1249	0	0	0	0	0	0	0
MC3-12	10000	2249	7643	9531	4036	0	323	0	2249	1474	2062	640	0	0	0	0	0	0	0
MC3-13	10000	5485	9036	9787	6203	1	253	0	5485	4930	5363	3342	0	0	0	0	0	0	0
MC3-14	10000	2957	9222	9843	6678	0	188	0	2957	2672	2905	1835	0	0	0	0	0	0	0
MC3-15	10000	5170	8926	9769	6293	3	431	0	5170	4574	5041	3152	1	1	0	1	1	0	0
MC3-16	10000	2691	9039	9834	6593	3	296	0	2691	2391	2630	1743	1	1	1	0	0	0	0

The original sample size for each combination is 10,000. Numbers indicate the numbers of admissible samples for each combination (row) of screening against combined criteria (column).

Quite different from the above two model candidates, Model Candidate 2 exhibits better screening results with many more remaining points that simultaneously satisfy the first 5 criteria (from *C*1 to *C*5). Specifically, eight combinations in MC2 (MC2-5, MC2-6, MC2-7, MC2-8, MC2-13, MC2-14, MC2-15, and MC2-16) contain candidates satisfying the first 5 criteria. As soon as the last criterion (*C*6) is added to the screening conditions, none of candidates exist in any of the 48 combinations for MC1, MC2 and MC3.

The combined criteria-driven candidate selection clearly shows that Model Candidate 2 shows much better performance than Model Candidates 1 and 3, and suggests the effectiveness of the corresponding EGFR data as input to the integrated system in reproducing observed experimental records. Additionally, the simulation results indicate eight specific combinations from MC2 (indices 5, 6, 7, 8, 13, 14, 15, and 16) that have many admissible candidates. This combined selection greatly reduce the size of possible parameter combinations from 16 to 8 (~50% reduction of parameter searching space), and also gives us some hints regarding the possible ranges of corresponding parameters they represent.

However, the current simulation finds no admissible sampling points that simultaneously satisfy all six screening criteria. One possible reason could be that the current sample size (10 thousand) is not large enough to sample the parameter space with over twenty dimensions. Another possible reason may be that the numerical assignments of the relatively "low" and "high" velocity ranges, which are currently expressed with the uniform distribution $U(10^{-4}, 10^{-3})$ and $U(10^{-3}, 10^{-2})$, are not large enough. This low numerical assignment could give smaller parameter values and thus lead to relatively slow biochemical reactions. Examining the relevant dynamic data utilized in criterion *C*6, we find that the H_2O_2 concentration increases very quickly

(first noticed at 10 seconds with a peak at 30 seconds after AngII treatment). This acute increase of H_2O_2 strongly indicates the relatively faster speed of involved biochemical reactions, suggesting that we might need to use larger numerical assignments to represent different velocity ranges.

4.3.3 Monte-Carlo Simulations for Integrated Model Candidate 2

Following the suggestions given in the above section, we implement another round of Monte-Carlo simulations particularly for the most promising Model Candidate 2. Different from the previous simulation settings, the sampling size for each possible combination in this round is increased by three times from 10,000 to 30,000. Also, a new numerical assignment for the relatively "low" and "high" speed ranges is used. Specifically, the relatively "low" speed range is represented with the uniform distribution $U(10^{-3}, 10^{-2})$, and the "high" speed range is assigned with $U(10^{-2}, 10^{-1})$. Compared to the previously used speed ranges, the relative ratios for "low" and "high" speed categories have not changed, but the absolute values for each range boundary increases by one order of magnitude. The independent parameters that need to be sampled, the evaluation criteria, and other simulation settings are kept exactly the same as before (section 4.2.4).

As before, the analysis begins with screening the sampled points against each individual criterion as well as the combined criteria. The filtered results are respectively summarized in corresponding rows in Table 4.14. With increased sampling size and new assigned numerical values of "low" and "high" speed ranges, the number of admissible samples has greatly increased especially for accumulated screening criteria. For instance, screening against the combined criteria of $C1$, $C2$, $C3$-2, $C4$ and $C5$, the previous Monte-Carlo simulations show a

total number of 151 admissible samples for 16 combinations in Model Candidate 2, while in the current round, the simulations increases the size of remaining points to 219 (~45% increase). More importantly, the current simulations successfully identify 12 admissible samples that simultaneously satisfy all 6 criteria (from *C*1 to *C*6), which could not be achieved in the previous round of Monte-Carlo simulations.

Independent of whether *C*3-1, *C*3-2 or *C*3-3 is utilized in the combined criteria, the selected 12 (or 11 when *C*3-3 is used) samples have the exactly same distribution over 16 combinations for MC2. Specifically, the existences of these samples focus on three combinations MC2-7, MC2-15, and MC2-16. As defined in Table 4.11, these three combinations can be directly translated into the index vectors [0 1 1 0], [1 1 1 0], and [1 1 1 1]. We find some common features of these three index vectors: the second and third elements in these vectors are always assigned with the numerical value "1", which indicates the rate constants in sets 2 and 3 are sampled from the relatively "high" speed range. In other words, this result suggests that the rate constants γ_3, γ_6, γ_4, and γ_8 always have relatively larger values compared to other rate constants.

Table 4.14 Monte-Carlo simulation results for Model Candidate 2.

Model Index	MC2-1	MC2-2	MC2-3	MC2-4	MC2-5	MC2-6	MC2-7	MC2-8	MC2-9	MC2-10	MC2-11	MC2-12	MC2-13	MC2-14	MC2-15	MC2-16
C1	30000	16502	30000	16600	30000	16502	30000	16591	30000	30000	30000	30000	30000	30000	30000	30000
C2	8278	16221	8160	16242	8242	16220	8162	16246	8080	5002	8037	4966	7972	5079	8141	4931
C3-1	29417	29730	29442	29762	29890	29950	29791	29903	29511	29658	29486	29611	29893	29942	29767	29846
C3-2	29975	29986	29951	29981	29996	29999	29980	29994	29976	29987	29951	29961	29995	29999	29980	29993
C3-3	23672	26342	23897	26248	25321	26668	23870	25893	23617	23880	23939	23813	25200	25027	23988	23527
C4	334	147	2	0	1090	430	436	189	143	114	0	0	1013	835	329	227
C5	1114	547	1194	524	1107	542	1185	525	1236	775	1203	792	1204	816	1156	790
C6	0	0	4	2	0	0	134	101	0	0	4	7	2	1	108	195
C1, C2	8278	2723	8160	2842	8242	2722	8162	2837	8080	5002	8037	4966	7972	5079	8141	4931
C1, C2, C3-1	8012	2607	7923	2754	8202	2706	8130	2806	7873	4869	7831	4836	7934	5061	8071	4888
C1, C2, C3-2	8262	2714	8137	2835	8240	2721	8158	2832	8067	4995	8015	4951	7968	5078	8131	4925
C1, C2, C3-3	6192	1979	6287	2207	7126	2338	6856	2362	6108	3762	6209	3824	6846	4382	6849	4112
C1, C2, C3-1, C4	133	39	2	0	261	89	162	64	85	59	0	0	267	193	147	109
C1, C2, C3-2, C4	135	42	2	0	263	89	163	64	86	60	0	0	269	193	148	109
C1, C2, C3-3, C4	92	30	2	0	200	66	115	39	59	41	0	0	200	139	101	82
C1, C2, C3-1, C4, C5	5	2	0	0	45	22	18	7	6	5	0	0	48	27	24	7
C1, C2, C3-2, C4, C5	5	2	0	0	47	22	18	7	6	5	0	0	49	27	24	7
C1, C2, C3-3, C4, C5	2	2	0	0	35	20	17	6	5	5	0	0	42	21	19	7
C1, C2, C3-1, C4, C5, C6	0	0	0	0	0	0	4	0	0	0	0	0	0	0	3	5
C1, C2, C3-2, C4, C5, C6	0	0	0	0	0	0	4	0	0	0	0	0	0	0	3	5
C1, C2, C3-3, C4, C5, C6	0	0	0	0	0	0	3	0	0	0	0	0	0	0	3	5

The original sample size for each combination is 30 thousand. Numbers in the table indicate the amount of satisfying samples for each combination (column) screening against the specific combined criteria (row).

The twelve selected samples are then further analyzed for their value distributions. The relative ratios between individual rate constants, including γ_2, γ_3, γ_4, γ_6, γ_8, γ_9, and γ_{16}, are calculated and displayed in Figure 4.12. Carefully examining these ratio distributions, we find some specific features of the investigated rate constants. First, comparing the rate constants associated with reversible reactions (γ_6, γ_8, and γ_9) and recycling pathways (γ_2, γ_3, and γ_4) (results displayed in the first row in Figure 4.12), we find that the rates associated with reversible reactions with positive signals (γ_6 and γ_8) tend to be higher than the rates associated with corresponding recycling reaction (γ_3 and γ_4). In contrast, the reversible reaction rate with negative signal (γ_9) seems to have the opposite trend: being smaller than the corresponding recycling rate (γ_2). Ten out of twelve (83.3%) selected samples follow this trend (with 2 exceptions).

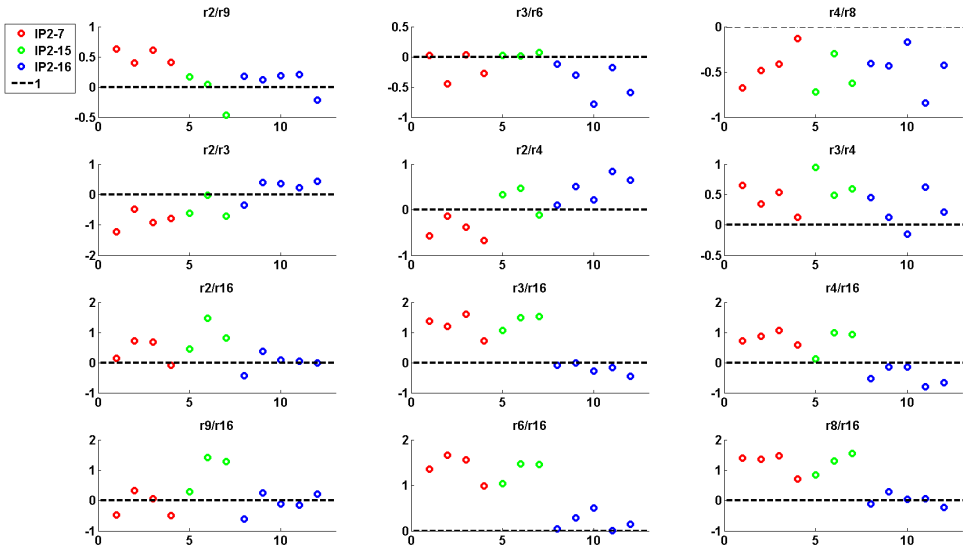

Figure 4.12 Relative ratio between individual independent rate constants for 12 selected samples.

The *x*-axis in each plot indicates the index of 12 selected samples. The *y*-axis in each plot is expressed in $\log_{10}$ space. Different colors indicate the samples from different parameter combinations.

Second, comparing the relative magnitudes between individual recycling reaction rates (γ_2, γ_3, γ_4) and the reaction rate for the efflux (γ_{16}), we find that the twelve admissible samples follow two specific patterns: The first pattern covers all samples selected from combinations MC2-7 and MC2-15 and retains the following relative magnitudes of the rate constants: $\gamma_3 > \gamma_4$, $\gamma_2 > \gamma_{16}$. With this specific pattern, the recycling pathway associated with γ_3 serves as the most efficient disassembly pathway in degrading $Nox1_{active}$. The second pattern holds for the samples selected from combination MC2-16, among which 80% samples (4 out of 5) have their rate constants follow the relationship $\gamma_2 > \gamma_{16} > \gamma_3, \gamma_4$, suggesting that the recycling pathway associated with γ_2 plays the dominant role in degrading $Nox1_{active}$. There is one exception in combination MC2-16 that follows a different order: $\gamma_{16} > \gamma_3 > \gamma_2 > \gamma_4$. Compared to the magnitude of γ_{16}, which is the smallest one in the first pattern, the magnitude of γ_{16} in the second pattern increases a lot, ranking from the last position to the first (or the second) place.

In addition to comparing the relative magnitudes of rate constants, we explore the distributions of other independent parameters as well. Figure 4.13 shows the distributions of all pertinent kinetic orders, which characterize the effect of input signals on relevant biochemical reactions. These kinetic orders are originally sampled with the same uniform distribution $U(0, 2)$, but turn out to have quite different histograms after screening against the six criteria. Among them, we are particularly interested in the kinetic orders g_1 and g_2, which respectively characterize the regulatory effects of two distinct signaling molecules PKC and cSrc on the same process of $p47^{phox}$ phosphorylation. As shown in Figure 4.13, g_1 has an uneven distribution ranging from 0.5 to 2; while g_2 has a rather even distribution ranging from 0 to 1. The following ratio analysis of g_1 over g_2 (shown in Figure 4.14 (a)) further reveals a trend for the relative magnitudes of these two parameters. 11 out of 12 (~92%) selected samples have a g_1 value at

least as large as g_2, and nine of them have a g_1 value at least one order of magnitude larger than g_2. This finding strongly indicates the relatively important and dominant role of the signaling molecule PKC in regulating $p47^{phox}$ phosphorylation.

In order to compare and validate the roles of PKC and cSrc in regulating $p47^{phox}$ phosphorylation further, simulations are implemented to mimic the scenarios when the regulation of PKC or cSrc is blocked in AngII treatment condition; this is accomplished by setting either $g_1 = 0$ or $g_2 = 0$. As shown in Figure 4.14 (b), when the regulation of PKC is blocked (denoted by the green line in Figure 4.14 (b)), the dynamics of phosphorylated $p47^{phox}$ is far different from its behavior in normal AngII treatment (denoted by red line). The most significant difference occurs during the first 30 seconds after AngII treatment when the phosphorylated $p47^{phox}$ completely loses its acute activation without the PKC-dependent regulation. Moreover, the stable increase of H_2O_2 lags far behind the normal one (~50% decrease) if the PKC-dependent regulation is absent. In contrast, when the regulation of cSrc on $p47^{phox}$ phosphorylation is blocked (denoted by the blue line in Figure 4.14 (b)), the dynamics of phosphorylated $p47^{phox}$ and the increase of H_2O_2 change insignificantly. However, the dynamics of $Rac1_{GTP}$ appears to change only insignificantly when compared to the normal case. From this set of comparative simulations, we can infer the different roles of PKC and cSrc in regulating $p47^{phox}$ phosphorylation, which could lead to totally different responses of Nox1 and its subsequent ROS production in AngII treatment condition. Although both signaling molecules have been documented to be able to regulate $p47^{phox}$ phosphorylation, our simulation analysis suggests that PKC seems to play a more dominant role and the dynamic behavior of the integrated system will change significantly if this PKC-dependent regulation is absent.

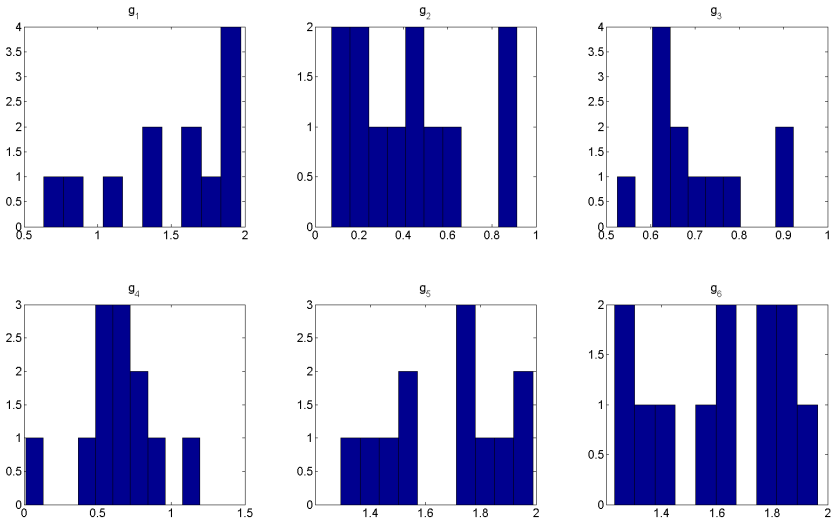

Figure 4.13 Distributions of kinetic orders for 12 selected samples.

Finally, we implement the dynamic simulations of the integrated model candidates for various scenarios. From the simulated results (displayed in APPENDIX C from Figure C.1 to C.12), we find some common features for 12 selected samples: (i) AngII-induced ROS increase happens immediately, and maintains at a higher plateau at 30 minutes; (ii) The simulated dynamics of $Rac1_{GTP}$ under AngII treatment is well consistent with experimental evidence; (iii) Increase of phosphorylated $p47^{phox}$ in AngII treatment happens in two phases: the first phase is acute and transient, and the second phase is sustained; (iv) The simulated levels of ROS (specifically, H_2O_2) are kept well consistent with the experimental records for all scenarios, including the treatment of PMA, AG1478, RacN17, PP1, and GF 10923X.

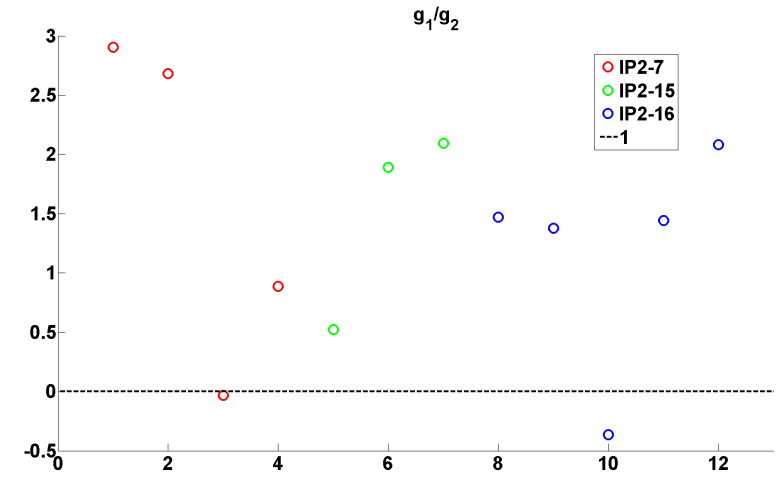

(a)

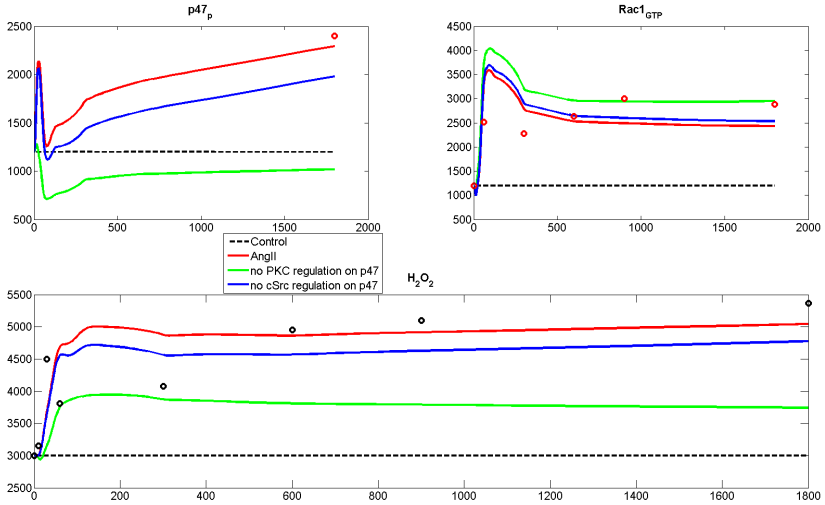

(b)

Figure 4.14 Simulation results illustrating the effects of PKC and cSrc on p47^{phox} phosphorylation.

(a) Ratio analysis of g_1/g_2 in $\log_{10}$ space. (b) Simulation results for scenarios with either g_1=0 or g_2=0. This simulation is a representative result, using one parameter set from 12 selected samples. The numerical values of parameters used in this simulation are: $Para_{in}$ = [0.0176 0.0908 0.02320.0769 0.0972 0.0512 0 0.0027 1.6792 1.5401 1.7832 0.2196 0.7376 0.6810 1.5133 1.6543 10].

4.3.4 cSrc- and Ca^{2+}-Dependent EGFR Activation

From the criteria-driven analysis in section 4.3.2, we know that Model Candidate 2 exhibits much better performance in reproducing most experimental observations under various scenarios than Model Candidates 1 and 3. This result strongly indicates the effectiveness of corresponding EGFR data, and at the same time raises several questions: Is this model able to reproduce the EGFR dynamics by using its upstream signal cSrc data? Why is the performance of respectively using cSrc and EGFR data as system input not consistent in the two cases?

In order to answer these questions, a mathematical model describing the mechanism of cSrc-dependent EGFR activation (model structure shown in Figure 4.15 (a)) is constructed and implemented (see details in APPENDIX C.3). The dynamic profile of cSrc is considered as an input, driving the downstream signal EGFR change correspondingly. The numerical values of pertinent parameters are found with nonlinear optimization functions in MATLAB, and large numbers of randomized initial conditions are used to ensure that a relatively better local optimal point is achieved. The simulated EGFR dynamics is then compared with experimental findings. Although there are local optimal points with distinct numerical parameter values, their simulated EGFR dynamics appears to show quite similar trends. As shown in Figure 4.15 (b), the simulation result well reproduces the long-term effect of EGFR activation (for time $t > 5$ minutes), but shows a dramatic difference to the experimental records for time $t < 5$ minutes: EGFR was observed to increase acutely and immediately during the first 5 minutes, peaking over 7 fold at 1 minute and decreasing gradually after that [259], while, the simulation shows a gradual and much slower and lower increase without any decline.

The comparison of the simulation result with experimental findings reveals an inconsistency, especially for the time interval t < 5 minutes. This inconsistency shows the fact that the sole use of the cSrc data does not reproduce the EGFR dynamics well. At the same time, it provides a good explanation for the demonstrated different results when cSrc and EGFR data are separately utilized as inputs in the previous Monte-Carlo simulations.

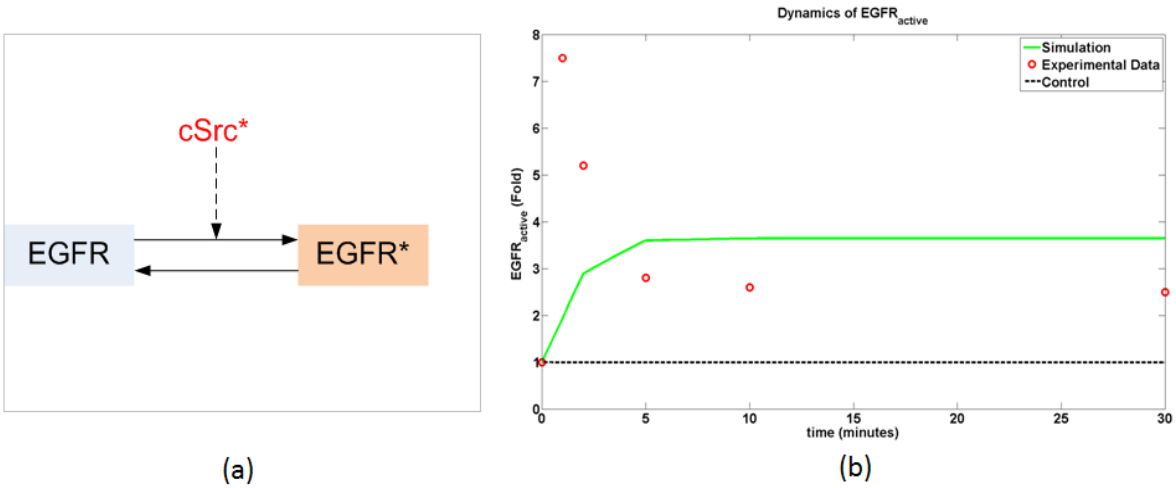

Figure 4.15. cSrc-dependent EGFR activation.

(a) Schematic representation of model structure. (b) Simulated EGFR dynamics. See detailed descriptions of mathematical equations and the optimal parameter values used in simulation in APPENDIX C.3.

Several potential factors may cause this inconsistency. One possible reason is that due to some limitations of the experimental set-ups or protocols, the measurements of cSrc, especially during the first few minutes, may not be accurate enough, and thus are not very reliable. An alternative reason with higher possibility is that except for cSrc, there exist other signaling molecules that could potentially activate EGFR independently. Because cSrc-independent EGFR activation mechanisms have not been incorporated in the present model, the current simulation is

not able to reproduce the EGFR dynamics even if the cSrc data are accurate and reliable. Thus, the task at hand is to search whether there are other important signaling molecules that can independently activate EGFR in VSMCs in AngII treatment condition.

One potential candidate is Ca^{2+}. Several studies have documented that Ca^{2+} is involved in AngII-induced EGFR transactivation The potential underlying mechanism is proposed to be redox-insensitive and thus differs from the cSrc-dependent redox-sensitive EGFR activation [38, 265]. In order to test whether Ca^{2+} is a possible missing signaling molecule in EGFR activation, we reconstruct a model that takes Ca^{2+} into account; the reconstructed model structure is shown in Figure 4.16 (a). The dynamic profile of Ca^{2+} in AngII (100nM) treatment condition is collected from the literature [257] and considered as a second input. The reconstructed system is then numerically implemented (see details in APPENDIX C.4) and the newly simulated EGFR dynamics is compared with experimental findings.

With the new mechanism incorporated in the model, the simulated EGFR dynamics (denoted by green line in Figure 4.16 (b)) is well consistent with its experimental records (denoted by red circles in Figure 4.16 (b)) during the entire simulated time intervals. This result, and especially the improved simulation during the first 5 minutes, effectively demonstrates the effect of Ca^{2+} on EGFR activation, particularly on the transient behavior of EGFR during the first few minutes. Moreover, the consistency between the new simulation result and experimental evidence validates our original hypothesis of the existence of a missing cSrc-independent EGFR activation mechanism.

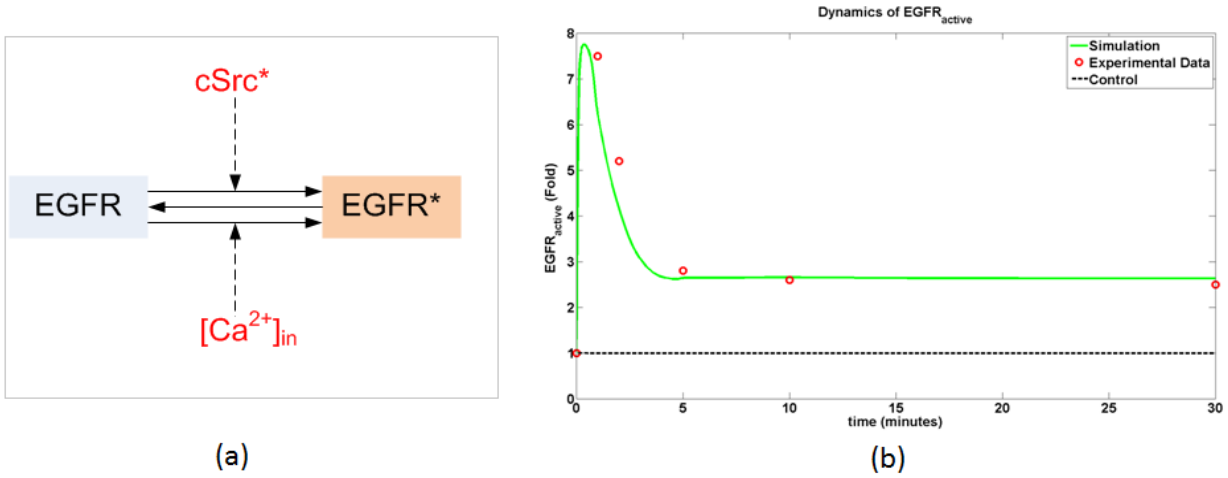

Figure 4.16 cSrc- and Ca^{2+}-dependent EGFR activation.

(a) Schematic representation of reconstructed model structure. (b) Simulated EGFR dynamics. See detailed descriptions of mathematical equations and the optimal parameter values used in simulation in APPENDIX C.4.

4.3.5 H_2O_2-Induced Positive Feedback

From the analyses of two rounds of Monte-Carlo simulations (section 4.3.2 and 4.3.3), we have not only identified EGFR data as the most effective input to the integrated model, but also generated 12 selected samples that are able to fulfill the requirements of both qualitative and quantitative criteria as well as to reproduce satisfactory systematic dynamics under all considered scenarios. Although these two Monte-Carlo simulations contain some subtle differences in settings, such as the sampling size and numerical assignments of parameter searching ranges, these simulations have been implemented in quite a similar fashion. They consider active PKC and the other signaling molecule from the cSrc/EGFR/PI3K signaling cascade (cSrc, EGFR, or PI3K) as two independent inputs, whose values will affect the system but are not affected by the system.

In reality, these two input signals are actually not independent of each other, and the activation of the second signal is in fact dependent on the availability of the first signal and its-induced acute activation of Nox1 and subsequent ROS release. More specifically, an AngII-induced PKC signal acutely enhances Nox1 activity and leads to the initial release of H_2O_2. This increased H_2O_2 then activates cSrc and its down-stream signals including EGFR and PI3K, which in turn further strengthens Nox1 activation by stimulating the activation process of $Rac1_{GDP}$, leading to more ROS generation [38]. Thus, this H_2O_2-dependent cSrc activation forms a positive feedback loop and plays an important role in maintaining Nox1 activation and sustained ROS generation.

In order to analyze the function of this specific H_2O_2-dependent positive feedback in regulating systematic behavior, we add to the model one more regulatory pathway from H_2O_2 to cSrc activation. At the same time, we allow one signal (PKC) instead of two as the input. Accounting for the cSrc-independent and Ca^{2+}-dependent EGFR activation mechanism proposed in section 4.3.4, Ca^{2+} is also considered as an independent input because this pathway is redox-insensitive and therefore not affected by the target system. As a result, AngII-induced Nox1 activation in VSMCs is represented by the modeled system as completely driven by AngII-induced PKC activation and Ca^{2+} mobilization.

The final model integrates three distinct modules, including the Nox1 activation-disassembly module, ROS metabolism module, and H_2O_2-dependent cSrc/EGFR/PI3K activation module, and has two independent inputs, namely PKC and Ca^{2+}. It contains 14 system dependent variables, 31 individual fluxes, and 43 parameters in total. Most parameter values are already found in previous simulations and analysis, and the few remaining parameter values, which are particularly involved in H_2O_2-induced cSrc activation, will be determined during the final

simulations. (See the details of mathematical description and numerical assignments for all parameters for the final model in APPENDIX C.5).

One representative simulation result is shown in Figure 4.17 (see other 11 simulation results in Figures C.13 to C.23). This result clearly demonstrates that the addition of H_2O_2-induced positive feedback into the system does not significantly change the overall system behavior. The simulated dynamics of most dependent variables, including cSrc, EGFR, H_2O_2, and GTP-bound Rac1 are well consistent with their experimental observations. However, there exist some discrepancies for PI3K: the simulation shows a similar up-regulation activity of PI3K, but it differs in transient patterns from experimental records.

4.4 Discussion

Angiotensin II (AngII)-induced Nox1 activation and subsequent ROS release in VSMCs have been investigated in numerous studies [31, 34, 36, 37, 96, 105] . These experimental and clinical studies have greatly enhanced our understanding of this complicated system in terms of the pertinent regulatory signals, key components, and the involved pathway structures. With this biological information and a variety of other biological data available in the literature, it is possible to assemble quite a detailed picture of how individual subunits of Nox1 are organized to form an active enzyme complex within response to a stimulus like AngII. While the components and basic interactions are known, the overall functionality of the Nox1 system is not easy to intuit, especially when the regulatory signals are dynamically changing. Another issue that complicates our understanding Nox1 dynamics is the Nox1 disassembly. Although Chapter 3 discussed some generic questions regarding Nox1 disassembly mechanisms under nominal,

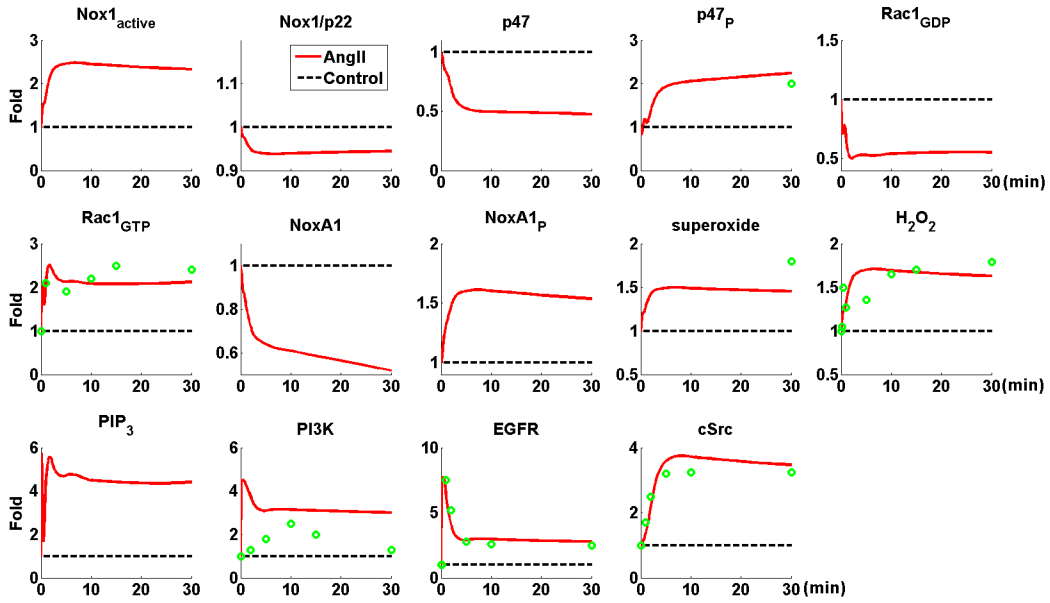

Figure 4.17 Simulation result of AngII-induced Nox1 activation in VSMCs with H_2O_2-dependent positive feedback.

Red solid line represents the simulation under AngII(100nM) treatment. Black dashed line represents the level of eachvariable in unstimulated control condition. Green circles are experimental records, which are recalculated into fold changes compared to the control level. The numerical values of parameters used in this simulation are: $Para_{in}$ = [0.0075 0.0629 0.0183 0.0580 0.0471 0.0018 0.0016 0.8242 5.9634 0.8130 0.8408 0.9224 0.9061 1.3807 1.7573 5].

unstimulated condition, there still remain open questions. For instance, does the order of importance of each individual Nox1 degradation pathway change in response to dynamic input signals? Can we extract more useful indications or conclusions from the currently available experimental observations? Is the current model structure sufficient? As we have shown with our computational analysis here, a specific order of importance of each individual disassembly pathway is needed to satisfy all qualitative and quantitative criteria, and the current model structure needs to be augmented with a new regulatory pathway to achieve better performance and data consistency.

A two-phased modeling strategy was pursued. In the first phase, the model was decomposed into four distinct modules, and each module was separately constructed and analyzed (see detailed description in section 4.2.2). As far as possible, the parameters in each module were separately estimated with available experimental data. In the second phase, the four individually constructed modules were integrated into a single computational model structure. The parameters were combined from the modules, and their potential numerical ranges or magnitudes were explored with Monte-Carlo methods. Available experimental data and other pieces of information, whether static or dynamic, quantitative or qualitative, were collected from the literature and used as evaluation criteria. Since there are three options for modeling the cSrc/EGFR/PI3K signaling cascade, depending on different data used as input, the modeling process resulted in three integrated model candidates (MC1, MC2, and MC3). These candidates required a total of 48 parameter combinations (16 combinations for each model candidate) to be explored and evaluated simultaneously.

The analysis of the initial round of Monte-Carlo simulations led to an interesting result. When the originally sampled points were screened with combined criteria from $C1$ to $C5$, all admissible candidates belonged to model candidate 2 (MC2), indicating the effectiveness of the available EGFR data as input. However, when we attempted to use cSrc data to reproduce the EGFR dynamics, we failed to regenerate consistent EGFR dynamics, especially for the time interval $t < 5$ minutes, no matter which parameter values were used. It is *a priori* not easy to explain why two datasets coming from up-stream and direct down-stream signals are not consistent with each other, suggesting that there was something missing in the model. This deduction led us to propose the hypothesis that some other EGFR activation mechanisms were missing in the model, and that these mechanisms should be cSrc-independent. Searching the

literature, we identified the signaling molecule Ca^{2+} as a candidate, and it turned out that it remedied the former inconsistency. Although the role of Ca^{2+} in AngII-induced Nox1 activation has not been particularly emphasized by the scientific community, Ca^{2+} has been suggested to be able to stimulate EGFR transactivation in a redox-insensitivity manner, which thus substantially differs from the redox-sensitive cSrc-dependent EGFR trans-activation. In order to validate our hypothesis, we revised the EGFR activation module by adding an activation pathway separately regulated by Ca^{2+}. With the newly added pathway, the simulated EGFR dynamics was well consistent with experimental records during the entire time interval.

Focusing on MC2, the second round of Monte Carlo simulations generated several good samples capable of satisfying all combined criteria from *C*1 to *C*6, which were achieved in the first round of simulations. These candidates are distributed in three specific combinations with indices MC2-7, MC2-15, and MC2-16 (see results shown in Table 4.14 and definition of these indices in Table 4.11). The correspondences between these index vectors and the relative magnitudes of related rate constants help us interpret this result. It suggests that among three different recycling pathways of Nox1, the disassembly pathway via dephosphorylation of $p47^{phox}$ (associated with γ_3) and the pathway via deactivation of $Rac1_{GTP}$ (associated with γ_4) are playing more important roles in effectively disassembling Nox1 since the numerical values of γ_3 are γ_4 are always shown to be sampled with larger values or magnitudes.

The subsequent ratio analysis of individual rate constants further revealed two specific patterns to describe the relative magnitudes of these rate constants. Specifically, in seven out of twelve selected samples (~60%), γ_3 has the largest numerical value, indicating its prominent role of dephosphorylation of $p47^{phox}$ in disassembling active Nox1. Four out of twelve admissible samples (~33%) follow a second pattern, with γ_2 having the largest numerical value, suggesting

the dominant role of phosphorylation of NoxA1 in disassembling active Nox1. This ratio analysis also investigates the possible ranges or relative magnitudes of other rate constants, providing for the first time detailed information about the importance of individual reactions within the Nox1 system.

Two distinct signaling molecules, PKC and cSrc, have been proposed to regulate the process of $p47^{phox}$ phosphorylation [33, 38, 233]. This duality raises the question of whether these two signaling molecules are equally important in regulating the target process. The ratio analysis of g_1 over g_2 (shown in Figure 4.14 (a)) demonstrates that g_1 is much larger than g_2 in most cases indicating the relatively dominant role of PKC on $p47^{phox}$ phosphorylation. This inference is further supported by subsequent scenario simulations where either PKC- or cSrc-dependent regulation was blocked by setting $g_1 = 0$ or $g_2 = 0$. When the regulation of PKC was completely blocked, the simulated system dynamics appeared to vary greatly from the normal case (Figure 4.13 (b)). By contrast, when the regulation of cSrc was absent from the system, the simulated system dynamics changed only insignificantly. This comparative simulation strongly demonstrates the more important role of PKC in regulating $p47^{phox}$ phosphorylation as well as the dynamic responses of the system.

One interesting feature of AngII-induced Nox1 activation in VSMCs is the existence of H_2O_2-induced positive feedback through the cSrc/EGFR/PI3K signaling cascade. Accounting for this feedback pathway enables the entire system to be driven exclusively by one input signal PKC and to run sustainably on its own. To test the importance of this positive feedback as well as to see whether our model is able to capture this prominent feature, we reconstructed the model by incorporating this H_2O_2-mediated cSrc activation pathway. After tuning the relevant parameters, the final integrated system reproduced the overall system dynamics for most

variables very well (Figure 4.17). The only remaining inconsistency is the dynamics of PI3K. One possible reason causing this inconsistency is that the current dynamic data of PI3K is collected from the assessment of the AngII-induced tyrosine phosphorylation of p85, a catalytic subunit of PI3K, through immunoprecipitation and Western blot analysis [261]. As a consequence, the data may not reflect the overall behavior of PI3K since AngII is also proposed to affect PI3K activity through other mechanisms, such as the AngII-induced distribution changes in the subcellular pools of PI3K and the translocation of the p85 subunit and its association with activated growth factor receptors as well as adapter proteins [261]. The existence of multiple regulatory mechanisms of AngII-induced PI3K activation may render the experimental observation from only one mechanism incomplete and insufficient to represent the overall PI3K behavior. This conclusion may suggest that other PI3K activation mechanisms need to be explored and evaluated.

CHAPTER 5

CONCLUSIONS AND FUTURE WORK

5.1 Conclusions

The body of work presented in this dissertation advances knowledge of the underlying regulatory mechanisms of NADPH oxidase 1 (Nox1) in vascular system. The systematic analysis of Nox1-mediated mechanotransduction pathway stimulated by different types of shear stresses in endothelial cells (ECs) (Chapter 2), the function and design analysis of a generic Nox1 activation-disassembly system regulated by static signals in vascular smooth muscle cells (VSMCs) (Chapter 3), and the dynamic analysis of Nox1 and its subsequent ROS production in response to the hormone angiotensin II in VSMCs (Chapter 4), provide novel insights into the possible Nox1 activation and disassembly mechanisms as well as their distinct roles under treatments with different extracellular stimuli.

As an important endogenous source of ROS, Nox1 often works in a collaborative and cooperative manner with other non-Nox ROS sources, as well as with other Nox homologues co-existing in the same cell. The resulting interactive network is complicated and makes interpretations and predictions of Nox1 activity and its dynamics difficult and non-intuitive. Additionally, the intrinsic properties of Nox1-catalyzed ROS, which are biochemically reactive and short-lived, complicate the experimental detection and often render measurements of these molecules less accurate than for stable molecules. Furthermore, these experimental measurements often reflect a global response of the target cell, which not only includes the Nox1-catalyzed ROS, but also contributions from other sources. As a result, it becomes difficult to infer the details of Nox1 activity with pure experimental methods. In order to overcome some of the limitations of experimental studies and to extract maximal information from available

experimental information, this research utilizes computational and modeling methods to study detailed properties of Nox1 activation and disassembly mechanisms in vascular cells.

Experimental evidence shows that Nox1 can be activated by a variety of stimuli. One prominent stimulus that is directly relevant to cardiovascular disease and atherosclerosis is shear stress, which is naturally generated on the surface of ECs when blood flows through arteries. Generally, two physiological or pathological shear stresses occur in different areas of arteries: laminar shear stress (LSS) in healthy, straight sections of vessels, and oscillatory shear stress (OSS) at branches and occlusions, which is mainly caused by disturbed flow. These two types of shear stress differently regulate Nox1 activity and subsequent ROS production, and therefore have essentially opposite roles in the initiation and genesis of atherosclerosis.

Nonetheless, an interesting experimental observation shows that these two shear stresses actually have similar short-term effects in increasing ROS production *in vitro* (t = 1 hour) but opposite long-term effects (t = 24 hour). In order to investigate this phenomenon, we developed a dynamic mathematical model (see pathway structure in Figure 2.1) that incorporates the main known Nox1 component in ECs ($p47^{phox}$ and Nox1 subunits) and accounts for regulation of Nox1 activity at multiples levels, including transcriptional and translational regulation, as well as signal-based regulation. The simulation analysis not only reproduced the experimental observations well (Figure 2.2 to Figure 2.4), but also illustrated the distinct roles for each individual type of regulation. The analysis revealed that the similar short-term effect of two shear stresses is mainly due to the acute signal-based regulation of $p47^{phox}$ phosphorylation (Figure 2.6 and Figure 2.7), while the opposite long-term effects may be caused by the different regulatory processes of two shear stresses on Nox1 mRNA and protein expression through a BMP4-dependent pathway. These longer-term transcriptional and translational processes were modeled

with time-delays (τ), and the simulations demonstrated that these delays are critical for good performance, thereby demonstrating the multi-time scale nature of the system.

The originally proposed model in Chapter 2 only contained two Nox1 subunits, namely the Nox1/$p22^{phox}$ complex (Nox1 is not stable outside a complex with $p22^{phox}$) and the organizer subunit $p47^{phox}$. Other pertinent components that could potentially affect Nox1 activity, such as Rac and the activator subunit, were not considered, because information regarding these regulatory subunits in ECs is scarce. Moreover, ECs contain three Nox homologues, among which Nox1 and Nox2 have very similar molecular compositions and activation mechanisms. As a result, it is not clear whether a specific regulatory subunit will complex with Nox1, Nox2, or both of them, to initiate the enzyme activity, and it is difficult to identify the exact sources of ROS from these two Nox homologues.

In order to overcome the limitations of the EC model, we switched to another type of cells, namely vascular smooth muscle cells (VSMCs), for which more information is available. Compared to ECs, Nox2 shows extremely low expression and its subunit requirements and the contribution to ROS can reasonably be ignored. Another expressed Nox homologue in VSMCs is Nox4. As discussed in section 1.2.2, Nox4 only requires $p22^{phox}$ (abundant in VSMCs) for its ROS-producing activity, and its activity is proposed to be mainly dependent on its protein expression. Thus, there is little subunit competition for Nox1 and Nox4. More importantly, as long as its protein expression is not significantly changed, Nox4 can be considered a constant supply to ROS. In summary, the simpler composition of the Nox family in VSMCs makes these cells a better template for exploring the specific properties of Nox1 activation and disassembly.

A detailed model describing the Nox1 activation-disassembly system in VSMCs is proposed in Chapter 3 (see pathway structure shown in Figure 3.1). Four different, potentially

simultaneous disassembly pathways of Nox1 were incorporated, and their ability to control Nox1 activity was explored by using different kinds of user-defined criteria. Assessments of these four deactivation mechanisms with respect to different criteria led to similar results (Figure 3.2 and Figure 3.3). For effective functioning, the flux associated with proteolytic pathway must be much smaller (by at least two orders of magnitude) than the fluxes associated with the recycling pathways, indicating the relative inefficiency of proteolysis for disassembling Nox1 under nominal, physiological conditions. Furthermore, the subsequent analysis revealed several generic design features that could possibly affect the system's optimal responsiveness. The identified features include the material distributions of key subunits in their active or inactive state (Figure 3.2), the rates and directional balances of reversible reactions (Figure 3.6 to Figure 3.8), and the relative magnitude of the system's efflux (Figure 3.6 to Figure 3.8). These findings enable us to understand the Nox1 system from an entirely different point of view and allow us identify potential strategies for controlling Nox1 activity (see discussion in Chapter 3).

Although the analysis in Chapter 3 revealed some specific features regarding the disassembly mechanisms of Nox1 as well as its optimal performance, this type of analysis was mainly executed at the steady state. As a consequence, it had limitations in providing further insights into the system when it is exposed to dynamic signals. To improve our understanding of the dynamic behavior of Nox1, we proposed in Chapter 4 a mathematical model focusing on the AngII-induced Nox1 dynamic activation in VSMCs (see pathway structure shown in Figure 4.1). This model incorporates not only the Nox1 activation-disassembly module proposed and discussed in Chapter 3, but also other signal relevant modules, such as AngII-induced PKC activation and the cSrc/EGFR/PI3K signaling cascade. Additionally, a simple module of ROS metabolism was added to relate the Nox1 system directly to available experimental observations.

Similar to the efforts in Chapter 3, Chapter 4 had to deal with many unknown parameters and scarce information. To solve this problem, we resorted again to a Monte-Carlo screening method, which was only minimally dependent on specific parameter values.

Three integrated model candidates were generated, and 48 parameter combinations in total were considered in Monte-Carlo simulation (see detailed description in section 4.3.2). Pertinent experimental information from the literature was collected and translated into a series of criteria, which were used to evaluate the performance of each Monte-Carlo sample. This criteria-driven analysis gave us intriguing results: In the first round of Monte Carlo simulation, Model Candidate 2 (MC2) was found to have better performance than the other two models (Table 4.13), indicating the effectiveness of using EGFR data as input. The results from the second round of Monte-Carlo simulation, which focused on MC2, further revealed the outstanding performance of three parameter combinations out of 16 (Table 4.13), and suggested two specific patterns for the relative magnitudes of investigated rate constants (see detailed discussion in section 4.4). These computationally inferred patterns clearly demonstrated the probably dominant disassembly pathway of Nox1 under different situations. Moreover, later simulations and comparisons of different data from cSrc helped us determine that a signaling pathway was missing from the model. This pathway is presumably associated with calcium. Although a Ca^{2+}-dependent and cSrc-independent EGFR trans-activation pathway has been documented in literature, its particular role in regulating EGFR dynamics, especially for its transient behavior, had not been emphasized by the scientific community. Finally, a known H_2O_2-induced positive feedback was added to complete the model integration. This integrated system well reproduces most observed system dynamics (see detailed discussion in section 4.4), which supports the structure and implementation of the proposed mathematical model.

5.2 Future Work

I have constructed and implemented two individual models for describing the relevant Nox1 system in ECs and VSMCs. Comparing their model structures, I find some common properties. For instance, both models target the Nox1 system, include some basic Nox1 components and interactions between components, and take various regulatory processes of Nox1 into account. At the same time, each model displays its own specific features. Therefore, these two models can learn from each other and may facilitate and expand each other's capabilities.

The model for Nox1-mediated mechanotransduction in ECs has a more "vertical" structure. It incorporates not only the shear stress-regulated BMP4 production located at the very top level of the pathway, but also the ROS-mediated NFκB signaling and subsequent monocyte adhesion located downstream. This vertical model structure enables us to connect the target system to its possible physiological functions. Specifically, any changes of Nox1 activity can be directly reflected in the level of bound monocyte molecules. As a result, it is easier for experimentalists and clinicians familiar with the importance of monocyte adhesion in the initiation and genesis of atherosclerosis to interpret the model within a familiar physiological context. However, detailed features with respect to Nox1 activation and disassembly processes are not described and explored in this model.

By contrast, the Nox1 model in VSMCs is particularly constructed in a "horizontal" way, which emphasizes the detailed interactions between Nox1 subunits, but pays less attention to the relevant physiological functions at the input and downstream levels. The analysis of this type of

model reveals more features of the Nox1 system itself, but does not directly link Nox1 to its physiological roles.

Thus, each type of model has its advantages and drawbacks with respect to its capabilities. One might consider the following aspects as direct extensions to the work presented here:

- Expand the Nox1 model in ECs "horizontally" by considering more Nox1 components and interactions between these components. Use the findings of potential Nox1 disassembly mechanisms in VMSCs to enrich the model structure in ECs.
- Expand the Nox1 model in VMSCs "vertically" by directly relating the Nox1-catalyzed ROS to down-stream signals and potential physiological functions regarding a specific disease. Since AngII is often used as a stimulus in this model, one could consider a connection between the Nox1 model in VSMCs and a specific disease like hypertension.
- Expand the Nox1 model in ECs by taking other Nox homologues into account and investigate the collaboration and cooperation between distinct Nox homologues if more biological information is available. In such an expansion, the issue of subunit competition and the identification of ROS sources between Nox1 and Nox2 need to be addressed.

Beyond the analysis of Nox1, the methodology used in this dissertation can be applied with relatively minor adaptations to investigations of other, similar biological systems. A particularly intriguing example is the Nox2 system, which is found in "professional" phagocytes and B lymphocytes, and is very similar to Nox1 in terms of molecular composition as well as its activation mechanisms. The superoxide generated by Nox2 serves as the starting material for the production of a vast assortment of reactive oxidants (including oxidized halogens, free radicals,

singlet oxygen, *etc.*), which are used by phagocytes to kill invading microorganisms. However, these oxidants can also cause a substantial collateral damage to nearby tissues. Thus, the production of these ROS has to be tightly regulated to ensure they are only generated when and where required. Therefore, the interesting question of how the Nox2 system and its subsequent ROS production are accurately regulated and controlled will require more detailed investigation. Using computational and modeling methods, as complimentary methods to experimental studies, can help to enhance our understanding of the Nox2 system in phagocytes by identifying and analyzing potential association and disassociation mechanisms as well as their interaction and cooperation. The combination of experiment and computational analysis might also help with the design of strategies to control Nox2 activity better.

Outside the Nox enzyme family, many biological systems exhibit properties and behaviors that are structurally similar to the assembly and disassembly of Nox1. For instance, other enzymes or complex proteins exist whose activation requires the assembly of multiple subunits and that can be triggered by different upstream signals in multiple steps. The computational and modeling methods used in this dissertation may be applied to these systems, where they could demonstrate the efficacy of their potential association and disassociation mechanisms and characterize how the system's performance is differentially regulated by different signals.

Moreover, the design principles that were discovered in this dissertation research may be applicable to other biological systems. For instance, with the simulation analysis in Chapter 3, I find that some subunits ($p47^{phox}$ and Rac1) are required to reside mainly in an inactive form under normal physiological conditions and that this arrangement is responsible for optimal system performance. Whether such an arrangement is a general rule for similar biological

systems that require signaling-based regulations is an interesting open question, and is therefore worthy of further investigation.

APPENDIX A

PARAMETER ESTIMATION AND SIMULATION SETTINGS IN SYSTEM ANALYSIS OF THE ROLE OF BMP4 IN ENDOTHELIAL INFLAMMATION

A.1 Parameter Estimation

Due to the paucity of available time-series and quantitative data, the rate constant and kinetic order parameter values (γ_i and g_i) were estimated in an *ad hoc* fashion as described in the Materials and Methods section. All constraints (both for kinetic orders and rate constants) derived from equations with two terms (see Eq. (2.3)) are presented in Table A.1.

Given these constraints and assigning a default value (such as 0.5 for substrate dependency or activation and -0.5 for inhibition) to one of the two relevant kinetic orders yields the value for the other one. This procedure requires knowledge of the ratio M_{iS_O} or M_{iS_L}. Either one of the ratios of experimental measurements to the control can be used for the computation. When both ratios are experimentally available, the ratio measured under OSS condition was used. The available ratios that were recalculated from experimental measurements are listed in Table A.2.

Once the kinetic orders are set, the rate constants are secondarily deduced with the constraint equations in a similar fashion. While these methods determine a good portion of the needed parameter values, other parameters require default assumptions, experience and additional efforts for fine tuning and validating, based on available biological observations.

Examples are the parameters in the system equations in Equation (2.3) that contain external inputs or more than two terms.

A.2 Simulation Settings

All simulations (with results displayed in Figure 2.2 to Figure 2.7 in the dissertation) use the same numerical sets of initial conditions (Table A.3) and parameter values (Table A.4), with the exception of parameters under investigation in a specific simulation, as described in the dissertation and the corresponding figure legends.

The signal of shear stress acting on the phosphorylation of $p47^{phox}$ is represented by an exponentially decaying function of the form

$$p = \begin{cases} \rho \cdot \exp(-\sigma \cdot (t - t_0)) + offset, & t \geq t_0 \\ 1, & t < t_0 \end{cases}, \tag{A.1}$$

where ρ represents the intensity of the phosphorylation signal after shear stress is added to the system at time $t=t_0$. The numerical values of ρ, σ and *offset* are listed in Table A.3.

Table A.1 Parameter constraint equations.

Kinetic Orders	Constraint Equations
g_2 and g_3	$\frac{g_2}{g_3} = \frac{\log(M_{2S_O})}{\log(M_{1S_O})} = \frac{\log(M_{2S_L})}{\log(M_{1S_L})}$
g_4 and g_7	$\frac{g_4}{g_7} = \frac{\log(M_{4S_O})}{\log(M_{3S_O})} = \frac{\log(M_{4S_L})}{\log(M_{3S_L})}$
g_9 and g_{10}	$\frac{g_9}{g_{10}} = \frac{\log(M_{5S_O})}{\log(M_{4S_O})} = \frac{\log(M_{5S_L})}{\log(M_{4S_L})}$
g_{12}, g_{13} and g_{14}	$\begin{cases} g_{14}\log(M_{6S_O}) = g_{12}\log(M_{7S_O}) + g_{13}\log(M_{8S_O}) \\ g_{14}\log(M_{6S_L}) = g_{12}\log(M_{7S_L}) + g_{13}\log(M_{8S_L}) \end{cases}$
g_{12}, g_{13} and g_{15}	$g_{15}\log(M_{9S_O}) = g_{12}\log(M_{7S_O}) + g_{13}\log(M_{8S_O})$ $g_{15}\log(M_{9S_L}) = g_{12}\log(M_{7S_L}) + g_{13}\log(M_{8S_L})$
g_{20} and g_{21}	$\frac{g_{20}}{g_{21}} = \frac{\log(M_{11S_O})}{\log(M_{10S_O})} = \frac{\log(M_{11S_L})}{\log(M_{10S_L})}$
g_{23} and g_{24}	$\frac{g_{23}}{g_{24}} = \frac{\log(M_{13S_O})}{\log(M_{11S_O})} = \frac{\log(M_{13S_L})}{\log(M_{11S_L})}$
g_{25} and g_{26}	$\frac{g_{25}}{g_{26}} = \frac{\log(M_{14S_O})}{\log(M_{13S_O})} = \frac{\log(M_{14S_L})}{\log(M_{13S_L})}$
Rate Constants	**Constraint Equations**
γ_3 and γ_4	$\frac{\gamma_3}{\gamma_4} = \frac{X_{2S_S}^{\ g_3}}{X_{1S_S}^{\ g_2}}$
γ_5 and γ_7	$\frac{\gamma_5}{\gamma_7} = \frac{X_{4S_S}^{\ g_7}}{X_{3S_S}^{\ g_4}}$
γ_9 and γ_{10}	$\frac{\gamma_9}{\gamma_{10}} = \frac{X_{5S_S}^{\ g_{10}}}{X_{4S_S}^{\ g_9}}$
γ_{13} and γ_{14}	$\frac{\gamma_{13}}{\gamma_{14}} = \frac{X_{7S_S}^{\ g_{12}} X_{8S_S}^{\ g_{13}}}{X_{6S_S}^{\ g_{14}}}$

γ_{13} and γ_{15}	$\frac{\gamma_{13}}{\gamma_{15}} = \frac{X_{7S_S}^{g_{12}} X_{8S_S}^{g_{13}}}{X_{9S_S}^{g_{15}}}$
γ_{19} and γ_{20}	$\frac{\gamma_{19}}{\gamma_{20}} = \frac{X_{11S_S}^{g_{21}}}{X_{10S_S}^{g_{20}}}$
γ_{23} and γ_{24}	$\frac{\gamma_{23}}{\gamma_{24}} = \frac{X_{13S_S}^{g_{24}}}{X_{11S_S}^{g_{23}}}$
γ_{25} and γ_{26}	$\frac{\gamma_{25}}{\gamma_{26}} = \frac{X_{14S_S}^{g_{26}}}{X_{13S_S}^{g_{25}}}$

$X_{iS_S}, X_{iS_O}, X_{iS_L}$ represent the steady state of variable X_i under Static control, OSS and ULS conditions.

$M_{iS_O} = \frac{X_{iS_O}}{X_{iS_S}}, M_{iS_L} = \frac{X_{iS_L}}{X_{iS_S}}$ represent the ratios of the steady-state values under OSS and ULS in relation to the static control condition.

Table A.2 Experimental ratios of steady-state values under OSS and LSS.

Variable Index (i)	M_{iS_O}	M_{iS_L}
1 (BMP4 mRNA)	1.5	0.3
2 (BMP4 precursor)	2	0.25
3 (mature BMP4)	1.2	0.15
5 (BMP4 antagonist)	1.25	0.1
6 (nox1 mRNA)	3.5	1.5
10 (superoxide)	1.7	0.3
11 (hydrogen peroxide)	2	-
13 ($NF\kappa B_{active}$)	3.4	-
14 (ICAM1)	3.0	-

The steady states for the above variables in static control are assumed to be 1 (100%). Listed numerical values are recalculated in relation to static control. ULS: 15 dyn/cm^2. OSS: ± 5 dyn/cm^2. Symbol "-" indicates that no experimental measurement are presently available.

Table A.3 Numerical values of initial conditions (ICs) and independent variables.

Dependent Variables	Numerical Value (IC)	Dependent Variables	Numerical Value (IC)	Independent Variable	Numerical Value
BMP4 mRNA	1	*nox1*	1	*S (ULS)*	5~15 dyn/cm^2
BMP4 precursor	1	*NADPH oxidase$_{active}$*	1	*S (OSS)*	± 5 dyn/cm^2
mature BMP4	1	*superoxide*	1	*S (STATIC)*	1
BMP4/R complex	1	*hydrogen peroxide*	1	Constant	Numerical Value
				C	1
				κ	1
BMP4 antagonist	1	*nitric oxide*	1	ρ	5
nox1 mRNA	1	*NFκB$_{active}$*	1	σ	0.1
p47$_{phoxphorylated}$	0.2	*ICAM1*	1	offset	1

Table A.4 Numerical values of rate constants, kinetic orders and time delays.

Kinetic Order	Numerical Value	Kinetic Order	Numerical Value	Rate Constant	Numerical Value	Rate Constant	Numerical Value
g_1	0.786	g_{17}	0.52	r_1	0.94	r_{17}	40
g_2	2.289	g_{18}	1	r_2	0.94	r_{18}	60
g_3	1.433	g_{19}	1	r_3	0.42	r_{19}	20
g_4	2.5	g_{20}	2	r_4	0.42	r_{20}	10
g_5	3.5	g_{21}	1.615	r_5	0.286	r_{21}	70
g_6	3.5	g_{22}	1	r_6	0.134	r_{22}	10
g_7	4.782	g_{23}	1	r_7	0.286	r_{23}	100
g_8	0.8	g_{24}	0.631	r_8	0.134	r_{24}	100
g_9	4.593	g_{25}	1	r_9	100	r_{25}	100
g_{10}	0.5	g_{26}	1.067	r_{10}	100	r_{26}	100
g_{11}	1	f_1(OSS)	0.2	r_{11}	0.6		
g_{12}	1	f_1(ULS)	-0.35	r_{12}	0.4	Time Delay	Numerical Value
g_{13}	1	f_1(STATIC)	0	r_{13}	2	τ_1	10h
g_{14}	0.8	f_2(OSS)	0.72	r_{14}	0.4	τ_2	11h
g_{15}	1	f_2(ULS)	-2	r_{15}	0.4	τ_3	0.1h
g_{16}	1	f_2(STATIC)	0	r_{16}	40	τ_4	0.1h

APPENDIX B

SUPPLEMENTARY INFORMATION OF FUNCTION AND DESIGN OF THE NOX1 ACTIVATION-DEACTIVATION SYSTEM IN VASCULAR SMOOTH MUSCLE CELLS

B.1 Stoichiometric Matrix

The matrix N in Eq. (3.1) is explicitly given as follows:

$$N_{8\times16} = \begin{bmatrix} 1 & -1 & -1 & -1 & 0 & 0 & 0 & 0 & 0 & 0 & 0 & 0 & 0 & -1 & 0 & 0 \\ -1 & 1 & 1 & 1 & 0 & 0 & 0 & 0 & 0 & 0 & 0 & 0 & 1 & 0 & 0 & 0 \\ 0 & 0 & 1 & 0 & -1 & 1 & 0 & 0 & 0 & 0 & 1 & 0 & 0 & 0 & 0 & 0 \\ -1 & 1 & 0 & 1 & 1 & -1 & 0 & 0 & 0 & 0 & 0 & 0 & 0 & 0 & 0 & 0 \\ 0 & 0 & 0 & 1 & 0 & 0 & -1 & 1 & 0 & 0 & 0 & 1 & 0 & 0 & 0 & 0 \\ -1 & 1 & 1 & 0 & 0 & 0 & 1 & -1 & 0 & 0 & 0 & 0 & 0 & 0 & 0 & 0 \\ -1 & 0 & 1 & 1 & 0 & 0 & 0 & 0 & -1 & 1 & 0 & 0 & & 0 & 1 & 0 \\ 0 & 1 & 0 & 0 & 0 & 0 & 0 & 0 & 1 & -1 & 0 & 0 & 0 & 0 & 0 & -1 \end{bmatrix}$$

B.2 Input Signal Vectors for the Assessment of Nox1 Disassembly (First Criterion)

The input signal vector ([S_1 S_2 S_3]) is represented by the numerical values listed in Table B.1.

Table B.1 Numerical values of input signals under different conditions.

Experimental Condition	S_1 signal added	S_2 signal added	S_3 signal added	S_1& S_2 signals added
Control	[1 1 1]	[1 1 1]	[1 1 1]	[1 1 1]
Stimulated	[10 1 1]	[1 10 1]	[1 1 10]	[10 10 1]

B.3 Assessment of Nox1 Disassembly Mechanisms According to the Second Criterion

Numerical values of initial conditions were assigned according to experimental observations (in consultation with experimentalists); they are summarized in Table B.2. The experimental treatment with angiotensin II (AngII) is translated in to a combination of input signals S_1 and S_2, and the treatment with 12-myristate-13-acetate (PMA) is translated in input signal S_1. Considering realistic magnitudes with which AngII and PMA can up-regulate these signals, the numerical values of S_1 and S_2 are conservatively considered as ~ 2 fold over control level (as "1") for AngII, and the numerical value of S_1 is considered as ~4 fold over control level for PMA. Therefore, the input signals of AngII and PMA treatments are respectively represented by [2 2 1] and [4 1 1] in this set of simulations.

The second criterion consists of a combination of three conditions. They are separately implemented in simulations as defined below:

(1) The first criterion, namely Nox1 protein conservation after 4 hours of AngII treatment, is implemented as

$$\left| \frac{X_1(t_{4hour}) + X_2(t_{4hour})}{X_1(t_0) + X_2(t_0)} - 1 \right| < 0.05.$$

(2) The second criterion of a (quasi-) steady state and up-regulated X_1 after 30 minutes of AngII treatment is implemented as:

(i) $norm(\frac{dX}{dt}|_{t=30\,\min}) < 0.1$

(ii) $\frac{X_1(t_{30\,\min})}{X_1(t_0)} - 1 > 0.1.$

(3) The third criterion of up-regulated X_1 under PMA treatment is implemented as $\frac{X_1(t_{30\,\min})}{X_1(t_0)} - 1 > 0.1.$

Table B.2 Steady-state values of initial conditions.

Variable	Steady-State Value
X_1	10^3 (molecules/cell)
X_2	$2.4 \cdot 10^4$ (molecules/cell)
X_3	$5.4 \cdot 10^3$ (molecules/cell)
X_4	$1.2 \cdot 10^3$ (molecules/cell)
X_5	$6 \cdot 10^3$ (molecules/cell)
X_6	$1.2 \cdot 10^3$ (molecules/cell)
X_7	$5.4 \cdot 10^3$ (molecules/cell)
X_8	$0.6 \cdot 10^3$ (molecules/cell)

B.4 A Thought Experiment Illustrating Responses of the Nox1 System to Persistent Signals of Type S1 under Three Extreme Scenarios

In order to illustrate the distinct roles of the three disassembly and recycling pathways in affecting the responses of the Nox1 system, we perform the following thought experiment. Suppose the Nox1 system is exposed to a persistent signal S_1, and only one recycling pathway is available, as depicted with modules 1, 2 and 3 in Figure 3.5 of the Text. Specifically, in scenario 1, only the recycling pathway via phosphorylation of NoxA1 is available (marked as f_2 in Figure 3.1 of the Text). In scenario 2, only the recycling pathway via dephosphorylation of $p47^{phox}$ (marked as f_3 in Figure 3.1) exists. In scenario 3, only the recycling pathway via deactivation of $Rac1_{GTP}$ (marked as f_4 in Figure 3.1) is present. The system's responses to S_1 are evaluated with respect to the new steady state of X_1 in one scenario compared to that in another scenario.

In all cases, the simulation settings are the same in terms of other parameter values and initial conditions for each round of simulation. Moreover, to reduce other possible discrepancies induced by different simulation settings, parameters and initial conditions are generated through uniform sampling within a relatively large range. For different rounds of simulations, parameters

are randomly sampled as follows: The independent rate constants γ_i are sampled from $U(0, 100)$, for $i = 6, 8, 10, 16$. Under different scenarios, γ_2 (or γ_3 or γ_4) is respectively set at 10. The steady states of dependent variables in unstimulated state are set as: $X_1 = 10$, $X_2 = 100$, $X_i \sim U(1, 99)$ for $i = 3, 4, \ldots 8$ with the assumption that X_3 and X_4, X_5 and X_6, X_7 and X_8, respectively, sum to 100. The overall sampling size is 10,000. All simulations were implemented in MATLABR2010a.

Figure B.3 shows the results. They consist of distributions resulting from Monte-Carlo simulations, where each entry represents one ratio between the steady-state values of X_1 in two scenarios. The top panel shows the ratios under scenario 2 over scenario 1. These ratios are distributed strictly to the right side of zero (in $\log_{10}$ space), demonstrating that the new steady state of X_1 in scenario 2 is always as high or higher than the one in scenario 1, no matter what the simulation setting is. Indeed, the ratios of new steady state of X_1 in scenario 2 differ up to ~2.5 fold ($10^{0.4} \approx 2.5$) over the corresponding steady state in scenario 1.

A similar result holds when we compare the ratios of new steady-state values of X_1 under scenario 2 versus scenario 3 (bottom panel): Scenario 2 always leads to as strong or stronger responses than scenario 3. Combined, the results in top and bottom panels suggest that, in the presence of a persistent signal S_1, recycling via dephosphorylation of $p47^{phox}$ (scenario 2) allows stronger responses than the other two recycling mechanisms (scenario 1 and 3). Between scenarios 1 and 3, the effectiveness of response is not much different (center panel of Figure B.3).

The example demonstrates that the effectiveness of a particular recycling pathway is interrelated with the demands of the system. For the specific case of a persistent signal S_1, which was studied here, the most efficient recycling mechanism appears to be the dephosphorylation of $p47^{phox}$ (scenario 2). This deduction becomes even stronger when the cell has the option of

selecting (or discarding) certain combinations of numerical settings for the rate constants, which in the results in Figure B.3 are based on random sampling. For persistent signals of type S_2, S_3, combinations of these signals, or other types of signal trains, the optimal recycling strategy is certainly different. Thus, under the assumption that the cell optimizes responses, one should expect that the cell has developed regulatory mechanisms that control the distribution of recycling fluxes, depending on signaling demands.

B.5 Supplementary Figures

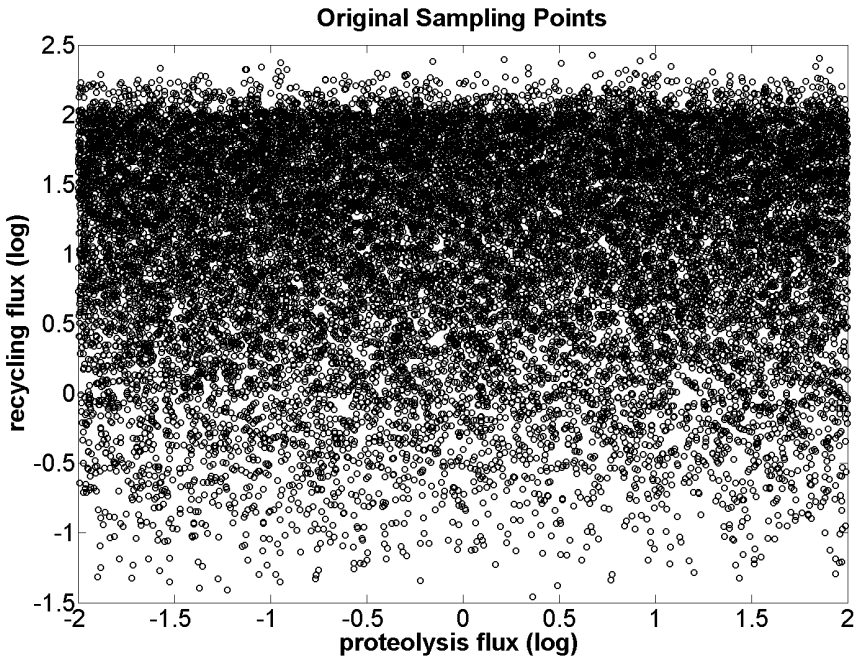

Figure B.1 Original result of Monte Carlo simulation with criterion of the second type.
Sample size: 20,000 points. Values of all independent fluxes were sampled from $U(0.01, 100)$. See text for further information.

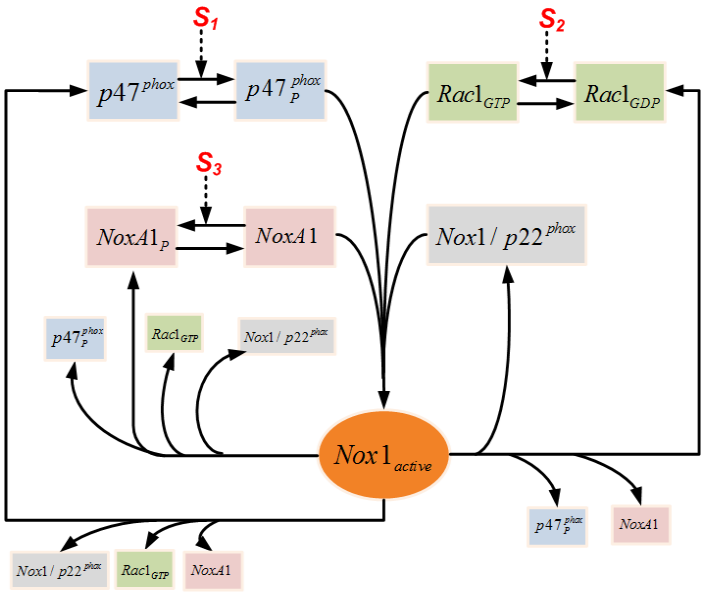

Figure B.2 Schematic representation of closed Nox1 system.

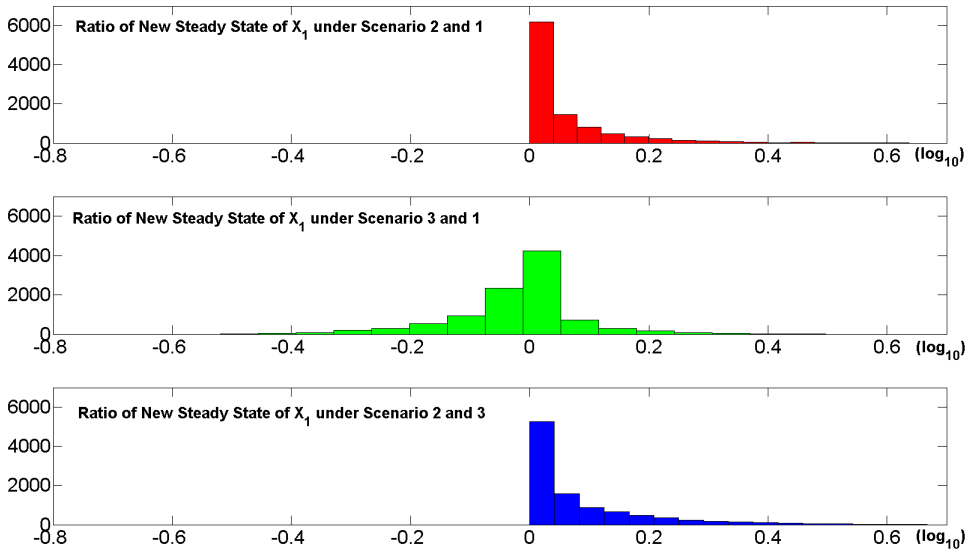

Figure B.3 Simulated responses of the Nox1 system to persistent signals of type S_1 under three extreme recycling mechanisms.

Scenario 1: Only the recycling pathway associated with phosphorylation of NoxA1 (marked as f_2 in Figure 3.1) exists; Scenario 2: Only the recycling pathway associated with dephosphorylation of $p47^{phox}$ (marked as f_3) exists; Scenario 3: Only the recycling pathway associated with deactivation of $Rac1_{GTP}$ (marked as f_4) exists. The horizontal axis indicates the ratio, in $\log_{10}$ space, of new steady-state values of X_1 under two different scenarios. For instance, the top panel shows the ratios of X_1 values in Scenario 2 in comparison to Scenario 1 in 10,000 Monte-Carlo simulations. See text for further details.

APPENDIX C

SUPPLEMENTARY INFORMATION OF SYSTEM ANALYSIS OF THE DYNAMICS OF ANGIOTENSIN II-INDUCED NOX1 ACTIVATION IN VSMCS

C.1 Stoichiometric Matrix

The stoichiometric matrix N_i, i = 1, 2, 3 in Eqs. (4.7), (4.8) and (4.9) are respectively given as follows:

$$N_1 = \begin{bmatrix}
1 & -1 & -1 & -1 & 0 & 0 & 0 & 0 & 0 & 0 & 0 & 0 & 0 & -1 & 0 & 0 & 0 & 0 & 0 & 0 & 0 & 0 & 0 & 0 \\
-1 & 1 & 1 & 1 & 0 & 0 & 0 & 0 & 0 & 0 & 0 & 0 & 1 & 0 & 0 & 0 & 0 & 0 & 0 & 0 & 0 & 0 & 0 & 0 \\
0 & 0 & 1 & 0 & -1 & 1 & 0 & 0 & 0 & 0 & 1 & 0 & 0 & 0 & 0 & 0 & 0 & 0 & 0 & 0 & 0 & 0 & 0 & 0 \\
-1 & 1 & 0 & 1 & 1 & -1 & 0 & 0 & 0 & 0 & 0 & 0 & 0 & 0 & 0 & 0 & 0 & 0 & 0 & 0 & 0 & 0 & 0 & 0 \\
0 & 0 & 0 & 1 & 0 & 0 & -1 & 1 & 0 & 0 & 0 & 1 & 0 & 0 & 0 & 0 & 0 & 0 & 0 & 0 & 0 & 0 & 0 & 0 \\
-1 & 1 & 1 & 0 & 0 & 0 & 1 & -1 & 0 & 0 & 0 & 0 & 0 & 0 & 0 & 0 & 0 & 0 & 0 & 0 & 0 & 0 & 0 & 0 \\
-1 & 0 & 1 & 1 & 0 & 0 & 0 & 0 & -1 & 1 & 0 & 0 & 0 & 0 & 1 & 0 & 0 & 0 & 0 & 0 & 0 & 0 & 0 & 0 \\
0 & 1 & 0 & 0 & 0 & 0 & 0 & 0 & 1 & -1 & 0 & 0 & 0 & 0 & 0 & -1 & 0 & 0 & 0 & 0 & 0 & 0 & 0 & 0 \\
0 & 0 & 0 & 0 & 0 & 0 & 0 & 0 & 0 & 0 & 0 & 0 & 0 & 0 & 0 & 0 & 1 & 1 & -1 & -1 & 0 & 0 & 0 & 0 \\
0 & 0 & 0 & 0 & 0 & 0 & 0 & 0 & 0 & 0 & 0 & 0 & 0 & 0 & 0 & 0 & 0 & 0 & 0.5 & 0 & 1 & -1 & 0 & 0 \\
0 & 0 & 0 & 0 & 0 & 0 & 0 & 0 & 0 & 0 & 0 & 0 & 0 & 0 & 0 & 0 & 0 & 0 & 0 & 0 & 0 & 0 & 1 & -1
\end{bmatrix}$$

$$N_2 = \begin{bmatrix}
1 & -1 & -1 & -1 & 0 & 0 & 0 & 0 & 0 & 0 & 0 & 0 & 0 & -1 & 0 & 0 & 0 & 0 & 0 & 0 & 0 & 0 & 0 & 0 & 0 & 0 \\
-1 & 1 & 1 & 1 & 0 & 0 & 0 & 0 & 0 & 0 & 0 & 0 & 1 & 0 & 0 & 0 & 0 & 0 & 0 & 0 & 0 & 0 & 0 & 0 & 0 & 0 \\
0 & 0 & 1 & 0 & -1 & 1 & 0 & 0 & 0 & 0 & 1 & 0 & 0 & 0 & 0 & 0 & 0 & 0 & 0 & 0 & 0 & 0 & 0 & 0 & 0 & 0 \\
-1 & 1 & 0 & 1 & 1 & -1 & 0 & 0 & 0 & 0 & 0 & 0 & 0 & 0 & 0 & 0 & 0 & 0 & 0 & 0 & 0 & 0 & 0 & 0 & 0 & 0 \\
0 & 0 & 0 & 1 & 0 & 0 & -1 & 1 & 0 & 0 & 0 & 1 & 0 & 0 & 0 & 0 & 0 & 0 & 0 & 0 & 0 & 0 & 0 & 0 & 0 & 0 \\
-1 & 1 & 1 & 0 & 0 & 0 & 1 & -1 & 0 & 0 & 0 & 0 & 0 & 0 & 0 & 0 & 0 & 0 & 0 & 0 & 0 & 0 & 0 & 0 & 0 & 0 \\
-1 & 0 & 1 & 1 & 0 & 0 & 0 & 0 & -1 & 1 & 0 & 0 & 0 & 0 & 1 & 0 & 0 & 0 & 0 & 0 & 0 & 0 & 0 & 0 & 0 & 0 \\
0 & 1 & 0 & 0 & 0 & 0 & 0 & 0 & 1 & -1 & 0 & 0 & 0 & 0 & 0 & -1 & 0 & 0 & 0 & 0 & 0 & 0 & 0 & 0 & 0 & 0 \\
0 & 0 & 0 & 0 & 0 & 0 & 0 & 0 & 0 & 0 & 0 & 0 & 0 & 0 & 0 & 0 & 1 & 1 & -1 & -1 & 0 & 0 & 0 & 0 & 0 & 0 \\
0 & 0 & 0 & 0 & 0 & 0 & 0 & 0 & 0 & 0 & 0 & 0 & 0 & 0 & 0 & 0 & 0 & 0 & 0.5 & 0 & 1 & -1 & 0 & 0 & 0 & 0 \\
0 & 0 & 0 & 0 & 0 & 0 & 0 & 0 & 0 & 0 & 0 & 0 & 0 & 0 & 0 & 0 & 0 & 0 & 0 & 0 & 0 & 0 & 1 & -1 & 0 & 0 \\
0 & 0 & 0 & 0 & 0 & 0 & 0 & 0 & 0 & 0 & 0 & 0 & 0 & 0 & 0 & 0 & 0 & 0 & 0 & 0 & 0 & 0 & 0 & 1 & 1 & -1
\end{bmatrix}$$

$$N_3 = \begin{bmatrix} 1 & -1 & 0 & -1 & 0 & -1 & -1 & 0 & 0 & 0 & 0 & 0 & 0 \\ -1 & 1 & 0 & 1 & 0 & 1 & 0 & 1 & 0 & 0 & 0 & 0 & 0 \\ -1 & 1 & 1 & 0 & 0 & 1 & 1 & 0 & 0 & 0 & 0 & 0 & 0 \\ -1 & 1 & 0 & 1 & 1 & 0 & 1 & 0 & 0 & 0 & 0 & 0 & 0 \\ 0 & 0 & -1 & 1 & 0 & 0 & 0 & 0 & 0 & 0 & 0 & 0 & 0 \\ 0 & 0 & 1 & -1 & 0 & 0 & 0 & 0 & 0 & 0 & 0 & 0 & 0 \\ 0 & 0 & 0 & 0 & -1 & 1 & 0 & 0 & 0 & 0 & 0 & 0 & 0 \\ 0 & 0 & 0 & 0 & 1 & -1 & 0 & 0 & 0 & 0 & 0 & 0 & 0 \\ 0 & 0 & 0 & 0 & 0 & 0 & -1 & 1 & 0 & 0 & 0 & 0 & 0 \\ 0 & 0 & 0 & 0 & 0 & 0 & 1 & -1 & 0 & 0 & 0 & 0 & 0 \\ 0 & 0 & 1 & 0 & 0 & 0 & 0 & 0 & 0 & 0 & 0 & 0 & 0 \\ 0 & 0 & 0 & 0 & 1 & 0 & 0 & 0 & 0 & 0 & 0 & 0 & 0 \\ 0 & 1 & 0 & 0 & 0 & 0 & 0 & 0 & 0 & 0 & 0 & 0 & 0 \\ -1 & 0 & 0 & 0 & 0 & 0 & 0 & 0 & 0 & 0 & 0 & 0 & 0 \\ 0 & 0 & 0 & 0 & 0 & 0 & 1 & 0 & 0 & 0 & 0 & 0 & 0 \\ 0 & 0 & 0 & 0 & 0 & 0 & 0 & -1 & 0 & 0 & 0 & 0 & 0 \\ 0 & 0 & 0 & 0 & 0 & 0 & 0 & 0 & 1 & 0 & 0 & 0 & 0 \\ 0 & 0 & 0 & 0 & 0 & 0 & 0 & 0 & 1 & 0 & 0 & 0 & 0 \\ 0 & 0 & 0 & 0 & 0 & 0 & 0 & 0 & -1 & 0.5 & 0 & 0 & 0 \\ 0 & 0 & 0 & 0 & 0 & 0 & 0 & 0 & -1 & 0 & 0 & 0 & 0 \\ 0 & 0 & 0 & 0 & 0 & 0 & 0 & 0 & 0 & 1 & 0 & 0 & 0 \\ 0 & 0 & 0 & 0 & 0 & 0 & 0 & 0 & 0 & -1 & 0 & 0 & 0 \\ 0 & 0 & 0 & 0 & 0 & 0 & 0 & 0 & 0 & 0 & 1 & 0 & 0 \\ 0 & 0 & 0 & 0 & 0 & 0 & 0 & 0 & 0 & 0 & -1 & 0 & 0 \\ 0 & 0 & 0 & 0 & 0 & 0 & 0 & 0 & 0 & 0 & 0 & 1 & 0 \\ 0 & 0 & 0 & 0 & 0 & 0 & 0 & 0 & 0 & 0 & 0 & -1 & 0 \\ 0 & 0 & 0 & 0 & 0 & 0 & 0 & 0 & 0 & 0 & 0 & 0 & 1 \\ 0 & 0 & 0 & 0 & 0 & 0 & 0 & 0 & 0 & 0 & 0 & 0 & -1 \end{bmatrix}^T$$

C.2 Dynamic Simulations with the Integrated Model for 12 Selected Samples

Various scenarios, including unstimulated conditions, AngII (100nM) treatment,a Nox1 knock-down experiment, a Nox4 knock-down experiment, treatments with AG1248, PP1, PMA, GF 10923X, and AdRacN17, are simulated for Model Candidate 2 (MC2). Totally, there are 12 sets of simulation results, which are respectively displayed in Figure C.1 to Figure C.12.

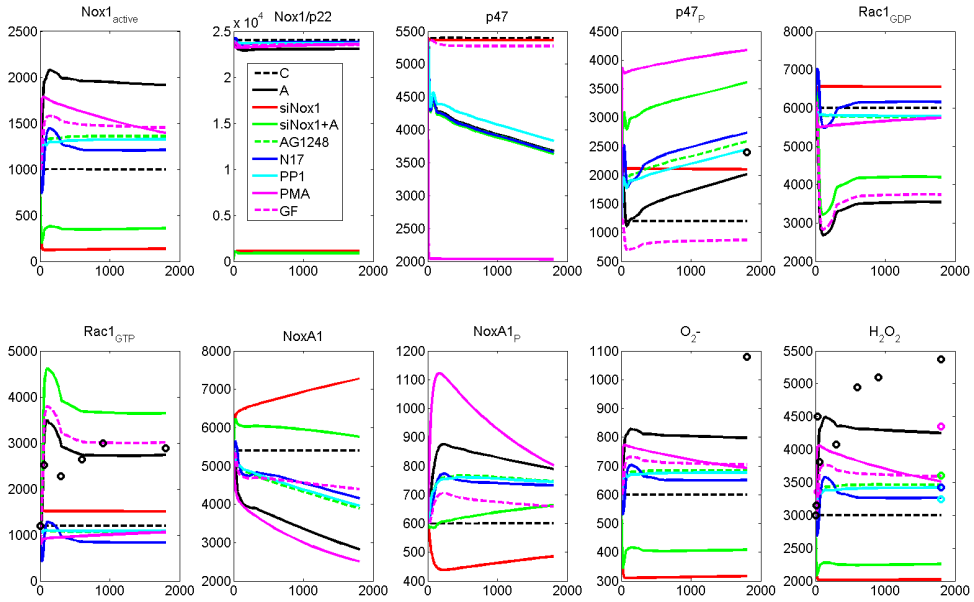

Figure C.1 Dynamic simulations of MC2 by using parameter values in selected sample set 1.

The units of the *x*-axis and *y*-axis are respectively seconds and # molecules/cell. Colored circles indicate experimental measurements under different scenarios: dark circles-AngII treatment; pink circle-AngII+GF 10923X; green circle-AngII+AG1248; light blue circle-AngII+PP1; dark blue circle-AngII+AdRacN17. Colored lines are simulated results under different scenarios: dashed dark line-control condition; solid dark line-AngII treatment; solid red line-Nox1 knocked-down condition; solid green line-Nox1 knocked-down condition with AngII treatment; dashed green line-AngII+AG1248; solid dark blue line-AngII+AdRacN17; solid light blue line-AngII+PP1; solid pink line-PMA treatment; dashed pink line-AngII+GF 10923X. (The indications of these symbols are the same for Figure C.1 to Figure C.12). The parameter values used in this simulation are: $Para_{in}$ = [0.0052 0.0879 0.0196 0.0830 0.0930 0.0012 0.0037 0.3393 0.7817 1.3660 0.0749 0.6380 0.7274 1.8914 6] (see detailed description of $Para_{in}$ in Table 4.10).

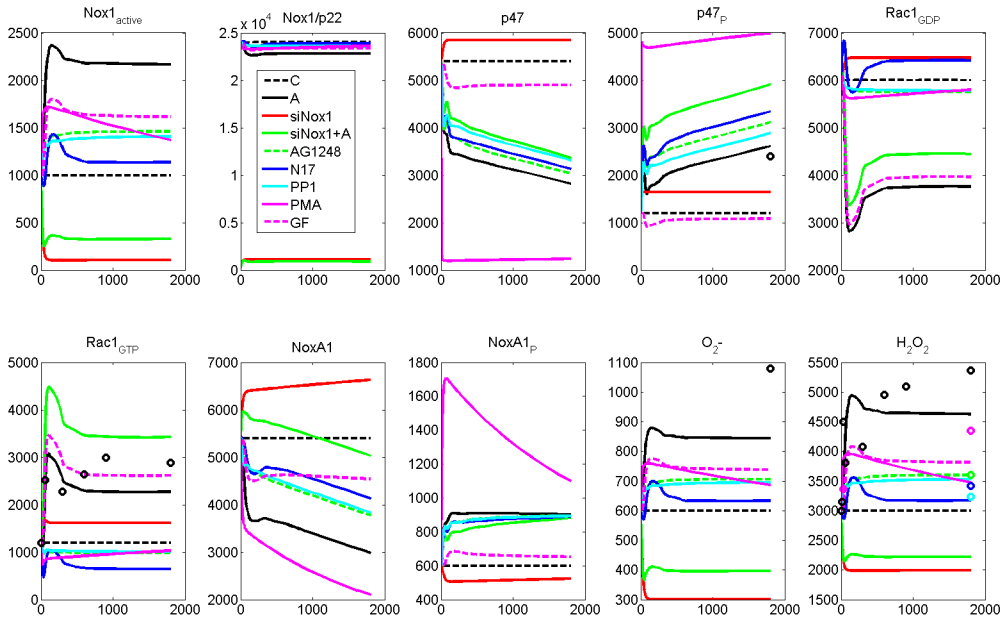

Figure C.2 Dynamic simulations of MC2 by using parameter values in selected sample set 2.

The parameter values used in this simulation are: $Para_{in}$ = [0.0093 0.0286 0.0130 0.0807 0.0395 0.0037 0.0018 0.5067 0.4351 0.9721 0.1349 0.6377 1.1940 1.7580 7]. See Figure C1 for further details.

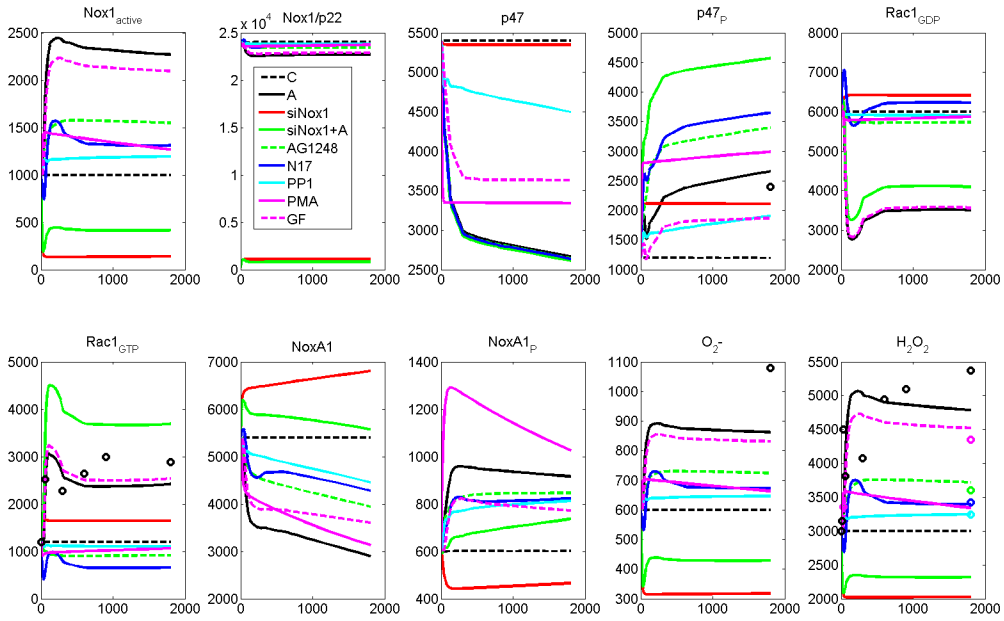

Figure C.3 Dynamic simulations of MC2 by using parameter values in selected sample set 3.

The parameter values used in this simulation are: $Para_{in}$ = [0.0075 0.0629 0.0183 0.0580 0.0471 0.0018 0.0016 0.8242 5.9634 0.8130 0.8408 0.9224 0.9061 1.3807 1.7573 5]. See Figure C1 for further details.

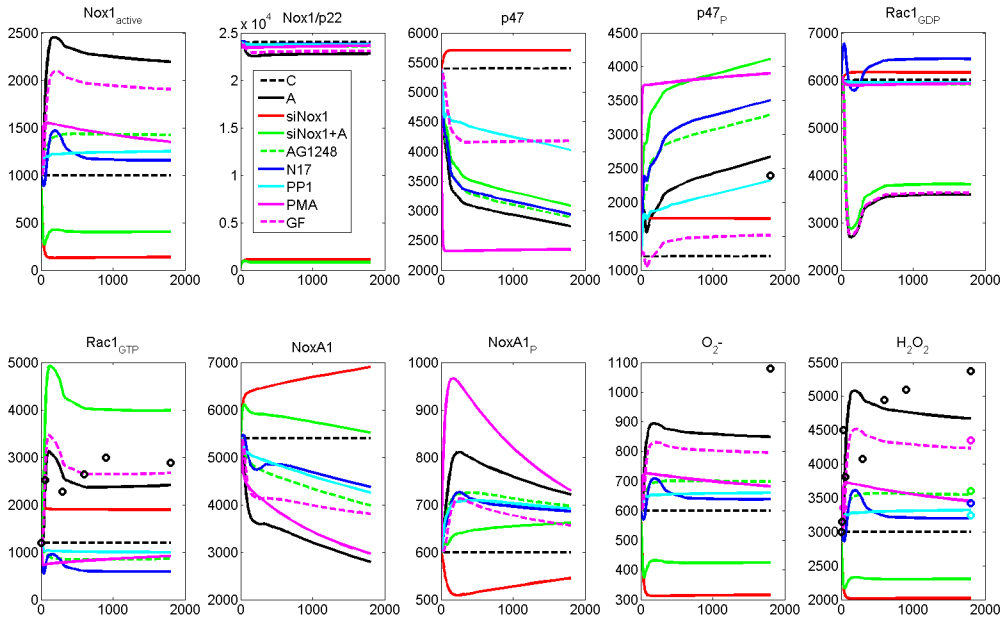

Figure C.4 Dynamic simulations of MC2 by using parameter values in selected sample set 4.

The parameter values used in this simulation are: $Para_{in}$ = [0.0038 0.0235 0.0177 0.0439 0.0238 0.0015 0.0046 2.8345 0.1232 1.3067 0.5391 0.6339 0.5274 1.4802 1.9632 9]. See Figure C1 for further details.

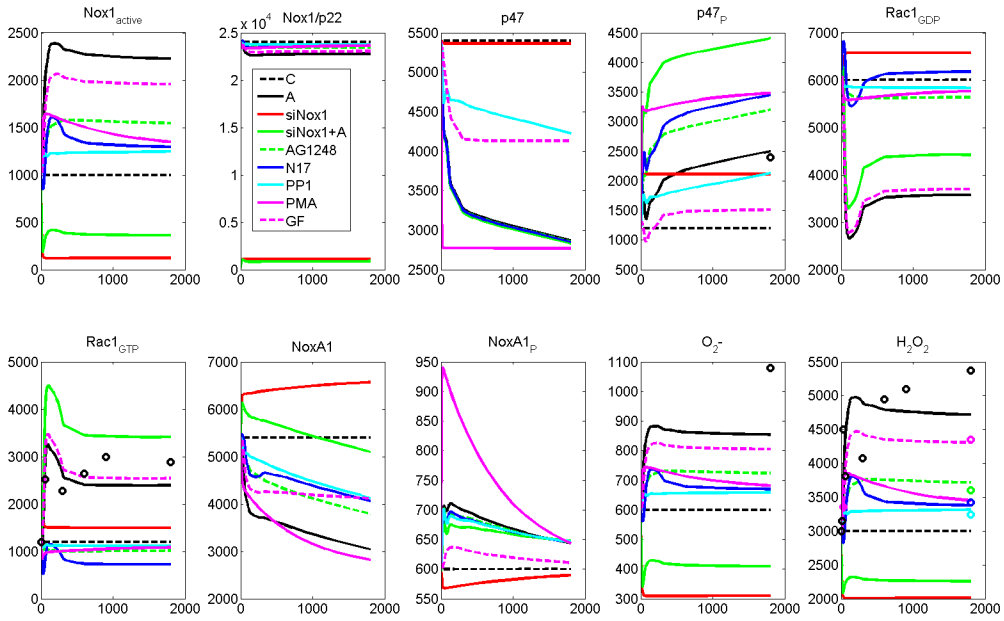

Figure C.5 Dynamic simulations of MC2 by using parameter values in selected sample set 5.

The parameter values used in this simulation are: $Para_{in}$ = [0.0235 0.0958 0.0109 0.0904 0.0577 0.0160 0.0083 0.4650 0.6545 1.0419 0.6188 0.5254 0.4659 1.7823 1.8502 10]. See Figure C1 for further details.

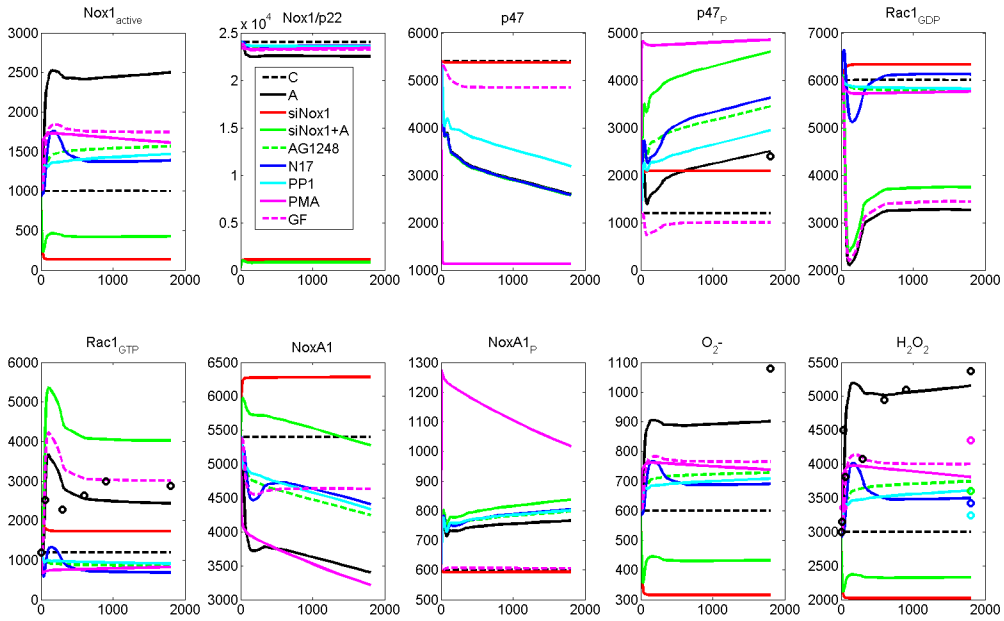

Figure C.6 Dynamic simulations of MC2 by using parameter values in selected sample set 6.

The parameter values used in this simulation are: $Para_{in}$ = [0.0362 0.0379 0.0123 0.0365 0.0243 0.0327 0.0012 0.5980 6.6175 1.8979 0.2865 0.6796 0.7615 1.7568 1.6002 10]. See Figure C1 for further details.

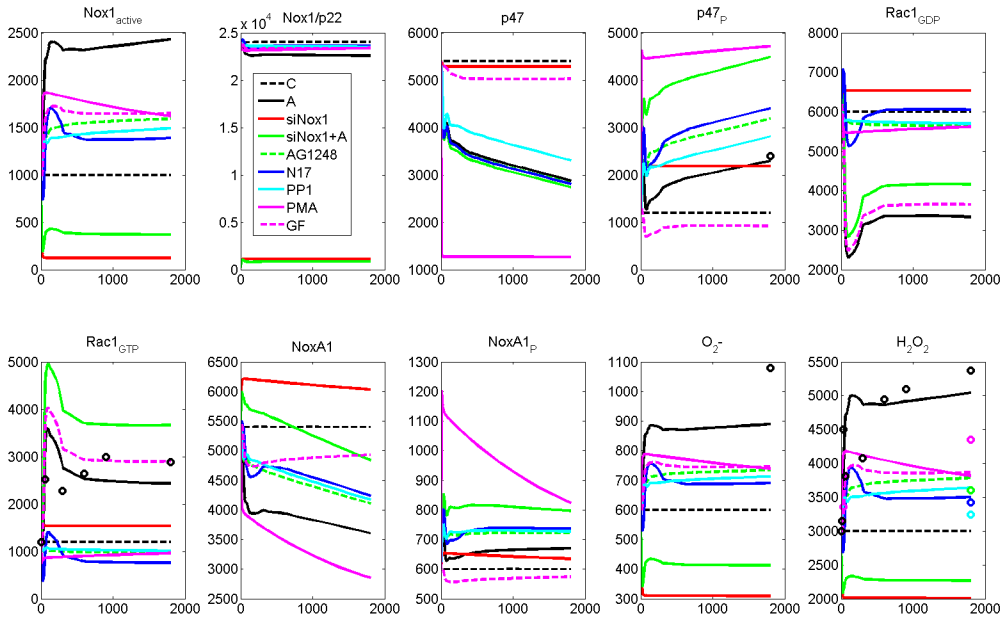

Figure C.7 Dynamic simulations of MC2 by using parameter values in selected sample set 7.

The parameter values used in this simulation are: $Para_{in}$ = [0.0176 0.0908 0.0232 0.0769 0.0972 0.0512 0.0027 1.6793 1.5401 1.7832 0.2196 0.7376 0.6810 1.5133 1.6543 10]. See Figure C1 for further details.

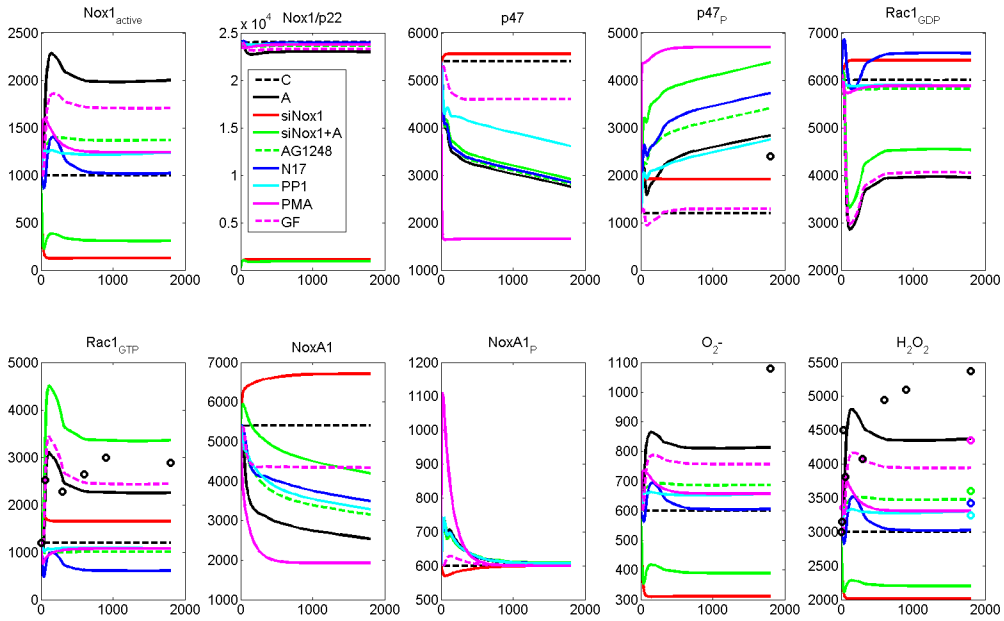

Figure C.8 Dynamic simulations of MC2 by using parameter values in selected sample set 8.

The parameter values used in this simulation are as the following: $Para_{in}$ = [0.0153 0.0344 0.0122 0.0456 0.0314 0.0102 0.0414 0.9806 2.5609 1.6142 0.3707 0.7949 0.6931 1.5375 1.2294 8]. See Figure C1 for further details.

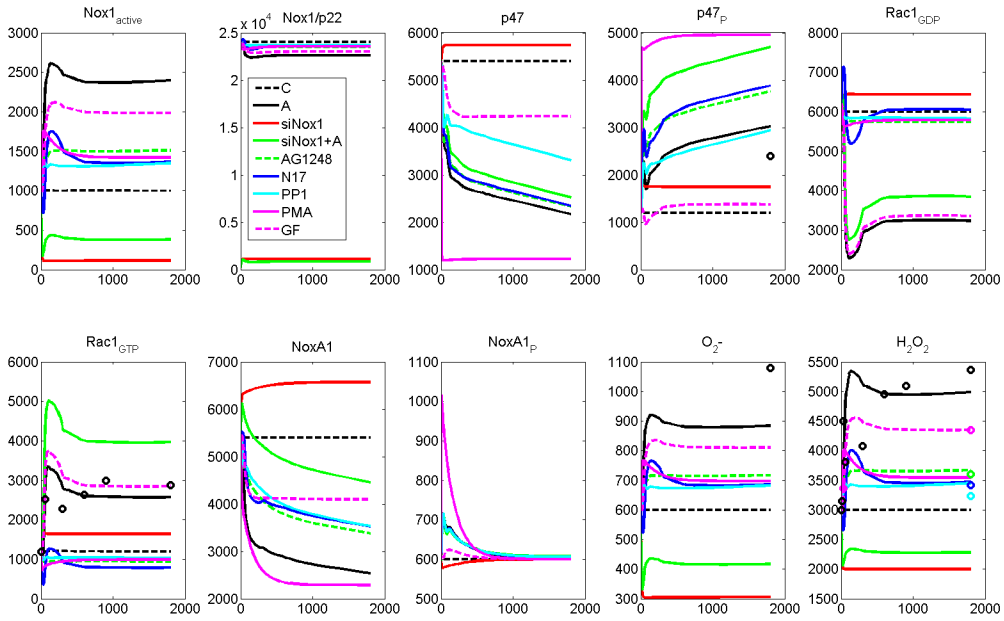

Figure C.9 Dynamic simulations of MC2 by using parameter values in selected sample set 9.

The parameter values used in this simulation are as the following: $Para_{in}$ = [0.0924 0.0373 0.0282 0.0747 0.0761 0.0698 0.0388 0.4009 2.4353 1.9377 0.4880 0.8860 0.5403 1.2936 1.8561 8]. See Figure C1 for further details.

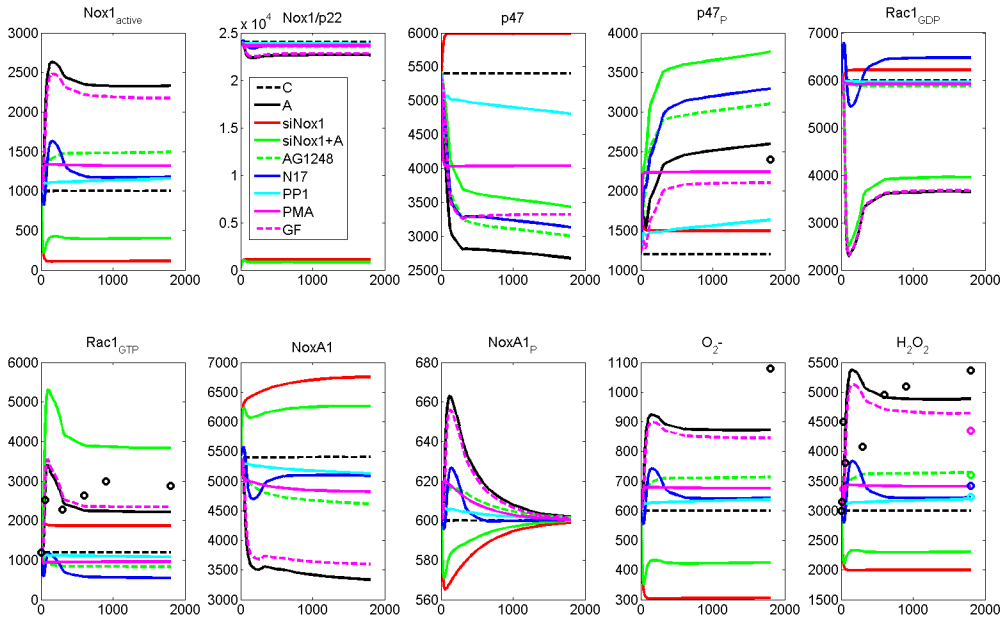

Figure C.10 Dynamic simulations of MC2 by using parameter values in selected sample set 10.

The parameter values used in this simulation are: $Para_{in}$ = [0.0296 0.0128 0.0179 0.0769 0.0264 0.0191 0.0245 3.7825 0.4957 0.6346 0.9127 0.6552 0.0139 1.9572 1.2572 10]. See Figure C1 for further details.

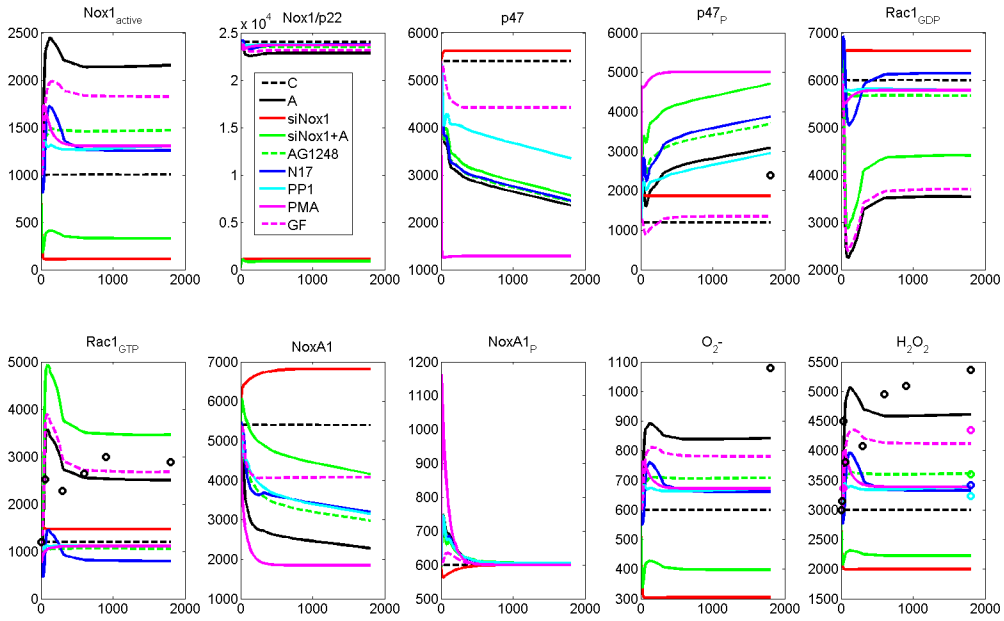

Figure C.11 Dynamic simulations of MC2 by using parameter values in selected sample set 11.

The parameter values used in this simulation are: $Para_{in}$ = [0.0741 0.0445 0.0107 0.0668 0.0748 0.0463 0.0661 9.7272 0.1711 1.8628 0.4397 0.6193 0.7049 1.9886 1.3945 10]. See Figure C1 for further details.

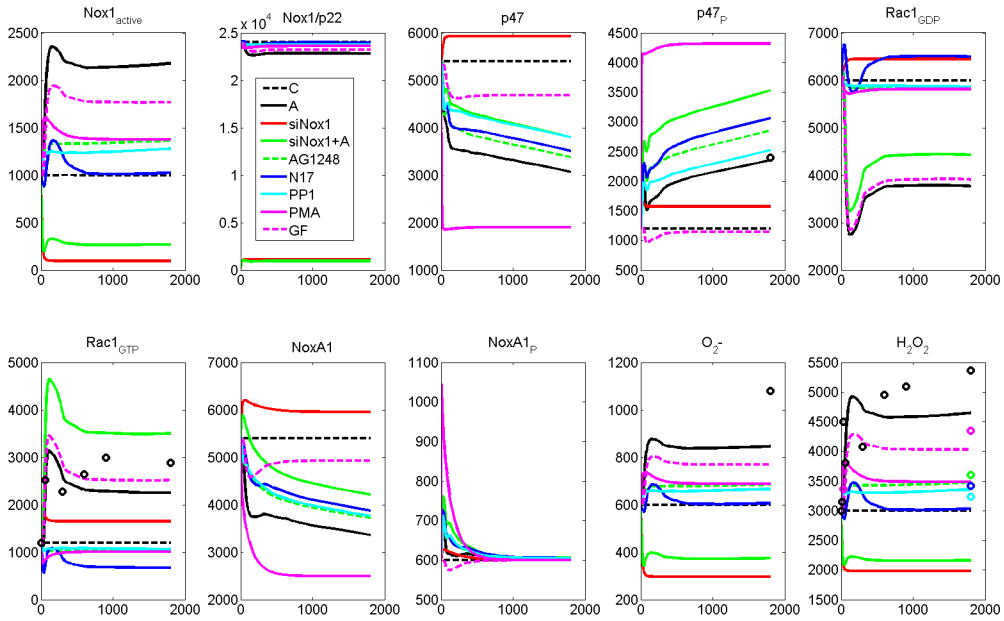

Figure C.12 Dynamic simulations of MC2 by using parameter values in selected sample set 12.
The parameter values used in this simulation are: $Para_{in}$ = [0.0452 0.0163 0.0100 0.0643 0.0270 0.0737 0.0455 0.4358 0.1940 1.5931 0.1986 0.7182 0.5257 1.7633 1.3120 7]. See Figure C1 for further details.

C.3 cSrc-Dependent EGFR Activation Module

The pathway structure (shown in Figure 4.15 (a)) is mathematically expressed in the GMA format shown in Eq. (C.1):

$$d(EGFR^*)/dt = \alpha \cdot (T_{EGFR} - EGFR^*) \cdot (cSrc^*)^g - \beta \cdot EGFR^*, \qquad \text{(C.1)}$$

where the symbols with * indicate active signaling molecules, whose values are assumed to be at "1" in unstimulated control condition. α and β are rate constants with non-negative values, and g is the real-valued kinetic order. T_{EGFR} represents the total amount of EGFR molecules in both active and inactive forms.

Under unstimulated control conditions, the whole Nox1 system dynamically operates at a stable state, and so does this cSrc-dependent EGFR signaling cascade. It requires not only the level of active EGFR stably staying at "1", but also the change of active EGFR over time

(represented by its derivative) equalling zero. Thus, this requirement adds one linear constraint to Eq. (C.1) and further simplifies it into Eq. (C.2) as follows:

$$d(EGFR^*)/dt = \alpha \cdot (T_{EGFR} - EGFR^*) \cdot (cSrc^*)^g - \alpha \cdot (T_{EGFR} - 1) \cdot EGFR^*, \quad \text{(C.2)}$$

Ultimately, there are three unknown parameters, namely α, g, and T_{EGFR}, whose numerical values need to be determined. According to experimental evidence (represented by green circles in Figure 4.8), the level of active EGFR increases over 7 fold in the cells stimulated with AngII (100nM), suggesting that the total amount of EGFR (represented by T_{EGFR}) should be at least 8. In order to simplify the later parameter estimation process, T_{EGFR} is set to take the numerical value of 8 during the simulation. As for the other two parameters, α and g, we use the nonlinear optimization function in MATLAB to find optimal values. Since little prior information is available about the possible ranges or magnitudes of these two parameters, we start with a wide range of random initial guesses (size = 100) for these two parameters. This procedure led to several parameter candidates with almost equivalent performances. The parameter values that are used to generate simulation results represented in Figure 4.15 (b) are: $\alpha = 1$, $g = 1.5$.

C.4 cSrc- and Ca^{2+}-Dependent EGFR Activation Module

The pathway structure depicted in Figure 4.16 (a) is mathematically expressed in the GMA format shown in Eq. (C.3):

$$d(EGFR^*)/dt = \alpha_1 \cdot (T_{EGFR} - EGFR^*) \cdot (cSrc^*)^{g_1} + \alpha_2 \cdot (T_{EGFR} - EGFR^*) \cdot (Ca^{2+*})^{g_2} - \beta \cdot EGFR^*, \quad \text{(C.3)}$$

where α_1, α_2, and β are rate constants with non-negative values; g_1 and g_2 are real-valued kinetic orders. The levels of all active signaling molecules (denoted by symbols with *), including

$EGFR_{active}$, $cSrc_{active}$, and Ca^{2+}, are again assumed to have values of "1" in unstimulated control conditions. Considering the steady state requirement for this signaling cascade, Eq. (4.3) simplifies to Eq. (C.4):

$$d(EGFR^*)/dt = \alpha_1 \cdot (T_{EGFR} - EGFR^*) \cdot (cSrc^*)^{g_1} + \alpha_2 \cdot (T_{EGFR} - EGFR^*) \cdot (Ca^{2+*})^{g_2} - (\alpha_1 + \alpha_2) \cdot (T_{EGFR} - 1) \cdot EGFR^* \,. \quad \text{(C.4)}$$

Totally, there are five unknown parameters, namely α_1, α_2, g_1, g_2, and T_{EGFR}. Similar to the specifications in section C.3, the value of T_{EGFR} is fixed at 8, and the values of other parameters are searched via nonlinear optimization function in MATLAB. Several candidate sets were found with quite similar performances. The parameter values used to generate the simulation result displayed in Figure 4.16 (b) are: $\alpha_1 = 0.5$, $\alpha_2 = 0.5$, $g_1 = 1.5$, $g_2 = 3.5$.

C.5 Integrated AngII-Induced Nox1 Activation with H_2O_2-Dependent Positive Feedback

Compared to Model Candidate 3 (detailed described in Table 4.4), the final integrated model with H_2O_2-induced positive feedback contains $cSrc_{active}$ as a dependent variable rather than an independent variable, which adds two fluxes to the system. As a consequence, the integrated model with H_2O_2-dependent positive feedback is mathematically expressed in Eq. (C.5):

$$dX/dt = N_{final} \cdot F_{final}, \quad \text{(C.5)}$$

where $X_{14\times1}$ is the variable vector, consisting of dependent variables $Nox1_{active}$, $Nox1/p22^{phox}$, $p47^{phox}$, $p47^{phox}{}_P$, $Rac1_{GDP}$, $Rac1_{GTP}$, NoxA1, $NoxA1_P$, $O_2^{\cdot-}$, H_2O_2, PIP_3, $PI3K_{active}$, $EGFR_{active}$, and $cSrc_{active}$. N_{final} is a 14×30 stoichiometric matrix, and F_{final} is the 30×1 flux vector. The explicit expression of both N_{final} and F_{final} are respectively given Eqs. (C.6) and (C.7), where

PKC_{active}, $Nox4_{active}$, PIP_2, and Ca^{2+} are considered as independent inputs; X_1 to X_{14} are dependent system variables.

Ultimately, the final integrated system has 31 rate constants, 9 kinetic orders, and three other parameters (T_{PI3K}, T_{EGFR}, T_{cSrc}). Among these parameters, only three parameters involved in H_2O_2-induced cSrc activation (γ_{30}, g_9, and T_{cSrc}) are unknown and need to be numerically determined. Using the nonlinear optimization function in MATLAB with different initials, we found several parameter candidates with quite similar performances. The parameter values used to generate simulation results displayed in Figure 4.17, and Figure C.13 to C.23 are: $\gamma_{30} = 0.001$, $g_9 = 4.5$, and $T_{cSrc} = 5$. Other parameter values are either retained from the 12 selected samples in the second round of Monte-Carlo simulation (see $Para_{in}$) or directly obtained from the simulation setting of cSrc- and Ca^{2+}-dependent EGFR activation (see section C.4): $\gamma_{27} = 0.5$, $\gamma_{28} = 0.5$, $g_7 = 1.5$, $g_8 = 3.5$, and $T_{EGFR} = 8$.

$$N_{final} = \begin{bmatrix} 1 & -1 & 0 & -1 & 0 & -1 & -1 & 0 & 0 & 0 & 0 & 0 & 0 & 0 \\ -1 & 1 & 0 & 1 & 0 & 1 & 0 & 1 & 0 & 0 & 0 & 0 & 0 & 0 \\ -1 & 1 & 1 & 0 & 0 & 1 & 1 & 0 & 0 & 0 & 0 & 0 & 0 & 0 \\ -1 & 1 & 0 & 1 & 1 & 0 & 1 & 0 & 0 & 0 & 0 & 0 & 0 & 0 \\ 0 & 0 & -1 & 1 & 0 & 0 & 0 & 0 & 0 & 0 & 0 & 0 & 0 & 0 \\ 0 & 0 & 1 & -1 & 0 & 0 & 0 & 0 & 0 & 0 & 0 & 0 & 0 & 0 \\ 0 & 0 & 0 & 0 & -1 & 1 & 0 & 0 & 0 & 0 & 0 & 0 & 0 & 0 \\ 0 & 0 & 0 & 0 & 1 & -1 & 0 & 0 & 0 & 0 & 0 & 0 & 0 & 0 \\ 0 & 0 & 0 & 0 & 0 & 0 & -1 & 1 & 0 & 0 & 0 & 0 & 0 & 0 \\ 0 & 0 & 0 & 0 & 0 & 0 & 1 & -1 & 0 & 0 & 0 & 0 & 0 & 0 \\ 0 & 0 & 1 & 0 & 0 & 0 & 0 & 0 & 0 & 0 & 0 & 0 & 0 & 0 \\ 0 & 0 & 0 & 0 & 1 & 0 & 0 & 0 & 0 & 0 & 0 & 0 & 0 & 0 \\ 0 & 1 & 0 & 0 & 0 & 0 & 0 & 0 & 0 & 0 & 0 & 0 & 0 & 0 \\ -1 & 0 & 0 & 0 & 0 & 0 & 0 & 0 & 0 & 0 & 0 & 0 & 0 & 0 \\ 0 & 0 & 0 & 0 & 0 & 0 & 1 & 0 & 0 & 0 & 0 & 0 & 0 & 0 \\ 0 & 0 & 0 & 0 & 0 & 0 & 0 & -1 & 0 & 0 & 0 & 0 & 0 & 0 \\ 0 & 0 & 0 & 0 & 0 & 0 & 0 & 0 & 1 & 0 & 0 & 0 & 0 & 0 \\ 0 & 0 & 0 & 0 & 0 & 0 & 0 & 0 & 1 & 0 & 0 & 0 & 0 & 0 \\ 0 & 0 & 0 & 0 & 0 & 0 & 0 & 0 & -1 & 0.5 & 0 & 0 & 0 & 0 \\ 0 & 0 & 0 & 0 & 0 & 0 & 0 & 0 & -1 & 0 & 0 & 0 & 0 & 0 \\ 0 & 0 & 0 & 0 & 0 & 0 & 0 & 0 & 0 & 1 & 0 & 0 & 0 & 0 \\ 0 & 0 & 0 & 0 & 0 & 0 & 0 & 0 & 0 & -1 & 0 & 0 & 0 & 0 \\ 0 & 0 & 0 & 0 & 0 & 0 & 0 & 0 & 0 & 0 & 1 & 0 & 0 & 0 \\ 0 & 0 & 0 & 0 & 0 & 0 & 0 & 0 & 0 & 0 & -1 & 0 & 0 & 0 \\ 0 & 0 & 0 & 0 & 0 & 0 & 0 & 0 & 0 & 0 & 0 & 1 & 0 & 0 \\ 0 & 0 & 0 & 0 & 0 & 0 & 0 & 0 & 0 & 0 & 0 & -1 & 0 & 0 \\ 0 & 0 & 0 & 0 & 0 & 0 & 0 & 0 & 0 & 0 & 0 & 0 & 1 & 0 \\ 0 & 0 & 0 & 0 & 0 & 0 & 0 & 0 & 0 & 0 & 0 & 0 & -1 & 0 \\ 0 & 0 & 0 & 0 & 0 & 0 & 0 & 0 & 0 & 0 & 0 & 0 & 0 & 1 \\ 0 & 0 & 0 & 0 & 0 & 0 & 0 & 0 & 0 & 0 & 0 & 0 & 0 & -1 \end{bmatrix}^T \quad \text{(C.6)}$$

$F_{final} = [f_1\ f_2\ f_3 \cdots f_{27}\ f_{28}\ f_{29}\ f_{30}]^T$, where each flux is given in the GMA format in Eq. (C.7).

$$
\begin{aligned}
f_1 &= \gamma_1 X_2 X_4 X_6 X_7 & f_9 &= \gamma_9 X_7 (PKC_{active})^{g_4} & f_{17} &= \gamma_{17} X_1 & f_{25} &= \gamma_{25} (T_{PI3K} - X_{12}) X_{13}^{\ g_6} \\
f_2 &= \gamma_2 X_1 & f_{10} &= \gamma_{10} X_8 & f_{18} &= \gamma_{18} (Nox4_{active}) & f_{26} &= \gamma_{26} X_{12} \\
f_3 &= \gamma_3 X_1 & f_{11} &= \gamma_{11} & f_{19} &= \gamma_{19} X_9 & f_{27} &= \gamma_{27} (T_{EGFR} - X_{13}) X_{14}^{\ g_7} \\
f_4 &= \gamma_4 X_1 & f_{12} &= \gamma_{12} & f_{20} &= \gamma_{20} X_9^{\ 2} & f_{28} &= \gamma_{28} (T_{EGFR} - X_{13}) (Ca^{2+})^{g_8} \\
f_5 &= \gamma_5 X_3 (PKC_{active})^{g_1} X_{14}^{\ g_2} & f_{13} &= \gamma_{13} & f_{21} &= \gamma_{21} (Nox4_{active}) & f_{29} &= \gamma_{29} X_{13} \\
f_6 &= \gamma_6 X_4 & f_{14} &= \gamma_{14} X_1 & f_{22} &= \gamma_{22} X_{10}^{\ 0.5} & f_{30} &= \gamma_{30} (T_{cSrc} - X_{14}) X_{10}^{\ g_9} \\
f_7 &= \gamma_7 X_5 X_{11}^{\ g_3} & f_{15} &= \gamma_{15} & f_{23} &= \gamma_{23} (PIP_2) X_{12}^{\ g_5} & f_{31} &= \gamma_{31} X_{14} \\
f_8 &= \gamma_8 X_6 & f_{16} &= \gamma_{16} X_8 & f_{24} &= \gamma_{24} X_{11}
\end{aligned}
\tag{C.7}
$$

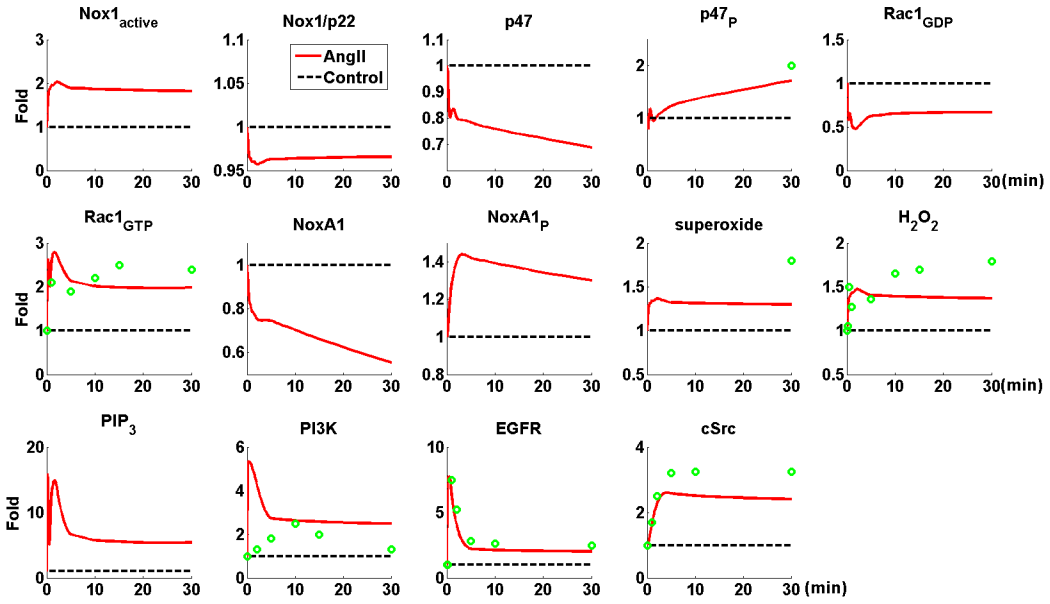

Figure C.13 Dynamic simulations of integrated model with H_2O_2-induced cSrc activation for selected sample set 1. The partial parameter values used in this simulation are: $Para_{in}$ = [0.0052 0.0879 0.0196 0.0830 0.0930 0.0012 0.0037 0.3393 0.7817 1.3660 0.0749 0.6380 0.7274 1.8914 6]. The values of other parameters are kept the same for Figure C.13 to C.23, and are defined in corresponding text in section C.5.

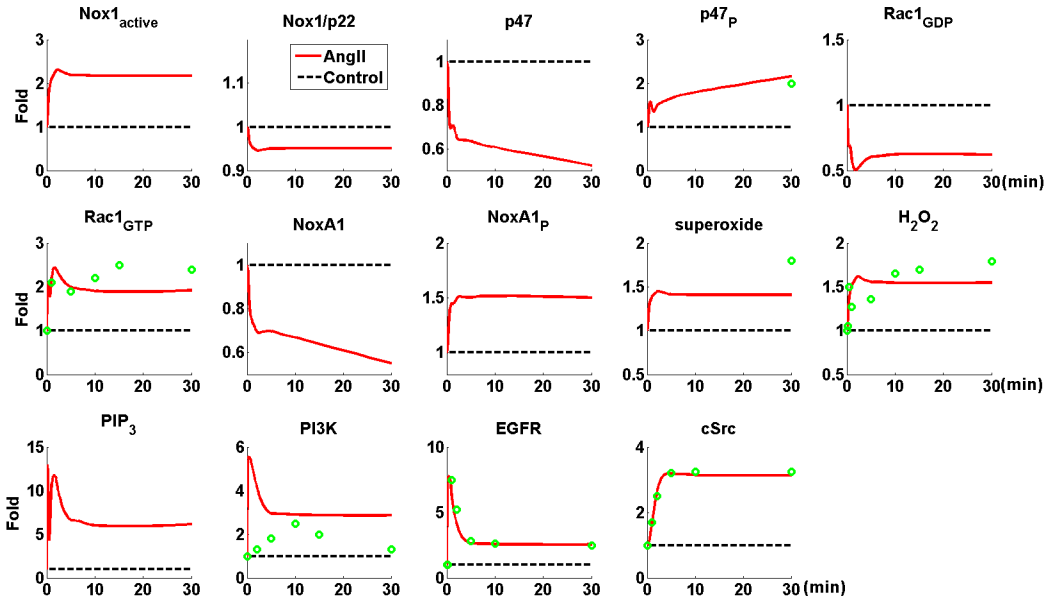

Figure C.14 Dynamic simulations of integrated model with H_2O_2-induced cSrc activation for selected sample set 2. The parameter values used in this simulation are: $Para_{in}$ = [0.0093 0.0286 0.0130 0.0807 0.0395 0.0037 0.0018 0.5067 0.4351 0.9721 0.1349 0.6377 1.1940 1.7580 7].

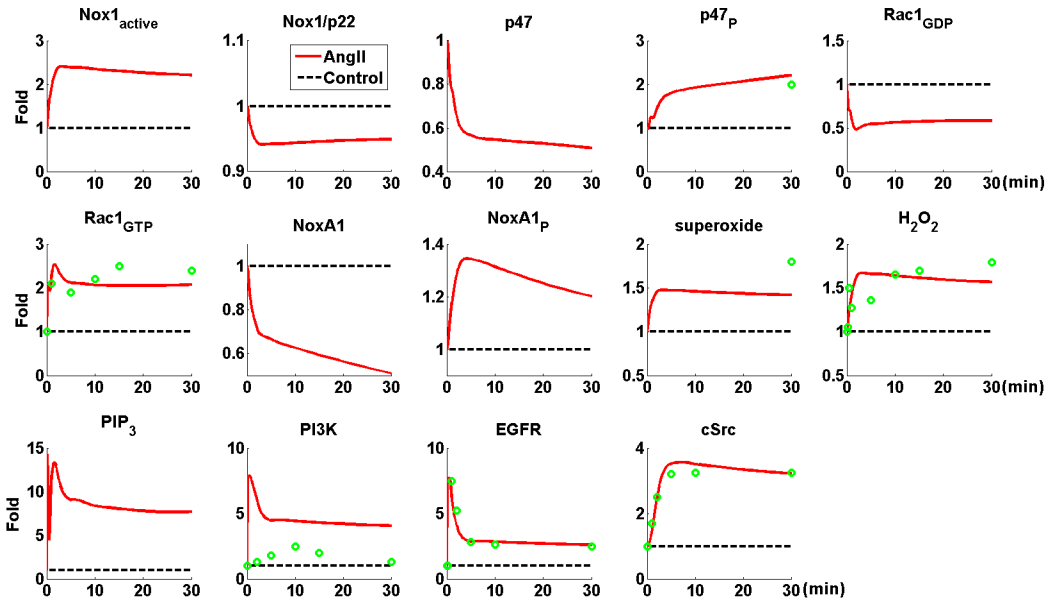

Figure C.15 Dynamic simulations of integrated model with H_2O_2-induced cSrc activation for selected sample set 4. The parameter values used in this simulation are: $Para_{in}$ = [0.0038 0.0235 0.0177 0.0439 0.0238 0.0015 0.0046 2.8345 0.1232 1.3067 0.5391 0.6339 0.5274 1.4802 1.9632 9].

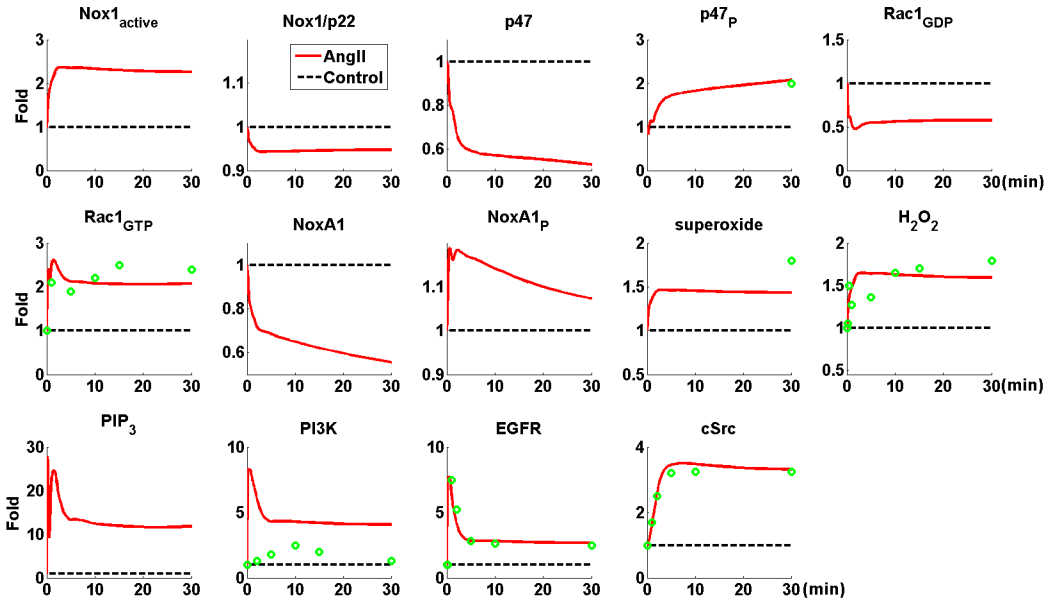

Figure C.16 Dynamic simulations of integrated model with H_2O_2-induced cSrc activation for selected sample set 5. The parameter values used in this simulation are: $Para_{in}$ = [0.0235 0.0958 0.0109 0.0904 0.0577 0.0160 0.0083 0.4650 0.6545 1.0419 0.6188 0.5254 0.4659 1.7823 1.8502 10].

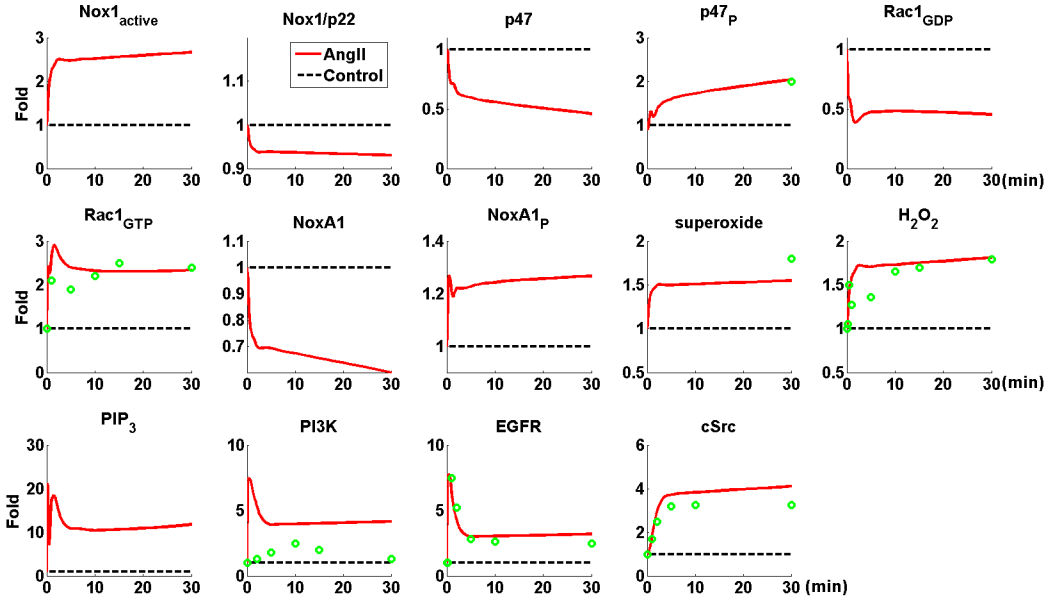

Figure C.17 Dynamic simulations of integrated model with H_2O_2-induced cSrc activation for selected sample set 6. The parameter values used in this simulation are: $Para_{in}$ = [0.0362 0.0379 0.0123 0.0365 0.0243 0.0327 0.0012 0.5980 6.6175 1.8979 0.2865 0.6796 0.7615 1.7568 1.6002 10].

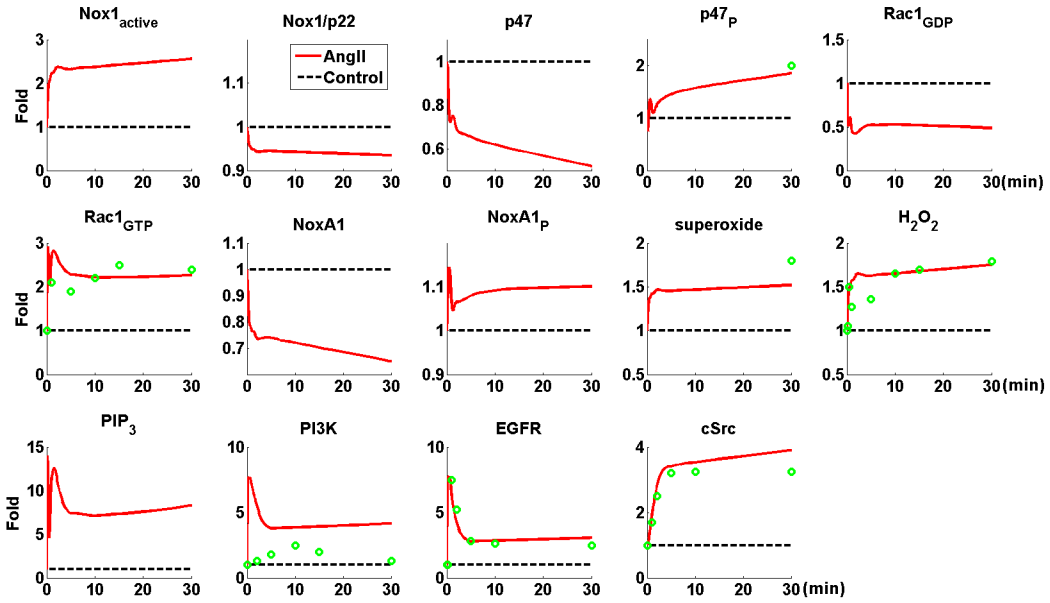

Figure C.18 Dynamic simulations of integrated model with H_2O_2-induced cSrc activation for selected sample set 7. The parameter values used in this simulation are: $Para_{in}$ = [0.0176 0.0908 0.0232 0.0769 0.0972 0.0512 0.0027 1.6793 1.5401 1.7832 0.2196 0.7376 0.6810 1.5133 1.6543 10].

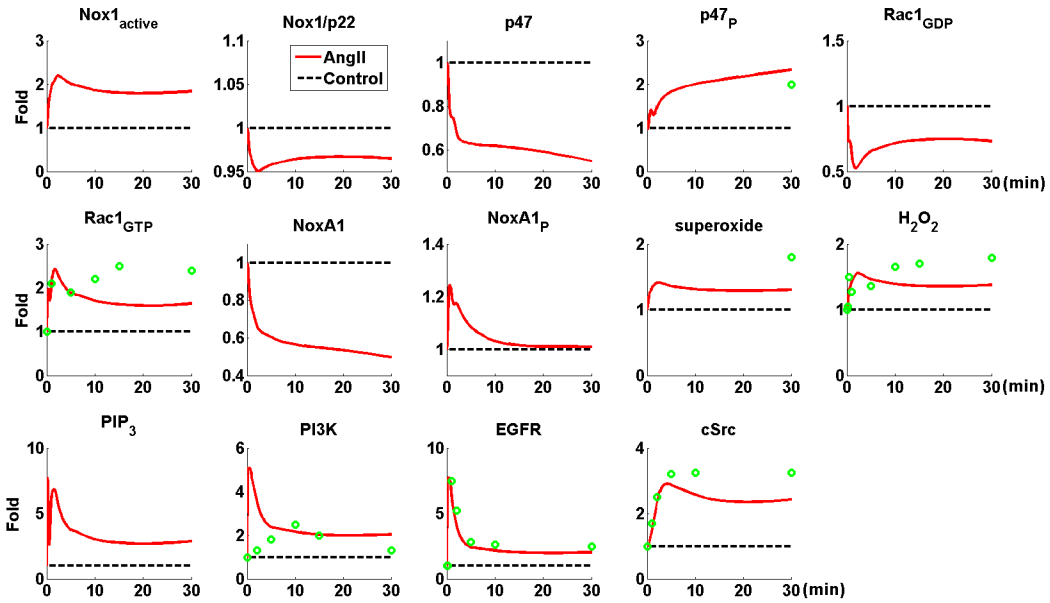

Figure C.19 Dynamic simulations of integrated model with H_2O_2-induced cSrc activation for selected sample set 8. The parameter values used in this simulation are: $Para_{in}$ = [0.0153 0.0344 0.0122 0.0456 0.0314 0.0102 0.0414 0.9806 2.5609 1.6142 0.3707 0.7949 0.6931 1.5375 1.2294 8].

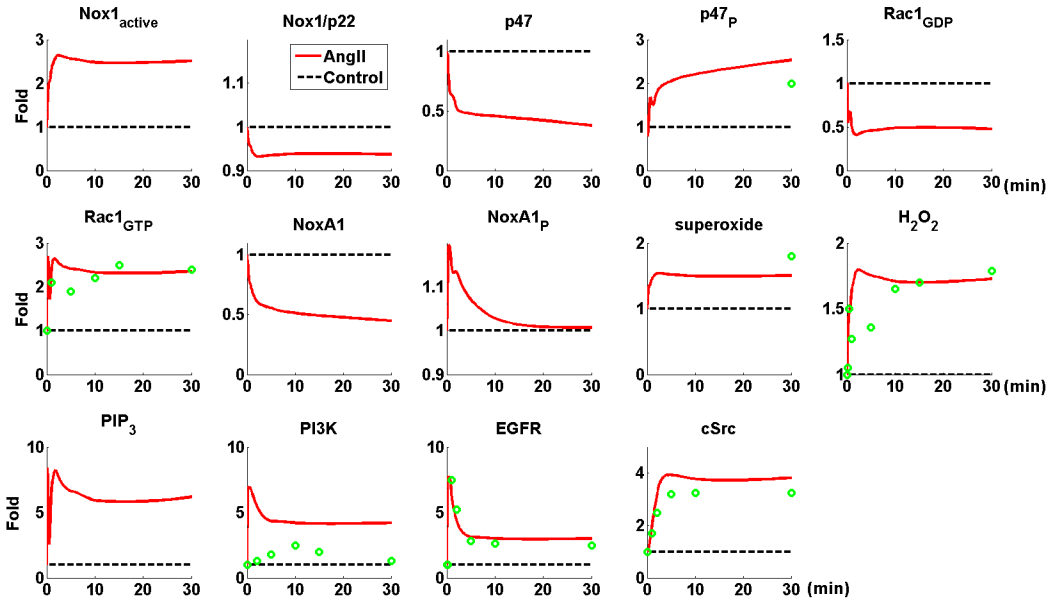

Figure C.20 Dynamic simulations of integrated model with H_2O_2-induced cSrc activation for selected sample set 9. The parameter values used in this simulation are: $Para_{in}$ = [0.0924 0.0373 0.0282 0.0747 0.0761 0.0698 0.0388 0.4009 2.4353 1.9377 0.4880 0.8860 0.5403 1.2936 1.8561 8].

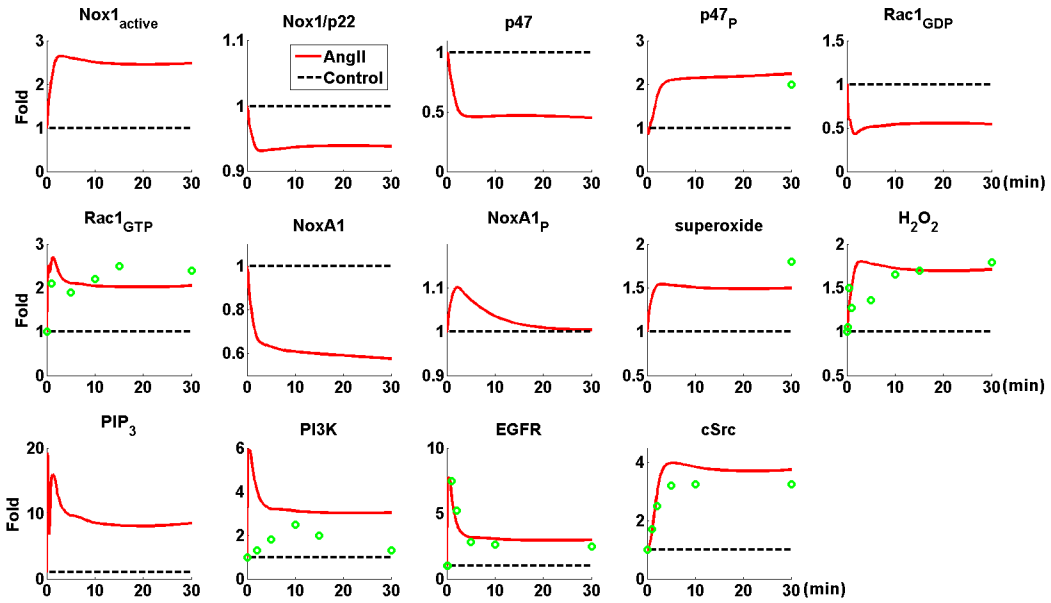

Figure C.21 Dynamic simulations of integrated model with H_2O_2-induced cSrc activation for selected sample set 10. The parameter values used in this simulation are: $Para_{in}$ = [0.0296 0.0128 0.0179 0.0769 0.0264 0.0191 0.0245 3.7825 0.4957 0.6346 0.9127 0.6552 0.0139 1.9572 1.2572 10].

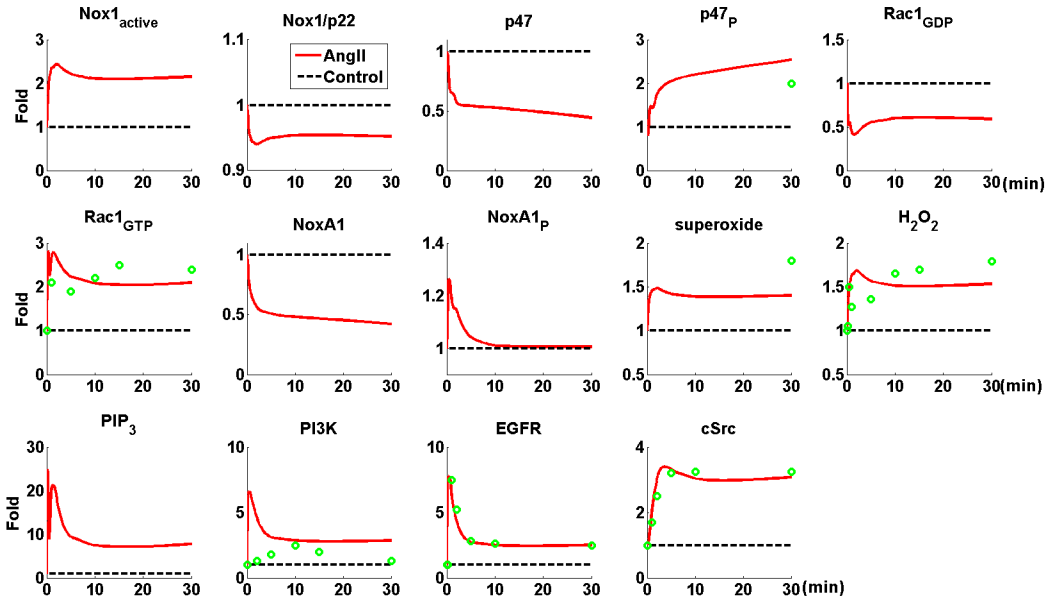

Figure C.22 Dynamic simulations of integrated model with H_2O_2-induced cSrc activation for selected sample set 11. The parameter values used in this simulation are: $Para_{in}$ = [0.0741 0.0445 0.0107 0.0668 0.0748 0.0463 0.0661 9.7272 0.1711 1.8628 0.4397 0.6193 0.7049 1.9886 1.3945 10].

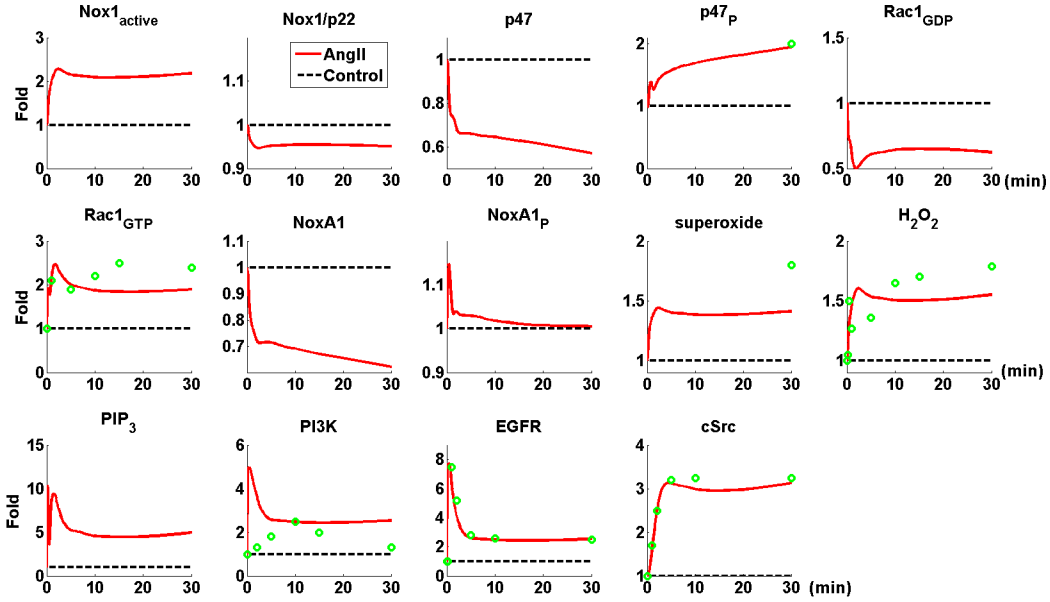

Figure C.23 Dynamic simulations of integrated model with H_2O_2-induced cSrc activation for selected sample set 12. The parameter values used in this simulation are: $Para_{in}$ = [0.0452 0.0163 0.0100 0.0643 0.0270 0.0737 0.0455 0.4358 0.1940 1.5931 0.1986 0.7182 0.5257 1.7633 1.3120 7].

REFERENCES

1. Valko, M., et al., Free radicals and antioxidants in normal physiological functions and human disease. Int J Biochem Cell Biol, 2007. 39(1): p. 44-84.

2. Nordberg, J. and E.S. Arner, Reactive oxygen species, antioxidants, and the mammalian thioredoxin system. Free Radic Biol Med, 2001. 31(11): p. 1287-312.

3. D'Autreaux, B. and M.B. Toledano, ROS as signalling molecules: mechanisms that generate specificity in ROS homeostasis. Nat Rev Mol Cell Biol, 2007. 8(10): p. 813-24.

4. Fridovich, I., Fundamental aspects of reactive oxygen species, or what's the matter with oxygen? Ann N Y Acad Sci, 1999. 893: p. 13-8.

5. Alom-Ruiz, S.P., N. Anilkumar, and A.M. Shah, Reactive oxygen species and endothelial activation. Antioxid Redox Signal, 2008. 10(6): p. 1089-100.

6. Stone, J.R. and S. Yang, Hydrogen peroxide: a signaling messenger. Antioxid Redox Signal, 2006. 8(3-4): p. 243-70.

7. Touyz, R.M., Reactive oxygen species, vascular oxidative stress, and redox signaling in hypertension: what is the clinical significance? Hypertension, 2004. 44(3): p. 248-52.

8. Touyz, R.M., Reactive oxygen species and angiotensin II signaling in vascular cells -- implications in cardiovascular disease. Braz J Med Biol Res, 2004. 37(8): p. 1263-73.

9. Guzik, T.J., et al., Vascular superoxide production by NAD(P)H oxidase: association with endothelial dysfunction and clinical risk factors. Circ Res, 2000. 86(9): p. E85-90.

10. Wolin, M.S., Reactive oxygen species and the control of vascular function. Am J Physiol Heart Circ Physiol, 2009. 296(3): p. H539-49.

11. Touyz, R.M. and E.L. Schiffrin, Reactive oxygen species in vascular biology: implications in hypertension. Histochem Cell Biol, 2004. 122(4): p. 339-52.

12. San Martin, A., et al., Reactive oxygen species-selective regulation of aortic inflammatory gene expression in Type 2 diabetes. Am J Physiol Heart Circ Physiol, 2007. 292(5): p. H2073-82.

13. Cave, A.C., et al., NADPH oxidases in cardiovascular health and disease. Antioxid Redox Signal, 2006. 8(5-6): p. 691-728.

14. Murdoch, C.E., et al., NADPH oxidase and heart failure. Curr Opin Pharmacol, 2006. 6(2): p. 148-53.

15. Murdoch, C.E., et al., NADPH oxidase-dependent redox signalling in cardiac hypertrophy, remodelling and failure. Cardiovasc Res, 2006. 71(2): p. 208-15.

16. Rhee, S.G., Redox signaling: hydrogen peroxide as intracellular messenger. Exp Mol Med, 1999. 31(2): p. 53-9.

17. Griendling, K.K. and M. Ushio-Fukai, Reactive oxygen species as mediators of angiotensin II signaling. Regul Pept, 2000. 91(1-3): p. 21-7.

18. Griendling, K.K., et al., Modulation of protein kinase activity and gene expression by reactive oxygen species and their role in vascular physiology and pathophysiology. Arterioscler Thromb Vasc Biol, 2000. 20(10): p. 2175-83.

19. Betteridge, D.J., What is oxidative stress? Metabolism, 2000. 49(2 Suppl 1): p. 3-8.

20. Droge, W., Free radicals in the physiological control of cell function. Physiol Rev, 2002. 82(1): p. 47-95.

21. Jones, D.P., Radical-free biology of oxidative stress. Am J Physiol Cell Physiol, 2008. 295(4): p. C849-68.

22. Cai, H. and D.G. Harrison, Endothelial dysfunction in cardiovascular diseases: the role of oxidant stress. Circ Res, 2000. 87(10): p. 840-4.

23. Mariani, E., et al., Oxidative stress in brain aging, neurodegenerative and vascular diseases: an overview. J Chromatogr B Analyt Technol Biomed Life Sci, 2005. 827(1): p. 65-75.

24. Fearon, I.M. and S.P. Faux, Oxidative stress and cardiovascular disease: novel tools give (free) radical insight. J Mol Cell Cardiol, 2009. 47(3): p. 372-81.

25. Cai, H., NAD(P)H oxidase-dependent self-propagation of hydrogen peroxide and vascular disease. Circ Res, 2005. 96(8): p. 818-22.

26. Cai, H., K.K. Griendling, and D.G. Harrison, The vascular NAD(P)H oxidases as therapeutic targets in cardiovascular diseases. Trends Pharmacol Sci, 2003. 24(9): p. 471-8.

27. Griendling, K.K., D. Sorescu, and M. Ushio-Fukai, NAD(P)H oxidase: role in cardiovascular biology and disease. Circ Res, 2000. 86(5): p. 494-501.

28. Sorescu, D., et al., Superoxide production and expression of nox family proteins in human atherosclerosis. Circulation, 2002. 105(12): p. 1429-35.

29. Babior, B.M., NADPH oxidase: an update. Blood, 1999. 93(5): p. 1464-76.

30. Babior, B.M., R.S. Kipnes, and J.T. Curnutte, Biological defense mechanisms. The production by leukocytes of superoxide, a potential bactericidal agent. J Clin Invest, 1973. 52(3): p. 741-4.

31. Brown, D.I. and K.K. Griendling, Nox proteins in signal transduction. Free Radic Biol Med, 2009. 47(9): p. 1239-53.

32. Brandes, R.P. and J. Kreuzer, Vascular NADPH oxidases: molecular mechanisms of activation. Cardiovasc Res, 2005. 65(1): p. 16-27.

33. Lassegue, B. and R.E. Clempus, Vascular NAD(P)H oxidases: specific features, expression, and regulation. Am J Physiol Regul Integr Comp Physiol, 2003. 285(2): p. R277-97.

34. Lassegue, B. and K.K. Griendling, NADPH oxidases: functions and pathologies in the vasculature. Arterioscler Thromb Vasc Biol, 2010. 30(4): p. 653-61.

35. Hilenski, L.L., et al., Distinct subcellular localizations of Nox1 and Nox4 in vascular smooth muscle cells. Arterioscler Thromb Vasc Biol, 2004. 24(4): p. 677-83.

36. Dikalov, S.I., et al., Distinct roles of Nox1 and Nox4 in basal and angiotensin II-stimulated superoxide and hydrogen peroxide production. Free Radic Biol Med, 2008. 45(9): p. 1340-51.

37. Lassegue, B., et al., Novel gp91(phox) homologues in vascular smooth muscle cells : nox1 mediates angiotensin II-induced superoxide formation and redox-sensitive signaling pathways. Circ Res, 2001. 88(9): p. 888-94.

38. Seshiah, P.N., et al., Angiotensin II stimulation of NAD(P)H oxidase activity: upstream mediators. Circ Res, 2002. 91(5): p. 406-13.

39. Dikalova, A., et al., Nox1 overexpression potentiates angiotensin II-induced hypertension and vascular smooth muscle hypertrophy in transgenic mice. Circulation, 2005. 112(17): p. 2668-76.

40. Lee, M.Y., et al., Mechanisms of vascular smooth muscle NADPH oxidase 1 (Nox1) contribution to injury-induced neointimal formation. Arterioscler Thromb Vasc Biol, 2009. 29(4): p. 480-7.

41. Schroder, K., et al., Nox1 mediates basic fibroblast growth factor-induced migration of vascular smooth muscle cells. Arterioscler Thromb Vasc Biol, 2007. 27(8): p. 1736-43.

42. Jo, H., H. Song, and A. Mowbray, Role of NADPH oxidases in disturbed flow- and BMP4-induced inflammation and atherosclerosis. Antioxid Redox Signal, 2006. 8(9-10): p. 1609-19.

43. Murphy, M.P., How mitochondria produce reactive oxygen species. Biochem J, 2009. 417(1): p. 1-13.

44. Balaban, R.S., S. Nemoto, and T. Finkel, Mitochondria, oxidants, and aging. Cell, 2005. 120(4): p. 483-95.

45. Cai, H., Hydrogen peroxide regulation of endothelial function: origins, mechanisms, and consequences. Cardiovasc Res, 2005. 68(1): p. 26-36.

46. Bannister, W.H., From haemocuprein to copper-zinc superoxide dismutase: a history on the fiftieth anniversary of the discovery of haemocuprein and the twentieth anniversary of the discovery of superoxide dismutase. Free Radic Res Commun, 1988. 5(1): p. 35-42.

47. Fridovich, I., Superoxide radical: an endogenous toxicant. Annu Rev Pharmacol Toxicol, 1983. 23: p. 239-57.

48. Ferrer-Sueta, G. and R. Radi, Chemical biology of peroxynitrite: kinetics, diffusion, and radicals. ACS Chem Biol, 2009. 4(3): p. 161-77.

49. Fritz, R., et al., Compartment-dependent management of H(2)O(2) by peroxisomes. Free Radic Biol Med, 2007. 42(7): p. 1119-29.

50. Angermuller, S., M. Islinger, and A. Volkl, Peroxisomes and reactive oxygen species, a lasting challenge. Histochem Cell Biol, 2009. 131(4): p. 459-63.

51. Serrander, L., et al., NOX4 activity is determined by mRNA levels and reveals a unique pattern of ROS generation. Biochem J, 2007. 406(1): p. 105-14.

52. Beckman, J.S. and W.H. Koppenol, Nitric oxide, superoxide, and peroxynitrite: the good, the bad, and ugly. Am J Physiol, 1996. 271(5 Pt 1): p. C1424-37.

53. Andrew, P.J. and B. Mayer, Enzymatic function of nitric oxide synthases. Cardiovasc Res, 1999. 43(3): p. 521-31.

54. Beck, K.F., et al., Inducible NO synthase: role in cellular signalling. J Exp Biol, 1999. 202(Pt 6): p. 645-53.

55. Bredt, D.S., Endogenous nitric oxide synthesis: biological functions and pathophysiology. Free Radic Res, 1999. 31(6): p. 577-96.

56. Kroncke, K.D., C.V. Suschek, and V. Kolb-Bachofen, Implications of inducible nitric oxide synthase expression and enzyme activity. Antioxid Redox Signal, 2000. 2(3): p. 585-605.

57. Drummond, G.R., et al., Transcriptional and posttranscriptional regulation of endothelial nitric oxide synthase expression by hydrogen peroxide. Circ Res, 2000. 86(3): p. 347-54.

58. Cai, H., et al., Induction of endothelial NO synthase by hydrogen peroxide via a Ca(2+)/calmodulin-dependent protein kinase II/janus kinase 2-dependent pathway. Arterioscler Thromb Vasc Biol, 2001. 21(10): p. 1571-6.

59. Davis, M.E., et al., Shear stress regulates endothelial nitric oxide synthase expression through c-Src by divergent signaling pathways. Circ Res, 2001. 89(11): p. 1073-80.

60. McNally, J.S., et al., Role of xanthine oxidoreductase and NAD(P)H oxidase in endothelial superoxide production in response to oscillatory shear stress. Am J Physiol Heart Circ Physiol, 2003. 285(6): p. H2290-7.

61. Ahmed, S.S., K.L. Napoli, and H.W. Strobel, Oxygen radical formation during cytochrome P450-catalyzed cyclosporine metabolism in rat and human liver microsomes at varying hydrogen ion concentrations. Mol Cell Biochem, 1995. 151(2): p. 131-40.

62. Mata-Greenwood, E., et al., eNOS function is developmentally regulated: uncoupling of eNOS occurs postnatally. Am J Physiol Lung Cell Mol Physiol, 2006. 290(2): p. L232-41.

63. Harrison, R., Physiological roles of xanthine oxidoreductase. Drug Metab Rev, 2004. 36(2): p. 363-75.

64. Schrader, M. and H.D. Fahimi, Mammalian peroxisomes and reactive oxygen species. Histochem Cell Biol, 2004. 122(4): p. 383-93.

65. Berendes, H., R.A. Bridges, and R.A. Good, A fatal granulomatosus of childhood: the clinical study of a new syndrome. Minn Med, 1957. 40(5): p. 309-12.

66. Segal, B.H., L. Romani, and P. Puccetti, Chronic granulomatous disease. Cell Mol Life Sci, 2009. 66(4): p. 553-8.

67. Segal, A.W. and O.T. Jones, Novel cytochrome b system in phagocytic vacuoles of human granulocytes. Nature, 1978. 276(5687): p. 515-7.

68. Babior, B.M., The leukocyte NADPH oxidase. Isr Med Assoc J, 2002. 4(11): p. 1023-4.

69. Oakley, F.D., et al., Signaling components of redox active endosomes: the redoxosomes. Antioxid Redox Signal, 2009. 11(6): p. 1313-33.

70. Sumimoto, H., K. Miyano, and R. Takeya, Molecular composition and regulation of the Nox family NAD(P)H oxidases. Biochem Biophys Res Commun, 2005. 338(1): p. 677-86.

71. Sumimoto, H., Structure, regulation and evolution of Nox-family NADPH oxidases that produce reactive oxygen species. FEBS J, 2008. 275(13): p. 3249-77.

72. Li, J.M. and A.M. Shah, Intracellular localization and preassembly of the NADPH oxidase complex in cultured endothelial cells. J Biol Chem, 2002. 277(22): p. 19952-60.

73. Pagano, P.J., et al., Localization of a constitutively active, phagocyte-like NADPH oxidase in rabbit aortic adventitia: enhancement by angiotensin II. Proc Natl Acad Sci U S A, 1997. 94(26): p. 14483-8.

74. Somers, M.J., J.S. Burchfield, and D.G. Harrison, Evidence for a NADH/NADPH oxidase in human umbilical vein endothelial cells using electron spin resonance. Antioxid Redox Signal, 2000. 2(4): p. 779-87.

75. Souza, H.P., et al., Vascular NAD(P)H oxidase is distinct from the phagocytic enzyme and modulates vascular reactivity control. Am J Physiol Heart Circ Physiol, 2001. 280(2): p. H658-67.

76. Gu, Y., et al., TNFalpha activates c-Jun amino terminal kinase through p47(phox). Exp Cell Res, 2002. 272(1): p. 62-74.

77. Hohler, B., B. Holzapfel, and W. Kummer, NADPH oxidase subunits and superoxide production in porcine pulmonary artery endothelial cells. Histochem Cell Biol, 2000. 114(1): p. 29-37.

78. Gorlach, A., et al., Thrombin activates the hypoxia-inducible factor-1 signaling pathway in vascular smooth muscle cells: Role of the p22(phox)-containing NADPH oxidase. Circ Res, 2001. 89(1): p. 47-54.

79. Barry-Lane, P.A., et al., p47phox is required for atherosclerotic lesion progression in ApoE(-/-) mice. J Clin Invest, 2001. 108(10): p. 1513-22.

80. De Keulenaer, G.W., et al., Oscillatory and steady laminar shear stress differentially affect human endothelial redox state: role of a superoxide-producing NADH oxidase. Circ Res, 1998. 82(10): p. 1094-101.

81. Landmesser, U., et al., Role of p47(phox) in vascular oxidative stress and hypertension caused by angiotensin II. Hypertension, 2002. 40(4): p. 511-5.

82. Cross, A.R., J.F. Parkinson, and O.T. Jones, The superoxide-generating oxidase of leucocytes. NADPH-dependent reduction of flavin and cytochrome b in solubilized preparations. Biochem J, 1984. 223(2): p. 337-44.

83. De Keulenaer, G.W., et al., Tumour necrosis factor alpha activates a p22phox-based NADH oxidase in vascular smooth muscle. Biochem J, 1998. 329 (Pt 3): p. 653-7.

84. Griendling, K.K., et al., Angiotensin II stimulates NADH and NADPH oxidase activity in cultured vascular smooth muscle cells. Circ Res, 1994. 74(6): p. 1141-8.

85. Mohazzab, K.M., P.M. Kaminski, and M.S. Wolin, NADH oxidoreductase is a major source of superoxide anion in bovine coronary artery endothelium. Am J Physiol, 1994. 266(6 Pt 2): p. H2568-72.

86. Suh, Y.A., et al., Cell transformation by the superoxide-generating oxidase Mox1. Nature, 1999. 401(6748): p. 79-82.

87. Banfi, B., et al., A mammalian H+ channel generated through alternative splicing of the NADPH oxidase homolog NOH-1. Science, 2000. 287(5450): p. 138-42.

88. Rokutan, K., et al., Nox enzymes and oxidative stress in the immunopathology of the gastrointestinal tract. Semin Immunopathol, 2008. 30(3): p. 315-27.

89. Helmcke, I., et al., Identification of structural elements in Nox1 and Nox4 controlling localization and activity. Antioxid Redox Signal, 2009. 11(6): p. 1279-87.

90. Miller, F.J., Jr., et al., Cytokine activation of nuclear factor kappa B in vascular smooth muscle cells requires signaling endosomes containing Nox1 and ClC-3. Circ Res, 2007. 101(7): p. 663-71.

91. Lassegue, B., How does the chloride/proton antiporter ClC-3 control NADPH oxidase? Circ Res, 2007. 101(7): p. 648-50.

92. Hanna, I.R., et al., Functional association of nox1 with p22phox in vascular smooth muscle cells. Free Radic Biol Med, 2004. 37(10): p. 1542-9.

93. Ambasta, R.K., et al., Direct interaction of the novel Nox proteins with p22phox is required for the formation of a functionally active NADPH oxidase. J Biol Chem, 2004. 279(44): p. 45935-41.

94. Takeya, R., et al., Novel human homologues of p47phox and p67phox participate in activation of superoxide-producing NADPH oxidases. J Biol Chem, 2003. 278(27): p. 25234-46.

95. Miyano, K., et al., Direct involvement of the small GTPase Rac in activation of the superoxide-producing NADPH oxidase Nox1. J Biol Chem, 2006. 281(31): p. 21857-68.

96. Cheng, G., et al., Nox1-dependent reactive oxygen generation is regulated by Rac1. J Biol Chem, 2006. 281(26): p. 17718-26.

97. Hassanain, H.H., et al., Hypertension caused by transgenic overexpression of Rac1. Antioxid Redox Signal, 2007. 9(1): p. 91-100.

98. Ambasta, R.K., et al., Noxa1 is a central component of the smooth muscle NADPH oxidase in mice. Free Radic Biol Med, 2006. 41(2): p. 193-201.

99. Niu, X.L., et al., Nox activator 1: a potential target for modulation of vascular reactive oxygen species in atherosclerotic arteries. Circulation, 2010. 121(4): p. 549-59.

100. Touyz, R.M., et al., p47phox associates with the cytoskeleton through cortactin in human vascular smooth muscle cells: role in NAD(P)H oxidase regulation by angiotensin II. Arterioscler Thromb Vasc Biol, 2005. 25(3): p. 512-8.

101. Sorescu, G.P., et al., Bone morphogenic protein 4 produced in endothelial cells by oscillatory shear stress induces monocyte adhesion by stimulating reactive oxygen species production from a nox1-based NADPH oxidase. Circ Res, 2004. 95(8): p. 773-9.

102. Maheswaranathan, M., et al., Platelet-derived growth factor (PDGF) regulates Slingshot phosphatase activity via Nox1-dependent auto-dephosphorylation of serine 834 in vascular smooth muscle cells. J Biol Chem, 2011. 286(41): p. 35430-7.

103. Wingler, K., et al., Upregulation of the vascular NAD(P)H-oxidase isoforms Nox1 and Nox4 by the renin-angiotensin system in vitro and in vivo. Free Radic Biol Med, 2001. 31(11): p. 1456-64.

104. Fukui, T., et al., p22phox mRNA expression and NADPH oxidase activity are increased in aortas from hypertensive rats. Circ Res, 1997. 80(1): p. 45-51.

105. Touyz, R.M., et al., Expression of a functionally active gp91phox-containing neutrophil-type NAD(P)H oxidase in smooth muscle cells from human resistance arteries: regulation by angiotensin II. Circ Res, 2002. 90(11): p. 1205-13.

106. Ni, W., et al., Ets-1 is a critical transcriptional regulator of reactive oxygen species and p47(phox) gene expression in response to angiotensin II. Circ Res, 2007. 101(10): p. 985-94.

107. Chanock, S.J., et al., The respiratory burst oxidase. J Biol Chem, 1994. 269(40): p. 24519-22.

108. Babior, B.M., J.D. Lambeth, and W. Nauseef, The neutrophil NADPH oxidase. Arch Biochem Biophys, 2002. 397(2): p. 342-4.

109. Ushio-Fukai, M., Localizing NADPH oxidase-derived ROS. Sci STKE, 2006. 2006(349): p. re8.

110. Li, Q., et al., Nox2 and Rac1 regulate H2O2-dependent recruitment of TRAF6 to endosomal interleukin-1 receptor complexes. Mol Cell Biol, 2006. 26(1): p. 140-54.

111. Dang, P.M., et al., Assembly of the neutrophil respiratory burst oxidase: a direct interaction between p67PHOX and cytochrome b558 II. Proc Natl Acad Sci U S A, 2002. 99(7): p. 4262-5.

112. Bokoch, G.M. and B.A. Diebold, Current molecular models for NADPH oxidase regulation by Rac GTPase. Blood, 2002. 100(8): p. 2692-6.

113. El Benna, J., et al., Phosphorylation of the respiratory burst oxidase subunit p47phox as determined by two-dimensional phosphopeptide mapping. Phosphorylation by protein kinase C, protein kinase A, and a mitogen-activated protein kinase. J Biol Chem, 1996. 271(11): p. 6374-8.

114. Babior, B.M., The activity of leukocyte NADPH oxidase: regulation by p47PHOX cysteine and serine residues. Antioxid Redox Signal, 2002. 4(1): p. 35-8.

115. Harfouche, R., et al., Roles of reactive oxygen species in angiopoietin-1/tie-2 receptor signaling. FASEB J, 2005. 19(12): p. 1728-30.

116. Dworakowski, R., S.P. Alom-Ruiz, and A.M. Shah, NADPH oxidase-derived reactive oxygen species in the regulation of endothelial phenotype. Pharmacol Rep, 2008. 60(1): p. 21-8.

117. Ushio-Fukai, M., VEGF signaling through NADPH oxidase-derived ROS. Antioxid Redox Signal, 2007. 9(6): p. 731-9.

118. Diebold, I., et al., Phosphodiesterase 2 mediates redox-sensitive endothelial cell proliferation and angiogenesis by thrombin via Rac1 and NADPH oxidase 2. Circ Res, 2009. 104(10): p. 1169-77.

119. Jung, O., et al., gp91phox-containing NADPH oxidase mediates endothelial dysfunction in renovascular hypertension. Circulation, 2004. 109(14): p. 1795-801.

120. Geiszt, M., et al., Identification of renox, an NAD(P)H oxidase in kidney. Proc Natl Acad Sci U S A, 2000. 97(14): p. 8010-4.

121. Krause, K.H., Tissue distribution and putative physiological function of NOX family NADPH oxidases. Jpn J Infect Dis, 2004. 57(5): p. S28-9.

122. Kuroda, J., et al., The superoxide-producing NAD(P)H oxidase Nox4 in the nucleus of human vascular endothelial cells. Genes Cells, 2005. 10(12): p. 1139-51.

123. Ellmark, S.H., et al., The contribution of Nox4 to NADPH oxidase activity in mouse vascular smooth muscle. Cardiovasc Res, 2005. 65(2): p. 495-504.

124. Lyle, A.N., et al., Poldip2, a novel regulator of Nox4 and cytoskeletal integrity in vascular smooth muscle cells. Circ Res, 2009. 105(3): p. 249-59.

125. Ago, T., et al., Nox4 as the major catalytic component of an endothelial NAD(P)H oxidase. Circulation, 2004. 109(2): p. 227-33.

126. Haurani, M.J., et al., Nox4 oxidase overexpression specifically decreases endogenous Nox4 mRNA and inhibits angiotensin II-induced adventitial myofibroblast migration. Hypertension, 2008. 52(1): p. 143-9.

127. Peshavariya, H., et al., Translation-linked mRNA destabilization accompanying serum-induced Nox4 expression in human endothelial cells. Antioxid Redox Signal, 2009. 11(10): p. 2399-408.

128. Hwang, J., et al., Pulsatile versus oscillatory shear stress regulates NADPH oxidase subunit expression: implication for native LDL oxidation. Circ Res, 2003. 93(12): p. 1225-32.

129. Clempus, R.E., et al., Nox4 is required for maintenance of the differentiated vascular smooth muscle cell phenotype. Arterioscler Thromb Vasc Biol, 2007. 27(1): p. 42-8.

130. Basuroy, S., et al., Nox4 NADPH oxidase mediates oxidative stress and apoptosis caused by TNF-alpha in cerebral vascular endothelial cells. Am J Physiol Cell Physiol, 2009. 296(3): p. C422-32.

131. Xiao, Q., et al., Embryonic stem cell differentiation into smooth muscle cells is mediated by Nox4-produced H2O2. Am J Physiol Cell Physiol, 2009. 296(4): p. C711-23.

132. Ismail, S., et al., NOX4 mediates hypoxia-induced proliferation of human pulmonary artery smooth muscle cells: the role of autocrine production of transforming growth factor-{beta}1 and insulin-like growth factor binding protein-3. Am J Physiol Lung Cell Mol Physiol, 2009. 296(3): p. L489-99.

133. Djordjevic, T., et al., Human urotensin II is a novel activator of NADPH oxidase in human pulmonary artery smooth muscle cells. Arterioscler Thromb Vasc Biol, 2005. 25(3): p. 519-25.

134. BelAiba, R.S., et al., NOX5 variants are functionally active in endothelial cells. Free Radic Biol Med, 2007. 42(4): p. 446-59.

135. Banfi, B., et al., A Ca(2+)-activated NADPH oxidase in testis, spleen, and lymph nodes. J Biol Chem, 2001. 276(40): p. 37594-601.

136. Jay, D.B., et al., Nox5 mediates PDGF-induced proliferation in human aortic smooth muscle cells. Free Radic Biol Med, 2008. 45(3): p. 329-35.

137. Cheng, G., et al., Homologs of gp91phox: cloning and tissue expression of Nox3, Nox4, and Nox5. Gene, 2001. 269(1-2): p. 131-40.

138. Brar, S.S., et al., NOX5 NAD(P)H oxidase regulates growth and apoptosis in DU 145 prostate cancer cells. Am J Physiol Cell Physiol, 2003. 285(2): p. C353-69.

139. Kawahara, T. and J.D. Lambeth, Phosphatidylinositol (4,5)-bisphosphate modulates Nox5 localization via an N-terminal polybasic region. Mol Biol Cell, 2008. 19(10): p. 4020-31.

140. Serrander, L., et al., NOX5 is expressed at the plasma membrane and generates superoxide in response to protein kinase C activation. Biochimie, 2007. 89(9): p. 1159-67.

141. Tirone, F. and J.A. Cox, NADPH oxidase 5 (NOX5) interacts with and is regulated by calmodulin. FEBS Lett, 2007. 581(6): p. 1202-8.

142. Banfi, B., et al., Mechanism of Ca2+ activation of the NADPH oxidase 5 (NOX5). J Biol Chem, 2004. 279(18): p. 18583-91.

143. Jagnandan, D., et al., Novel mechanism of activation of NADPH oxidase 5. calcium sensitization via phosphorylation. J Biol Chem, 2007. 282(9): p. 6494-507.

144. McNally, J.S., et al., Regulation of xanthine oxidoreductase protein expression by hydrogen peroxide and calcium. Arterioscler Thromb Vasc Biol, 2005. 25(8): p. 1623-8.

145. Harrison, R., Structure and function of xanthine oxidoreductase: where are we now? Free Radic Biol Med, 2002. 33(6): p. 774-97.

146. Waud, W.R. and K.V. Rajagopalan, The mechanism of conversion of rat liver xanthine dehydrogenase from an NAD+-dependent form (type D) to an O2-dependent form (type O). Arch Biochem Biophys, 1976. 172(2): p. 365-79.

147. Rasmussen, J.T., M.S. Rasmussen, and T.E. Petersen, Cysteines involved in the interconversion between dehydrogenase and oxidase forms of bovine xanthine oxidoreductase. J Dairy Sci, 2000. 83(3): p. 499-506.

148. Kerr, S., et al., Superoxide anion production is increased in a model of genetic hypertension: role of the endothelium. Hypertension, 1999. 33(6): p. 1353-8.

149. Pou, S., et al., Generation of superoxide by purified brain nitric oxide synthase. J Biol Chem, 1992. 267(34): p. 24173-6.

150. Vasquez-Vivar, J., et al., Superoxide generation by endothelial nitric oxide synthase: the influence of cofactors. Proc Natl Acad Sci U S A, 1998. 95(16): p. 9220-5.

151. Heinzel, B., et al., Ca2+/calmodulin-dependent formation of hydrogen peroxide by brain nitric oxide synthase. Biochem J, 1992. 281 (Pt 3): p. 627-30.

152. Laursen, J.B., et al., Endothelial regulation of vasomotion in apoE-deficient mice: implications for interactions between peroxynitrite and tetrahydrobiopterin. Circulation, 2001. 103(9): p. 1282-8.

153. Schwartz, S.M., M.W. Majesky, and R.J. Dilley, Vascular Remodeling in Hypertension and Atherosclerosis. Hypertension: Pathophysiology, Diagnosis and Management, ed. J.H. Laragh and B.M. Brenner1990, New York: Brenner Raven Press.

154. Rajagopalan, S., et al., Angiotensin II-mediated hypertension in the rat increases vascular superoxide production via membrane NADH/NADPH oxidase activation. Contribution to alterations of vasomotor tone. J Clin Invest, 1996. 97(8): p. 1916-23.

155. Wang, H.D., et al., Role of NADPH oxidase in the vascular hypertrophic and oxidative stress response to angiotensin II in mice. Circ Res, 2001. 88(9): p. 947-53.

156. Ushio-Fukai, M., et al., p22phox is a critical component of the superoxide-generating NADH/NADPH oxidase system and regulates angiotensin II-induced hypertrophy in vascular smooth muscle cells. J Biol Chem, 1996. 271(38): p. 23317-21.

157. Zafari, A.M., et al., Role of NADH/NADPH oxidase-derived H2O2 in angiotensin II-induced vascular hypertrophy. Hypertension, 1998. 32(3): p. 488-95.

158. Libby, P., Inflammation in atherosclerosis. Nature, 2002. 420(6917): p. 868-74.

159. Ross, R., Atherosclerosis--an inflammatory disease. N Engl J Med, 1999. 340(2): p. 115-26.

160. Zarins, C.K., et al., Carotid bifurcation atherosclerosis. Quantitative correlation of plaque localization with flow velocity profiles and wall shear stress. Circ Res, 1983. 53(4): p. 502-14.

161. Nagel, T., et al., Shear stress selectively upregulates intercellular adhesion molecule-1 expression in cultured human vascular endothelial cells. J Clin Invest, 1994. 94(2): p. 885-91.

162. Sucosky, P., et al., Altered shear stress stimulates upregulation of endothelial VCAM-1 and ICAM-1 in a BMP-4- and TGF-beta1-dependent pathway. Arterioscler Thromb Vasc Biol, 2009. 29(2): p. 254-60.

163. Nam, D., et al., A model of disturbed flow-induced atherosclerosis in mouse carotid artery by partial ligation and a simple method of RNA isolation from carotid endothelium. J Vis Exp, 2010(40).

164. Rodrigo, R., et al., Decrease in oxidative stress through supplementation of vitamins C and E is associated with a reduction in blood pressure in patients with essential hypertension. Clin Sci (Lond), 2008. 114(10): p. 625-34.

165. Plantinga, Y., et al., Supplementation with vitamins C and E improves arterial stiffness and endothelial function in essential hypertensive patients. Am J Hypertens, 2007. 20(4): p. 392-7.

166. Czernichow, S., et al., Effect of supplementation with antioxidants upon long-term risk of hypertension in the SU.VI.MAX study: association with plasma antioxidant levels. J Hypertens, 2005. 23(11): p. 2013-8.

167. Maxwell, S. and L. Greig, Anti-oxidants-- a protective role in cardiovascular disease? Expert Opin Pharmacother, 2001. 2(11): p. 1737-50.

168. Shi, J., et al., PR-39, a proline-rich antibacterial peptide that inhibits phagocyte NADPH oxidase activity by binding to Src homology 3 domains of p47 phox. Proc Natl Acad Sci U S A, 1996. 93(12): p. 6014-8.

169. Ikeda, Y., et al., PR-39, a proline/arginine-rich antimicrobial peptide, exerts cardioprotective effects in myocardial ischemia-reperfusion. Cardiovasc Res, 2001. 49(1): p. 69-77.

170. Butler, J., Thermodynamic Considerations of Free Radical Reactions. Toxicology of the Human Enviroment, ed. C.J. Rhodes2000, · London: Taylor and Francis.

171. Schafer, F.Q. and G.R. Buettner, Redox environment of the cell as viewed through the redox state of the glutathione disulfide/glutathione couple. Free Radic Biol Med, 2001. 30(11): p. 1191-212.

172. Kovacic, H.N., K. Irani, and P.J. Goldschmidt-Clermont, Redox regulation of human Rac1 stability by the proteasome in human aortic endothelial cells. J Biol Chem, 2001. 276(49): p. 45856-61.

173. Djordjevic, T., et al., The expression of the NADPH oxidase subunit p22phox is regulated by a redox-sensitive pathway in endothelial cells. Free Radic Biol Med, 2005. 38(5): p. 616-30.

174. Chalupsky, K. and H. Cai, Endothelial dihydrofolate reductase: critical for nitric oxide bioavailability and role in angiotensin II uncoupling of endothelial nitric oxide synthase. Proc Natl Acad Sci U S A, 2005. 102(25): p. 9056-61.

175. Landmesser, U., et al., Oxidation of tetrahydrobiopterin leads to uncoupling of endothelial cell nitric oxide synthase in hypertension. J Clin Invest, 2003. 111(8): p. 1201-9.

176. Lenaz, G., Role of mitochondria in oxidative stress and ageing. Biochim Biophys Acta, 1998. 1366(1-2): p. 53-67.

177. Tampo, Y., et al., Oxidative stress-induced iron signaling is responsible for peroxide-dependent oxidation of dichlorodihydrofluorescein in endothelial cells: role of transferrin receptor-dependent iron uptake in apoptosis. Circ Res, 2003. 92(1): p. 56-63.

178. Dhanasekaran, A., et al., Supplementation of endothelial cells with mitochondria-targeted antioxidants inhibit peroxide-induced mitochondrial iron uptake, oxidative damage, and apoptosis. J Biol Chem, 2004. 279(36): p. 37575-87.

179. Gavalas, G.R., Nonlinear Differential Equations of Chemically Reacting Systems1968, Berlin: Springer-Verlag.

180. Heinrich, T. and S. Schuster, The Regulation of Cellular Systems1996, New York: Chapman and Hall.

181. Stephanopoulos, G., A.A. Aristidou, and J. Nielsen, Metabolic Engineering: Principles and Methodologies1998, San Diego, CA: Academic Press.

182. Palsson, B.Ø., Systems Biology: Properties of Reconstructed Networks.2006, New York: Cambridge University Press.

183. Savageau, M.A., Biochemical systems analysis. II. The steady-state solutions for an n-pool system using a power-law approximation. J Theor Biol, 1969. 25(3): p. 370-9.

184. Savageau, M.A., Biochemical systems analysis. I. Some mathematical properties of the rate law for the component enzymatic reactions. J Theor Biol, 1969. 25(3): p. 365-9.

185. Savageau, M.A., Biochemical Systems Analysis: A Study of Function and Design in Molecular Biology1976: Addison-Wesley Pub (Sd).

186. Voit, E.O., Computational Analysis of Biochemical Systems. A Practical Guide for Biochemist and Molecular Biologists2000, Cambridge, UK: Cambrige University Press.

187. Torres, N.V. and E.O. Voit, Pathway Analysis and Optimization in Metabolic Engineering2002, Cambridge, UK: Cambridge University Press.

188. Savageau, M.A., Design principles for elementary gene circuits: Elements, methods, and examples. Chaos, 2001. 11(1): p. 142-159.

189. Vera, J., et al., Power-law models of signal transduction pathways. Cell Signal, 2007. 19(7): p. 1531-41.

190. Atkinson, M.R., et al., Development of genetic circuitry exhibiting toggle switch or oscillatory behavior in Escherichia coli. Cell, 2003. 113(5): p. 597-607.

191. Davies, P.F., Flow-mediated endothelial mechanotransduction. Physiol Rev, 1995. 75(3): p. 519-60.

192. Gimbrone, M.A., Jr., et al., Endothelial dysfunction, hemodynamic forces, and atherogenesis. Ann N Y Acad Sci, 2000. 902: p. 230-9; discussion 239-40.

193. Resnick, N. and M.A. Gimbrone, Jr., Hemodynamic forces are complex regulators of endothelial gene expression. FASEB J, 1995. 9(10): p. 874-82.

194. Go, Y.M., et al., Protein kinase B/Akt activates c-Jun NH(2)-terminal kinase by increasing NO production in response to shear stress. J Appl Physiol, 2001. 91(4): p. 1574-81.

195. Sorescu, G.P., et al., Bone morphogenic protein 4 produced in endothelial cells by oscillatory shear stress stimulates an inflammatory response. J Biol Chem, 2003. 278(33): p. 31128-35.

196. Hwang, J., et al., Oscillatory shear stress stimulates endothelial production of O2- from p47phox-dependent NAD(P)H oxidases, leading to monocyte adhesion. J Biol Chem, 2003. 278(47): p. 47291-8.

197. Dimmeler, S., et al., Upregulation of superoxide dismutase and nitric oxide synthase mediates the apoptosis-suppressive effects of shear stress on endothelial cells. Arterioscler Thromb Vasc Biol, 1999. 19(3): p. 656-64.

198. Brooks, A.R., P.I. Lelkes, and G.M. Rubanyi, Gene expression profiling of human aortic endothelial cells exposed to disturbed flow and steady laminar flow. Physiol Genomics, 2002. 9(1): p. 27-41.

199. Voit, E.O., Cannonical Nonlinear Modeling. S-System Approach to Understanding Complexity1991, New York: Van Nostrand Reinhold.

200. Leong, L.M. and P.M. Brickell, Bone morphogenic protein-4. Int J Biochem Cell Biol, 1996. 28(12): p. 1293-6.

201. Chang, K., et al., Bone morphogenic protein antagonists are coexpressed with bone morphogenic protein 4 in endothelial cells exposed to unstable flow in vitro in mouse aortas and in human coronary arteries: role of bone morphogenic protein antagonists in inflammation and atherosclerosis. Circulation, 2007. 116(11): p. 1258-66.

202. Massague, J., TGF-beta signal transduction. Annu Rev Biochem, 1998. 67: p. 753-91.

203. Clempus, R.E. and K.K. Griendling, Reactive oxygen species signaling in vascular smooth muscle cells. Cardiovasc Res, 2006. 71(2): p. 216-25.

204. Sauer, H., M. Wartenberg, and J. Hescheler, Reactive oxygen species as intracellular messengers during cell growth and differentiation. Cell Physiol Biochem, 2001. 11(4): p. 173-86.

205. Kroll, M.H., et al., Protein kinase C is activated in platelets subjected to pathological shear stress. J Biol Chem, 1993. 268(5): p. 3520-4.

206. Mohan, S., et al., IkappaBalpha-dependent regulation of low-shear flow-induced NF-kappa B activity: role of nitric oxide. Am J Physiol Cell Physiol, 2003. 284(4): p. C1039-47.

207. Collins, T., Endothelial nuclear factor-kappa B and the initiation of the atherosclerotic lesion. Lab Invest, 1993. 68(5): p. 499-508.

208. Goel, G., I.C. Chou, and E.O. Voit, Biological systems modeling and analysis: a biomolecular technique of the twenty-first century. J Biomol Tech, 2006. 17(4): p. 252-69.

209. Kreyszig, E., Advanced Engineering Mathematics 7th ed. 1993, New York: John Wiley and Sons.

210. Voit, E.O., Computational Analysis of Biochemical Systems. A Practical Guide for Biochemists and Molecular Biologists2000, Cambridge, UK: Cambridge University Press. 531.

211. Boo, Y.C. and H. Jo, Flow-dependent regulation of endothelial nitric oxide synthase: role of protein kinases. Am J Physiol Cell Physiol, 2003. 285(3): p. C499-508.

212. Mowbray, A.L., et al., Laminar shear stress up-regulates peroxiredoxins (PRX) in endothelial cells: PRX 1 as a mechanosensitive antioxidant. J Biol Chem, 2008. 283(3): p. 1622-7.

213. Boo, Y.C., et al., Shear stress stimulates phosphorylation of eNOS at Ser(635) by a protein kinase A-dependent mechanism. Am J Physiol Heart Circ Physiol, 2002. 283(5): p. H1819-28.

214. Inoue, N., et al., Shear stress modulates expression of Cu/Zn superoxide dismutase in human aortic endothelial cells. Circ Res, 1996. 79(1): p. 32-7.

215. Oyehaug, L., E. Plahte, and S.W. Omholt, Targeted reduction of complex models with time scale hierarchy--a case study. Math Biosci, 2003. 185(2): p. 123-52.

216. Mocek, W.T., R. Rudnicki, and E.O. Voit, Approximation of delays in biochemical systems. Math Biosci, 2005. 198(2): p. 190-216.

217. Chou, I.C. and E.O. Voit, Recent developments in parameter estimation and structure identification of biochemical and genomic systems. Math Biosci, 2009. 219(2): p. 57-83.

218. Goel, G., I.C. Chou, and E.O. Voit, System estimation from metabolic time-series data. Bioinformatics, 2008. 24(21): p. 2505-11.

219. Vilela, M., et al., Parameter optimization in S-system models. BMC Syst Biol, 2008. 2: p. 35.

220. Sasaki, K., S. Bannai, and N. Makino, Kinetics of hydrogen peroxide elimination by human umbilical vein endothelial cells in culture. Biochim Biophys Acta, 1998. 1380(2): p. 275-88.

221. Duerrschmidt, N., et al., NO-mediated regulation of NAD(P)H oxidase by laminar shear stress in human endothelial cells. J Physiol, 2006. 576(Pt 2): p. 557-67.

222. Csiszar, A., et al., Downregulation of bone morphogenetic protein 4 expression in coronary arterial endothelial cells: role of shear stress and the cAMP/protein kinase A pathway. Arterioscler Thromb Vasc Biol, 2007. 27(4): p. 776-82.

223. Li, J.M. and A.M. Shah, Mechanism of endothelial cell NADPH oxidase activation by angiotensin II. Role of the p47phox subunit. J Biol Chem, 2003. 278(14): p. 12094-100.

224. Mehta, P.K. and K.K. Griendling, Angiotensin II cell signaling: physiological and pathological effects in the cardiovascular system. Am J Physiol Cell Physiol, 2007. 292(1): p. C82-97.

225. Papaharalambus, C.A. and K.K. Griendling, Basic mechanisms of oxidative stress and reactive oxygen species in cardiovascular injury. Trends Cardiovasc Med, 2007. 17(2): p. 48-54.

226. Mueller, C.F., et al., ATVB in focus: redox mechanisms in blood vessels. Arterioscler Thromb Vasc Biol, 2005. 25(2): p. 274-8.

227. Yin, W., H. Jo, and E.O. Voit, Systems analysis of the role of bone morphogenic protein 4 in endothelial inflammation. Ann Biomed Eng, 2010. 38(2): p. 291-307.

228. Banfi, B., et al., Two novel proteins activate superoxide generation by the NADPH oxidase NOX1. J Biol Chem, 2003. 278(6): p. 3510-3.

229. Lassegue, B. and K.K. Griendling, Nox is playing with a full deck in vascular smooth muscle, a commentary on "Noxa1 is a central component of the smooth muscle NADPH oxidase in mice". Free Radic Biol Med, 2006. 41(2): p. 185-7.

230. Kroviarski, Y., et al., Phosphorylation of NADPH oxidase activator 1 (NOXA1) on serine 282 by MAP kinases and on serine 172 by protein kinase C and protein kinase A prevents NOX1 hyperactivation. FASEB J, 2010. 24(6): p. 2077-92.

231. Moskwa, P., et al., Participation of Rac GTPase activating proteins in the deactivation of the phagocytic NADPH oxidase. Biochemistry, 2002. 41(34): p. 10710-6.

232. Decoursey, T.E. and E. Ligeti, Regulation and termination of NADPH oxidase activity. Cell Mol Life Sci, 2005. 62(19-20): p. 2173-93.

233. Touyz, R.M., G. Yao, and E.L. Schiffrin, c-Src induces phosphorylation and translocation of p47phox: role in superoxide generation by angiotensin II in human vascular smooth muscle cells. Arterioscler Thromb Vasc Biol, 2003. 23(6): p. 981-7.

234. Karathanassis, D., et al., Binding of the PX domain of p47(phox) to phosphatidylinositol 3,4-bisphosphate and phosphatidic acid is masked by an intramolecular interaction. EMBO J, 2002. 21(19): p. 5057-68.

235. Touyz, R.M. and E.L. Schiffrin, Ang II-stimulated superoxide production is mediated via phospholipase D in human vascular smooth muscle cells. Hypertension, 1999. 34(4 Pt 2): p. 976-82.

236. Zafari, A.M., et al., Arachidonic acid metabolites mediate angiotensin II-induced NADH/NADPH oxidase activity and hypertrophy in vascular smooth muscle cells. Antioxid Redox Signal, 1999. 1(2): p. 167-79.

237. Kim, J.S., et al., Regulation of Nox1 activity via protein kinase A-mediated phosphorylation of NoxA1 and 14-3-3 binding. J Biol Chem, 2007. 282(48): p. 34787-800.

238. Voit, E.O., A First Course in Systems Biology2012, New York, NY: Garland Science.

239. Lyle, A.N. and K.K. Griendling, Modulation of vascular smooth muscle signaling by reactive oxygen species. Physiology (Bethesda), 2006. 21: p. 269-80.

240. Garrido, A.M. and K.K. Griendling, NADPH oxidases and angiotensin II receptor signaling. Mol Cell Endocrinol, 2009. 302(2): p. 148-58.

241. Lavigne, M.C., et al., Genetic demonstration of p47phox-dependent superoxide anion production in murine vascular smooth muscle cells. Circulation, 2001. 104(1): p. 79-84.

242. Touyz, R.M., et al., Redox-dependent MAP kinase signaling by Ang II in vascular smooth muscle cells: role of receptor tyrosine kinase transactivation. Can J Physiol Pharmacol, 2003. 81(2): p. 159-67.

243. Ueyama, T., M. Geiszt, and T.L. Leto, Involvement of Rac1 in activation of multicomponent Nox1- and Nox3-based NADPH oxidases. Mol Cell Biol, 2006. 26(6): p. 2160-74.

244. Nishizuka, Y., Protein kinase C and lipid signaling for sustained cellular responses. FASEB J, 1995. 9(7): p. 484-96.

245. Nishizuka, Y. and S. Nakamura, Lipid mediators and protein kinase C for intracellular signalling. Clin Exp Pharmacol Physiol Suppl, 1995. 22(1): p. S202-3.

246. Griendling, K.K., T. Tsuda, and R.W. Alexander, Endothelin stimulates diacylglycerol accumulation and activates protein kinase C in cultured vascular smooth muscle cells. J Biol Chem, 1989. 264(14): p. 8237-40.

247. Shinomura, T., et al., Synergistic action of diacylglycerol and unsaturated fatty acid for protein kinase C activation: its possible implications. Proc Natl Acad Sci U S A, 1991. 88(12): p. 5149-53.

248. Lang, U. and M.B. Vallotton, Effects of angiotensin II and of phorbol ester on protein kinase C activity and on prostacyclin production in cultured rat aortic smooth-muscle cells. Biochem J, 1989. 259(2): p. 477-83.

249. Chardonnens, D., et al., Comparison of the effects of angiotensin II and vasopressin on cytosolic free calcium concentration, protein kinase C activity, and prostacyclin production in cultured rat aortic and mesenteric smooth muscle cells. J Cardiovasc Pharmacol, 1989. 14 Suppl 6: p. S39-44.

250. Griendling, K.K., et al., Sustained diacylglycerol formation from inositol phospholipids in angiotensin II-stimulated vascular smooth muscle cells. J Biol Chem, 1986. 261(13): p. 5901-6.

251. Delafontaine, P., et al., Potassium depletion selectively inhibits sustained diacylglycerol formation from phosphatidylinositol in angiotensin II-stimulated, cultured vascular smooth muscle cells. J Biol Chem, 1987. 262(30): p. 14549-54.

252. Griendling, K.K., et al., Angiotensin II stimulation of vascular smooth muscle phosphoinositide metabolism. State of the art lecture. Hypertension, 1987. 9(6 Pt 2): p. III181-5.

253. Lassegue, B., et al., Phosphatidylcholine is a major source of phosphatidic acid and diacylglycerol in angiotensin II-stimulated vascular smooth-muscle cells. Biochem J, 1993. 292 (Pt 2): p. 509-17.

254. Lassegue, B., et al., Angiotensin II-induced phosphatidylcholine hydrolysis in cultured vascular smooth-muscle cells. Regulation and localization. Biochem J, 1991. 276 (Pt 1): p. 19-25.

255. Rao, G.N., et al., Angiotensin II stimulates phosphorylation of high-molecular-mass cytosolic phospholipase A2 in vascular smooth-muscle cells. Biochem J, 1994. 299 (Pt 1): p. 197-201.

256. Brock, T.A., et al., Angiotensin increases cytosolic free calcium in cultured vascular smooth muscle cells. Hypertension, 1985. 7(3 Pt 2): p. I105-9.

257. Alexander, R.W., et al., Angiotensin increases inositol trisphosphate and calcium in vascular smooth muscle. Hypertension, 1985. 7(3 Pt 1): p. 447-51.

258. Adimora, N.J., D.P. Jones, and M.L. Kemp, A model of redox kinetics implicates the thiol proteome in cellular hydrogen peroxide responses. Antioxid Redox Signal, 2010. 13(6): p. 731-43.

259. Ushio-Fukai, M., et al., Epidermal growth factor receptor transactivation by angiotensin II requires reactive oxygen species in vascular smooth muscle cells. Arterioscler Thromb Vasc Biol, 2001. 21(4): p. 489-95.

260. Ushio-Fukai, M., et al., Angiotensin II receptor coupling to phospholipase D is mediated by the betagamma subunits of heterotrimeric G proteins in vascular smooth muscle cells. Mol Pharmacol, 1999. 55(1): p. 142-9.

261. Saward, L. and P. Zahradka, Angiotensin II activates phosphatidylinositol 3-kinase in vascular smooth muscle cells. Circ Res, 1997. 81(2): p. 249-57.

262. Basset, O., et al., NADPH oxidase 1 deficiency alters caveolin phosphorylation and angiotensin II-receptor localization in vascular smooth muscle. Antioxid Redox Signal, 2009. 11(10): p. 2371-84.

263. Touyz, R.M. and E.L. Schiffrin, Increased generation of superoxide by angiotensin II in smooth muscle cells from resistance arteries of hypertensive patients: role of phospholipase D-dependent NAD(P)H oxidase-sensitive pathways. J Hypertens, 2001. 19(7): p. 1245-54.

264. Bhalla, U.S. and R. Iyengar, Emergent properties of networks of biological signaling pathways. Science, 1999. 283(5400): p. 381-7.

265. Eguchi, S., et al., Calcium-dependent epidermal growth factor receptor transactivation mediates the angiotensin II-induced mitogen-activated protein kinase activation in vascular smooth muscle cells. J Biol Chem, 1998. 273(15): p. 8890-6.

VITA

Weiwei Yin

Weiwei Yin was born in Dalian, a beautiful coastal city in North China. She received a B.A. in Electrical Engineering from Zhejiang University and a M.A. in Computer Science from Institute of Automation, Chinese Academy of Science. In fall 2005, she entered the bioengineering program in Georgia Institute of Technology and joined Dr. Voit's lab to start another M.A study. During the following two years, she focused on the research of human sleep-wake cycle and investigated the particular role of the neurotransmitter - orexin by using pure mathematical modeling method. In the spring of 2007, she has completely finished her master courses and thesis and successfully passed her thesis defense and got the M.A degree. After this successful experience, she realized the power of mathematical modeling and computational methods as complementary methods to experiments in the field of system biology as well as the demand and necessity of using the system point of view to investigate the traditional issues in cell biology and molecular biology. Therefore, she decided to continue to pursue a doctorate in the same program and the same lab and use again the mathematical modeling and computational methods to investigate the diseases in traditional cardiovascular system. During her doctoral studies, she published several papers for both theoretical models and real applications of these models to investigate complex biological systems. She also presented her work at several worldwide conferences, including two International Conferences on Molecular System Biology (ICMSB 2006 and 2009) and the BMES Annual Meeting 2010.